



Virginia Tech

Wake Forest University

School of Biomedical Engineering and Sciences

12th Annual Graduate Student Research Symposium



May 16th, 2013

The Inn at Virginia Tech
Skelton Conference Center
Blacksburg, VA

Sponsored By:



A Letter from the Organizers

Dear Attendees,

Welcome to the 12th Annual School of Biomedical Engineering & Sciences Graduate Student Research Symposium, hosted by the VT-WFU Biomedical Engineering Society Student Chapter!

The Virginia Tech-Wake Forest University School of Biomedical Engineering & Sciences (SBES) is a joint graduate program that was formed in 2003 to bring together three prestigious academic institutions: the College of Engineering at Virginia Tech, the Wake Forest University School of Medicine, and the Virginia-Maryland College of Veterinary Medicine. Each university contributes diverse educational and research opportunities to the students, providing a unique graduate experience.

The VT-WFU Biomedical Engineering Society (BMES) Student Chapter was founded to bridge the gap between these academic institutions and foster communication and collaboration among various research groups. Our mission is to encourage the development, dissemination, integration and utilization of knowledge in biomedical engineering, as well as enhance interaction within the scientific community. The chapter offers unique ways for students to become involved in outreach projects, research collaborations, and social events with other biomedical engineering students, faculty and industry. We are involved in many service and outreach opportunities within the local community and participate annually at the BMES National meeting.

Our BMES Student Chapter hosts the SBES Graduate Student Research Symposium to provide students and faculty the opportunity to interact and exchange research ideas with colleagues and industry personnel. We would like to thank our sponsors Altair, BMES, Cook Medical, Medtronic, and Simulia for their generous support. We greatly appreciate your participation and hope that this symposium will promote enhanced discussion and collaboration among researchers. Thank you for your attendance!

The VT-WFU BMES Executive Committee

Vanessa Alphonse
Ashley Hayes
Presidents

Patrick Thayer
Jill Urban
Vice Presidents

Laura Reese
Emma Moran
Secretaries

Alana Sampson
Nick Vavalle
Treasurers

Chris Rylander
VT Faculty Advisor

Joel Stitzel
WFU Faculty Advisor



8:00

REGISTRATION, Skelton Foyer
POSTER SET UP, Latham B and Drillfield
REFRESHMENTS, Latham B

9:00 -
5:00

ADVISORY BOARD MEETING, Smithfield Conference Room

9:00

ALL - WELCOME, Latham A: Vanessa Alphonse & Ashley Hayes, VT-WFU BMES Presidents

M.S. Oral Presentations- Session 1

9:30-10:30 , Latham A

M.S. Oral Presentations- Session 2

9:30-10:30 , Duck Pond

	Page Number		Page Number
9:30 Determining the Effectice Time Period of Slip-Induced Gait Adaptations	1	9:30 Contactless Dielectrophoresis: Development of New Microdevices for Cell Sorting	9
<i>Danielle N. Beringer¹, Michael L. Madigan¹, and Sara L. Matrangola¹</i> ¹ Virginia Tech, Blacksburg, VA		<i>Elizabeth Savage Elvington¹, Mike Sano¹, and Rafael V. Davalos¹</i> ¹ Virginia Tech, Blacksburg, VA	
9:45 Comparative Studies of System Models for Iterative CT Image Reconstruction	3	9:45 A Comparison of Methods for Measuring Damage in Medial Collateral Ligaments	11
<i>Chuang Miao¹, and Hengyong Yu^{1,2}</i> ¹ Virginia Tech, Blacksburg, VA, ² Wake Forest University, Winston-Salem, NC		<i>Victor A. Stewart¹, Raffaella De Vita¹, Michael Madigan¹, Jake Socha¹</i> ¹ Virginia Tech, Blacksburg, VA	
10:00 Validation of Simulated Data in Frontal and Lateral Loading Using a Human Body Finite Element Model	5	10:00 Magnetic Resonance Imaging Movies for Multivariate Analysis of Speech	13
<i>Ashley R. Hayes¹, Nicholas A. Vavalle¹, Daniel P. Moreno¹, Joel D. Stitzel¹, and F. Scott Gayzik¹</i> ¹ Wake Forest University, Winston-Salem, NC		<i>Kate McRoberts¹, Johnathan Lisinski¹, Brad Sutton², and Stephen LaConte¹</i> ¹ Virginia Tech, Blacksburg, VA, ² University of Illinois, Urbana-Champaign, IL	
10:15 Cell Death Characterization in Tumor Constructs Using Irreversible Electroporation	7	10:15 Validation and Sensitivity Analysis of a Finite Element Model of THOR-NT Dummy for Injury Prediction under Vertical Impact Loading	15
<i>Katherine J. Prokop¹, Paulo A. Garcia¹, Christopher B. Arena¹, and Rafael V. Davalos¹</i> ¹ Virginia Tech, Blacksburg, VA		<i>Jacob B. Putnam¹, and Costin D. Untaroiu¹</i> ¹ Virginia Tech, Blacksburg, VA	

10:30

COFFEE BREAK, Latham B

Ph.D. Oral Presentations- Session 1

10:45-11:45 , Latham A

Ph.D. Oral Presentations- Session 2

10:45-11:45 , Duck Pond

- 10:45 Development of a Novel Tissue Engineered Muscle Repair Construct with Potential for Enhanced Motor End Plate Formation and Function** 17
John B. Scott¹, Benjamin T. Corona², Catherine L. Ward², Benjamin S. Harrison¹, Justin M. Saul³, and George J. Christ¹
¹ Wake Forest University, Winston-Salem, NC, ² US Army Institute of Surgical Research, ³ Miami University, Hamilton OH
- 10:45 Augmenting Convection-Enhanced Delivery of Malignant Glioma through Simultaneous Co-Delivery of Fluid Agents and Laser Energy with a Fiberoptic Microneedle Device** 25
R. Lyle Hood¹, Rudy T. Andrian¹, John L. Roberston¹, John H. Rossmeisl¹, and Christopher G. Rylander¹
¹ Virginia Tech, Blacksburg, VA
- 11:00 The Potential of Cellulose Nanocrystals for Targeted Delivery Applications in Cancer** 19
Katelyn R. Colacino¹, Shuping Dong¹, Christopher Arena¹, Rafael Davalos¹, Maren Roman¹, and Yong Woo Lee¹
¹ Virginia Tech, Blacksburg, VA
- 11:00 Effects of Cervical Arthroplasty on Neck Response During a Simulated Frontal Impact** 27
Nicholas A. White¹, Daniel P. Moreno¹, F. Scott Gayzik¹, Wesley Hsu¹, Alexander Powers¹, and Joel D. Stitzel¹
¹ Wake Forest University, Winston-Salem, NC
- 11:15 Investigating Dielectrophoretic Properties of Cells for Cancer Treatment and Detection Applications** 21
A. Salmanzadeh¹, E.S. Elvington¹, P.C. Roberts¹, E. M. Schmelz¹, and R. V. Davalos¹
¹ Virginia Tech, Blacksburg, VA
- 11:15 Hybrid True-Color Micro-CT: Design and Applications** 29
James Bennett¹, Hengyong Yu², Guohua Cao¹, Aaron Moh³, and Ge Wang²
¹ Virginia Tech, Blacksburg, VA, ² Wake Forest University, Winston-Salem, NC, ³ Rensselaer Polytechnic Institute, Troy, NY
- 11:30 Evaluation of Repeated Biphasic Conducting Materials for Peripheral Nerve Repair** 23
Tabitha Rosenbalm¹, Nicole Levi-Polyachenko¹, Louis Argenta¹, William D. Wagner¹, and Michael Morykwas¹
¹ Wake Forest University, Winston-Salem, NC
- 11:30 Injury Mechanisms in Roadside Motorcycle Collisions** 31
Allison Daniello¹ and H. Clay Gabler¹
¹ Virginia Tech, Blacksburg, VA

11:45

LUNCH, Latham CDEF

Poster Session A
1:00-1:30 , Latham B

Poster Session A
1:00-1:30 , Drillfield

Poster Session B
1:30-2:00, Latham B

Poster Session B
1:30-2:00 , Drillfield

Ph.D. Oral Presentations- Session 3
2:15-3:15 , Latham A

Ph.D. Oral Presentations- Session 4
2:15-3:15 , Duck Pond

- | | |
|--|---|
| <p>2:15 Morphological Analysis of Changes in the Thoracic Skeleton with Age and Gender 33
<i>Ashley A. Weaver¹, Callistus M. Nguyen¹, Samantha L. Schoell¹, and Joel D. Stitzel¹</i>
¹ Wake Forest University, Winston-Salem, NC</p> | <p>2:15 Case Study on High-Frequency Irreversible Electroporation (H-FIRE) for the Treatment of Squamous Cell Carcinoma 41
<i>Christopher B. Arena¹, Michael B. Sano¹, Paulo A. Garcia¹, M. Nichole Rylander¹, J. Mike Cissell¹, John L. Roberston¹, and Rafael V. Davalos¹</i>
¹ Virginia Tech, Blacksburg, VA</p> |
| <p>2:30 Shear Stress-Mediated Tumor-Endothelial Cross Talk Reulgates the Angiogenic Potential of Breast Tumors <i>In Vitro</i> 35
<i>Cara F. Buchanan¹, Elizabeth E. Voigt¹, Pavlos P. Vlachos¹, and M. Nichole Rylander¹</i>
¹ Virginia Tech, Blacksburg, VA</p> | <p>2:30 Chemotactic Live Autonomous Drug Delivery Agents with Different Body Shapes 43
<i>Ali Sahari¹, Mahama A. Traore¹, and Bahareh Behkam¹</i>
¹ Virginia Tech, Blacksburg, VA</p> |
| <p>2:45 Neuroglial Differentiation of Adult Mammalian Enteric Neuronal Progenitor Cells as a Function of Extracellular Matrix Composition 37
<i>Shreya Raghavan¹, and Khalil N. Bitar¹</i>
¹ Wake Forest University, Winston-Salem, NC</p> | <p>2:45 Myo-Inositol as a Biomarker in the Rats Exposed to Blast Overpressure with Observed Impaired Working Memory and Elevated Anxiety 45
<i>Sujith Sajja¹, Shane A. Perrine², Farhad Ghoddouss², Matthew P. Galloway², Pamela J. VandeVord^{1,3}</i>
¹ Virginia Tech, Blacksburg, VA, ² Wayne State University, Detroit, MI, ³ John D. Dingell Veteran's Administration Medical Center, Detroit, MI</p> |
| <p>3:00 The Effects of Ethanol Exposure on Non-Human Primate Brain Networks 39
<i>Qawi K. Telesford¹, April T. Davenport¹, Robert A. Kraft¹, Paul J. Laurienti¹, and James A. Daunais¹</i>
¹ Wake Forest University, Winston-Salem, NC</p> | <p>3:00 Skeletal Muscle Contraction and System Tracking in Feedback Control 47
<i>Paola Jaramillo¹, Adam Shoemaker¹, and Alexander Leonessa¹</i>
¹ Virginia Tech, Blacksburg, VA</p> |

3:15

COFFEE BREAK, Latham B

Ph.D. Oral Presentations- Session 5

3:30-4:30 , Latham A

Ph.D. Oral Presentations- Session 6

3:30-4:30, Duck Pond

3:30 Abdominal Injury Biomechanics 49
Meghan K. Howes¹ and Warren N. Hardy¹
¹ Virginia Tech, Blacksburg, VA

3:30 Development of Methodologies for High Accuracy Wall Shear Stress Estimations in Medical Devices 57
Jaime S. Raben¹ and Pavlos Vlachos¹
¹ Virginia Tech, Blacksburg, VA

3:45 Kerateine Biomaterials Bridge Critically-Sized Rat Mandibular Defects with Minimal Ectopic Bone Growth through Controlled Release of Bone Morphogenic Protein-2 51
Christine Kowalczewski^{1,2}, Seth Tombylin³, David Wasnick², Mary Ellenburg³, Michael Callahan¹, Thomas Smith¹, Mark Van Dyke¹, Luke Burnett³, and Justin Saul²
¹ Wake Forest University, Winston-Salem, NC, ² Miami University, Hamilton, OH, ³ KeraNetics, LLC Winston-Salem, NC

3:45 Detecting Burn Severity and the Associated Inflammation Responses Using Thermal Measurements in Living Tissue-Modeling and Experimental Approaches 59
Abdusalam I. K. Al-Khwaji¹, Tom Diller¹, and Brian Vick¹
¹ Virginia Tech, Blacksburg, VA

4:00 Smarter Cars: Injury and Fatality Reductions of Collision Avoidance Technologies 53
Kristofer D. Kusano¹ and Hampton C. Gabler¹
¹ Virginia Tech, Blacksburg, VA

4:00 Influence of Freeze-Thawed Effect on the Stress-Strain Curves of Bovine Liver Tissues 61
Yuan-Chiao Lu¹, Costin D. Untaroui¹
¹ Virginia Tech, Blacksburg, VA

4:15 Development of Mechanical Optical Clearing Devices for Improved Light Delivery in Optical Diagnostics 55
William C. Vogt¹, and Christopher G. Rylander¹
¹ Virginia Tech, Blacksburg, VA

4:15 Injury Risk in Side Impact of Non-Tracking Vehicles into Guardrail 63
Nicholas S. Johnson¹ and Hampton C. Gabler¹
¹ Virginia Tech, Blacksburg, VA

4:45

ALL - AWARDS AND CLOSING REMARKS, Latham A

Poster Number	Room	Session	Poster Title and Authors	Page Number
1	Latham B	A	Non-Destructive Imaging and Characterization of Tissue-Engineered Blood Vessel Growth within a Bioreactor Using OCT <i>Abhijit A. Gurjarpadhye¹, and Christopher G. Rylander¹</i> ¹ Virginia Tech, Blacksburg, VA	65
2	Latham B	B	Analysis of Event Data Recorder Survivability in Crashes with Fire, Immersion, and High Delta-V <i>Ada H. Tsoi¹, John C Hinch¹, and Hampton C. Gabler¹</i> ¹ Virginia Tech, Blacksburg, VA	67
3	Latham B	A	The Influence of Combinatorial Shear and Thermal Stress on Pre-Osteoblasts for Bone Regeneration <i>Alana Sampson¹ and Nichole Rylander¹</i> ¹ Virginia Tech, Blacksburg, VA	69
4	Latham B	B	Mechanics of Collagen Type I and its Crosslinks <i>Albert Kwansa¹, Raffaella De Vita¹, and Joseph W. Freeman²</i> ¹ Virginia Tech, Blacksburg, VA, ² Rutgers University, Brunswick, NJ	71
5	Latham B	A	Three Dimensional <i>In Vitro</i> Tumor Model to Study Folic Acid Conjugated Cellulose Nanocrystals Binding and Uptake Ability to Folate Receptor Positive Cancer Cells <i>Alexander L. Callo¹, Katelyn R. Colacino¹, Shuping Dong¹, Maren Roman¹, and Yong Woo Lee¹</i> ¹ Virginia Tech, Blacksburg, VA	73
6	Latham B	B	Age-Related Changes to Shoulder Musculature in a Vervet Monkey Model <i>Anthony C. Santango II¹, Johannes F. Plate¹, Thomas L. Smith¹, and Katherine R. Saul¹</i> ¹ Wake Forest University, Winston-Salem, NC	75
7	Latham B	A	FEA Simulation Comparison for Crash Test Modeling of Frontal Impacts using Hybrid-III ATD <i>Caitlin M. Weaver¹, Kerry A. Danelson¹, Adam J. Golman¹, and Joel D. Stitzel¹</i> ¹ Wake Forest University, Winston-Salem, NC	77
8	Latham B	B	3D Integrated Organ Printing for Ear Reconstruction <i>Carlos Kengla¹, Hyun-Wook Kang¹, and Sang Jin Lee¹</i> ¹ Wake Forest University, Winston-Salem, NC	79
9	Latham B	A	Electroporation-Delivered Protein Biosensors for Study of Molecular Activity <i>Chen Sun¹, Yi Wang², Yingxiao Wang¹, and Chang Lu¹</i> ¹ Virginia Tech, Blacksburg, VA, ² University of California-San Diego, La Jolla, CA	81
10	Latham B	B	Ankle and Knee Mechanics during Athletic Maneuvers in Adults With and Without Ankle Instability <i>Courtney A. (Haynes) Webster¹, Maury A. Nussbaum¹</i> ¹ Virginia Tech, Blacksburg, VA	83
11	Latham B	A	Sensitivity of Shoulder Joint Forces to Muscle Changes Associated with Brachial Plexus Birth Palsy <i>Dustin L. Crouch¹, Johannes F. Plate¹, Zhongyu Li¹, and Katherine R. Saul¹</i> ¹ Wake Forest University, Winston-Salem, NC	85
12	Latham B	B	Tubular Esophageal Tissue Construct Bioengineered from Isolated Esophageal Circular Smooth Muscle Cells <i>Elie Zakhem¹ and Khalil N. Bitar¹</i> ¹ Wake Forest University, Winston-Salem, NC	87
13	Latham B	A	META-ICA Reveals MEG Networks in Pediatric Subjects <i>Elizabeth M. Davenport¹, Christopher T. Whitlow¹, Alexander K. Powers¹, Justin B. Rawley¹, Inna V. McGowin¹, Greg Alberto¹, Taylor Bungo¹, Dwayne W. Godwin¹, Megan M. Thompson¹, Jillian E. Urban¹, Joel D. Stitzel¹, and Joseph A. Maldjian¹</i> ¹ Wake Forest University, Winston-Salem, NC	89
14	Latham B	B	Effect of Multi-Walled Carbon Nanotubes on Breast Cancer Adhesion <i>Elizabeth G. Graham¹, and Nicole H. Levi-Polyachenko¹</i> ¹ Wake Forest University, Winston-Salem, NC	91
15	Latham B	A	Estimation of Skull Table Thickness from Clinical CT <i>Elizabeth M. Lillie¹, Jillian E. Urban¹, Ashley A. Weaver¹, and Joel D. Stitzel¹</i> ¹ Wake Forest University, Winston-Salem, NC	93

Poster Number	Room	Session	Poster Title and Authors	Page Number
18	Latham B	B	Fiber Based Imaging on Electrospun Scaffold <i>Etai Sapoznik¹, Peng Lu², Guoguang Niu¹, Tracy L. Criswell¹, Young Xu², and Shay Soker¹</i> ¹ Wake Forest University, Winston-Salem, NC, ² Virginia Tech, Blacksburg, VA	99
19	Latham B	A	Migratory Behavior of Cells in the Presence of Dual and Opposing Cues <i>Gaurav Jain¹, and Padmavathy Rajagopalan¹</i> ¹ Virginia Tech, Blacksburg, VA	101
20	Latham B	B	Silk Based Tissue Engineered Muscle Repair (TEMR) Construct for Controlled Recovery in Volumetric Muscle Loss (VML) Injuries <i>Hannah B. Baker¹, Catherine Ward², Benjamin T. Corona², Masood Machingal¹, Jelana Rnjak³, David L. Kaplan³, and George J. Christ¹</i> ¹ Wake Forest University, Winston-Salem, NC ² USA Institute for Surgical Research, ³ Tufts University, Medford, MA	103
21	Latham B	A	Preliminary fMRI Study of Verbal-Associative Memory <i>Harshawardhan U. Deshpande¹, and Stephen M. La Conte¹</i> ¹ Virginia Tech, Blacksburg, VA	105
22	Latham B	B	Fabrication of Engineered Porcine Kidney Scaffold for <i>In Vivo</i> Implantation <i>Jennifer Huling¹, In Kap Ko¹, Anthony Atala¹, and James Yoo¹</i> ¹ Wake Forest University, Winston-Salem, NC	107
23	Latham B	A	Cumulative Impact Analysis of Head Impact Exposure in Youth Football <i>Jillian E. Urban¹, Elizabeth M. Davenport¹, Alexander K. Powers¹, Joseph A. Maldjia¹, Christopher T. Whitlow¹, and Joel D. Stitzel¹</i> ¹ Wake Forest University, Winston-Salem, NC	109
24	Latham B	B	Particulate Oxygen Generating Substances (POGS) as Oxygen Source for Islet Isolation and Processing <i>JP McQuilling¹, Sivanandane Sittadjody¹, Shruti Balaji¹, Benjamin Harrison¹, Alan C Farney¹, and Emmanuel C Opara¹</i> ¹ Wake Forest University, Winston-Salem, NC	111
25	Latham B	A	Molecular and Cellular Mechanisms of Blast-Induced Neurotrauma <i>Hyung Joon Cho¹, Sujith Sajja¹, Pamela J. VandeVord^{1,2}, and Yong Woo Lee¹</i> ¹ Virginia Tech, Blacksburg, VA, ² Veterans Affairs Medical Center, Salem, VA	113
26	Latham B	B	Design of a Force Probe System for Active Pull of a Single Cell <i>Kevin T. Sheets¹, and Amrinder S. Nain¹</i> ¹ Virginia Tech, Blacksburg, VA	115
27	Latham B	A	Short Term Mild Traumatic Brain Injury Mechanisms Characterized in an <i>In Vivo</i> Gottingen Minipig Model <i>Liz M. Fievisohn¹, Sujith V. Sajja¹, Bethany M. Vaughn¹, Pamela J. VandeVord¹ and Warren Hardy¹</i> ¹ Virginia Tech, Blacksburg, VA	117
28	Latham B	B	Quantification of the Transport of Live Autonomously Drug Particles (Drugbots) in Tumor Spheroids Interstitium <i>Mahama A. Traore¹, Ali Sahari¹, and Bahareh Behkam¹</i> ¹ Virginia Tech, Blacksburg, VA	119
29	Latham B	A	The Development of Volumetric Organs from a Multi-Modality Image Dataset for Use in a Small Female Full-Body Finite Element Model <i>Matthew L. Davis¹, Ashley R. Hayes¹, F. Scott Gayzik¹, Daniel P. Moreno¹, and Joel D. Stitzel¹</i> ¹ Wake Forest University, Winston-Salem, NC	121
30	Latham B	B	Elucidating the Temporal Effects of Temperature On Transport Properties and Efficacy of Multimodal Photothermal and Chemotherapy Treatments <i>Matthew R. DeWitt¹, Kristen A. Zimmermann¹, and Marissa N. Rylander¹</i> ¹ Virginia Tech, Blacksburg, VA	123
31	Latham B	A	Arterial Transit Time Mapping with Pseudo-continuous Arterial Spin Labeling MRI: Monte Carlo Simulation and Implementation with Variable TR <i>Megan E. Johnston¹, Joseph A. Maldjian¹, and Youngkyoo Jun¹</i> ¹ Wake Forest University, Winston-Salem, NC	125

Poster Number	Room	Session	Poster Title and Authors	Page Number
32	Drillfield	B	Coronary Artery Cross Sectional Area with Non-Contrast Cardiac CT: Technique and Feasibility Testing Mingna Zheng ¹ , John Jeffrey Carr ¹ , Yankua Yang ¹ , and Yaorong Ge ¹ ¹ Wake Forest University, Winston-Salem, NC	127
33	Drillfield	A	Blood-Brain Barrier on Chip: Drug Delivery Enhancement by Electroporation Mohammad Bonakdar ¹ , and Rafael V. Davalos ¹ ¹ Virginia Tech, Blacksburg, VA	129
34	Drillfield	B	Experimental Measurement of the Utricle's Dynamic Response Myles Dunlap ¹ and Wally Grant ¹ ¹ Virginia Tech, Blacksburg, VA	131
35	Drillfield	A	The Development of a Simplified Thorax Model for Parametric Studies of a Full Body Finite Element Model Nicholas A. Vavalle ¹ , Daniel P. Moreno ¹ , Joel D. Stitzel ¹ , and F. Scott Gayzik ¹ ¹ Wake Forest University, Winston-Salem, NC	133
36	Drillfield	B	A Composite Mesh for Ligament Tissue Engineering Patrick S. Thayer ¹ , Anna F. Dimling ¹ , Daniel S. Plessl ¹ , Mariah R. Hahn ² , Scott A. Guelcher ² , and Aaron S. Goldstein ¹ ¹ Virginia Tech, Blacksburg, VA, ² Rensselaer Polytechnic Institute, Troy, NY, ³ Vanderbilt University, Nashville, TN	135
37	Drillfield	A	Natural Aging Effects on Tendon-to-Bone Healing in a Rat Model of Rotator Cuff Repair Johannes Plate ¹ , Philip Brown ¹ , Jordan Walters ¹ , John Clark ¹ , Thomas Smith ¹ , Christopher Tuohy ¹ , and Sandeep Mannava ¹ ¹ Wake Forest University, Winston-Salem, NC	137
38	Drillfield	B	Cancer Cell Migration Dynamics in Mechanistically Tunable Fibrous Scaffolds Puja Sharma ¹ , Shikha Bhatia ¹ , Carolyn Hughes ¹ , Colin Ng ¹ , and Amrinder S. Nain ¹ ¹ Virginia Tech, Blacksburg, VA	139
39	Drillfield	A	Smartphone Based Clinical Assessments in Frail Patients Rahul Soangra ¹ and Thurmon E. Lockhart ¹ ¹ Virginia Tech, Blacksburg, VA	141
40	Drillfield	B	Head Impact Exposure in Middle School Football Ray W. Daniel ¹ , Steven Rowson ¹ , and Stefan Duma ¹ ¹ Virginia Tech, Blacksburg, VA	143
41	Drillfield	A	Injectable and Self-Assembling Sponge as a Protective Layer at Device-Tissue Interfaces in Wound Repair Rui Wang ¹ , Louis C. Argenta ¹ , Michael J. Morykwas ¹ , and William D. Wagner ¹ ¹ Wake Forest University, Winston-Salem, NC	145
42	Drillfield	B	Electroporation Enhances Antisense Effect of Peptide Nucleic Acids Against Intracellular Bacteria Sai Ma ¹ , Mammalwar Sriranganathan ¹ , and Chang Lu ¹ ¹ Virginia Tech, Blacksburg, VA	147
43	Drillfield	A	Development of an Occult Metric for Common Motor Vehicle Crash Injuries Samantha L. Schoell ¹ , Ashley Weaver ¹ , and Joel Stitzel ¹ ¹ Wake Forest University, Winston-Salem, NC	149
44	Drillfield	B	Knowledge Intensive Learning in Disease Risk Prediction Shuo Yang ¹ , and Siraam Natarajan ¹ ¹ Wake Forest University, Winston-Salem, NC	151
45	Drillfield	A	Kinetics of Relaxed Volunteers, Braced Volunteers, and Hybrid III ATD in Low-Speed Frontal Sled Tests Stephanie Beeman ¹ , Andrew R. Kemper ¹ , Michael L. Madigan ¹ , and Stefan M. Duma ¹ ¹ Virginia Tech, Blacksburg, VA	153
46	Drillfield	B	Jumping on Water: Locomotion Dynamics of <i>Acris Spp.</i> and <i>E. Cyanophlyctis</i> Talia M. Weiss ¹ ¹ Virginia Tech, Blacksburg, VA	155

<i>Poster Number</i>	<i>Room</i>	<i>Session</i>	<i>Poster Title and Authors</i>	<i>Page Number</i>
47	Drillfield	A	Development of Hyaluronan Based Nanoparticles for Intraoperative Breast Cancer Imaging <i>Tanner Hill¹ and Aaron Mohs¹</i> ¹ Wake Forest University, Winston-Salem, NC	157
48	Drillfield	B	Head Impact Exposure in Youth Football: Elementary School Ages 7 to 8 Years and the Effect of Returning Players <i>Tyler J. Young¹, Ray W. Daniel¹, Steven Rowson¹, and Stefan M. Duma¹</i> ¹ Virginia Tech, Blacksburg, VA	159
49	Drillfield	A	Porcine Eye Response to Blast Overpressure <i>Vanessa D. Alphonse¹, Andrew R. Kemper¹, Craig McNally¹, Ian P. Herring¹, Philip J. Brown¹, Joel D. Sitzel², and Stefan M. Duma¹</i> ¹ Virginia Tech, Blacksburg, VA, ² Wake Forest University, Winston-Salem, NC	161
50	Drillfield	B	Creation of Novel Flow Systems Inspired by Insects Utilizing Microfabrication Techniques <i>Yahya Hosseini¹ and Masoud Agah¹</i> ¹ Virginia Tech, Blacksburg, VA	163
51	Drillfield	A	Ultrasensitive Microfluidic Device for the Studying of DNA-Protein Interactions from Small Number of Cells <i>Zhenning Cao¹, Changya Chen², Kai Tan², and Chang Lu¹</i> ¹ Virginia Tech, Blacksburg, VA, ² University of Iowa, Iowa City IA	165



Special thanks to Cook Medical for their continued support of the SBES Graduate Student Research Symposium. We encourage you to visit their website to learn how they have impacted the medical world with their research.

Cook Medical, Endoscopy Division, was founded in Winston-Salem in 1982 by Don Wilson and Cook Medical founder Bill Cook. Originally called Wilson-Cook Medical, the small start-up company has grown dramatically in 26 years and now has a workforce of approximately 600 area employees who occupy six buildings at its campus on Bethania Station Road.

Those employees design, develop and manufacture medical devices – used mostly in conjunction with a flexible endoscope, which is used to treat esophageal, stomach, pancreatic, liver and colon disorders. The products are distributed to clinics and hospitals around the country and around the world. With its special focus on innovative medical accessories, the company has been able to significantly reduce procedure times, and consequently, overall healthcare costs.

The company's dedication to advancing medical technology is further evidenced by educational and support programs. The company allocates grants and fellowships to a large number of organizations and facilities – including Wake Forest Baptist Medical Center – to enhance education and growth within the medical field.

Cook Medical Endoscopy Division's parent company, Cook Medical – headquartered in Bloomington, Indiana – manufactures more than 15,000 different products across 42 physician specialties, making it the largest privately held medical device manufacturer in the world.

For more information, please visit Cook Medical's website at www.cookmedical.com

**Cook Medical
Endoscopy Division
4900 Bethania Station Rd.
Winston-Salem, NC 27105**



Thank you to the Biomedical Engineering Society for their gracious sponsorship of the 2013 SBES Graduate Student Research Symposium. Please visit their website to learn how they have become the leading society of professionals devoted to developing and using engineering to advance human health and well being.

Who We Are

The Biomedical Engineering Society (BMES) is the leading organization for innovators in biomedical research and development. Our members are researchers from major universities, government agencies, students, doctors and BME industry leaders in all biomedical disciplines worldwide.

The Vision of BMES is to serve as the world's leading society of professionals devoted to developing and using engineering and technology to advance human health and well-being.

The Mission of the BMES is to build and support the biomedical engineering community, locally, nationally and internationally, with activities designed to communicate recent advances, discoveries, and inventions; promote education and professional development; and integrate the perspectives of the academic, medical, governmental, and business sectors.

Leading and emerging researchers use BMES as a platform for sharing the latest information and research in the profession. BMES provides industry members exposure to an expanding market. Advertising and sponsorship opportunities can help increase your company's publicity year-round.

For more information, please visit the BMES website at www.bmes.org

Contact: Jennifer Edwards
8201 Corporate Drive, Suite 1125
Landover, MD 20785-2224
301-459-1999
regina@bmes.org



Thank you to Medtronic for their gracious sponsorship of the 2013 SBES Graduate Student Research Symposium. Visit Medtronic's website to discover how they are creating life-changing therapies to help people with chronic diseases.

Medtronic

When Life Depends on Medical Technology

At Medtronic, we're changing the face of chronic disease. By working closely with physicians around the world, we create therapies to help patients do things they never thought possible. Our medical technologies help make it possible for millions of people to resume everyday activities, return to work, and live better, longer. We're able to do this with the help of some very special people around the world: 38,000 dedicated employees who share a passionate purpose to improve lives, thousands of medical professionals who share their insights and ideas, and hundreds of advocacy associations that help us share information so people with debilitating diseases know relief is possible.

For more information, visit Medtronic's website at www.medtronic.com.

Medtronic
Vascular Innovations
3576 Unocal Place
Santa Rosa, CA 95403-1774



Altair

Thank you to Altair for their gracious sponsorship of the 2013 SBES Graduate Student Research Symposium. Visit Altair's website to discover how they are impacting health.

Altair empowers client innovation and decision-making through technology that optimizes the analysis, management and visualization of business and engineering information.

Privately held with more than 1,800 employees, Altair operates more than 40 offices throughout 19 countries.

With a 27-year-plus track record for product design, advanced engineering software, on-demand computing technologies and enterprise analytics solutions, Altair consistently delivers a competitive advantage to more than 3,000 corporate clients representing the automotive, aerospace, government and defense, heavy equipment and consumer products verticals. Altair also has a growing client presence in the electronics, architecture engineering and construction, and energy markets.

For more information, visit Altair's website at <http://www.altair.com/>.

World Headquarters

1820 East Big Beaver Rd
Troy, MI 48083
USA



Thank you to Simulia for their gracious sponsorship of the 2013 SBES Graduate Student Research Symposium. Visit Simulia's website to discover how they are impacting the life sciences.

Since it was created in 1981, Dassault Systemes has helped its industrial customers maximize product design and development. First used to design complex shapes, 3D now makes it possible to design and manufacture products creating digital mockups. Today, Dassault Systemes anticipates the industrial processes of tomorrow, with solutions that provide a 3D view of a product's lifecycle, from creation to maintenance, including manufacturing and recycling.

Historically, simulation has not played as large a role in Life Sciences as it has in more traditional engineering industries like Automotive or Aerospace. This is due to the fact that the Life Sciences industry is often driven by innovators - a select few inventors who create products that are then marketed by larger companies. In addition, the simulation of human systems and their interaction is considerably more difficult and less evolved than the simulation of metal components. Human tissue response is complex and not easily simulated with simplified models. Material modeling of medical devices, such as composite implants, for example, is also challenging. Finally, the loads applied to both tissue and devices are often not well understood.

For more information, visit Simulia's website at <http://www.3ds.com/products/simulia>.

**Rising Sun Mills
166 Valley Street
Providence, RI 02909-2499
United States**

12th Annual Graduate Student
Research Symposium
Oral and Poster Abstracts

DETERMINING THE EFFECTIVE TIME PERIOD OF SLIP-INDUCED GAIT ADAPTATIONS

Danielle N. Beringer¹, Michael L. Madigan^{1,2}, and Sara L. Matrangola¹

1. Virginia Tech, School of Biomedical Engineering and Sciences

1. Virginia Tech, Engineering Science and Mechanics

Corresponding Author: Danielle N. Beringer, Email: dberinger@vt.edu

INTRODUCTION

Falls are a significant source of unintentional injury and medical costs in the United States. In 2005, there were more than 8.7 million emergency department visits made to U.S. hospitals due to fall-related injuries, making up 20% of all injury visits [1]. Claims for occupational fall-related injuries make up about 25% of all worker's compensation costs in the United States, estimated to total more than \$6 billion annually [2]. The high rates of fall-related injuries and associated medical costs highlight the importance of research into the mechanisms and prevention of falls.

Slipping events are responsible for the loss of balance that leads to a large proportion of falls [2, 3, 4]. The U.S. National Health Interview Survey determined that 64% of all occupational falls resulting in injury were due to slipping, tripping, or stumbling [2]. The relationship between frictional properties at the shoe-floor interface and the minimum friction required by an individual to support walking is the primary determinant of a slipping event [4, 6]. The minimum frictional requirement during walking, or required coefficient of friction (RCOF), is determined by gait biomechanics and can be altered to reduce the risk of slipping [6].

The biomechanics of slips are commonly studied in laboratory settings in an effort to improve the understanding of slip mechanics for the advancement of slip and fall prevention strategies and risk assessment methods [3, 5]. One challenge in this research area has been the ability to reproduce natural slips in experimental settings. Previous studies have demonstrated that both awareness of a slippery environment and prior slip experience alter an individual's gait. Since most experimental slips occur with prior awareness or

experience of a slip, the validity of extrapolating results to slips occurring in the real world is limited [3, 5, 7].

This study aimed to determine the duration of time that gait alterations remain effective after a laboratory slip experience. Results from this study will aid in the experimental design of future studies involving laboratory slips. An understanding of the effective time period of gait adaptations will facilitate future researchers in refraining from analyzing this altered gait, ensuring results are descriptive of natural, unexpected slips.

METHODOLOGY

Thirty-one healthy individuals between the ages of 18 and 31 were recruited to participate in the study. The Virginia Tech Institutional Review Board approved this study and informed consent was obtained from each subject prior to participation.

Each subject completed four sessions consisting of several walks at a controlled speed. Subjects were told they may be slipped at any point during the study and were instructed to walk normally rather than anticipating a slip. Baseline gait measures were collected for several trials during the first three sessions before the subjects were slipped. During the third session subjects experienced a slip on a thin layer of vegetable. The walkway and shoes were cleaned and dried to restore their original state and walking trials were immediately continued to document post-slip gait alterations. Subjects returned for a final session 1, 2, 4, or 6 weeks after the slip experience to reassess gait measures after the break period.

Using ground reaction force and 3-D motion data, eight dependent variables were generated to quantify gait: RCOF, foot and shank angle, stance time, step time, step length, peak braking shear, and loading rate. Repeated measures ANOVA and post hoc Tukey HSD tests were used to investigate differences in each parameter between baseline, post-slip, and post-break measurements. Statistical analyses were performed using JMP 9 (SAS Institute Inc., Cary, NC).

RESULTS AND DISCUSSION

Analyzing all 31 participants collectively, most gait parameters significantly decreased from baseline after the slip experience, including shank angle, step time, peak braking shear, RCOF ($p < 0.0001$), foot angle ($p < 0.005$), and stance time ($p < 0.05$) as shown in figure 1. On average, step length increased and loading rate decreased, but neither was significant.

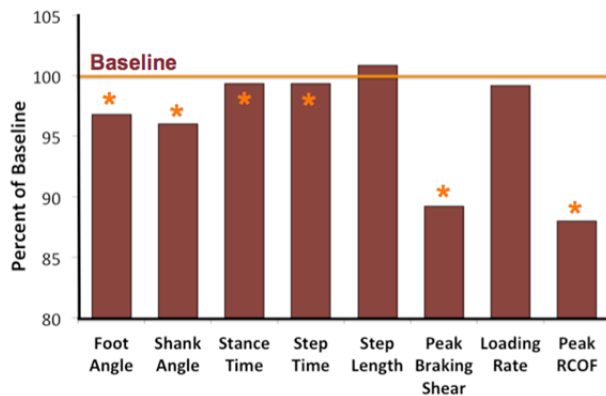


Figure 1: Change of gait parameters from baseline after a slip experience.

The gait alterations observed post-slip correlated with findings from previous studies [3, 7]. Decreases in peak braking shear, RCOF, foot angle, and shank angle have been correlated with a reduced risk of slipping. Therefore, the subjects adopted a cautious gait in response to the slip experience even though they were instructed to walk naturally.

To investigate the effect of various length post-slip break periods on the return of gait parameters to baseline, the subjects were grouped by break length (1, 2, 4, or 6 weeks) for analysis. Due to the smaller sample size, RCOF was the only parameter that showed statistical significance between baseline, post-slip, and post-break sessions. The RCOF was not significantly different between the post-slip and four post-break sessions, which were all significantly lower than the RCOF at the three collective baseline sessions.

There were several limitations of this study that should be addressed in future work. RCOF was the only gait parameter able to be analyzed long-term to determine if the gait biomechanics returned to baseline. Future work should use larger sample sizes to enable analysis of additional gait parameters. Also, the long-term effects were only analyzed up to six weeks after the slip experience, which was not sufficient for gait recovery to baseline. Longer post-slip breaks should be investigated in future studies.

CONCLUSIONS

This study determined that some aspects of the gait alterations observed in response to a slip experience remain altered for up to six weeks after the slip. Future work is needed to assess the long-term alteration in RCOF beyond the six-week time period, as well as the long-term changes in additional gait parameters relevant to risk of slipping. A more complete understanding of the effective time period of post-slip gait alterations will aid in the experimental design of future studies involving laboratory slips, which will facilitate future researchers in refraining from analyzing altered gait, ensuring results are descriptive of natural, unexpected slips.

REFERENCES

1. Nawar EW, Niska RW, Xu J. National hospital ambulatory medical care survey: 2005 emergency department summary. *Emergency*. 2007;110:4,000.
2. Courtney TK, Sorock GS, Manning DP, et al. Occupational slip, trip, and fall-related injuries – can the contribution of slipperiness be isolated? *Ergonomics*. 2001;44(13):1118-1137.
3. Cham R, Redfern MS. Changes in gait when anticipating slippery floors. *Gait & Posture*. 2002;15(2):159-171.
4. Redfern MS, Cham R, Gielo-Perczak K, et al. Biomechanics of slips. *Ergonomics*. 2001;44(13):1138-1166.
5. Grönqvist R, Abeysekera J, Gard G, et al. Human-centred approaches in slipperiness measurement. *Ergonomics*. 2001;44(13):1167-1199.
6. Chang W-R, Chang C-C, Matz S. Comparison of different methods to extract the required coefficient of friction for level walking. *Ergonomics*. 2012;55(3):308-315.
7. Heiden TL, Sanderson DJ, Inglis JT, et al. Adaptations to normal human gait on potentially slippery surfaces: the effects of awareness and prior slip experience. *Gait & Posture*. 2006;24(2):237-246.

COMPARATIVE STUDIES OF SYSTEM MODELS FOR ITERATIVE CT IMAGE RECONSTRUCTION

Chuang Miao¹, Hengyong Yu^{1,2}

1. Biomedical Imaging Division, VT-WFU School of Biomedical Engineering and Sciences
 2. Department of Radiology, Division of Radiologic Sciences, Wake Forest University Health Sciences
- Corresponding Author: Hengyong Yu, Email: hyu@wakehealth.edu

INTRODUCTION

Computed tomography (CT) image reconstruction is a process of recovering a cross sectional image from projection data. The system model is required for image reconstruction, artefact correction, or simulation purposes. To our best knowledge, current system models can be divided into three categories [1]. The first is the *pixel-driven* model (PDM), which is usually used for implementations of backprojection. The second is the *ray-driven* model (RDM), which is used for projection. The third is called the *distance-driven* model (DDM), which combines the advantages of the PDM and RDM [2]. Recently, a finite-detector-based system model was proposed by Yu and Wang [3], which was also called area integral model (AIM).

In this paper, we propose an improved distance-driven model (IDDM) whose computational cost is as low as DDM and the accuracy is comparable with AIM. The performance of different system models, such as PDM, RDM, AIM, DDM and IDDM, are compared in the content of iterative CT image reconstruction algorithms. One of the key factors that limit the clinical application of an iterative reconstruction algorithm is the high computational cost which mainly depends on system models. This study will have a direct impact on development of fast and accurate iterative CT image reconstruction algorithms.

METHODOLOGY

PDM: The PDM based approach refers to the main loop is the image pixel index. By connecting a line from the focal spot through each pixel center, a location of interaction on the detector is determined. A value is obtained from the detector samples via interpolation,

usually by linear interpolation, and this value is used to update the pixel values [4]. The corresponding projection is the transpose of the backprojecction operation. Simple PDM based approach with linear interpolation is rarely used for projection because it causes high-frequency artifacts [1].

RDM: The RDM based approach refers to the main loop is the detector element index. This approach is basically used for projection operation. In general, it connects a line from the focal spot through the image to the detector element centre. Then the weighting coefficients can be determined by bilinear interpolation [5]. Ray-driven approach is rarely used in the backprojection because it tends to introduce high frequency artifacts [1].

AIM: The AIM refers to the name by qualifying the contribution of each pixel related to the overlapped area between each pixel and each ray path. Instead of considering each ray path as an ideal line (PDM and RDM), the AIM considers an x-ray has width. In a typical fan beam geometry with curved detector, for each pixel, the weighting coefficient is defined as the corresponding overlapped area between the ray path and this pixel, which is normalized by corresponding fan-arc length. For details, please refer to [3].

DDM: The state of the art is the DDM, which combines the advantages of the PDM and RDM [1,2]. It avoids both image domain and projection domain artifacts. Therefore, it can be used in the projection and/or backprojection processes. In order to calculate the normalized weighting coefficients, the key is to calculate the length of overlap between each image pixel and each detector cell, which is used to calculate the weighting coefficient. For details, please refer to [1].

IDDM: The IDDM also considers the x-ray has width. In order to compute the weighting coefficient, instead of mapping the x-ray to the center line of the image row of interest like DDM does, we map the x-ray to the upper and lower boundaries of the row of interest. In each boundary, similar way as DDM was used to compute the weighting coefficient, the ultimate weighting coefficient is the average of the weighting coefficients computed in the upper and lower boundaries. Compare to the DDM, the IDDM considers all the contributions of related pixels in each row. Because the lower boundary in one row is the upper boundary in the next row, the computational cost of IDDM based method is similar to the DDM based method.

RESULTS

We compared different models by experiments assuming a typical fan beam geometry. The selected detector element size is larger than the pixel size. It can test the reconstruction accuracy, the likelihood of introducing artifacts and the ability of high resolution reconstruction.. This is because the reconstructed images with a pixel size smaller than the detector element size can be views as high resolution reconstruction compare to the detector resolution.

Projection of a Uniform Disk: In order to examine the forward projection model, we project a uniform disk in only one view to examine the forward projection model (especially the PDM). The magnifications of the projection are shown in Figure 1. We can see that the vibrations of PDM (upper left) based approach are very larger compare to others. Vibrations of DDM (lower left) based approach is larger compare to IDDM (lower right) and AIM (upper right). The vibrations of IDDM based approach are even smaller than AIM.

Backprojection of a Uniform View: We backproject a uniform projection in only one direction (45 degrees) to compare the backprojection model (especially the RDM). As indicated in Figure 2, there are some artifacts in the backprojection by RDM.

DISCUSSION AND CONCLUSIONS

In terms of accuracy, likelihood of introducing artifacts and high resolution reconstruction ability, AIM, DDM and IDDM based approaches outperform PDM based approach in the projection, outperform RDM based approach in the backprojection. AIM, DDM and IDDM can be used for both projection and backprojection comparing to PDM and RDM. IDDM outperforms DDM, even AIM at least in the projection operation. In the near future, we will further investigate the AIM, DDM and

IDDM by simulated and physical phantom experiments in terms of computational cost, noise performance and spatial resolution, etc.

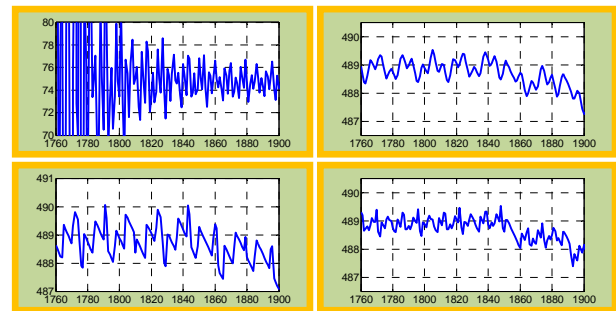


Figure 1: Magnification of projection of a uniform disk in one direction (45 degrees) with the detector element size is larger than the image pixel size. The system models are PDM (upper left), AIM (upper right), DDM (lower left) and IDDM (lower right).

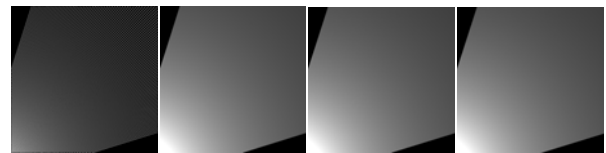


Figure 2: Backprojection of a uniform view in one direction (45 degrees) with the detector element size is larger than the image pixel size. The system models from left to right are RDM, AIM, DDM and IDDM.

REFERENCES

- [1] B. De Man and S. Basu, "Distance-driven projection and backprojection in three dimensions", *Phys. Med. Biol.*, vol. 49, p. 13, 2004.
- [2] De Man B and Basu S, "3D distance-driven projection and backprojection", *Proc. 7th Int. Conf. on Fully 3D Reconstruction in Radiology and Nuclear Medicine (Saint Malo)*, 2003.
- [3] Yu H and Wang G, "Finite detector based projection model for super resolution CT", *11th Int. Meeting on Fully Three-Dimensional Image Reconstruction in Radiology and Nuclear Medicine (Potsdam, 2011)* pp 387-90, 2011.
- [4] Peters, T.M., Algorithms for Fast Back- and Re-Projection in Computed Tomography. *IEEE transactions on nuclear science*, 1981. **28**(4): p. 3641-3647
- [5] Joseph, P.M., *An Improved Algorithm for Reprojecting Rays through Pixel Images*. Medical Imaging, IEEE Transactions on, 1982. **1**(3): p. 192-196.

VALIDATION OF SIMULATED DATA IN FRONTAL AND LATERAL LOADING USING A HUMAN BODY FINITE ELEMENT MODEL

Ashley R. Hayes^{1,2}, Nicholas A. Vavalle^{1,2}, Daniel P. Moreno^{1,2}, Joel D. Stitzel^{1,2}, and F. Scott Gayzik^{1,2}

1. Wake Forest School of Medicine

2. VT-WFU School of Biomedical Engineering and Sciences

Corresponding Author: Ashley R. Hayes, Email: arhayes@wakehealth.edu

INTRODUCTION

One method that is gaining popularity among biomechanics researchers is the use of finite element (FE) computer models [1]. More recently, researchers are turning to computational modeling of the human body for prediction and prevention of crash injuries. In this study, the Global Human Body Models Consortium (GHBM) mid-sized male seated (M50) FE model was used to examine chestband contour deformations.

Chestbands are commonly used in biomechanical studies. They are non-invasive devices placed around the thorax region that measure deformations in a transverse plane throughout an impact [2]. For this study, data from Forman et al. (2006) and Pintar et al (1997) were used as a basis of comparison for simulated chestband data [3, 4]. In the present study, the model was simulated in one of the four configurations presented by Forman; the driver position at 48 km/h with onboard force-limited 3-point belt and airbag restraints. Pintar et al. (1997) and later Maltese et al. (2002) examined chestband response in left-side lateral impacts under various conditions [5]. For this study, the impact into a rigid wall at 24 km/h was simulated. The purpose of this study is to present a methodology for extracting and analyzing virtual chestband data from a full body FE model. The method is applied to quantify the regional difference between model results and literature data in frontal and lateral impacts.

METHODOLOGY

The model was pre-programmed with an upper, middle, and lower chestband each comprised of 32 nodes. The upper and middle chestbands were used for the frontal case and the upper, middle, and lower chestbands were used for the lateral case. Chestband locations matched descriptions provided in the literature. All impact

simulations were run using LS-DYNA (LSTC, Livermore, CA, R. 4.2.1.).

Model chestband results were analyzed by using the post processor, LS-PrePost (LSTC, Livermore CA, V 4.0), and custom MATLAB (The Mathworks, R 10) code. LS-PrePost was used to visualize chestband response and obtain Cartesian coordinates of each chestband node over time. The code calculated a percent compression using the methods of Kuppa and Eppinger 1998 for the frontal case, and the methods of Pintar et al. 1997 for the lateral case [6]. The chestband coordinates from each simulation at time equal to zero and the time of maximum deflection were plotted and compared to the respective response from literature.

The chestband response of the model was compared to literature in three ways: an analysis of gross compression, an analysis of the full chestband contour, and an analysis of regional differences. To examine regional differences, a quadrant-based analysis technique for the results was introduced that enabled regional comparisons between the model and the experimental data in the anterior, posterior, right and left sections of the chestband.

RESULTS

Quantitative gross compression from the chestbands is found in .

Table 1. The table shows the maximum percent compression of each chestband from the frontal case.

Table 1. Comparison of peak percent compression of the model vs. literature chestbands in frontal case

Cases	Chestband Location	Model: % Compression	Literature: % Compression
Frontal	Upper	13.6%	23±5.6%

	Middle	12.9%	12±6.9%
--	--------	-------	---------

Figure 1 shows an example of the chestband contour response in the frontal case from literature and of the simulated model at maximum compression state. For this figure, negative Y is the model's left side, and positive X is anterior.

In regards to regional analysis, the percent difference between the chestband in the undeformed and deformed configuration, considering the upper chestband in the frontal load case, was found to range from 1.6% (5.6mm) to 11.5% (25.7mm) [Figure 2]. The largest percent difference was seen in the anterior direction in the undeformed and deformed states. As noted on Figure 2, the Δ value, difference between undeformed and max deformed states, is used to analyze the results.

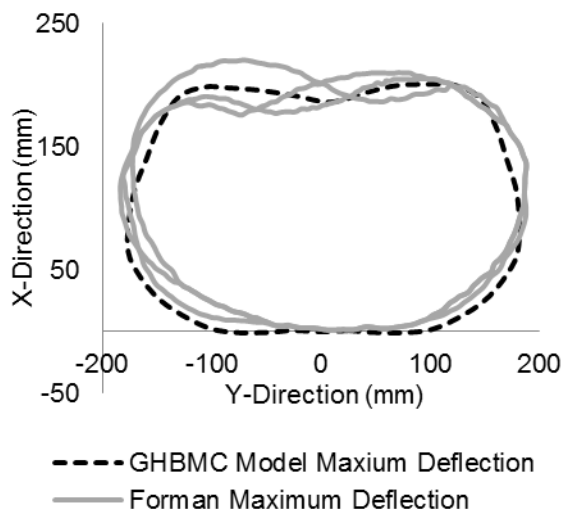


Figure 1. M50 model and literature response for upper chestband in maximum deflection state for simulated 48km/h frontal driver impact.

DISCUSSION

We have presented a method to extract virtual chestband data from a full body finite element model, quantified the response in a regional sense, and showed results relative to experimental data from two impact cases. When comparing the M50 model chestband results to the experimental data, there are clear similarities in shape at the time of maximum loading. In all cases, except the middle chestband in the frontal case, the model was found to have a smaller percent compression than the percent compression reported in the literature. These differences could result from variations in morphology and age of cadavers versus living humans. Regional analysis findings indicate that the simulated chestband reasonably captured the deformation observed in all regions. This method can now be expanded to examine loading of underlying organs during impact, and to determine if any relationships exist between organ loading and chestband profiles.

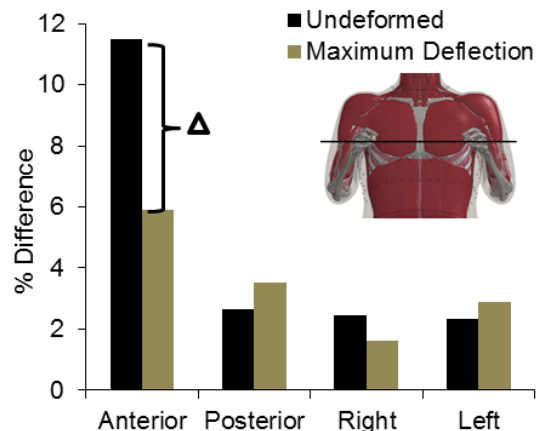


Figure 2. Percent difference between the undeformed and deformed state for the upper chestband, frontal impact case. The horizontal line in the schematic shows the location of the chestband on the model. The Δ value is difference between undeformed and max deformed states.

CONCLUSIONS

While this work was focused on techniques to extract and analyze chestband data from FE models, the comparative results provide further validation of the model used in this study. The results suggest the importance of evaluating comparisons between virtual and experimental chestband data on a regional basis. This data also provides the potential to correlate chestband deformations to the loading of underlying thoraco-abdominal structures.

ACKNOWLEDGMENTS

This work was funded and supported by the Global Human Body Models Consortium, LLC.

REFERENCES

1. Yang, K.H., et al., *Development of numerical models for injury biomechanics research: a review of 50 years of publications in the Stapp Car Crash Conference*. Stapp Car Crash J, 2006. **50**: p. 429-90.
2. Hallman, J.J., et al., *Technique for chestband contour shape-mapping in lateral impact*. J Biomech, 2011. **44**(12): p. 2328-32.
3. Forman, J., et al., *Whole-body kinematic and dynamic response of restrained PMHS in frontal sled tests*. Stapp Car Crash J, 2006. **50**: p. 299-336.
4. Pintar, F.A., et al., *Chestband analysis of human tolerance to side impact*. SAE, 1997. **106**: p. 12.
5. Maltese, M.R., et al., *Response corridors of human surrogates in lateral impacts*. Stapp Car Crash J, 2002. **46**: p. 321-51.
6. Kuppa, S. and R. Eppinger, *Development of an Improved Thoracic Injury Criterion*. Stapp Car Crash J, 1998. **42**.

CELL DEATH CHARACTERIZATION IN TUMOR CONSTRUCTS USING IRREVERSIBLE ELECTROPORATION

Katherine J. Prokop¹, Paulo A. Garcia¹, Christopher B. Arena¹, and Rafael V. Davalos¹

1. School of Biomedical Engineering and Science (SBES), Virginia Tech-Wake Forest University

Corresponding Author: Katherine Prokop, Email: kprokop@vt.edu

INTRODUCTION

Prostate cancer is one of the most prevalent cancers in the US with an estimated 238,590 new cases developing in 2013. According to the American Cancer Society 29,720 of these cases will result in death (1,2). Prostate cancer is the most frequently diagnosed cancer in men often not presenting symptoms until more advanced stages at which time metastasis to bone can occur. While the survival rates for prostate cancer are high compared to many others with 5 year survival rates of 100% and 93% 15 year survival, new therapies for the disease need to be investigated. Current treatments include surgery, chemotherapy, radiation therapy, immunotherapy, and vaccine therapy (2).

Current treatments are often complicated by prostate anatomy making tumors inoperable and increasing the risk of urinary and erectile dysfunction (1). New therapies are necessary to eradicate these challenges and improve treatment of cancer. Irreversible electroporation (IRE) is a non-thermal ablation method to kill cancer cells utilizing pulsed electric fields (PEF) that disrupt the plasma membranes of cancer cells to such a point that they cannot recover. IRE treatments use short duration, high-intensity PEF to create defects in the plasma membranes of cells that become irreversible if performed above an electric field threshold (3-6). IRE offers benefits over other cancer therapies in that it can be performed near large blood vessels and ducts without damage or heat sink effects, sparing the extracellular matrix (3,5).

While clinical trials for prostate, pancreatic, kidney, liver, and lung cancer are in the beginning phases, more information about the electric field thresholds required to kill cancer cells are necessary as well as to improve

treatment planning (6). Here we use a 3D platform to extrapolate the electric field information.

METHODOLOGY

A 3D in vitro tumor model was used to determine the electric field thresholds for prostate cancer. This hydrogel model consists of a collagen I matrix seeded with cancer cells at a concentration of 5×10^6 cells/mL. This in vitro tumor offers a more in vivo like environment for obtaining cell thresholds over in vitro studies without requiring the use of animal models. Cells spread out and attach in an in vivo like manner within the collagen I matrix which is a main component of both tumors and the extracellular matrix in your body.

Grade IV prostate adenocarcinoma cells (PC 3) were seeded within ~10mm diameter hydrogels composed of rat tail collagen I at a concentration of 8mg/mL and neutralizing buffer (10X DMEM, 1N NaOH, and dH₂O). The hydrogels were incubated overnight and treated the following day with 3.35 mm center-to-center spaced stainless steel electrodes having a 1.3mm diameter. IRE treatments consisted of 80 pulses with 100 μ s duration at voltages of 300V, 375V, and 450V. Following treatment, hydrogels were incubated for 2 hours, 24 hours, and 48 hours in order to eliminate reversible effects as well as to determine the appropriate time post-treatment for analysis. A live/dead assay of calcein AM and propidium iodide assessed cell viability and a Leica DMI 6000 fluorescent microscope (Leica Microsystems, Buffalo Grove, IL) was used to tile images, reconstructing the entire hydrogel. Lesion areas were measured from these images and the electric field threshold calculated by correlating the experimental and computational lesion dimensions.

Calculations of the electric field threshold required for cell death were determined using finite element analysis (COMSOL Multiphysics 4.2a, Stockholm, Sweden). The model reconstructed the 3D geometry of the hydrogel and electrode set-up and the electric field was calculated at points from the center to the edge along the hydrogel as seen in Figure 2a and b. The width measurements of the lesion area were the most variable and therefore were used to determine the electric field threshold at the transition between live and dead cells as previously described in Arena *et al* (6).

RESULTS

The electric field threshold required for cell death remained consistent between the treatment time groups as well as the applied voltages of 300V, 375V, and 450V. The lesion areas produced from the IRE treatment increased in size with increasing voltage. With 300V pulses applied, the lesion dimensions produced were 4.91 ± 0.04 mm in length by 3.89 ± 0.09 mm in width. The lesion dimension increased with increasing voltage so that at 375 V the lesion measured 5.21 ± 0.06 mm by 4.59 ± 0.04 mm and at 450V applied the lesion dimensions were 5.52 ± 0.10 mm by 5.54 ± 0.12 mm. The treatment groups were randomly chosen and all 36 treatments were performed at the same time. Staining with a live/dead assay took place 2hrs, 24hrs, and 48hrs post-treatment. Imaging on a Leica DMI 6000 fluorescent microscope (Leica Microsystems, Buffalo Grove, IL) allowed visualization of the lesion area as seen in Figure 1 of which length and width of the cell death area were measured in the LAS software (Leica Application Suite).

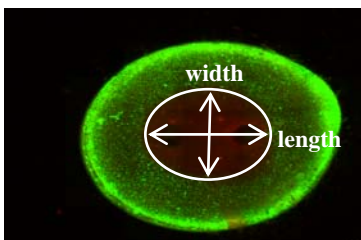


Figure 1: PC-3 hydrogel with 450V

By correlating the experimental lesions with the calculated electric field distribution, it was found that the electric field threshold for cell death for PC-3 cells is 533 ± 7 V/cm. Additionally, the electric field threshold was similar between the 2hr, 24hr, and 48hr time points indicating that analysis at all of these time points should be comparable.

The electric field thresholds between different cell lines needs to be determined for IRE. Further research plans to use other prostate cell lines to determine whether the electric field threshold between different prostate cell lines is similar. Additionally, research will be done to determine the difference or similarities in the electric field

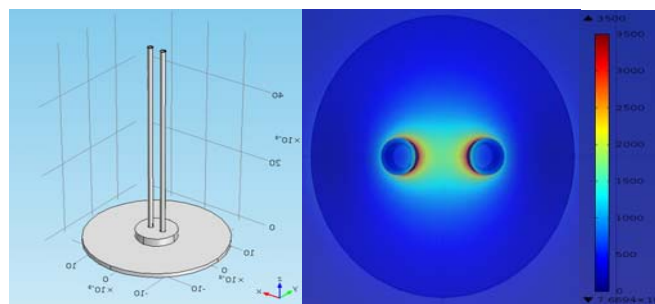


Figure 2: a) Hydrogel finite element model and b) electric field distribution (V/cm) between the electrodes

threshold between different cancerous cell lines such as pancreatic and brain cancer.

CONCLUSIONS

IRE is a promising new ablation therapy to treat cancer with pulsed electric fields, however, the electric field thresholds for cell death are still not known between cell lines. This research determined that the electric field threshold required to kill prostate cancer cells (PC-3 cells) seeded within an in vitro tumor was 533 ± 7 V/cm. Further research needs to be done to look into whether the cell death threshold is consistent between prostate cancer cell lines and whether it is consistent between different cancer cell lines. Expansion of this model will help IRE gain further acceptance as a cancer therapy.

ACKNOWLEDGMENTS

This work was supported by MultiSTEPS IGERT and AngioDynamics. The author thanks Dr. Christopher Szot for help with this work.

REFERENCES

1. American Cancer Society. Cancer Facts & Figures 2013. Atlanta: American Cancer Society; 2013.
2. National Cancer Institute. *Prostate Cancer* <<http://www.cancer.gov/cancertopics/types/prostate>> 2013.
3. Davalos, R. V., I. L. Mir, and B. Rubinsky. 2005. Tissue ablation with irreversible electroporation. *Ann. Biomed. Eng.* 33:223–231.
4. Onik, G., P. Mikus, and B. Rubinsky. 2007. Irreversible electroporation: implications for prostate ablation. *Technol. Cancer Res. Treat.* 6:295–300.
5. Onik, G., and B. Rubinsky. 2010. Irreversible electroporation: first patient experience focal therapy of prostate cancer. In *Irreversible Electroporation*. B. Rubinsky, editor. Springer, Berlin/Heidelberg. 235–247.
6. Arena, C. B., C. S. Szot, et al. (2012). "A three-dimensional in vitro tumor platform for modeling therapeutic irreversible electroporation." *Biophysical journal* 103(9): 2033-2042.

CONTACTLESS DIELECTROPHORESIS: DEVELOPMENT OF NEW MICRODEVICES FOR CELL SORTING

Elizabeth Savage Elvington¹, Mike Sano¹, Rafael V. Davalos¹

1. School of Biomedical Engineering & Sciences, Virginia Tech-Wake Forest University

Corresponding Author: Rafael Davalos, Email: davalos@vt.edu

INTRODUCTION

Contactless dielectrophoresis is a microfluidic cell manipulation and characterization strategy based on the phenomenon dielectrophoresis (DEP), the translational motion of polarized particles in a non-uniform electric field.¹ DEP is useful for sorting, enrichment, and isolation of cells² based on their intrinsic biophysical properties. In contrast to common cell isolation techniques such as flow cytometry and magnetic-activated cell sorting, DEP does not require prior knowledge and labeling of surface markers of target cells. However, traditional DEP requires metal electrodes patterned within a sample microchannel.³ Direct contact between metal electrode and a biological sample can result in adverse effects such as electrolysis, fouling, and electrode delamination.

To eliminate these issues, cDEP replaces metallic electrodes with fluidic electrode channels filled with a highly conductive fluid. Upon applying an alternating current (AC) signal, the electrode channels are capacitively coupled to the sample channel. cDEP has been used to isolate different stages of breast cancer cell lines,⁴ tumor initiating cells from cancer cells,⁵ and cancer cells from blood cells,⁶ among other applications.

A challenge for current cDEP devices is achieving high-throughput sufficient for isolate-and-culture applications. A multilayer design has showed promise in demonstrating DEP forces at flows reaching 1 ml/hr and theoretically operates at low frequencies.⁷ Here, we introduce a new multilayer cDEP device consisting of a straight sample channel below curved interdigitated electrode channels. By including slightly tapered, curved electrodes, the DEP force varies across the channel width, which we suggest will allow continuous sorting of more two or more cell types simultaneously.

METHODOLOGY

The dielectrophoretic force on a particle is described by the equation

$$\mathbf{F}_{DEP} = 2\pi r^3 \epsilon_m Re[(\epsilon_p^* - \epsilon_m^*) / (\epsilon_p^* + 2\epsilon_m^*)] \nabla(\mathbf{E} \cdot \mathbf{E}),$$

which includes contributions from the particle biophysics and the geometry of the device. To optimize the design, the performance of devices with varied electrode geometries was predicted by a parametric study (Table 1).

Table 1: Values for Parametric Study on $\nabla(\mathbf{E} \cdot \mathbf{E})$

<i>Geometric Parameter</i>	<i>Values</i>
Angle of curvature	35, 40, 45, 50, 55, 60, 65
Electrode width-to-gap ratio	1:1, 2:1, 3:1, 4:1
Number of electrode pairs	4, 6, 8, 10, 12

A 2D Autocad (Autocad 2012—Student Version, Autodesk Inc, San Rafael, CA, USA) drawing of each electrode geometry was created and imported into COMSOL Multiphysics 4.3 (Comsol Inc., Burlington, MA, USA) to solve for the electric field distribution. The Laplace equation, $\nabla \cdot (\sigma^* \nabla \phi) = 0$ (where σ^* is the complex conductivity) was solved for the potential distribution ϕ , given boundary conditions of 100 V and ground applied at the inlets of the source and ground electrode channels, respectively. $\nabla(\mathbf{E} \cdot \mathbf{E})$ was calculated using ϕ . Design performance was first assessed by the ability to generate field gradients of magnitude greater than $1 \times 10^{12} \text{ (m} \cdot \text{kg}^2 \text{) / (s}^6 \text{ - A}^2 \text{)}$, the minimum threshold for manipulation of cells by cDEP (Figure 1).⁸ If the minimum threshold was surpassed for all or most electrode pairs, the design was then compared against the next parametrically-varied geometry. The objective was the generation of sufficient DEP force across each electrode pair. The parameter value that led to the greatest magnitude of $\nabla(\mathbf{E} \cdot \mathbf{E})$ consistently across all electrode pairs was selected as the optimized value for that particular parameter.

Experimental devices consisted of stacked polydimethylsiloxane (PDMS) (Sylgard 184, Dow Corning, USA) layers containing microfluidic channels. The PDMS channel layers were fabricated from a master silicon stamp etched with the device geometry. The PDMS layers were bonded together upon exposure to air plasma, and the stacked device was then bonded to a glass microscope slide.

RESULTS & DISCUSSION

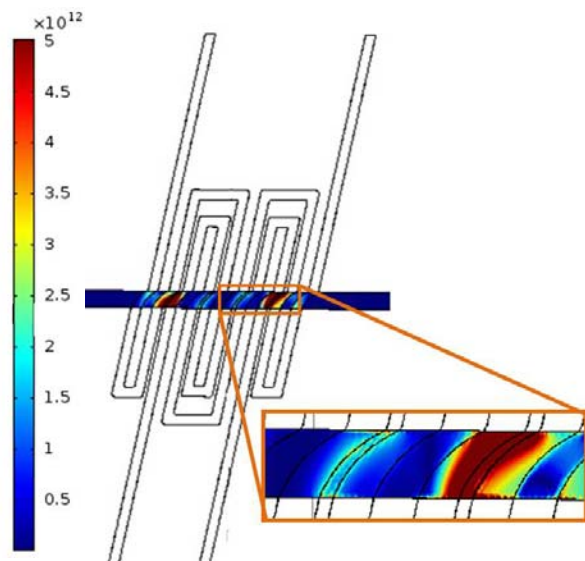


Figure 1: Surface plot of $\nabla(\mathbf{E} \cdot \mathbf{E})$ 15 μm below the sample channel ceiling. This device had 45° curves, 4 pairs of electrodes, and a 3:1 electrode width-to-gap ratio.

It was determined that fewer pairs of electrodes in series provide more consistent DEP force along the sample channel. Intuitively, it would be expected that more pairs of electrodes in series would expose cells flowing through the sample channel to DEP force for a longer time, which would result in increased separation resolution. However, the length of these interdigitated electrodes leads to high electrical resistance, resulting in a significant voltage drop down the channel, and virtually no voltage drop across channels in the center of the series. This prevents sufficient dielectrophoretic force in those regions. Therefore, increasing the number of electrode pairs in this design is actually detrimental to cell sorting. However, increasing the depth of the electrode channel or breaking it into segments and adding more inlets can reduce the resistance. The magnitude of $\nabla(\mathbf{E} \cdot \mathbf{E})$ was greater for wider electrodes, with a ratio of 4:1 producing the highest values. Based on Green *et al's* numerical solution for DEP force generated using straight interdigitated electrodes, higher electrode width-to-gap ratios were expected to produce greater gradients far from the electrodes.⁹ Preliminary computational results suggest no

clear trend between the angle of curvature and the magnitude of $\nabla(\mathbf{E} \cdot \mathbf{E})$. However, we predict that the effect of curvature is on the direction of the DEP force and thus will be more visible in an experimental setting when observing cell response. Finally, we expected slight tapering of the curve to slightly increase $\nabla(\mathbf{E} \cdot \mathbf{E})$ near the top of the channel, which was generally confirmed by plotting $\nabla(\mathbf{E} \cdot \mathbf{E})$ near the bottom of the channel, at the centerline, and near the top of the channel (Figure 2).

CONCLUSIONS

This study presents a new cDEP device and theoretical modeling used to choose specific design parameters. Previous devices have focused on inducing DEP force by changing the geometry of the sample channel, while this design allows the sample to flow unimpeded through a straight channel and induces DEP force by the shape of the electrodes. Validation studies will be conducted using live cells in a low conductivity buffer. Future work will explore the effect of reducing electrode channel resistance to enable inclusion of more electrode pairs, which we expect to increase resolution of cell separations. Additionally, we will fabricate this device using techniques that can deepen the sample channel, increasing throughput to the scale of 1 ml/hr.

ACKNOWLEDGMENTS

This material is based in part on work supported by the National Science Foundation under grant no. EFRI 0938047. The authors would like to thank members of the BEMS lab, specifically Alireza Salmanzadeh and Lisa Anders, for their support.

REFERENCES

1. H. A. Pohl, *Dielectrophoresis*, Cambridge University Press, 1978.
2. Z. R. Gagnon, *Electrophoresis*, 2011, **32**, 2466-2487.
3. R. Pethig, *Biomicrofluidics*, 2010, **4**.
4. E. A. Henslee, M. B. Sano, A. D. Rojas, E. M. Schmelz and R. V. Davalos, *ELECTROPHORESIS*, 2011, **32**, 2523-2529.
5. A. Salmanzadeh, L. Romero, H. Shafiee, R. C. Gallo-Villanueva, M. A. Stremmer, S. D. Cramer and R. V. Davalos, *Lab Chip*, 2011, **12**, 182-189.
6. M. B. Sano, J. L. Caldwell and R. V. Davalos, *Biosensors and Bioelectronics*, 2011, **30**, 13-20.
7. M. B. Sano, A. Salmanzadeh and R. V. Davalos, *ELECTROPHORESIS*, 2012, **33**, 1938-1946.
8. H. Shafiee, J. L. Caldwell, M. B. Sano and R. V. Davalos, *Biomed Microdevices*, 2009, **11**, 997-1006.
9. N. G. Green, A. Ramos and H. Morgan, *J Electrostat*, 2002, **56**, 235-254.

A COMPARISON OF METHODS FOR MEASURING DAMAGE IN MEDIAL COLLATERAL LIGAMENTS

Victor A. Stewart^{1,2}, Raffaella De Vita^{1,2}, Michael Madigan^{1,2}, Jake Socha^{1,2}

1. Virginia Tech-Wake Forest University, School of Biomedical Engineering and Sciences
2. Virginia Polytechnic Institute and State University, Engineering Science and Mechanics

Corresponding Author: Victor Stewart, Email: vicria@vt.edu

INTRODUCTION

The knee is the largest joint in the human body. It acts as a synovial hinge that allows flexion and extension as well as medial and lateral rotation. The knee consists of a system including bone, muscle, tendons, and ligaments that help support the majority of the body's weight. The knee joint is very complex and deals with repetitive loads on a daily basis. The knee complex has four main ligaments: the medial collateral ligament (MCL), the lateral collateral ligament (LCL), the anterior cruciate ligament (ACL), and the posterior cruciate ligament (PCL).

The MCL is a commonly injured body part in athletes due to rapid impact trauma. Ninety percent of knee ligament injuries involve the ACL and the MCL (Miyasaka et al., 1991). These ligaments are similarly injured in people involved in automotive crashes. If the MCL is torn, the loss of its functionality affects the surrounding ligaments and can create compound damage if not treated correctly and in a timely manner. Rupture of these ligaments upsets the balance between knee mobility and stability, resulting in abnormal knee kinematics and damage to other tissues in and around the joint that lead to morbidity and pain (Almarza, 2007).

Severe sprains involving complete disruption of the ligament and resulting in significant joint laxity constitute <15% of all ligament sprains. This leaves >85% of the sprains in which subfailure damage is the dominant issue. Microtrauma or subfailure injury in tendon and ligament may occur either as a result of overuse or as a single traumatic event (Buckwalter JA et al., 1994).

METHODOLOGY

This study investigates different methods of characterizing damage that occurs in medial collateral ligaments. The Harlan Sprague Dawley rat was used as the animal model for this study. Dissection methods were used to expose the MCL by removing the surrounding skin, muscle, and fascia tissues. The hind limbs were amputated distal to the hip joint and the tibia was amputated from the ankle joint. This extracted component of the hind limb is known as the femur-MCL-tibia complex (FMTC) used in testing.

The testing method used an innovative stretching method to a single ligament until failure and recorded the load-displacement data for each stretch. Each MCL was stretched to a series of incremental displacement values d_k ($k=1,2,3,\dots$) with $d_1=0.4$ mm and $d_{k+1}-d_k=0.2$ mm at a displacement rate of 1 mm/sec until failure occurred. The three methods of determining damage in the MCL were monitoring the changes in tangent stiffness, changes in chord stiffness, and the changes in the load value at 0.4 mm of the load-displacement curves obtained from testing the FMTCs. The testing system used in this experiment was an Instron ElectroPuls E1000 with a static 50 N load cell (accuracy: 0.05N). Changes in ligament length were taken from the actuator displacements. Changes in load were recorded by the load cell of the machine. A total of thirty FMTCs were tested in this study.

RESULTS

The typical load-displacement data for each of the tested FMTCs is shown in **Figure 2**. Each load-displacement curve was obtained by stretching the ligament to increasing displacements and using a 0.1 N preload as the reference starting point. These changes in the tensile

behavior of the ligament have been associated with the initiation and propagation of damage.

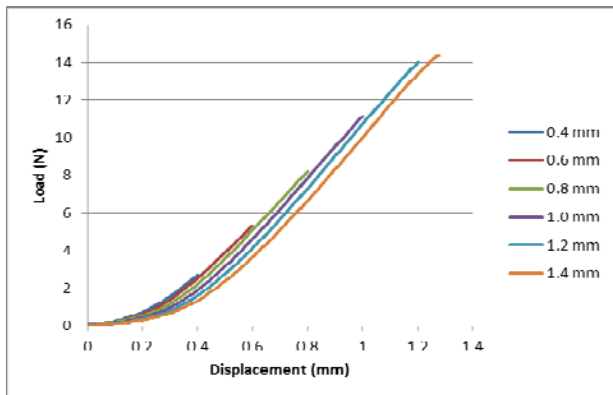


Figure 2: The load-displacement curves of one of the FMTCs tested in this study

After the load-displacement curves were obtained for all of the FMTCs, the tangent stiffness values were calculated from the linear regions of each respective stretch. A linear trend line was fitted to the load-displacement curve in the linear portion of the plot and the slope of that section of the data was used as the tangent stiffness. Similarly, the chord stiffness values were obtained from each stretch of the MCL by calculating the slope from the minimum load value of the stretch to the maximum load value of the stretch.

The tangent stiffness decreased after the 0.6 mm stretch on two out of the thirty (6.7%) FMTC tests. One out of the thirty (3.3%) FMTC tests decreased after the 1.0 mm stretch. Finally, for twenty-seven out of thirty (90%) FMTC tests, the tangent stiffness decreased after the 0.8 mm stretch. Similarly with the chord stiffness, one out of the thirty (3.3 %) FMTCs decreased after the 0.6 mm stretch, nine out of the thirty (30%) FMTCs decreased after the 0.8 mm stretch, sixteen out of thirty (53.3%) FMTCs decreased after the 1.0 mm stretch, and four out of thirty (13.4%) FMTCs decreased after the 1.2 mm stretch.

The load values at the 0.4 mm displacement point steadily decreased after each incremental stretch. Using a Wilcoxon Signed Rank test for validation, there is a significant difference in load between all of the stretches, except between the 1.2 mm and the 1.4 mm stretches.

DISCUSSION

Comparing the three different testing parameters analyzed in this study, there seems to be an agreement between the decreases in tangent stiffness with the elongation of the toe region of the load-displacement curve. A main

difference between the change in tangent stiffness and chord stiffness is the point in which the stiffness values decrease in respect to the consecutive stretches. The drop in chord stiffness seems to be more of a measure of an indicator of imminent failure of the tissue rather than an indicator of damage propagation as the specimen fails after the drop in chord stiffness. The statistical results of the decreases in the load value at 0.4 mm indicate that damage in the MCL occurs early on in the consecutive stretch testing, congruent with the decreases in tangent stiffness.

CONCLUSIONS

The overall goal of this study was to determine which methods of categorizing damage propagation are appropriate and effective in regard to the MCL. This study has shown that decreases in tangent stiffness and the elongation of the toe region indicate damage propagation in the MCL. Decreases in chord stiffness do not indicate damage propagation, but rather only pending failure. As more advances occur in the biomechanical field, the opportunity to test in in-vivo situations becomes more idealistic. This may remove some discrepancies that may have occurred in this in-vitro study. This can only increase the accuracy of the testing once these methods become more available.

ACKNOWLEDGMENTS

I would like to thank my committee members and my advisor Dr. Raffaella De Vita for her continued support throughout this study. Special thanks goes towards Andrea Martin of KemPharm Inc. for the supply of murine specimens for this experiment. I have been fortunate enough to work with my fellow lab researchers. Personally, I would like to give a heartfelt thanks to my family especially my father, mother, and sister for all of their love and support throughout my life.

REFERENCES

- Almarza, A.; Fisher, M.; Liang, R.; Woo, S. (2007). *Transitional Approaches in Tissue Engineering & Regenerative Medicine. Chapter 9: Functional Tissue Engineering of Ligament and Tendon Injuries*. Boston. Artech House Publishers. 163-179.
- Buckwalter JA; Woo SLY. (1994). *Effects of repetitive loading and motion on the musculoskeletal tissues*. In: *Orthopaedic Sports Medicine: Principles and Practice*. Philadelphia, PA: Saunders.
- Miyasaki, K.C.; Daniel, D.M.; Stone, M.L.; Hirshman, P., (1991). *The incidence of knee ligament injuries in the general population*. *American Journal of Knee Surgery* 4, 3-8.

MAGNETIC RESONANCE IMAGING MOVIES FOR MULTIVARIATE ANALYSIS OF SPEECH

Kate McRoberts^{1,2}, Jonathan Lisinski², Brad Sutton^{3,4}, and Stephen LaConte^{1,2}

1. Virginia Tech – Wake Forest University School of Biomedical Engineering and Sciences
2. Virginia Tech Carilion Research Institute
3. University of Illinois, Department of Bioengineering
4. University of Illinois, Beckman Institute for Advanced Science and Technology

Corresponding Author: Kate McRoberts, Email: kmcr@vt.edu

INTRODUCTION

The average person takes for granted that speech is both a complex motor function and a skill fundamental to personal well-being. Although those with speech disorders can greatly benefit from surgical or therapeutic approaches, speech remains poorly quantified in terms of brain activity and vocal tract dynamics.

Magnetic resonance imaging (MRI) remains a powerful and relatively untapped tool for studying speech, as it can dynamically image soft-tissue articulators in the vocal tract with high spatial and temporal resolution. Furthermore, unlike other existing techniques for speech visualization, MRI is non-ionizing, non-invasive, and non-interfering.

Most unique, though, is that MRI can also dynamically track the neurocorrelates of speech in the brain, and thus exhibits potential to examine brain-articulator relationships during speech production. Understanding where and when the brain goes awry in the speech production process could enable novel developments for the diagnoses and treatment of communication disorders.

As a first step toward this aim, this thesis project sought to determine MRI’s capability to capture meaningful information about speech by comparing MR images taken during speech production with one another, and with corresponding speech audio recordings.

METHODOLOGY

Data were collected at the University of Illinois Urbana-Champaign using a novel spiral-navigated Cartesian FLASH MRI sequence [1-3]. Speech dynamics were imaged using a single midsagittal slice acquisition with

280x280 mm field of view and 2.2x2.2x6.5 mm voxel size, captured at a striking rate of 102.2 fps.

The subject was cued to repeat certain linguistically interesting phoneme (sound) pairs, listed in Table 1, aloud. The dynamic structural images and sound were acquired simultaneously.

Table 1: Phoneme Pairs

Phoneme #1	/ata/	/ata/	/ita/	/bababa/
Phoneme #2	/ana/	/ati/	/iti/	/pataka/

Data were analyzed using custom Matlab and Unix shell scripts. Because such MRI measurements are inherently spatiotemporal in nature, multivariate analysis approaches such as support vector machines (SVM) and canonical correlation analysis (CCA) proved to be powerful methods to explore these relationships.

The support vector machine, a machine-learning tool, seeks to distinguish between two classes of data by determining the features in the data that most readily differentiate between the two groups; once this rule is developed, new data may be introduced to the SVM for classification.

Here, the SVM was trained to distinguish each phoneme from its pair as a method of computer-based “mouth-reading,” and classification accuracy was obtained by using leave-one-out cross-validation. The input vector to the SVM was formed from a short movie clip of the mid-sagittal slice through the mouth. Because we set up the SVM with spatiotemporal features, the linear kernel-based weight vector could be displayed as a “movie” showing the relative contribution of each MRI voxel in

both space and time. In other words, we were able to apply the SVM results in a novel, image-mapped way; SVM training highlighted the most important spatial regions in a time-resolved manner for discriminating between two categories of syllable.

A complimentary step in this work was to use CCA to examine the multivariate relationships between the audio recording of speech and the MRI data. The goal of CCA is to examine relationships between two data matrices (\mathbf{X} and \mathbf{Y}) by finding two sets of \mathbf{a} and \mathbf{b} vectors such that the correlations between $\mathbf{a}^T\mathbf{X}$ and $\mathbf{b}^T\mathbf{Y}$ are maximized. In this process, we defined \mathbf{X} as our spatiotemporal MRI matrix (with rows and columns of time by voxels-in-time), and formed \mathbf{Y} as a time by frequency matrix from the spectrogram of the speech audio signal, as shown in Fig. 1. This correlation provides a means to computationally link articulatory dynamics with their resultant sound.

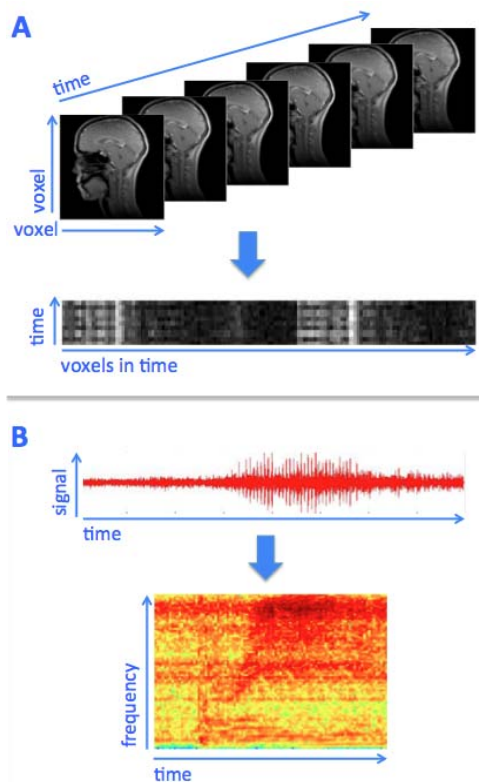


Figure 1: CCA methodology. In A, original data are the MRI movies of speech production; this information is recast as a time-by-voxel matrix, \mathbf{X} . In B, the corresponding audio signal is represented with a time-by-frequency spectrogram, \mathbf{Y} . Canonical correlation analysis is then performed using \mathbf{X} and \mathbf{Y} .

RESULTS

Our cross-validated accuracy was 96% to 100% for all syllable pairs (chance = 50%), demonstrating the utility of

our recently developed MRI sequence, and verifying that quantifiable information about the physical production of speech can be decoded from dynamic structural MR images. Figure 2 shows a representative image selected from a /ba/ vs. /ta/ classifier. In Fig. 2, the red and orange voxels represent areas of the vocal tract that correspond to the first word (/ba/); likewise, the cyan and blue pixels indicate vocal tract regions corresponding to the second word (/ta/). As the bilabial plosive [b] is formed with the lips, and the alveolar plosive [t] is formed with the tongue, we would expect these results.

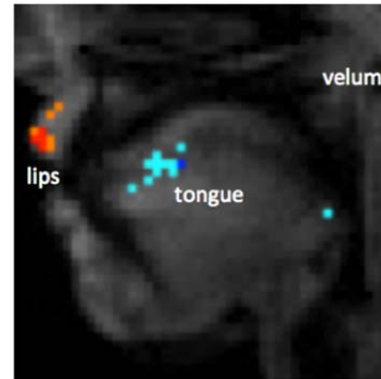


Figure 2: Example image with SVM weight-mapping.

CONCLUSIONS

In conclusion, this thesis project applied multivariate methods to explore the relationships between articulation dynamics and speech recordings. Dynamic MRI of speech is technically challenging, but our results demonstrate that such measurements capture important information about the corresponding speech signal. Applications and extensions of this work include extracting more refined behavioral descriptions for combined structural and functional brain imaging studies and monitoring speech as a tool for speech therapy and diagnosis.

REFERENCES

- [1] Liang, Z.-P. Spatiotemporal imaging with partially separable functions. *IEEE Intl Symp Biomedical Imaging* 2007. pp. 988-991.
- [2] Fu M, Christodoulou AG, Naber AT, Kuehn DP, Liang ZP, Sutton BP. High-frame-rate multislice speech imaging with sparse sampling of (K,t)-space. *Intl Soc Magn Reson Med*, 2012. p. 12.
- [3] Zhao B, Haldar JP, Liang ZP. PSF model-based reconstruction with sparsity constraint: algorithm and application to real-time cardiac MRI. *Conf Proc IEEE Eng Med Biol Soc*. 2010; 2010: 3390-3.
- [4] LaConte, S.M. et al. 2005. *NeuroImage* 26, 317-329.
- [5] Cox, R. W. 1996. *Comp. and Biomed. Res* 29, 162-173.

VALIDATION AND SENSITIVITY ANALYSIS OF A FINITE ELEMENT MODEL OF THOR-NT DUMMY FOR INJURY PREDICTION UNDER VERTICAL IMPACT LOADING

Jacob B. Putnam¹, Costin D. Untaroiu¹

1. Virginia Tech, Center For Injury Biomechanics

Jacob Putnam: Email: jacobp@vt.edu

INTRODUCTION

The use of a reliable finite element (FE) model to assess crashworthiness standards in a vertical impact scenario provides an effective means for testing current and future aerospace transport technologies to insure and improve safety. The THOR dummy, developed and continuously improved by National Highway Traffic Safety Administration, exhibits improved biofidelity over the automobile industry standard, the Hybrid III anthropometric test device (ATD) [Ref. 1]. The THOR-NT was chosen over the latest THOR-K model as it was available for testing and a readily available FE model existed. To assess the THOR-NT FE model's reliability under vertical crash loading, a series of vertical drop tests were performed at the NASA Langley Research Center (LaRC) [Ref. 2]. This study evaluates the current THOR FE model [Ref. 3] in comparison to both kinematic and loading response of the physical THOR-NT recently tested at NASA LaRC. Additionally injury criteria values calculated from the responses of both physical and ATD model are compared. Finally, a sensitivity analysis was performed to evaluate the effect of pre-impact body position on dummy response.

METHODOLOGY

Prior to simulation, a series of updates were applied to the latest available version of the THOR NT dummy FE model to improve its performance. Loading output mechanisms were redefined in the upper neck, lower neck, and lumbar spine locations in order to improve result accuracy. The OC-Joint mechanism was simplified as a defined joint. This resolved instability issues found in the original friction based mechanism. The positioning tree of the dummy model was also updated to improve positioning ability for vertical impact conditions. A rotational axis was added at the neck and lower thoracic spine pitch change mechanism. This allowed the model to be positioned in an upright manner matching that of the simulated vertical loading scenario.

Simulation setup was established based on the physical test setup and procedures [Ref. 2]. A seat model was developed to the specifications of the seat used in the physical tests [Ref. 4]. The THOR-NT dummy FE model was positioned within the seat based on photogrammetric imagery of the dummy recorded prior to testing (Fig. 1).

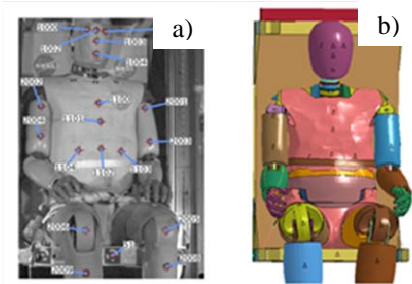


Figure 1: Comparison between pretest conditions of experiment (a) and FEM (b).

FE simulations were run in LS-DYNA software (LSTC, Livermore, CA). Kinematic conditions were matched in FE simulation using the pre-impact velocity and crash pulse deceleration data measured during testing. FE dummy acceleration response was calculated at the head CG, T1 vertebrae, and T12 vertebrae locations. Force and moment response were calculated at the upper neck, lower neck, and lumbar spine load cell locations. To evaluate the response of the dummy model in a more comprehensive way, injury prediction comparisons were made using the following injury criteria: Head Injury Criterion (HIC), Lumbar Load Criterion (LL), and Lower Neck Beam Criterion (BC) [Ref. 5,6]. Sensitivity analysis was performed to investigate the effects of pre-impact head and thorax position variation on vertical impact response. Head position was varied by rotation around the OC-Joint. Thorax position was varied by rotation around the lumbar spine. The resultant head CG acceleration in addition to BC and LL injury criteria were used as response metrics in this analysis.

RESULTS

The experimental and simulated time histories were compared (Figure 2). The results show a similar shape between simulation and the test responses. Initial peaks match closely in both acceleration and load response. Disparities are seen after initial peak with a sharp drop in all calculated model responses. Additionally a spike in neck force is observed in simulation. In addition to this analysis the full data set including results from three separate impact loading scenarios will be presented and discussed.

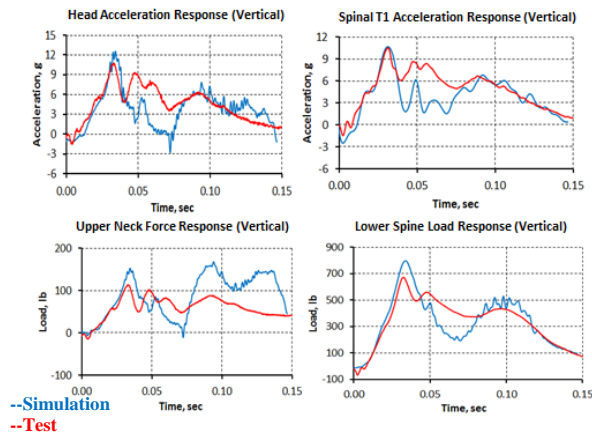


Figure 2: Time history comparisons between experimental and simulation results.

Results demonstrate that both methods conclude a low risk of injury in the conditions tested (Table 1). Injury risk is seen to increase as the injury region approaches the area of impact (pelvis). Overall the simulation predicts a higher risk of injury than the test results. HIC_{36} is the one exception. This is due to the sharp drop-off seen simulation response, resulting in lower head acceleration over the longer time period used in the HIC_{36} calculation.

Table 1: Summary of Injury Criterion Results

Injury Criterion	Allowable	Test (% Allowable)	Simulation (% Allowable)
HIC_{15}	700	2.93 (.42%)	3.89 (.56%)
HIC_{36}	1000	6.3 (.63%)	3.65 (.37%)
BC	1	0.2341 (23%)	0.3764 (38%)
LL	1500	671.5 (45%)	797.4 (53.2%)

Sensitivity analysis shows head angle to have a significant effect on HIC and BC values, with little effect on LL values. Thorax rotation is shown to only significantly affect LL values (figure 3). The sensitivity due to the head rotation is likely due to a change in moment around the respective joints. This leading to an increase in neck moment and acceleration of the head as its center of gravity diverges from normal to the rotational axis around the neck. Vertical load in the lumbar spine begins to

decrease after approximately 5° . This is a sign that a change in loading path through the pelvis into the thorax occurs at higher angles.

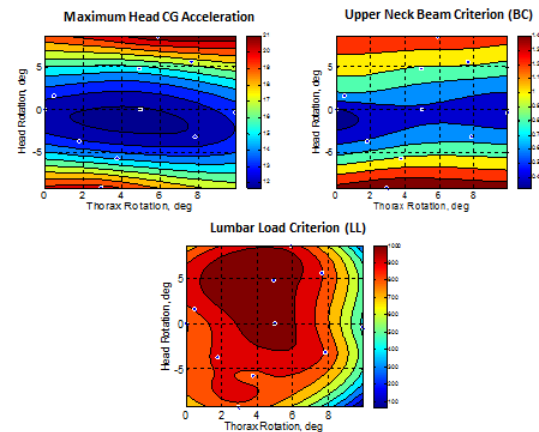


Figure 3: Sensitivity Analysis Results

CONCLUSIONS

With safety a priority in all fields of aerospace transport, the development and validation of a capable and efficient means for crash testing is important. This study focuses on the evaluation of the THOR-NT FE model to fulfill such criteria. The THOR-NT FE model was validated in vertical loading by a qualitative comparison exhibiting similar response to the ATD during 3 unique impact scenarios. Similar injury criteria predictions were shown in the scenarios tested. In addition Pre-Impact positioning is shown to have a significant effect on overall model response.

ACKNOWLEDGMENTS

Justin Littell & Martin Annett from NASA LaRC

REFERENCES

- [1] G. Shaw, J. R. Crandall, J. Butcher, "Biofidelity Evaluation of the Thor Advanced Frontal Crash Test Dummy." Proceedings of the IRCOBI Conference, 2000.
- [2] Littell, J., and Annett, M., "The Evaluation of a Test Device for Human Occupant Restraint (THOR) Under Vertical Loading Conditions: Experimental Setup and Results" 69 AHS Forum, Phoenix, AZ, May 21-23, 2013
- [3] Untaroiu, C. and Lu, Y., "A Simulation-Based Calibration and Sensitivity Analysis of a Finite Element Model of THOR Head-Neck Complex," SAE Technical Paper 2011-01-1123, 2011, doi:10.4271/2011-01-1123.
- [4] Polanco, M., and Littell, J. D., "Vertical Drop Testing and Simulation of Anthropomorphic Test Devices," 67th AHS Forum, Virginia Beach, VA, May 3-5, 2011
- [5] Tabiei, A., Lawrence, C., and Fasanella, E., "Validation of Finite Element Crash Test Dummy Models for Predicting Orion Crew Member Injuries During a Simulated Vehicle Landing," NASA/TM-2009-217476, March, 2009.
- [6] Salzar, R. S., et al. (2009). "Ejection Injury to the Spine in Small Aviators: Sled Tests of Manikins vs. Post Mortem Specimens." Aviation, Space, and Environmental Medicine 80(7): 621-628.

DEVELOPMENT OF A NOVEL TISSUE ENGINEERED MUSCLE REPAIR CONSTRUCT WITH POTENTIAL FOR ENHANCED MOTOR END PLATE FORMATION AND FUNCTION

John B. Scott^{1,2}, Benjamin T. Corona³, Catherine L. Ward³, Benjamin S. Harrison^{1,2}, Justin M. Saul⁴, and George J. Christ^{1,2}

1. Virginia Tech – Wake Forest University School of Biomedical Engineering and Sciences

2. Wake Forest Institute for Regenerative Medicine

3. US Army Institute of Surgical Research

4. Miami University School of Engineering and Applied Science

Corresponding Author: George J. Christ, Email: gchrist@wakehealth.edu

INTRODUCTION

Though skeletal muscle possesses an impressive ability for self-repair, large traumatic injuries and congenital defects can produce a volume of muscle loss that cannot be repaired by native processes, resulting in permanent cosmetic and functional deficits. The field of tissue engineering holds promise in developing an adequate solution for these injuries, which cannot currently be restored to normal function or appearance by the clinical standard of care. One need in the development of a successful tissue engineered muscle strategy is the maintenance of a skeletal muscle phenotype, including motor endplates (MEPs), long enough for host nerves to reinnervate regenerated muscle. Two major challenges to this goal are (1) development of suitable biomaterials and (2) pharmacological or other approaches to maintain skeletal muscle phenotype.

We have previously developed a templated fibrin biomaterial to support directed cell attachment and growth while offering good mechanical properties for soft tissue repair [1]. It has also been demonstrated pharmacologically that delivery of nerve-derived agrin to mature muscle cells *in vitro* triggers formation of acetylcholine receptor (AChR) clusters [2], the presumptive equivalent of MEPs *in vivo*. The objective of the current study is to wed these biomaterial and pharmacological technologies for the creation of a tissue engineered muscle repair (TEMR) construct capable of long-term maintenance of the appropriate skeletal muscle phenotype.

METHODOLOGY

2-D cell substrates mimicking the mechanical properties of the TEMR construct were formed by creating a homogenous layer of fibrin on glass. C2C12 mouse myoblasts or expanded primary rat muscle precursor cells were placed on the gels and allowed to attach, multiply, and subsequently differentiate. Meanwhile, functionalized or control microparticles were created by adsorption or covalent linkage of agrin to the particle surface or by leaving particles untreated, respectively. After differentiation, myotubes were treated with particles to stimulate AChR clustering. Cells were then stained for AChR localization using fluorescently-labeled α -bungarotoxin and imaged using epifluorescence or confocal microscopy.

Cells were also similarly cultured, differentiated, stained, and imaged on gels containing immobilized agrin-delivering particles bound to the seeded surface.

RESULTS AND DISCUSSION

Figure 1 summarizes the response of differentiated C2C12 cells to various stimuli, each presented for 16-24 hours prior to staining. Unconditioned cells are diffusely fluorescent when stained (Fig. 1A), indicating the expression of AChRs within the membrane. When treated with culture medium containing agrin in solution, AChRs cluster together in a spatially uncoordinated fashion (Fig. 1B). Though untreated microparticles are visible due to autofluorescence (Fig. 1C) after addition, they do not induce a clustering response. Cell membranes in contact with agrin-adsorbed microparticles generate AChR clusters (Fig. 1D), potentially allowing spatial control of the clustering response. Microparticle-mediated (green) agrin delivery generates a clustering response (red) even

in complex cell topographies (Fig. 1E), as visualized by 3D render of confocal z-stack. This phenomenon can be visualized clearly by computerized thresholding of confocal stacks into bead and cluster surfaces (Fig. 1F). Arrows highlight AChR clusters.

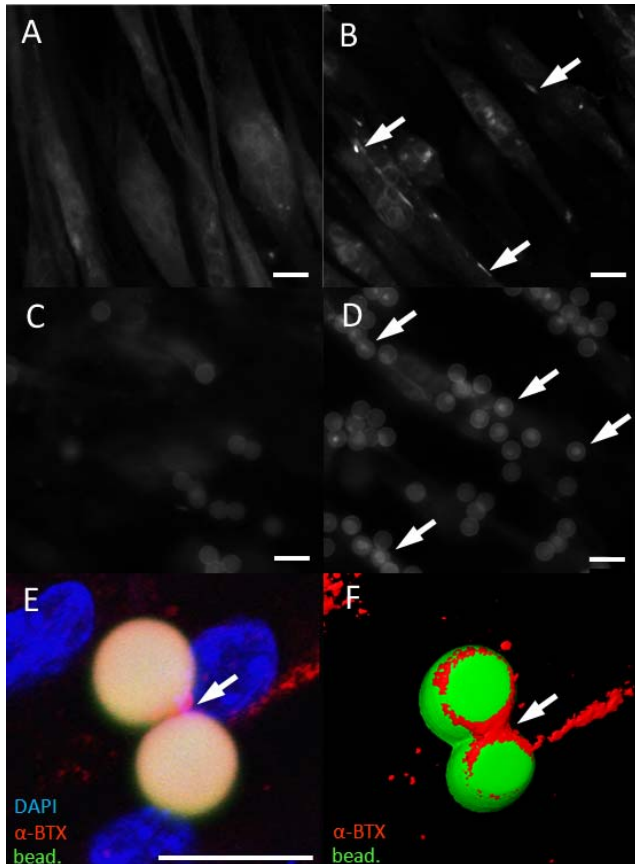


Figure 1: Summary of agrin effects on differentiated C2C12 cells.

Similar results were obtained using agrin-delivering particles immobilized within the biomaterial, as shown in Figure 2. By mixing these particles within the scaffold components prior to gelation, a surface was created with both bulk hydrogel properties and agrin delivery via the particles bound within the surface and extending into the surrounding space. Rotational views around the 3D render (Fig. 2A-C) show a robust clustering response after seeding and differentiating cells on this engineered surface.

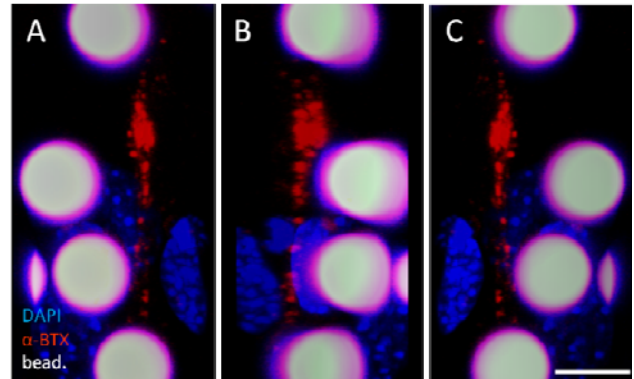


Figure 2: Acetylcholine receptor clustering in cells seeded on agrin-presenting scaffold.

CONCLUSIONS

Agrin-presenting microparticles signaled the formation of acetylcholine receptor clusters, a key marker of a mature skeletal muscle phenotype, in a fashion compatible with a fibrin biomaterial construct previously shown to successfully support soft tissue regeneration. This study highlights the ability to combine novel biomaterials with controllable pharmacological approaches (agrin delivery) to promote a skeletal muscle phenotype that may be better preserved *in vivo* during natural re-innervation.

Approaches to achieve full repair of the most devastating skeletal muscle defects will require a multidisciplinary approach. A three-dimensional fibrin scaffolding system functionalized with agrin delivery on a locally-controllable scale, a technology made potentially viable by microparticle delivery systems as shown here, would be a significant step toward a TEMR construct with a wider range of clinical applications.

ACKNOWLEDGMENTS

The authors acknowledge funding through the Wake Forest University Department of Biomedical Engineering and the Telemedicine and Advanced Technology Research Center.

The authors would also like to thank Hannah Baker, Christopher Bergman, Christopher Booth, Hayden Holbrook, Venu Kesireddy, Cathy Mathis, Juliana Passipieri, Pooja Patil, Mevan Siriwardane, Claire Staley, and Taylor Zak for experimental assistance and expertise.

REFERENCES

1. Scott JB. *Biomaterials*. 2011;32(21):4830-9.
2. Daggett DF. *Mol Cell Neurosci*. 1996;8(4):272-85.

THE POTENTIAL OF CELLULOSE NANOCRYSTALS FOR TARGETED DELIVERY APPLICATIONS IN CANCER

Katelyn R. Colacino¹, Shuping Dong², Christopher Arena¹, Rafael Davalos¹, Maren Roman², Yong Woo Lee^{1,3}

1. Virginia Tech-Wake Forest University, School of Biomedical Engineering and Sciences, Blacksburg, VA 24061
 2. Virginia Tech, Macromolecules and Interfaces Institute and Department of Sustainable Biomaterials, Blacksburg, VA 24061
 3. Virginia Tech, Department of Biomedical Sciences and Pathobiology, Blacksburg, VA 24061
- Corresponding Author: Katelyn R. Colacino, colacino@vt.edu

INTRODUCTION

Cancer is a class of diseases which varies widely from type to type, making multiple treatment options limited to certain forms. Conventional cancer therapies, including chemotherapy, radiation therapy, and surgery, have serious side effects which harm normal tissue in addition to the tumors. A quite popular research topic is investigations into drug delivery nanocarriers in which selective targeting agents, therapeutic drugs and imaging probes are conjugated to the surface^{1,2}. In addition, cancer imaging through multiple receptor targeting sites has been an attractive approach for the early detection of cancer in recent years³. In this study we exploit the folate receptor (FR) as it has been observed to be overexpressed in multiple cancer types including breast, ovarian, lung, kidney, brain, and endometrium, and has a high affinity for folic acid (FA).

Cellulose nanocrystals (CNCs) are rod-shaped particles ranging in length from 50-200 nm and a width of 4-5 nm. This aspect ratio increases fenestration penetration compared to spherical particles, which many carriers are by design⁴⁻⁶. Furthermore, it has been observed that the CNC size range is expected to be too large for renal clearance yet small enough to evade the mononuclear phagocytic system⁷, increasing blood circulation time. The starting material, cellulose, is extremely abundant in nature, with low cost and high strength properties^{8,9}. The surface of CNCs contains multiple hydroxyl groups which are amendable to functionalized groups for ligand targeting, labeling of image probes, and drug conjugating.

In recent years, a new type of therapy promises minimally invasive localized treatment of cancerous tissue, with little to no side effects¹⁰. Irreversible electroporation (IRE), a non-thermal focal ablation technique, exposes cells to electric pulses to increase the permeability of the plasma membrane past the point of recovery¹¹. While IRE affects the cell membrane of living cells, it does not cause damage to the supporting stroma in the vicinity, including major blood vessels, nerves, and extracellular matrices¹². This enables the treatment of tumors that are normally considered surgically inoperable due to their close proximity to these sensitive structures. Another important feature of IRE is the high degree of control over the regions of tissue that experience irreversible, lethal electroporation and sub-lethal doses, made possible by careful selection of the electric field distribution and visualization in real-time on multiple imaging platforms, such as ultrasound¹³.

CNCs have been studied widely for a variety of applications. Despite their advantages, investigations of their abilities in the biomedical field have not been explored. The goal of this project is to delve into the potential uses of CNCs in detection, targeted drug delivery, and potentiation of IRE-induced cell death in folate receptor FR-positive cancers.

METHODOLOGY

CNCs and Conjugations: CNCs were synthesized via sulfuric acid hydrolysis of cellulose microfibrils¹⁴. CNCs conjugated with the targeting ligand FA, fluorescent probe fluorescein-5'-isothiocyanate (FITC), or

doxorubicin (DOX) were synthesized and characterized as previously described¹⁴.

Cell Cultures: KB, MDA-MB-468 and A549 cells were purchased from American Type Culture Collection (ATCC). Cells were grown in a 37°C, 5% CO₂/95% air, humidified cell culture incubator using folate free RMPI 1640 growth medium.

Cell Viability Assay: Effects of various treatments and/or nanoparticle exposure were determined *via* CellTiter Blue® Cell Viability Assay (Promega).

Pulsed Electric Fields (PEF): Application of PEF to KB monolayers was performed using a pulse generator (Model ECM 830, Harvard Apparatus). The conditions kept constant were number of pulses (80 pulses) at a frequency of 1 Hz. The remaining parameters, pulse length, CNC-FA incubation time, and PEF strength were optimized to demonstrate synergistic effect on cytotoxicity.

RESULTS AND DISCUSSION

We observed that FITC-CNC-FA's has the ability to specifically target FR-positive cancer cells *in vitro*, while non-targeted CNCs (FITC-CNC) were not able to bind to these cell types (Figure 1).

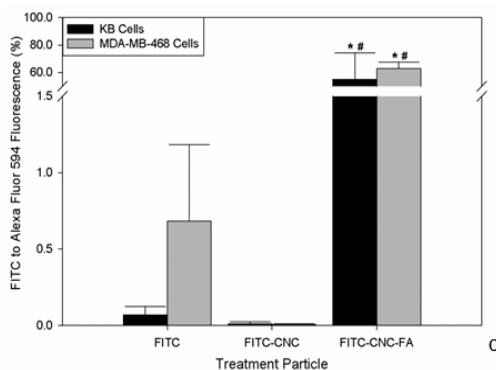


Figure 1: Cellular binding/uptake of nanoparticles.

Furthermore, similar particles containing the chemotherapeutic doxorubicin (DOX-ALAL-CNC-FA) was observed to increase cytotoxicity in FR-positive KB cells compared with DOX alone (Figure 2).

Lastly, we have shown CNCs' ability to potentiate a new technique for tumor ablation, IRE. Pre-incubation with FA-conjugated CNCs (CNC-FA) have shown an increase in cytotoxicity in FR-positive cancer cells induced by IRE (Figure 3). In addition, CNC-FA did not potentiate IRE-induced cytotoxicity in an FR-negative cancer cell type.

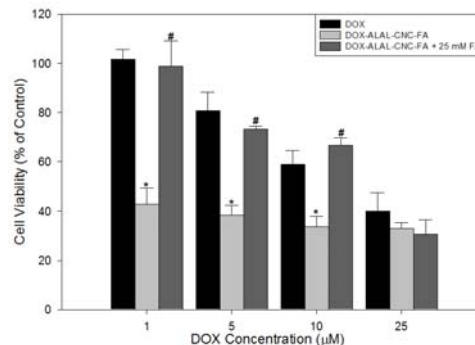


Figure 2: Cytotoxicity of doxorubicin containing nanoparticles.

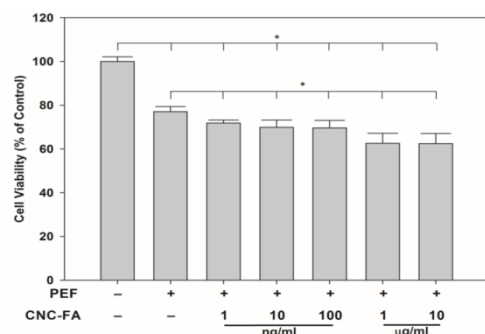


Figure 3: Effects of CNC-FA on IRE-induced cytotoxicity in MDA-MB-468 cells

CONCLUSIONS

These studies showcase CNCs as efficient and effective nano-carriers in tumor detection and treatment.

ACKNOWLEDGEMENTS

This work was supported by Virginia Tech's Institute for Critical Technology and Applied Science (ICTAS) and the National Science Foundation (DMR0907567).

REFERENCES

- Kona, S., et al., *Int J Pharm*, 2012. **423**(2)
- Comprehensive Cancer Information*. 2012 [cited 2012]
- Bai, M., et al., *Curr Med Chem*, 2012. **19**(28)
- Kamps, J.A.A.M., et al., *J Vasc Res*, 2006. **43**
- Boso, D.P., et al., *Int J Nanomedicine*, 2011. **6**
- Decuzzi, P., et al., *J Control Release*, 2010. **141**(3)
- Owens, D.E., et al., *Int J Pharm*, 2006. **307**(1)
- Dong, S., et al., *Nano LIFE*, 2012. **2**(3)
- Lima, M.M.D., et al., *Macromol Rapid Comm*, 2004. **25**(7)
- Thomson, K.R., et al., *J Vasc Interv Radiol*, 2011. **22**(5)
- Davalos, R.V., et al., *Ann Biomed Eng*, 2005. **33**(2)
- Maor, E., et al., *Technol Cancer Res Treat*, 2007. **6**(4)
- Lee, E.W., et al., *Technol Cancer Res Treat*, 2007. **6**(4)
- Roman, M., et al., *Cellulose Nanocrystals for Drug Delivery*. 2009. p. 81-91.

INVESTIGATING DIELECTROPHORETIC PROPERTIES OF CELLS FOR CANCER TREATMENT AND DETECTION APPLICATIONS

A. Salmanzadeh,^{1,2} E. S. Elvington,¹ P. C. Roberts,³ E. M. Schmelz,⁴ and R. V. Davalos^{1,2}

1. School of Biomedical Engineering and Sciences
 2. Department of Engineering Science and Mechanics
 3. Department of Biomedical Sciences and Pathobiology
 4. Department of Human Nutrition, Foods, and Exercise
- Virginia Tech, Blacksburg, Virginia 24061

Corresponding Author: Rafael V. Davalos, Email: Davalos@vt.edu

INTRODUCTION

Conventional cancer treatment strategies rely upon toxic chemotherapeutics or target oncogenes that are variably expressed within the heterogeneous cell population of tumors. There is a need for novel treatment regimens that could treat cells independently of expressed biomarkers and be non-toxic but able to partially reverse the aggressive phenotype of the disease to a benign or very slow-growing state. In this study a label-independent rapid microfluidic cell manipulation platform known as contactless dielectrophoresis (cDEP) [1] is used to investigate the effect of non-toxic concentrations of two metabolites on the intrinsic electrical properties of mouse ovarian surface epithelial (MOSE) cancer cells. These metabolites are sphingosine (So), considered a tumor-suppressor, and sphingosine-1-phosphate (S1P), which has tumor-promoting effects.

METHODOLOGY

cDEP uses microfluidic electrode channels to provide a non-uniform electric field (Figure 1(a)), avoiding direct contact between metal electrodes and the sample that is traditionally required by conventional dielectrophoresis-based techniques. This contactless method eliminates electrochemical contamination, extensive sample preparation (no antibody labeling), and maintains sterility of the sample. cDEP microdevices are fabricated using standard soft lithography, an inexpensive and simple technique. MOSE cells were cultured in high glucose DMEM (Sigma Aldrich) supplemented with 4% fetal bovine serum (Atlanta Biologicals), 3.7 g/L NaHCO₃, and 1% penicillin/streptomycin (Sigma Aldrich). MOSE-E and -L cells were treated with 1.5 μM So or 500 nM S1P as BSA complexes (BSA, fatty acids-free fraction V,

Calbiochem) for three passages, allowing 3-4 days between each passage. These treatments were not toxic to the cells.

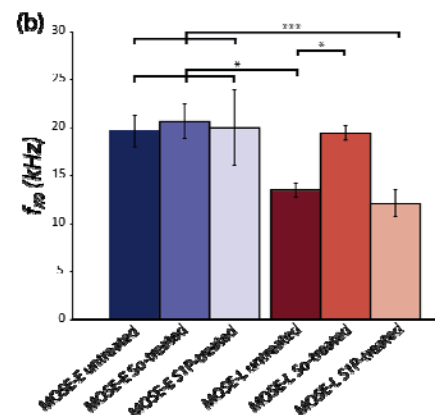
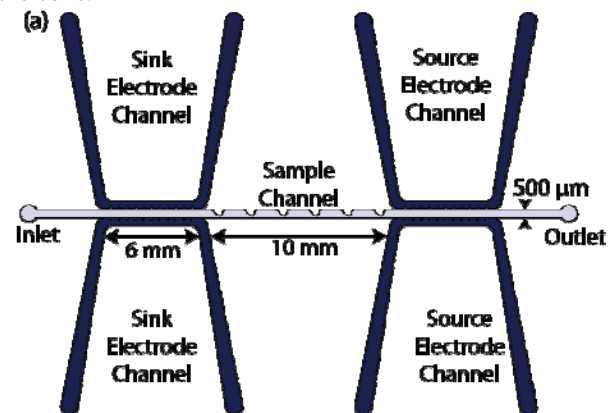


Figure 1: (a) Schematic of the cDEP microdevice. (b) Crossover frequency of treated and untreated early and late stages of MOSE cells (* and *** represent $p < 0.0005$, and 0.05, respectively).

RESULTS

Previously, we demonstrated that electrical properties change as MOSE cells progress from a benign early stage (MOSE-E) to later malignant stages [2]. Here, we demonstrate a correlation between So treatment and a shift in the bioelectrical characteristics of late stage MOSE cells towards a more benign profile. The crossover frequency of MOSE-L cells shifted toward that of MOSE-E cells (Figure 1(b)), decreasing from 13.5 ± 0.7 to 19.4 ± 0.7 mF/m² after So treatment, correlated to a decrease in membrane protrusions of the cells. S1P did not reverse the electrical properties of MOSE-L cells. This work is the first to indicate that treatment with non-toxic doses of So associates with changes in cells electrical properties and surface roughness.

CONCLUSIONS

This study suggests that the electrical properties of cancer cells can be targets of cancer preventative efforts. It also demonstrates the potential for cDEP microfluidic platform to be used as a new, rapid technique for drug efficacy studies, and eventually designing more personalized treatment regimens.

ACKNOWLEDGMENTS

This material is based upon work supported in part by NIH 1R21 CA173092-01 (to RVD), NIH RO1 CA118846 (to EMS and PCR), and by National Science Foundation under Grant No. EFRI 0938047.

REFERENCES

1. H. Shafiee, J. L. Caldwell, M. B. Sano and R. V. Davalos, *Biomed Microdevices*. **11**, 5 (2009).
2. A. Salmanzadeh, M. B. Sano, R. C. Gallo-Villanueva, P. C. Roberts, E. M. Schmelz, and R. V. Davalos, *Biomicrofluidics*. **7**, 011809 (2013).

EVALUATION OF REPEATED BIPHASIC CONDUCTING MATERIALS FOR PERIPHERAL NERVE REPAIR

Tabitha Rosenbalm^{1,2}, Nicole Levi-Polyachenko^{1,2}, Louis Argenta², William D. Wagner^{1,2}, Michael Morykwas^{1,2}

1. Biomedical Engineering Department (WFUBSM/SBES)
 2. Wake Forest Baptist Health, Department of Plastic and Reconstructive Surgery
- Corresponding Author: Tabitha N Rosenbalm, Email: trosenba@wakehealth.edu

INTRODUCTION

Each year 400,000 Americans require surgical repair of transected nerves. Nerve conduits and autografts are treatment options for patients with nerve gaps < 3 cm. However, ~90% of patients have **no treatment options** since nerve gaps > 3 cm fail to repair since rapid scar formation blocks nerve outgrowth. **Accelerating axon growth is key** to nerve repair. The most promising results show axon outgrowth increased by 3x normal rate using electrical stimulation across the gap. Repair of nerve in cornea injury suggests that electric fields less than or equal to 600 μm can effectively direct and stimulate axon outgrowth. We **hypothesize** that repeated electric field gradients of up to 600 μm may maximize axonal outgrowth. The **purpose** of this project was to develop a bioresorbable tube capable of producing repeated electric field gradients.

it is a bioresorbable polymer which meets the target mechanical properties.

Table 1. Target Materials Properties

Property	Elastic Modulus [N/mm ²]	Tensile Strength [N]	Degradation Rate [months]	High Conductivity [S/cm]	Low Conductivity [S/cm]
Material Target Value	0.4 - 0.7	0.21 - 1.49	3 - 12	1E-6 to 1E-4	0 to 1E-5

¹H NMR and ATR-FTIR were used to confirm PGS prepolymer and 25, 30, 35, and 40% acrylation of PGSA. Following confirmation, materials were treated for use in cell culture and dog bone shaped samples were prepared for tensile testing using an Instron 5500 R mechanical tester. Fibroblast (HEPM) and Neuronal (B35) cell lines were grown on 1 cm squares of materials and quantified using the BCA protein assay. PGSA was doped with Soluble PPy to enhance conductivity. Conductivity of PGSA doped with PPy was measured using a Keithley 6621 current source and collinear four point probe. Finally, tubes were prepared from the developed materials using the method shown in Figure 2.

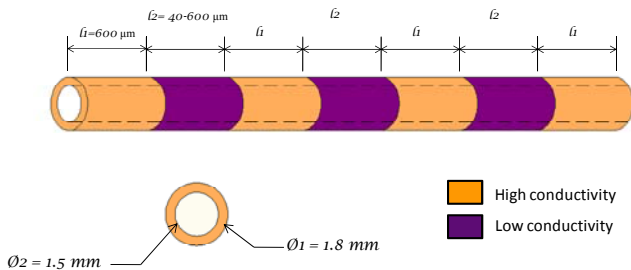


Figure 1. Schematic of Biphasic Conducting Tube

METHODOLOGY

Target materials properties were determined based on mechanical properties of excised nerve, human nerve healing time frame, and ohms law applied to known electric field properties surrounding nerve tissue. (Table 1) Poly (glycerol sebacate) acrylate was synthesized since

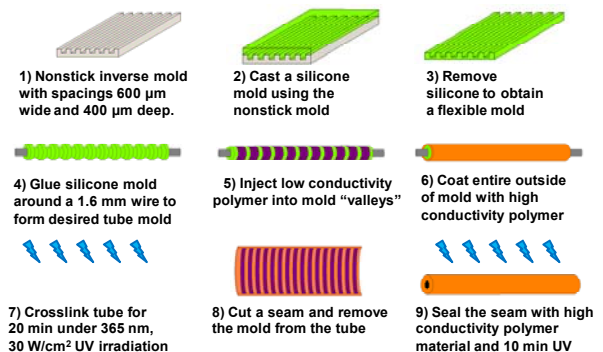


Figure 2. Biphasic Tube Preparation Method

RESULTS

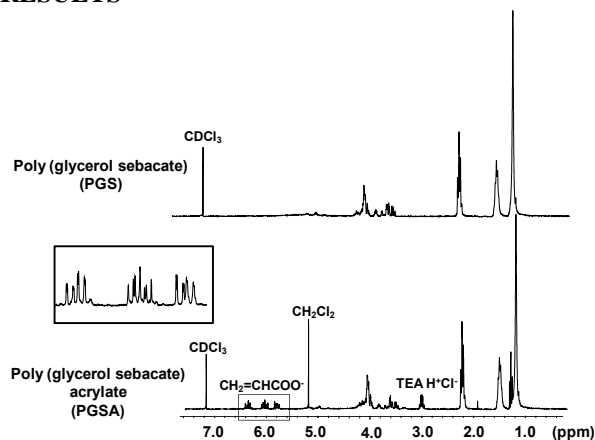


Figure 3. ^1H - NMR confirmed synthesis of PGS prepolymer and 25, 30, 35, and 40% acrylation of PGSA. 35% A is shown

ATR-FTIR distinguishes differences between PGS and PGSA. The key observations are that acrylation peaks are only present in PGSA and carbonyl peaks diminish with increased acrylation for all samples.

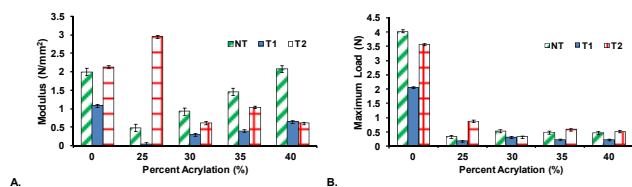


Figure 4. A. Tensile Strength and B. Modulus Parameters are satisfied by 40% A of PGSA with Treatment 2.

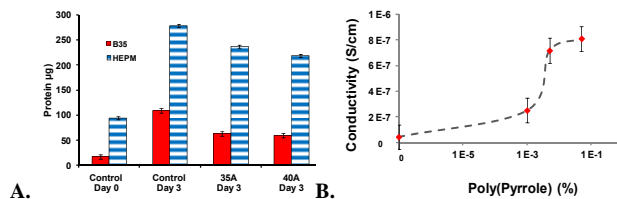


Figure 5. A. BCA Results indicate good cell growth with neuronal (B35) and fibroblastic (HEPM) cell lines. B. Conductivity target was achieved via 0.05% PPy.

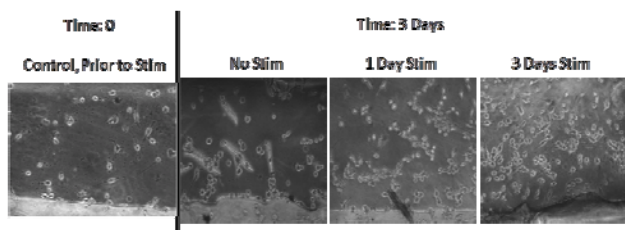


Figure 6. *In Vitro* results show maximal proliferation and migration of B35s at 3 days growth occur for 3 days stimulation.



Figure 7. Formation of Biphasic Conducting Tube for Nerve Implantation. A. Cross section View B. Transverse View.

CONCLUSIONS

- 1) Synthesized PGSA with target mechanical and electrical properties needed for nerve repair.
- 2) Demonstrated cell growth on the designed materials.
- 3) Cell proliferation and migration were dramatically enhanced by the new materials coupled with 3 days of stimulation at 3V, 20 Hz.
- 4) Prepared conduits composed of high and low conductivity materials suitable for implantation.

Conclusion: We have successfully prepared a tube based on the schematic suitable for implantation in the rat sciatic nerve model for nerve repair. *In Vitro* evaluations indicate stimulation for 3 days at 3V, 20 Hz dramatically enhanced neuronal cell proliferation and migration. *In Vivo* evaluations are presently underway with promising preliminary results. Present data indicate this therapy should extend therapeutic options for peripheral nerve repair to patients who were previously untreatable and improve surgical success for treatable patients!

ACKNOWLEDGMENTS

We thank the Department of Plastic Surgery for funding. Thanks to Dr. Ghosh and Aylin Toprakci at NC State University for use of their high resistivity four point probe.

REFERENCES

- [1] Al-Majed, A.A., *et al.* J Neurosci, 2000, 7, 2602 – 2608.
- [2] Song, B., *et al.* J Cell Sci, 2004, 20, 4681-4690.
- [3] Borschel, G.H., *et al.* J Surg Res, 2003, 114, 133-139.

AUGMENTING CONVECTION-ENHANCED DELIVERY OF MALIGNANT GLIOMA THROUGH SIMULTANEOUS CO-DELIVERY OF FLUID AGENTS AND LASER ENERGY WITH A FIBEROPTIC MICRONEEDLE DEVICE

R. Lyle Hood¹, Rudy T. Andriani², John L. Robertson¹, John H. Rossmeisl^{1,3}, and Christopher G. Rylander^{2,3}

1. Virginia Tech, School of Biomedical Engineering and Sciences

2. Virginia Tech, Department of Mechanical Engineering

3. Virginia-Maryland Regional College of Veterinary Medicine

Corresponding Author: R. Lyle Hood, Email: robert86@vt.edu

INTRODUCTION

Systemic delivery of high molecular-weight therapeutic agents for lesions in the central nervous system is demonstrably regulated by the blood-brain barrier (BBB). One method developed for overcoming regulation imposed by the BBB is convection-enhanced delivery (CED), where the BBB is bypassed by transdural insertion of a slender cannula and active infusion directly into lesions. CED has been demonstrated to deliver high molecular weight macromolecules up to 2 cm into the brain parenchyma after a 2 hour infusion without causing cerebral edema [1]. Unfortunately, the first phase III FDA trial utilizing CED failed due to insufficient fluid dispersal and saturation of tumors and their margins.

Thermochemotherapy is defined as the heating of chemotherapeutic agents to enhance tumor penetration. On a macroscale level, this enhancement can be attributed to temperature-based increases in fluid diffusion and convection, as well as a reduction in fluid viscosity [2]. The synergistic potential of facilitating CED by inclusion of sub-lethal hyperthermia may improve the efficacy of CED, making it a viable and effective treatment for the treatment of cerebral disorders like malignant glioma.

To determine if CED could be augmented with aspects of thermochemotherapy, the fiberoptic microneedle device (FMD) technology, developed by this group, was adapted for intracranial use. FMD technology is based on light-guiding, silica capillary tubing capable of simultaneously co-delivering laser energy and fluid agents. For this study, the FMD was used to generate mild hyperthermia (3-5 °C) through photothermal heating with 1064 nm laser energy at the point of infusion. We hypothesized that concurrent generation of hyperthermia through FMD photothermal heating during CED would improve volumetric dispersal.

METHODOLOGY

FMDs capable of co-delivering laser energy and fluid agents through single, light-guiding capillary tubes were fabricated through a previously described method [3]. Anesthetized rats had identical FMDs inserted symmetrically into either hemisphere of their brains. For each pair of infusions (except for a no treatment control), one FMD co-delivering laser energy and fluid agents while the other infused fluids alone. Fluid and light delivery were begun simultaneously and continued for 1 hour. Gadolinium-Evans blue-albumin complex solution (Gd-EBA) or liposomal rhodamine (LR) were infused at a flow rate of 0.1 $\mu\text{L}/\text{min}$. Laser powers were 0 (control), 100, and 200 mW. After the infusion, the rodents were humanely sacrificed and their brains were removed and frozen. The brains were serially sectioned with a cryostat and volumes were determined through area measurement through threshold analysis followed by interpolation between slices. Determination of mechanical and thermal damage to the brain tissue was conducted through hemotoxylin and eosin staining followed by histopathological examination.

RESULTS

Brain regions infused with LR and Gd-EBA through the FMD were clearly and sharply demarcated from untreated regions on and pathological analyses. Co-delivery was associated with significantly increased Vd compared to fluid-only controls, with measured dispersal volumes of $15.8 \pm 0.6 \text{ mm}^3$ and $10.01 \pm 0.4 \text{ mm}^3$ for 100 mW co-delivery and its symmetric hemisphere fluid only controls, respectively. The 200 mW co-delivery and its symmetric hemisphere fluid only controls were measured at $18.0 \pm 0.3 \text{ mm}^3$ and $10.3 \pm 0.7 \text{ mm}^3$, respectively. A graph depicting these measurements is shown in Figure 1. Higher laser power (200 mW) was associated with a significant and positive effect on infusate Vd. There were no significant

differences in V_d between infusions performed with Gd-EBA or LR ($p=0.7912$).

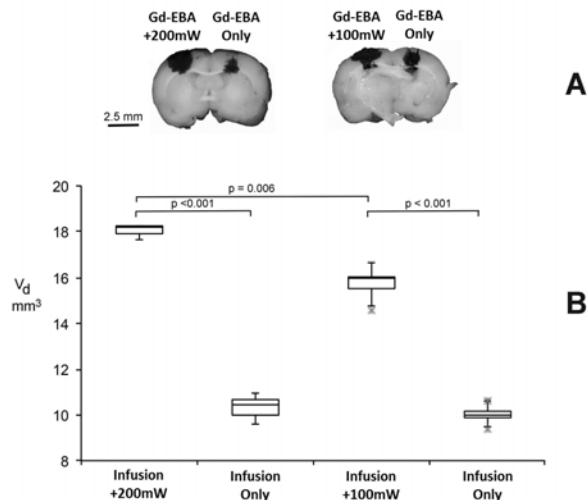


Figure 1: The effects of FMD-CED laser co-delivery on infusate V_d demonstrated with gross brain specimens (A) and quantitative analyses (B). Cerebral hemispheres receiving co-delivery have significantly larger V_d compared to controls, and increasing laser co-delivery power was associated with a significant increase in the V_d .

Thermal damage from photothermal heating was only identified in the 200 mW co-delivery. Tissue disruption for 0 and 100 mW co-deliveries were solely attributable to FMD insertion damage. Tissue sections at each laser power and a description of associated damage are shown in Figure 2.

DISCUSSION

Volumetric dispersal was shown to increase with laser co-delivery during infusion independent of which of the two infusates was employed. The authors can only speculate on contributing mechanisms involved in causing the increased V_d . Fluid and mass transport in biological tissues occur by multiple simultaneous pathways, and each are known to have temperature dependence. Such pathways include both passive and active transport across cells membranes, interstitial flow between cells, and blood perfusion. As the brain is highly cellular, it is possible that sub-lethal thermal permeabilization of cell membranes allows molecular transport intra- and inter-cellularly, which would act as an increase in net tissue porosity. Contributing factors of multifarious influence are almost certainly influencing the hyperthermic effect of laser co-delivery.

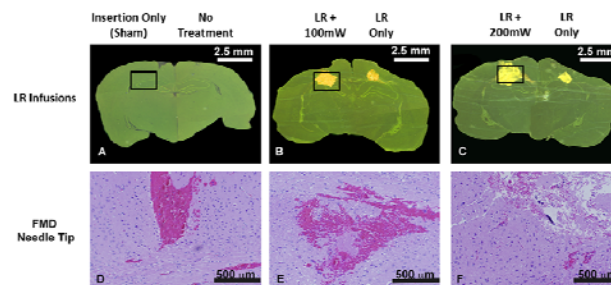


Figure 2: Pathology of rat brains infused with LR. Subgross fluorescent brain slice preparations (A-C) demonstrating larger LR distributions (yellow-gold regions) associated with laser co-delivery (B and C) compared to infusion only and an untreated control (A). Zoomed Morphologic changes in the brain at the level of the FMD needle tips in sham (D; solid inset A), 100 mW co-delivery (E; solid inset B) and 200 mW co-delivery (F; solid inset C) treated cerebral hemispheres. Compared to the sham and 100 mW co-delivery regions, there is prominent malacia induced by the 200 mW treatment.

CONCLUSIONS

This study investigated whether concurrent delivery of photothermal heating during infusion would significantly enhance fluid dispersal in brain tissue. FMDs were inserted symmetrically into either hemisphere of healthy rodents, one device co-delivered fluids and laser energy while the other infused fluid only. Analyses of serial sections demonstrated that dispersal volume increased with increasing laser power. This finding indicated that laser co-delivery during CED procedures could significantly shorten infusion timeframes and enable greater clinician control of fluid distribution. Future work in canine veterinary patients with malignant glioma will be commenced within the next two months.

ACKNOWLEDGMENTS

The authors would like to acknowledge the Coulter Foundation for their funding of this project. Fiberoptic microneedle device fabrication methods and applications are described in US 13/203,800 and PCT/US2012/026,968, which are managed by the Virginia Tech Intellectual Properties Group. The authors would like to thank Michelle Theus, Ph.D. for use of the Stereo Investigator software.

REFERENCES

- Vandergrift, W.A., et al., Convection-enhanced delivery of immunotoxins and radioisotopes for treatment of malignant gliomas. *Neurosurg Focus*, 2006. 20(4): p. E13.
- Munson, B.R., D.F. Young, and T.H. Okiishi, *Fundamentals of fluid mechanics*. 5th ed. 2006, Hoboken, NJ: J. Wiley & Sons.
- Hood, R.L., et al., Intracranial hyperthermia through local photothermal heating with a fiberoptic microneedle device. *Lasers Surg Med*, 2013.

EFFECTS OF CERVICAL ARTHROPLASTY ON NECK RESPONSE DURING A SIMULATED FRONTAL IMPACT

Nicholas A. White¹, Daniel P. Moreno¹, F. Scott Gayzik¹, Wesley Hsu², Alexander Powers² and Joel D. Stitzel¹

1. Virginia Tech-Wake Forest University Center for Injury Biomechanics
 2. Wake Forest University School of Medicine, Department of Neurosurgery
- Corresponding Author: Nicholas A. White, Email: niwhite@wakehealth.edu

INTRODUCTION

Cervical degenerative disc disease (CDDD) is a common spinal disorder which can lead to debilitating axial neck pain, radiculopathy and myelopathy. When non-surgical treatment is ineffective, a surgical anterior cervical discectomy and fusion (ACDF) may be required. Adjacent segment degeneration (ASD) is not uncommon following an ACDF, possibly attributed to the reduction in range of motion (ROM) and subsequent increase in adjacent-level loading. In an effort to maintain ROM and load transmission, cervical arthroplasty has become increasingly more popular over the past decade. Arthroplasty involves the implantation of a cervical total disc replacement (CTDR) designed to maintain a more physiological ROM and therefore loading.

The literature contains a variety of studies on the on cervical spine kinematics and loading from CTDRs in volunteers, cadaveric specimens and finite element (FE) models using quasi-static, non-injurious loading conditions. However, very little data exists for dynamic loading events. The objective of this study was to investigate the effects of arthroplasty on neck response during a simulated frontal automobile collision.

METHODOLOGY

A 13.3 m/s ΔV frontal automobile impact was simulated in LS-DYNA with the Global Human Body Model Consortium (GHBMC) full-body FE model (Figure 1).¹ A total of three simulations were conducted, one with a non-modified cervical spine and two with either a Prestige-ST or ProDisc-C CTDR between C5-6. The Prestige ST is a 2-piece stainless steel, ball-and-trough implant allowing for three-degrees of rotation and pure anterior-posterior (AP) translation (Figure 2a). Bone screws secure the implant into the superior and inferior vertebral bodies (VBs). The ProDisc-C is a 3-piece, ball-and-socket



Figure 1: Belted driver subjected to a frontal impact with 13.3 m/s ΔV and airbag deployment

implant with cobalt-chromium-molybdenum endplates and a semi-spherical ultra-high-molecular-weight polyethylene insert, allowing for three-degrees of rotation (Figure 2b). The central keels on the endplates are press-fit between adjoining vertebrae.

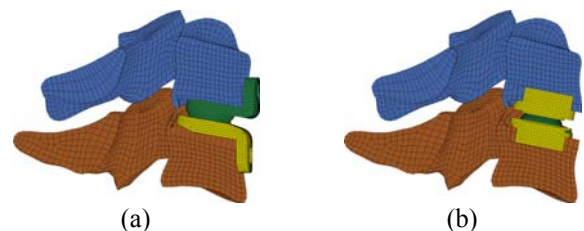
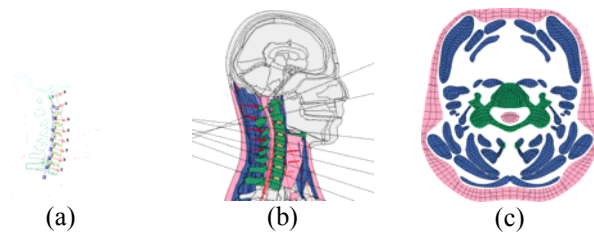


Figure 2: Midsagittal cross-section of the C5-6 vertebrae with a (a) Prestige ST and (b) ProDisc-C CTDR.

Local coordinate systems (LCSYSs) were defined for each level of the cervical spine with origins at the center of gravity (CG) for the respective vertebrae (Figure 3a). A series of cross-sections (Figure 3b) were included to capture the loading at each cervical level of the neck using a methodology previously described by White, et al.² Each cross-section captured the force and moment contributions from the bones, ligaments, active muscles, passive muscles and soft tissue (Figure 3c). The total contributions of these forces and moments about the VB CGs were reported in the local coordinate systems.

Table 1: Peak adjacent-level, cross-section loading and maximum midsagittal rotation for C5 and C6.

Simulation	VB	AP Shear (N)		Ten/Comp (N)		Flex/Ext (Nm)		Rot (deg)
IVD	C5	5.7	-365.6	1053.4	-2.1	63.4	-0.4	-39.0
	C6	28.6	-236.8	1121.2	-4.8	64.6	-0.3	-34.2
Prestige ST	C5	8.7	-395.8	1052.6	-3.1	62.8	-0.3	-37.6
	C6	31.2	-247.3	1125.7	-6.9	64.9	-0.3	-35.2
ProDisc-C	C5	10.2	-397.0	1058.3	-2.2	62.8	-0.3	-38.6
	C6	35.7	-268.7	1127.5	-2.7	65.1	-0.3	-34.0

**Figure 3:** (a) VB LCSYSs. (b) Cross-section planes defined coplanar with the xy-planes of each LCSYS. (c) Projected C5 cross-sectional view of the bone, passive muscles and soft tissue.

RESULTS

Peak adjacent-level, cross-section loading is reported in Table 1 for C5 and C6 along with maximum midsagittal VB rotation about their CGs. Negative AP shear is larger for both CTDRs, at both cervical levels, compared to the non-modified model. Peak tension, flexion and VB rotations are almost identical between the three simulations.

Peak interbody forces between C5 and C6 are reported in Table 2 from a cross-section of the intervertebral disc (IVD) for the non-modified model and from contact forces for the CTDRs. The forces are reported in the C6 LCSYS. Negative AP shear and compression is larger for both CTDRs as compared to the IVD. Unlike the IVD, the CTDRs experience negligible tension.

Table 2: Peak interbody forces between C5 and C6.

Simulation	Peak Interbody Load (N)			
	AP Shear		Ten/Comp	
IVD	0.5	-405.4	325.8	-1187.0
Prestige ST	0.4	-439.0	0.6	-1263.3
ProDisc-C	0.1	-411.0	0.0	-1351.9

DISCUSSION

This study was the first dynamic finite element analysis of a frontal automobile impact which evaluated the effects of a C5-6 cervical arthroplasty on neck response. Results from this study suggest that the ROM and the load transmission were maintained during a dynamic impact event. Difference in VB midsagittal rotation between the IVD and CTDR simulations was less than 2° for both levels, indicating that the ROM was maintained. The cross-section axial loading and bending moment above

and below the operative level was maintained in the CTDR simulations, with a maximum difference less than 6N for tension and 1Nm for flexion. The larger negative peak adjacent-level AP shear of the CTDRs may be due to the design of the implants. The maximum AP translation of the Prestige ST was reached during the simulation, potentially increasing the adjacent-level shear loading. The ProDisc-C does not innately allow for AP translation, potentially increasing the shear.

The CTDRs did not support tension within the interbody space. Some interbody separation occurred between the superior and inferior components during flexion-induced tension of the cervical spine, as was evident by the negligible peak interbody tension and the simulation animations. Interbody compression was greater for the CTDRs than the IVD, possibly due to a change in center of rotation and subsequent effects on facet loading.

CONCLUSIONS

Overall, cervical arthroplasty at C5-6 did not appear to significantly alter the neck kinematics and adjacent-level loading during a simulated frontal automobile impact. Further analysis is required to understand the role of the facets on neck response, particularly on interbody loading.

ACKNOWLEDGMENTS

The authors would like to acknowledge the GHBMC for use of the FE model and the United States Army Medical Research and Materiel Command for funding this research. The authors would also like to acknowledge Medtronic and Synthes Spine for supplying sample CTDRs for reverse engineering purposes. All computations were performed on the Wake Forest University DEAC Cluster.

REFERENCES

- Forman (2006). Whole-body kinematic and dynamic response of restrained PMHS in frontal sled tests. *Stapp Car Crash J*, 50, 299-336.
- White (2013). Cross-section neck response of a total human body FE model during simulated frontal and side automobile impacts. *Comput Methods Biomech Biomed Engin*, IN PRESS.

HYBRID TRUE-COLOR MICRO-CT: DESIGN AND APPLICATIONS

James Bennett¹, Hengyong Yu³, Guohua Cao¹, Aaron Mohs² and Ge Wang³

1. School of Biomedical Engineering and Sciences, Virginia Tech
 2. School of Biomedical Engineering and Sciences, Wake Forest University
 3. Department of Biomedical Engineering, Rensselaer Polytechnic Institute
- Corresponding Author: James Bennett, Email: jrbennet@vt.edu

INTRODUCTION

X-ray beams are comprised of high energy photons and like visible light they are generally polychromatic. X-ray detectors in traditional computed tomography (CT) and micro-CT scanners are known as energy-integrating, or intensity integrating, because their output signal is proportional to the detected photon flux integrated across the entire energy spectrum. However, x-ray attenuation varies non-linearly with photon energy; spectral information is lost with energy-integrating detectors in much the same way as color information is lost with black and white photography. Recently, significant progress has been made in true-color (i.e., multi-energy, spectral, spectroscopic, etc.) x-ray detectors that are sensitive to the incident photon energy. Yet, there remain significant hurdles to clinical and even pre-clinical implementation of this technology: cost, size and radiation dose [1].

In 2012, Xu et al reported that near-term implementation of true-color imaging could be enhanced by a hybrid architecture: a narrow-beam spectral ‘interior’ imaging chain integrated with a traditional wide-beam ‘global’ imaging chain [2]. This integration coupled with compressive sensing (CS)-based interior tomography demonstrated promising results for improved contrast resolution, and decreased system cost and radiation dose. In order to validate the merits of this proposed approach, the authors designed and built a first-of-its-kind hybrid true-color micro-CT scanning system. The approach and applications with the system are the topic of this abstract.

METHODOLOGY

Figure 1 shows the proposed system design schematic with the traditional energy integrating imaging chain in blue and the spectral imaging chain in pink. The system

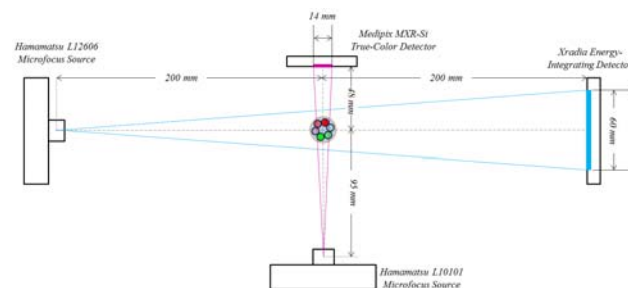


Figure 1. Hybrid true-color micro-CT design schematic.

design was implemented with the following components: Medipix MXR-Si detector; Xradia energy-integrating detector; Hamamatsu L10101 X-ray source for true-color imaging chain; Hamamatsu L12606 X-ray source for Xradia energy-integrating imaging chain; and Xradia sample rotation stage.

A contrast agent (CA) phantom was built to test the spectral contrast and spatial resolution capabilities of the system prototype and is shown in Figure 2 (left: image, right: axial schematic where blue indicates water, red indicates Magnevist, and green indicates Omnipaque).

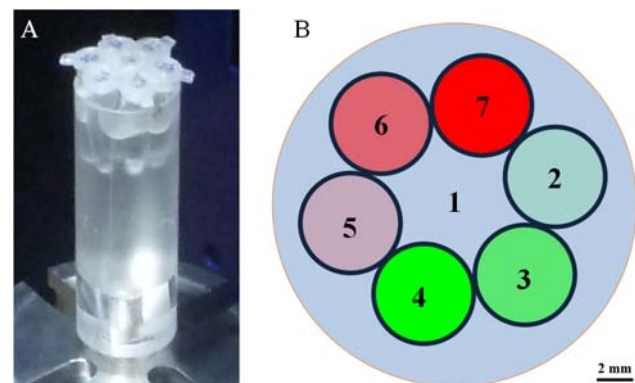


Figure 2. CA phantom.

RESULTS

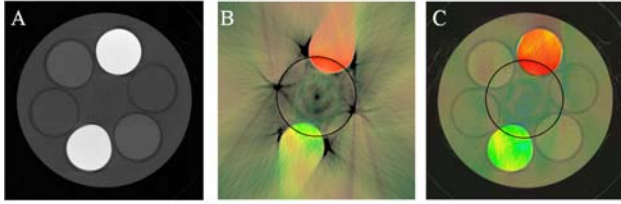


Figure 3. Hybrid true-color micro-CT reconstruction results of the CA phantom. The black circle denotes the interior field of view.

The contrast agent was alternately scanned by both the hybrid and energy integrating imaging chains, and reconstructed with a CS-based iterative algorithm described in [2]. Figure 3 shows (A) reconstruction of the global gray-scale projections; (B) is the reconstruction of the interior true-color projections without the global grayscale image; (C) is the reconstruction of the interior true-color with global gray-scale projection data.

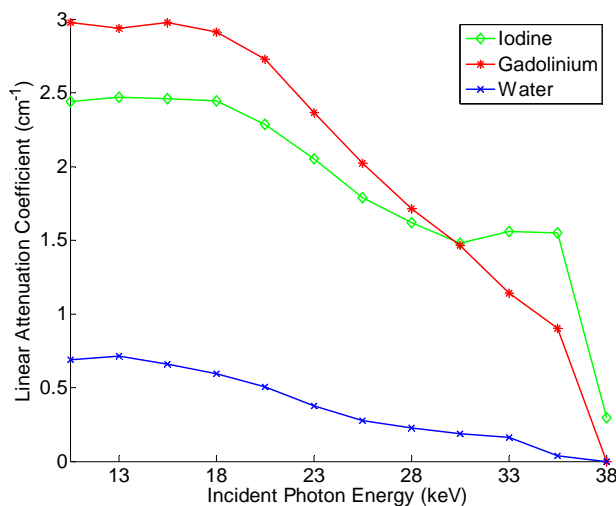


Figure 4. Attenuation versus energy plot.

The interior regions of the CA phantom containing Omnipaque (iodine), Magnevist (gadolinium) and water were reconstructed at various energy energies to produce Figure 4. This figure shows the average linear attenuation coefficient for the aforementioned regions as a function of the spectral energy bin or window. The most prominent feature is the increase in iodine attenuate above its 33 keV K-edge. The silicon-based spectral detector has <1% efficiency at energies above 35 keV, hence the signal drop-off at 38 keV.

Additionally, the spatial and contrast resolution of the system was tested with the CA phantom. The hybrid spectral reconstructions showed an approximately four-fold improvement in its contrast difference to noise ratio

(CDNR) compared with the traditional gray-scale reconstructions [3]. The spatial resolution was calculated using the edge spread function [4], which resulted in the full width at half maximum (FWHM) values of 106 μm , 124 μm and 339 μm for the grayscale, hybrid and interior reconstructions, respectively.

CONCLUSIONS

The experimental results from the hybrid true-color micro-CT prototype demonstrate the feasibility and the merits of this particular system architecture. There is an obvious synergy between the high-resolution grayscale imaging chain and the spectral resolution of the true-color imaging chain. The CS-based reconstruction technique utilizes the respective strengths of each imaging chain to produce images with both high spatial and contrast resolution. This concept was theoretically proven in [2], and the results from the actual implementation in this paper support its assertions.

Future work will build upon these results, and will include a study of the effect of reducing the number of global grayscale and interior true-color projections on the contrast and spatial resolution, in order to reduce the x-ray dose. Another study will seek to optimize the interior true-color energy window width for specific CA k-edge(s) to improve contrast resolution. Finally, we would like to implement a pre-clinical hybrid true-color micro-CT architecture (i.e. rotating gantry) for *in vivo* biomedical applications.

ACKNOWLEDGMENTS

A special thanks to the MARS Bioimaging group (Christchurch, New Zealand) for their collaboration and support with this project.

REFERENCES

- [1] K. Taguchi, S. Srivastava, H. Kudo, and W. C. Barber, "Enabling photon counting clinical X-ray CT," in *Nuclear Science Symposium Conference Record (NSS/MIC)*, 2009 IEEE, 2009, pp. 3581-3585.
- [2] Q. Xu, H. Yu, J. Bennett, P. He, R. Zainon, R. Doesburg, A. Opie, M. Walsh, S. Haiou, A. Butler, P. Butler, X. Mou, and G. Wang, "Image Reconstruction for Hybrid True-Color Micro-CT," *Biomedical Engineering, IEEE Transactions on*, vol. 59, pp. 1711-1719, 2012.
- [3] P. He, B. Wei, W. Cong, and G. Wang, "Optimization of K-edge imaging with spectral CT," *Medical Physics*, vol. 39, pp. 6572-6579, 2012.
- [4] S. M. Bentzen, "Evaluation of the spatial resolution of a CT scanner by direct analysis of the edge response function," *Medical Physics*, vol. 10, pp. 579-581, 1983.

INJURY MECHANISMS IN ROADSIDE MOTORCYCLE COLLISIONS

Allison Daniello¹ and H. Clay Gabler¹

¹Virginia Tech, School of Biomedical Engineering and Sciences

Corresponding Author: Allison Daniello, Email: adaniell@vt.edu

INTRODUCTION

In the United States, more motorcyclists are fatally injured each year in highway barrier crashes than passengers of any other vehicle, though they only account for about 3% of the vehicle fleet. Although there have been extensive efforts to redesign barrier to improve car crash safety [1], there has unfortunately been little accomplished or attempted to improve safety for motorcyclists—who carry the greatest fatality risk in these crashes. One of every eight motorcyclists who strike guardrail will be killed.

In the U.S, a fierce debate is raging between motorcycle groups and state highway designers over the perceived danger of some barrier designs. Motorcycle groups derisively refer to cable barrier as “human cheese-cutters”. Barrier designers counter by pointing out that cable barrier is one of the safest barrier designs for car occupants. However, neither has produced data to support their positions.

Detailed injury data for riders involved in crashes is crucial to understanding serious injury mechanisms in motorcycle-barrier crashes. This is also a required first step towards the design of injury countermeasures. Unfortunately, in the U.S. there is little information on serious injuries in motorcycle crashes, unlike that available for passenger vehicle crashes. The last in-depth study investigating motorcycle crashes in the U.S. was conducted over 30 years ago by Hurt et al. [2]. Since this study was conducted, significant changes have been made in barrier, helmet, and motorcycle design, and these data do not accurately reflect crashes today.

The objective of this research is to determine injury mechanisms in motorcycle-barrier crashes through

clinical studies and crash investigation to develop potential countermeasures to reduce fatalities in these crashes.

METHODOLOGY

Cases in our study were identified and enrolled by Wake Forest Baptist Medical Center (Winston-Salem, NC) from patients involved in motorcycle-barrier crashes who were admitted to their Level 1 trauma center. There were three main components of each crash investigation in our study: (1) environment and barrier, (2) motorcycle, and (3) rider. To collect these data, an investigator visited the crash site soon after the crash to collect the environmental data elements. Additionally, the investigator inspected the motorcycle to detail the damage to the motorcycle. Both the site and the motorcycle were photographed, with particular attention paid to factors altered by the crash, such as fabric transfers, blood, scrapes, or skid marks.

Detailed injury data was also gathered from medical records for each patient in the study. All injuries were tabulated and given an injury severity score using the Abbreviated Injury Scale (AIS). This scale ranks the threat to life of an injury, ranging from 1 (minor) to 6 (not survivable). An AIS-score of 3 or greater is a serious injury. Imagery for each injury was also incorporated, including CT scans, x-ray images, and patient photos showing external injuries.

The team at Virginia Tech coupled evidence from the crash investigations with the injury data from the patient and determined the likely crash scenario for each crash. For these reconstructions, we reviewed the evidence from the scene, motorcycle, helmet and injuries and determined potential crash scenarios and the impact point(s) that caused each injury.

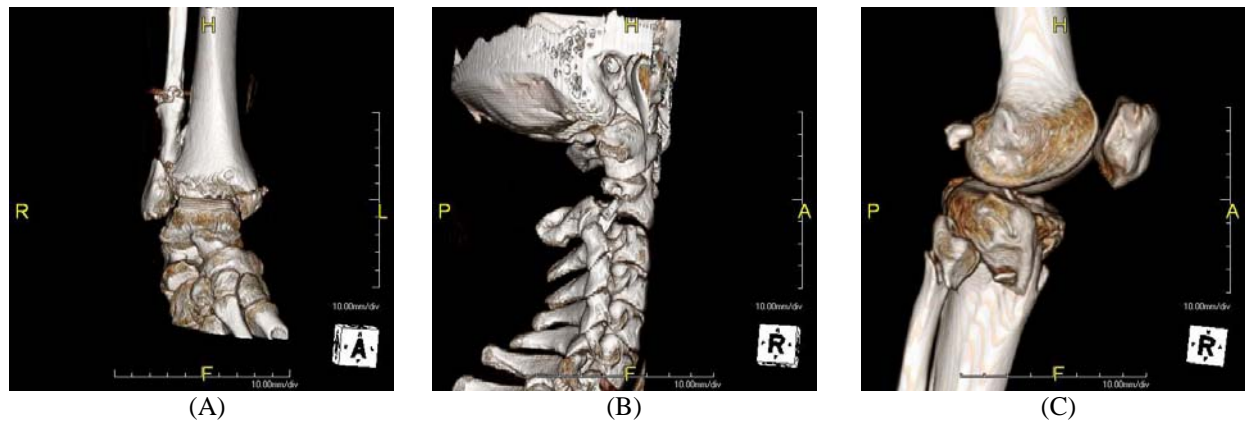


Figure 1: Injury Reconstructions (A) Right Ankle Fracture, (B) C2 Fracture, (C) Tibial Plateau and Fibular Fractures

RESULTS

To date, we investigated 9 motorcycle-to-barrier collisions, involving 10 motorcyclists. There were 7 crashes with W-beam guardrail, 1 crash with cable barrier, and 1 crash with both W-beam guardrail and cable barrier. Between the ten riders, there were 111 AIS-coded injuries. Figure 1 shows some examples of injuries investigated.

The thorax suffered the greatest number of serious injuries; however, the extremities suffered the greatest number of non-serious injuries. In the crashes investigated, direct contact between the rider and the barrier was thought to cause the greatest number of serious and non-serious injuries. The second most common cause of serious and non-serious injuries was contacting the ground.

Contact with the face and lower edge of the w-beam barrier rail were thought to cause the majority of injuries. The post was thought to cause the same number of serious injuries as the faces of the rail. However, the upper edge of the rail and upper edges of the posts were also thought to cause a large number of serious and non-serious injuries.

DISCUSSION AND CONCLUSIONS

Motorcyclists are highly overrepresented in fatalities in highway barrier crashes. There is no current in-depth crash and injury data available in the U.S. to determine how motorcyclists are injured in these crashes. Through this research, a methodology was developed to investigate these crashes and applied to determine the injury sources for 111 injuries across 10 riders.

The thorax suffered the most severe injuries in the cases investigated, though the extremities suffered the greatest number of injuries. These findings are consistent with

those of previous studies conducted in other countries [3, 4]. In crashes with w-beam guardrail, both main components of the barrier system (rail and post) were thought to cause serious injury. Riders were believed to interact primarily with the top of the rail. Providing a protective covering to the top edge of the rail and the upper faces of the posts may mitigate injuries. Previous interventions have typically focused on protecting the rider from the posts of the guardrail; however, all components were thought to cause injury.

ACKNOWLEDGMENTS

Thank you to the National Academies of Science Transportation Research Board for funding this research. Thanks also go to the teams at Wake Forest and Virginia Tech for their assistance in data collection and case reviews.

REFERENCES

1. The American Traffic Safety Services Association (ATSSA). *Toward Zero Deaths: A vision for Safer Roads in America*, 2008.
2. Hurt, H., Ouellet, J.V., and Thom, D., *Motorcycle Accident Cause Factors and Identification of Countermeasures, Volume I*, DOT Technical Report, Contract No. DOT HS-5-01160, Washington DC, 1981.
3. Bambach, M.R. Grzebieta, R.H. McIntosh, A.S. Injury typology of fatal motorcycle collisions with roadside barriers in Australia and New Zealand, *Accident Analysis and Prevention*, accepted for publication, 2011, Ref. No.: AAP-D-10-00443R1.
4. Hefny, A.F., Barss, P., Eid, H.O., and Abu-Zidan, F.M. Motorcycle-related injuries in the United Arab Emirates. *Accident Analysis and Prevention*, 2011, doi: 10.1016/j.aap.2011.05.003.

MORPHOLOGICAL ANALYSIS OF CHANGES IN THE THORACIC SKELETON WITH AGE AND GENDER

Ashley A. Weaver^{1,2}, Callistus M. Nguyen^{1,2}, Samantha L. Schoell^{1,2}, and Joel D. Stitzel^{1,2}

1. Virginia Tech-Wake Forest University Center for Injury Biomechanics

2. Wake Forest University School of Medicine

Corresponding Author: Ashley A. Weaver, Email: asweaver@wakehealth.edu

INTRODUCTION

In motor vehicle crashes (MVCs), thoracic injury ranks second only to head injury in terms of the number of fatalities and serious injuries, the body region most often injured, and the overall economic cost [1, 2]. Age and gender-specific variations in the geometry and mechanics of the thoracic skeleton are expected to relate to thoracic injury. The motivation of the study was to improve the understanding of thoracic injury by quantifying age and gender-specific variations in the thoracic skeletal morphology for males and females of ages 0-100.

METHODOLOGY

Age and gender-specific size and shape variations in the ribs and sternum were quantified using the following steps: 1) Radiological Scan Collection, 2) Image Segmentation, 3) Atlas Development, 4) Image Registration, and 5) the Generalized Procrustes Analysis (GPA) [3].

A minimum of 10 normal chest computed tomography (CT) scans for each gender were collected from a radiological database for the following ages: newborns, 3,

6, and 9 month, and 1, 3, and 6 year olds. Beginning with 10 year olds, a minimum of 10 CT scans for each gender were collected by decade up to age 100. A semi-automated method was used to segment the ribs and sternum from CT scans of each of the 345 subjects in the study. Atlases were created from an average male for the 24 ribs and the sternum and between 3,000 to 11,000 landmarks were placed on each atlas. Rigid, affine, and non-linear transformations were used in a semi-automated registration algorithm to morph the appropriate atlas and its landmarks to the corresponding rib or sternum segmentation of each subject (Figure 1). This allowed for the collection of homologous rib and sternal landmarks that are comparable across subjects of all ages.

Following the collection of homologous landmarks, a geometric morphometrics technique known as the GPA was used to analyze the landmark data to formulate age and gender-dependent functions describing changes in the size and shape of the ribs and sternum. Quadratic functions were produced quantifying the location of homologous landmarks for subjects of a particular age and gender. Permutation testing was employed to assess the significance of rib and sternum morphology changes with age and gender [3].

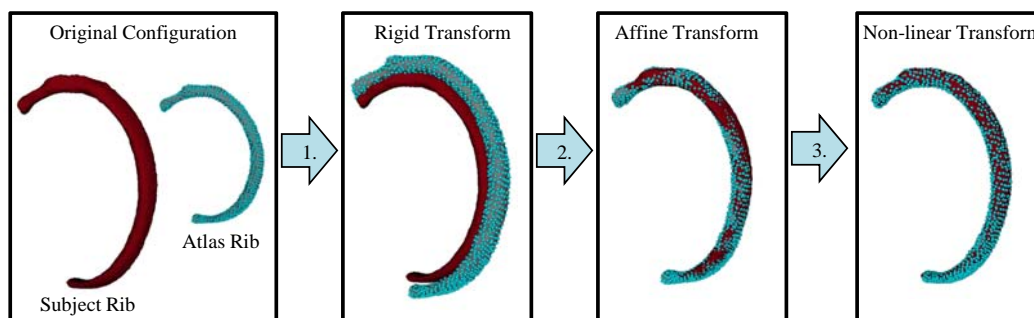


Figure 1: Example of the registration algorithm applied to register a rib. Steps 1-3: Rigid, affine, and nonlinear transforms applied to register the atlas rib to the subject rib and transform the atlas landmarks (1,000 atlas landmarks are shown).

RESULTS

A total of 100 quadratic regression functions describing size and shape changes in the ribs and sternum were produced. Four regression functions were produced for each of the 25 structures (24 ribs and sternum): 1) the combined size and shape variation with age for females, 2) the shape variation with age for females, 3) the combined size and shape variation with age for males, and 4) the shape variation with age for males. Regression functions for the ribs were produced for ages 0-100 years. Regression functions for the sternum were produced for ages 10-100 years due to the incomplete ossification of the sternum in pediatric subjects younger than 10 years.

The combined size and shape changes were found to be significant with age in males and females for all 25 structures ($p < 0.001$ for all structures). When isolating just the shape changes, the shape was found to vary significantly with age for the male left and right ribs 1-12 (p ranged from <0.001 to 0.002). The shape was found to vary significantly with age for the female sternum and the female left and right ribs 1-12 (p ranged from <0.001 to 0.006). Only the male sternum was found to have non-significant shape changes with age ($p = 0.127$). An illustration of the GPA results for the sternum is provided in Figure 2. There were also visible differences in the morphology of the sternum between ages and genders, particularly in the manubrium.

CONCLUSIONS

In conclusion, the image segmentation and registration algorithm developed allowed for the collection of extensive homologous landmark data in the ribs and sternum. This algorithm could be similarly applied to other body regions to quantify size and shape changes in skeletal and soft tissue anatomy. Significant changes in size and shape for all 24 ribs and the sternum were found to occur with age in both genders. Significant changes in shape alone were found to occur with age for the female sternum and the left and right ribs 1-12 in both genders. The variation functions describe the size and shape changes in the thoracic skeleton and will be used in future work to generate a parametric finite element model of the thorax. The results of this study provide an improved understanding of the complex relationship between thoracic anthropometry, age, gender, and injury risk.

ACKNOWLEDGMENTS

Funding was provided by the National Science Foundation Graduate Research Fellowship Program and the National Highway Traffic Safety Administration under Cooperative Agreement Number DTN22-09-H-

00242. Views expressed are those of the authors and do not represent the views of NHTSA. The following people assisted with study design and data collection: Dr. Leon Lenchik, Dr. Joseph Maldjian, Dr. Chris Wyatt, AJ Allen, Elizabeth Armstrong, Elizabeth Davenport, John Keller, Hannah Kim, Lauren Moody, Chelsea Price, Hannah Reynolds, Colby White, and Haiyong Xu.

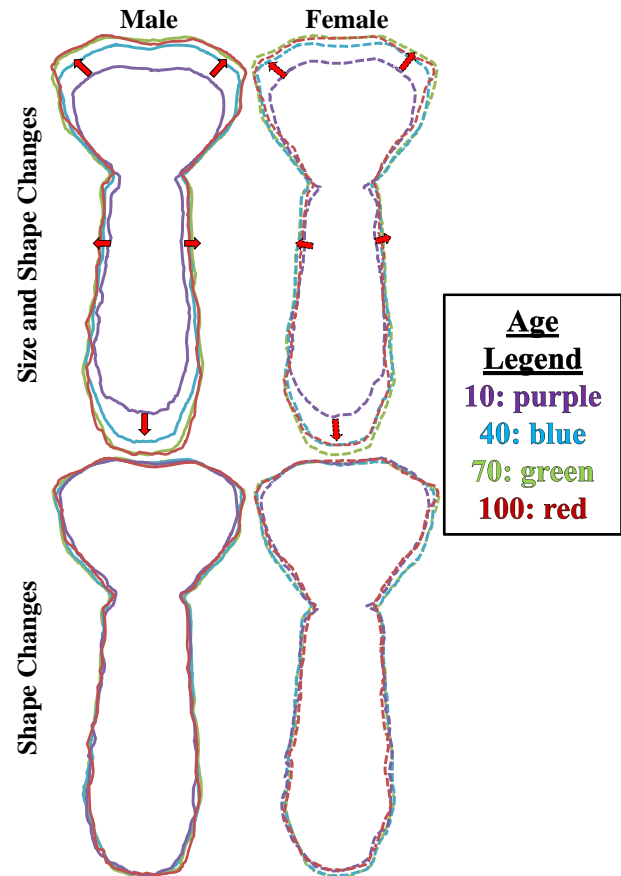


Figure 2: Size and shape changes (top) and isolated shape changes (bottom) for the male and female sternums are indicated by outlines for ages 10, 40, 70, and 100.

REFERENCES

1. Cavanaugh, J.M., *Biomechanics of Thoracic Trauma*, in *Accidental Injury: Biomechanics and Prevention*, J.M. Alan M. Nahum, Editor. 2002, Springer-Verlag: New York. p. 374-404.
2. Ruan, J., et al., *Prediction and analysis of human thoracic impact responses and injuries in cadaver impacts using a full human body finite element model*. Stapp Car Crash J, 2003. **47**: p. 299-321.
3. Gunz, P., Mitterocker, P, Bookstein, FL, *Semilandmarks in three dimensions*, in *Modern Morphometrics in Physical Anthropology*, D.E. Slice, Editor. 2005, Kluwer/Plenum: New York.

SHEAR STRESS-MEDIATED TUMOR-ENDOTHELIAL CROSS TALK REGULATES THE ANGIOGENIC POTENTIAL OF BREAST TUMORS *IN VITRO*

Cara F. Buchanan¹, Elizabeth E. Voigt¹, Pavlos P. Vlachos^{1,2}, and M. Nichole Rylander^{1,2}

1. Virginia Tech-Wake Forest University School of Biomedical Engineering and Sciences

2. Virginia Tech, Department of Mechanical Engineering

Corresponding Author: Cara Buchanan, Email: cfbuchan@vt.edu

INTRODUCTION

Endothelial cells lining blood vessels are exposed to various hemodynamic forces including fluid shear, the tangential force derived from the friction of blood flowing across the luminal cell surface, tensile stress due to deformation of the vessel wall by transvascular flow, and normal stress caused by the pressure differential across the vessel wall [1]. While it is known that fluid forces induce changes in endothelial morphology, cytoskeletal reorganization, and gene expression, the effect of flow on endothelial organization within the context of the tumor microenvironment is largely unknown.

In this study, we utilized a collagen based *in vitro* microfluidic tumor vascular model to investigate flow-mediated endothelial barrier function and tumor angiogenic potential [2]. Target microvascular wall shear stresses (WSS) ranging from low ($\tau_w=1$ dyn/cm²), normal ($\tau_w=4$ dyn/cm²), and high ($\tau_w=10$ dyn/cm²) were estimated based on Poiseuille assumptions and experimentally measured using micro-particle image velocimetry (μ -PIV). It is hypothesized that WSS will alter the endothelial phenotype such that vascular permeability and tumor-expressed angiogenic factors are enhanced. Results demonstrate that fluid flow increases endothelial alignment in the direction of flow and decreases vascular permeability as a function of WSS. Co-culture with tumor cells increases permeability relative to mono-cultures, which may be attributed to tumor-VEGF-induced permeability. In addition, high WSS significantly down-regulates tumor-expressed angiogenic factors. This result was not observed in tumor mono-cultures, suggesting flow-mediated paracrine signaling elicits an angiogenic response.

METHODOLOGY

In vitro tumor vascular models were fabricated by polymerizing type I collagen (8 mg/ml) around a 2.0”

22G (711 μ m) needle fit concentrically in fluorinated ethylene propylene (FEP) tubing housed in 35 mm petri dishes. MDA-MB-231 breast cancer cells were suspended in the collagen matrix (1×10^6 cells/ml), and microvascular endothelial cells (TIME) were seeded on the microchannel lumen (10×10^6 cells/ml). Flow was introduced by inserting 0.5” 22G needles into the microchannel and maintained using a syringe pump. A 72 hr low flow-preconditioning scheme was used to establish a confluent endothelialized microchannel, after which the endothelium was exposed to one of the three target WSS ($\tau_w=1, 4, \text{ or } 10$ dyn/cm²) for 6 hrs. WSS were quantified using μ -PIV. Briefly, 3.2 μ m fluorescent particles were perfused through the channel, illuminated with a 523 nm laser, and imaged using a 1MP camera. Particle image pairs were correlated to obtain a mean velocity field [3] and WSS were then calculated based on the velocity gradient and measured viscosity of the culture media (0.78 cP) using thin-plate spline radial basis functions [4].

To visualize shear-induced morphological changes in the endothelium, cells were stained with Oregon green phalloidin and DAPI. Endothelial barrier function was assessed by perfusing 70 kDa Oregon green-conjugated dextran (10 μ g/ml) through the microchannel for 1 hr, as selectively permeable mature capillaries are known to be impermeable to dextrans over a molecular weight of 65 kDa [5]. Imaging was performed using an inverted fluorescence microscope and ImageJ was used to measure average fluorescence intensity in a ROI spanning the width of the endothelialized microchannel. The effective permeability coefficient, P_d , which describes the ability of a solute to escape uniformly from the vascular lumen [6], was calculated by the following equation:

$$P_d = \frac{1}{I_1 - I_b} \left(\frac{I_2 - I_1}{\Delta t} \right) \frac{d}{4}$$

where d is the microchannel diameter, I_b is the average background intensity, I_1 is the average initial intensity,

and I_2 is the average intensity after the recovery time Δt [6]. P_d was measured as a function of each target WSS and normalized to the preconditioned endothelium.

To determine the effect of WSS on tumor-endothelial cross-talk, expression levels of target genes in MDA-MB-231 cells were determined quantitatively by RT-PCR. Total tumor mRNA was isolated by the phenol-chloroform extraction method from co-cultures or mono-cultures following exposure to each τ_w .

RESULTS

F-actin staining demonstrated that endothelial cells develop a confluent endothelium along the microchannel lumen and maintain integrity after exposure to each target WSS, with increased spreading and alignment in the direction of flow with increasing WSS (Fig. 1).

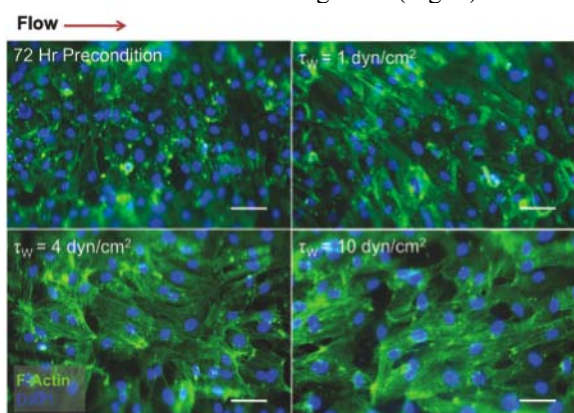


Fig. 1. TIME cells increase spreading and alignment as a function τ_w . Scale bar = 200 μm .

RT-PCR results indicate that in the presence of an endothelium, high WSS significantly down-regulates all MDA-MB-231-expressed angiogenic factors probed in this experiment (Fig. 2). In contrast, WSS did not have an effect on tumor mono-cultures (data not shown), suggesting fluid forces acting on the endothelium regulate cross-talk with surrounding tumor cells.

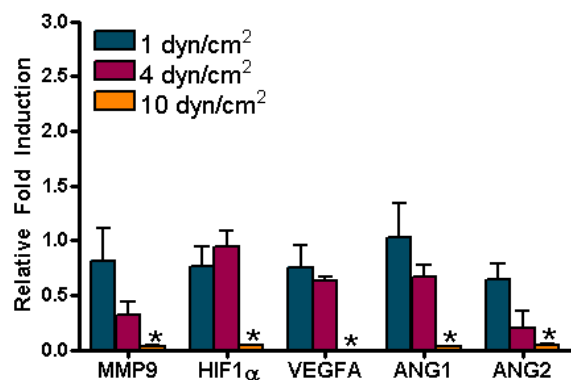


Fig. 2. High WSS (10 dyn/cm^2) down-regulates tumor expressed angiogenic factors only in the presence of an endothelium. * $p < 0.05$ (n=4).

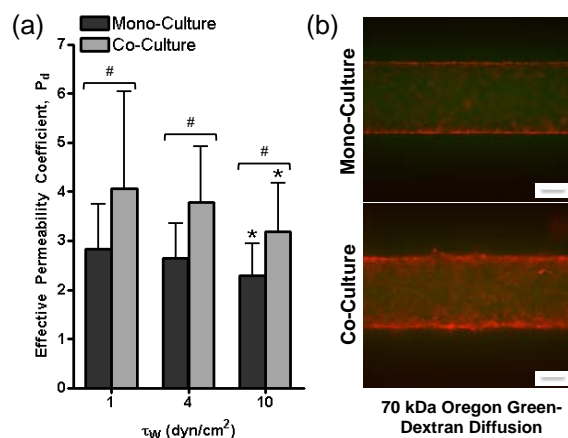


Fig. 3. a) Endothelial P_d significantly decreases at $\tau_w=10 \text{ dyn}/\text{cm}^2$ while co-culture significantly increased P_d for all τ_w . b) Oregon green dextran permeating endothelium. Scale bar = 200 μm .

The effective permeability coefficient, P_d , decreases with increasing WSS for both endothelial mono-culture and co-culture with tumor cells (Fig. 3a). This decreased permeability is likely due to flow-mediated endothelial alignment, in which high WSS significantly decreased P_d . The presence of tumor cells also increased P_d relative to endothelial mono-cultures for all τ_w . Images for the case of $\tau_w = 10 \text{ dyn}/\text{cm}^2$ qualitatively show greater distribution of dextran across the endothelium during co-culture with tumor cells (Fig. 3b), with a disorganized endothelium that may contribute to increased permeability.

CONCLUSION

With the advent of anti-angiogenesis therapies targeting the tumor vasculature, it is important to understand how cells respond to changes in blood velocity and vessel structure. Results from this work underscore the importance of flow-mediated tumor-endothelial cross-talk to regulate barrier function and expression of angiogenic growth factors. These findings have significant implications regarding low blood velocities commonly seen in the tumor vasculature, suggesting high shear stress-regulation of angiogenic activity is lacking in many vessels, thereby driving tumor angiogenesis.

ACKNOWLEDGMENTS

Funding for this project was provided by the NSF Early CAREER Award and NIH Grant IR21CA158454-01A1.

REFERENCES

- [1] Shieh, A.C., *Ann Biomed Eng*, 2011. **39**(5): 1379-89.
- [2] Buchanan C.F., *et al.*, *Tissue Eng C. In Review*
- [3] Voigt, E.E., *et al.*, *Cardiovas Eng & Tech*, 2012. **3**(1).
- [4] Karri S., *et al.*, *Meas Sci & Tech*, 2009. **20**(4).
- [5] Grainger, S.J., *et al.*, *PLoS One*, 2011. **6**(7): e22086.
- [6] Price, G.M., *et al.*, *Meth Mol Bio*, 2011. **671**: 281-93.

NEUROGLIAL DIFFERENTIATION OF ADULT MAMMALIAN ENTERIC NEURONAL PROGENITOR CELLS AS A FUNCTION OF EXTRACELLULAR MATRIX COMPOSITION

Shreya Raghavan^{1,2}, and Khalil N. Bitar^{1,2}

1. Virginia Tech-Wake Forest School of Biomedical Engineering and Sciences
2. Wake Forest Institute for Regenerative Medicine

Corresponding Author: Khalil N. Bitar, Email: kbitar@wakehealth.edu

INTRODUCTION

A fully developed and continuous enteric nervous system is essential for normal gastrointestinal physiology, modulating motility, secretion, absorption and excretion. Aganglionosis, enteric neuropathy and/or neurodegeneration are hallmarks of several conditions including Hirschsprung's disease, achalasia, Parkinson's disease, inflammation and aging [1]. Enteric neuronal progenitor cells are neural crest-derived stem cells that can be isolated from fetal, post-natal and adult gut. Neural stem cell transplantation is an emerging therapeutic paradigm to replace dysfunctional or lost enteric neurons in several aganglionic disorders. A matrix composed primarily of Collagen IV, Laminin and a Heparan sulfate proteoglycan surrounds adult mammalian myenteric ganglia in vivo. Extracellular matrix composition can modulate stem cell fate and direct differentiation by providing adhesion, structural and mechanical cues. The impetus to identify an appropriate microenvironment for enteric neuronal progenitor cells derives from the need to improve survival and phenotypic stability following transplantation. Tissue engineering offers an elegant approach to characterize in vitro differentiation of post-natal mammalian enteric neuronal progenitor cells, as a function of ECM composition. The development of neural crest stem cells into neurons and glia is studied within this paradigm as a function of ECM composition and correlated to structural and rheological properties of ECM hydrogels.

METHODOLOGY

ECM gels with various combinations of Collagen I, Collagen IV, Laminin and Heparan sulphate were characterized for viscoelastic moduli using oscillatory rheometry. Fiber diameters were measured using scanning

electron microscopy to characterize gel architecture. Enteric neuronal progenitor cells were isolated from full thickness jejunal biopsies from rabbits and cultured to generate neurosphere-like bodies (enteric neurospheres). Neuronal and glial differentiation was studied in two dimensional on coverslips coated with ECM components. Poly lysine was used as control. Immunofluorescence was used to detect neurons and glia at two time points (Day 5 and Day 15). Neurite lengths were measured to quantify neuronal differentiation. Red fluorescent intensity was quantified to identify the number of differentiated glia.

RESULTS

1) Characterization of ECM gels: The addition of Collagen IV to Collagen I significantly increased viscoelastic modulus of ECM gels (236 ± 13.3 Pa compared to 72.63 ± 4 Pa). Addition of 1 % (wt) heparan sulfate further significantly increased modulus to 314.7 ± 9.53 Pa. Table 1 summarizes viscoelastic moduli for ECM gels. Modulus readings were consistent with fiber diameters, where the addition of Collagen IV and heparan sulphate increased fiber diameters of Collagen I gels ($770.1 \pm 50.4 \mu\text{m}$ compared to $478.3 \pm 19.31 \mu\text{m}$).

2) Characterization of neuronal differentiation: Culture substrata containing either laminin, Collagen I or Collagen IV demonstrated substantial neuronal differentiation evident by day 5. Neurite lengths varied ranged between $193 \mu\text{m}$ and $288 \mu\text{m}$. By day 15, laminin-containing substrata had significantly longer neurites ($326.9 \pm 13.25 \mu\text{m}$). The addition of laminin and/or heparan sulphate to collagen containing substrata significantly enhanced neuronal differentiation and neurite lengths (ranging from 212.8 ± 9.46 to $325 \pm 19 \mu\text{m}$). Neuronal networking was initiated on heparan sulphate substrata.

3) Characterization of glial differentiation: Enteric neurospheres on poly lysine culture substrata

demonstrated significant GFAP staining (day 5: 15.29 ± 1.29 AU; day 15: 28.56 ± 1.14 AU). In contrast, enteric neurospheres on pLL coverslips did not demonstrate significant neuronal differentiation at day 5, indicating the preferential differentiation in to glia at the early time point on pLL coverslips. Collagen I, Collagen IV, Laminin, Heparan sulfate and supported glial differentiation at both time points, to varying extents ranging from 10.16 ± 0.8 to 16.54 ± 0.32 AU. Figure 1 compares neurite lengths and glial differentiation on primary ECM coated substrata.

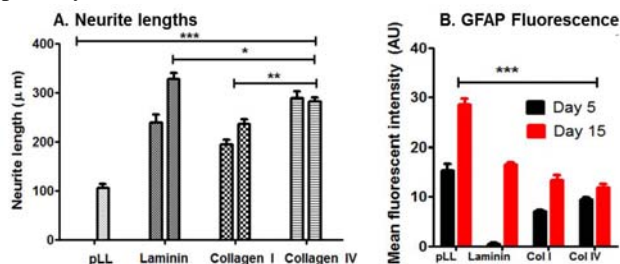


Figure 1: (A) Neurite lengths on primary ECM coated substrata demonstrate significantly long neurites on laminin substrates. (B) Quantification of GFAP immunofluorescence indicates the presence of a significantly large population of glial cells on poly lysine substrates.

Table 1: Summary of Viscoelastic moduli determined by oscillatory rheometry

Sample (ECM composition)	Viscoelastic modulus (Pa; mean \pm SEM)
Collagen I (800 μ g/ml)	72.63 ± 4.86
Collagen I (800 μ g/ml) + Collagen IV (200 μ g/ml)	236 ± 13.53
Collagen I + IV + Laminin (10 μ g/ml)	220 ± 16.27
Collagen I + IV + Laminin + Heparan sulphate (10 μ g/ml)	314.7 ± 9.53

DISCUSSION

Viscoelastic modulus values indicated that ECM gels were within the mechanical range of supporting neuronal and glial differentiation. The range of values was consistent with those reported in literature for the developing gut mesenchyme.

Addition of laminin to collagen substrates improved neurite outgrowth with longer neurite lengths owing to its ability to stimulate neural cell attachment and neurite outgrowth [2]. Indeed, migratory neural crest cells have been shown to acquire a neurally-related laminin receptor upon entering the gut mesenchyme that facilitates differentiation [3].

Heparan sulfate and its interaction with GDNF and other neurotrophic factors stabilizes and makes these factors locally available [4, 5]. Heparan sulfate interacts with both Collagen IV and with Laminin, to positively modulate neuronal differentiation, evidenced by the enhanced neurite lengths and initiation of neuronal networking.

CONCLUSIONS

Various neural ECM components were evaluated individually and in combination to study their effect of neuroglial differentiation of adult enteric neuronal progenitor cells. Individually, all evaluated culture substrates supported neuronal and glial differentiation to varying degrees by day 15. Enteric neurospheres demonstrated a clear tendency to differentiate into glia on poly lysine coated substrates as well as on composite collagen substrates in the absence of laminin and heparan sulfate. In contrast, culture substrates with laminin and heparan sulfate promoted extensive neuronal differentiation while simultaneously supporting only a minimal glial cell population.

Our results indicate that specific ECM substrates that include type IV Collagen, laminin and heparan sulfate support and maintain neuronal and glial differentiation to different extents. Here, we identify a matrix composition optimized to tissue engineer transplantable innervated GI smooth muscle constructs to remedy aganglionic disorders.

ACKNOWLEDGMENTS

This work was supported by NIHR01DK071614, RO1DK042876.

REFERENCES

- De Giorgio, R. and M. Camilleri, *Human enteric neuropathies: morphology and molecular pathology*. Neurogastroenterol Motil, 2004. **16**(5): p. 515-31.
- Martin, G.R. and R. Timpl, *Laminin and other basement membrane components*. Annu Rev Cell Biol, 1987. **3**: p. 57-85.
- Pomeranz, H.D., et al., *Expression of a neurally related laminin binding protein by neural crest-derived cells that colonize the gut: relationship to the formation of enteric ganglia*. J Comp Neurol, 1991. **313**(4): p. 625-42.
- Barnett, M.W., et al., *Signalling by glial cell line-derived neurotrophic factor (GDNF) requires heparan sulphate glycosaminoglycan*. J Cell Sci, 2002. **115**(Pt 23): p. 4495-503.
- Mammadov, B., et al., *Cooperative effect of heparan sulfate and laminin mimetic peptide nanofibers on the promotion of neurite outgrowth*. Acta Biomaterialia, 2012. **8**(6): p. 2077-2086.

THE EFFECTS OF ETHANOL EXPOSURE ON NON-HUMAN PRIMATE BRAIN NETWORKS

Qawi K. Telesford¹, April T. Davenport², Robert A. Kraft¹, David P. Friedman², Paul J. Laurienti³, and James A. Daunais²

1. Virginia Tech-Wake Forest University, School of Biomedical Engineering and Sciences
2. Wake Forest University School of Medicine, Department of Physiology and Pharmacology
3. Wake Forest University School of Medicine, Department of Radiology

Corresponding Author: Qawi Telesford, Email: qtelesfo@wakehealth.edu

INTRODUCTION

Neuropathological and neuroimaging studies have demonstrated morphological and functional consequences of alcoholism in humans. However, this data does not provide a clear sense of how whole-brain connectivity is affected by ethanol exposure. Network science is a valuable tool for understanding the brain as a system by showing how different regions of the brain interact with each other.

Non-human primates (NHP) provide a unique research model to study complex behavioral issues. Many aspects of their physiology, behavior and development parallel those seen in humans, which facilitate translation of animal models to the human condition. NHP models are useful because changes in behavioral, pharmacological, and neurobiological variables can be identified and investigated in large part due to the control maintained over their experimental and medical histories. Using a non-human primate (NHP) model of ethanol self-administration, we investigated the effect of acute ethanol intoxication on NHP brain network organization.

METHODOLOGY

Two cohorts (n=19) of vervet monkeys (*Chlorocebus aethiops*) were used in this study. Animals were scanned at two time points: in the treatment naïve state and after 12 months of free access to ethanol. Scans were acquired on a 3.0T GE Scanner equipped with a Twin Speed Gradient Coil in Zoom Mode (maximum gradient strength 4G/cm and a slew rate of 150mT/m/ms). Resting state fMRI analysis was acquired with a gradient echo EPI sequence using an 8-channel receive only RF head coil with a form factor designed specifically for the nonhuman primate. The scanning parameters for the animals were

based on an optimized sequence developed for NHPs. An anatomic scan was also collected for normalization of functional images.

From each voxel, fMRI time courses were extracted and corrected for physiological noise (Fox, Snyder et al. 2005). Mean time courses from the entire brain (the average of voxel values within the brain parenchyma mask including gray and white matter), the deep white matter, and the ventricles were regressed from the filtered time series. The six rigid-body motion parameters from the motion correction process were also regressed from the time series.

A correlation matrix was produced by computing the Pearson correlation between all possible pairs of voxels within the fMRI time series. A threshold was applied to the correlation matrix, whereby voxel pairs above the threshold were considered functionally connected and assigned a value of 1 and voxel pairs below the threshold were considered not connected and assigned a value of 0. The discretization of the correlation matrix produces a binary adjacency matrix.

From the adjacency matrix, community structure analysis was performed on each animal. Community structure analysis detects the level of interconnectedness in the network. Community structure was used in this study to determine how modular structure was affected by acute ethanol exposure. Scaled inclusivity (SI) was used to determine the consistency of community structure across subjects (Steen, Hayasaka et al. 2011).

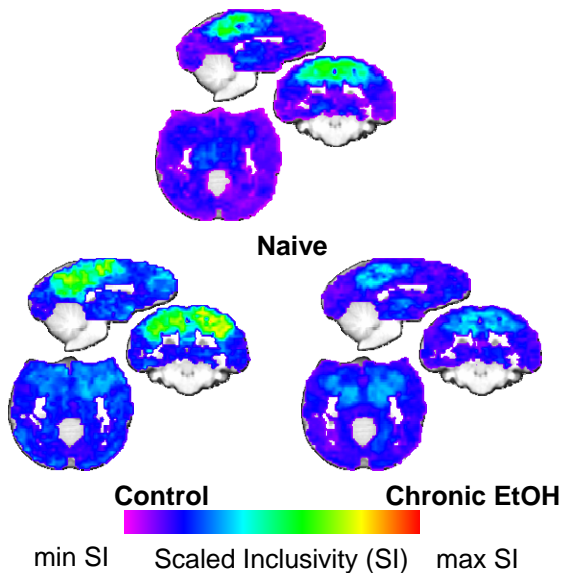


Figure 1: Scaled inclusivity maps for treatment-naïve animals compared to 12-month maps after free access to ethanol for chronic EtOH group.

RESULTS

The most consistent regions across animals in both states were the precuneus and parietal region. Comparing the drinking and non-drinking cohort, it is apparent that after 12 months, the control group shows more consistency in their community structure, while the animals in the drinking group show less consistency (Figure 1). Further comparison of the maps in the control and naïve groups show that the consistency of the animals in the treatment-naïve state is maintained after 12 months. Within the drinking cohort, there appears to be more consistency in the region of the thalamus.

Stratifying the drinking group into high drinkers (animals that consume >2.0 g/kg ethanol per day) and low drinkers (animals that consume ≤2.0 g/kg ethanol per day), maps were compared to see if community structure consistency was intake dependent. As seen in Figure 2, while the chronic EtOH shows some consistency for both the precuneus/parietal and thalamic regions seen in Figure 1, the precuneus/parietal region is more consistent in the low drinkers, while the thalamic region is more consistent in the high drinkers.

DISCUSSION

Within the control group, there isn't much deviation in the brain networks of the animals from the treatment-naïve state. This result suggests that any changes seen in consistency can be attributed to alcohol. While the drinking group showed the same regions at a lower level consistency in the precuneus/parietal region, stratification

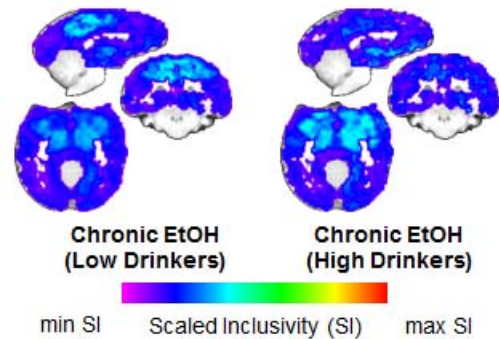


Figure 2: Scaled inclusivity maps for low drinkers and high drinkers after 12-months chronic EtOH exposure.

of the animals into high and low drinkers suggests show within the group there are differences based on intake. Quite startlingly, the low drinkers show brain organization that is similar to the control and the high drinking group. These similarities show that low drinkers are an intermediary between non-consumption and high consumption of alcohol.

CONCLUSION

Chronic alcohol consumption is known to have an effect on behavior. In our study we have shown that this change in behavior may be linked to the functional organization of the brain. Animals that have no exposure to alcohol tend to maintain the consistency of their network structure over time; however, animals that chronically consume alcohol appear to have different functional topology. These results show that alcohol does have an effect on the brain as early as a year into the drinking history of an animal. What is more striking is these changes appear to be intake dependent.

ACKNOWLEDGMENTS

Supported in part by AA019893 (QKT), AA019432, AA017710 (JBD), AA014106 (DPF). The authors would also like to thank the Center for Biomolecular Imaging for developmental time on the scanner.

REFERENCES

- Fox, M. D., A. Z. Snyder, et al. (2005). "The human brain is intrinsically organized into dynamic, anticorrelated functional networks." *Proceedings of the National Academy of Sciences of the United States of America* **102**(27): 9673-9678.
- Steen, M., S. Hayasaka, et al. (2011). "Assessing the consistency of community structure in complex networks." *Phys Rev E Stat Nonlin Soft Matter Phys* **84**(1): 016111.

CASE STUDY ON HIGH-FREQUENCY IRREVERSIBLE ELECTROPORATION (H-FIRE) FOR THE TREATMENT OF SQUAMOUS CELL CARCINOMA

Christopher B. Arena¹, Michael B. Sano¹, Paulo A. Garcia¹, M. Nichole Rylander¹, J. Mike Cissell², John L. Robertson², and Rafael V. Davalos¹

1. Virginia Tech-Wake Forest University, School of Biomedical Engineering and Sciences
2. Virginia-Maryland Regional College of Veterinary Medicine, College of Veterinary Medicine

Corresponding Author: Christopher B. Arena, Email: carena@vt.edu

INTRODUCTION

Irreversible electroporation (IRE) is a minimally invasive focal ablation technique capable of treating localized tumors in a non-thermal manner [1-3]. The procedure involves applying a series of unipolar electric pulses through electrodes inserted directly into the targeted tissue. IRE exhibits many advantages over thermal ablation techniques, including its ability to be performed safely on surgically inoperable tumors located in close proximity to major nerves and blood vessels [4, 5] and its ability to create predictable lesions with sub-millimeter resolution based on the electric field distribution in the tissue [6].

One challenge in clinical adaptation of IRE is the required administration of neuromuscular agents in order to mitigate intense muscle contractions associated with the delivery of unipolar electric pulses (amplitude ≈ 1000 V, duration ≈ 100 μ s) [7]. Aggressive use of muscle relaxants is undesirable for patients and expensive for hospitals, as it requires general anesthesia with continual monitoring of respiratory function. We have previously shown that by alternating pulse polarity and reducing pulse duration by two-orders of magnitude, it is possible to achieve results that are characteristic of IRE without causing muscle contractions [8]. This technology, termed high-frequency irreversible electroporation (H-FIRE), has the potential to be performed outside the operating room. Here, this is evaluated by performing H-FIRE on an equine patient maintained under standing sedation in restraint stocks.

METHODOLOGY

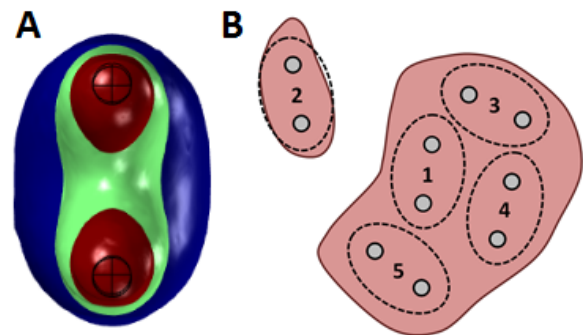


Figure 1: (A) Predicted electric field distribution for the selected pulse protocol (1000 V/cm – blue, 1500 V/cm – green, and 2000 V/cm – red). (B) Overlay of the estimated lethal threshold (1000 V/cm – dotted lines) on a schematic diagram of the targeted tumor.

The equine patient was a 12 year old American Saddlebred mare that presented with a squamous cell carcinoma. Prior to arrival, the tumor had recurred following multiple courses of cisplatin implant therapy. The H-FIRE treatment was performed with a linear array of two electrodes (NanoKnife Single Electrode, AngioDynamics, Queensbury, NY) spaced at 5 mm center-to-center and inserted to a depth of 1 cm from the surface of the skin. A custom pulse generator (Applied Energetics, Tucson, AZ) was used to deliver a 1000 V bipolar burst once per second for 2 minutes in synchrony with the heartbeat. Each burst consisted of 2 μ s pulses of alternating polarity totaling 100 μ s of energized time.

The number of H-FIRE applications and their location were determined by solving the electric field distribution around the needle electrodes according to the Laplace

equation ($\nabla^2\phi = 0$) using a finite element software (Comsol Multiphysics 4.2a, Stockholm, Sweden). It was conservatively estimated that the lethal electric field was 1000 V/cm for bursts comprised of 2 μ s pulses based on *in vitro* results (data not shown). This field contour was superimposed on an illustration of the visible tumor mass to ensure sufficient coverage (Figure 1). In total, H-FIRE was performed five times in a single round of treatment. It is important to note that the patient was given two rounds of treatment separated by a three week interval.

RESULTS AND DISCUSSION

The entire procedure, including sedation, H-FIRE treatment, and recovery lasted under 1 hour, at which point the patient returned under their own power to the clients trailer. Despite ECG synchronization, heart rate increased significantly during treatment by an average of 32 bpm. This change was immediately reversible following pulse delivery and likely due to intrinsic stimulation of the sympathetic nervous system. In the first two days following treatment, there was evidence of edema and scab formation. Within two weeks of treatment, the edema had subsided and the scab was replaced with healthy skin. Additionally, there was a marked reduction in the size and extent of the mass, which resolved to a small focus of granulating skin. All images shown in Figure 2 are taken following the second round of H-FIRE.

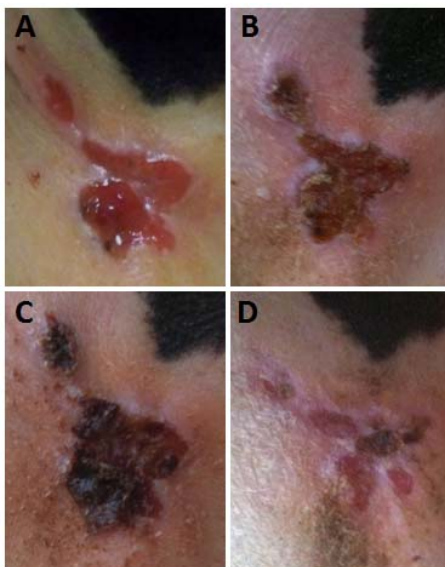


Figure 2: Images of tumor progression (A) prior to treatment, (B) 1 day post-treatment, (C) 2 days post-treatment, and (D) 14 days post-treatment.

CONCLUSIONS

H-FIRE was performed safely and effectively on a chemoresistant squamous cell carcinoma. The treatment was conducted outside the operating room without the use of a neuromuscular blockade or general anesthesia. This greatly reduced the risks and costs associated with the procedure without compromising the outcome. A full clinical trial is now being prepared to build off this positive result.

ACKNOWLEDGMENTS

We thank Lisa McKenzie for allowing us to treat “Fergie,” and Eduardo Latouche and Jo Restaino for documenting the procedure.

REFERENCES

1. Davalos RV, Mir LM, Rubinsky B (2005) Tissue Ablation with Irreversible Electroporation. *Ann Biomed Eng* 33: 223-31.
2. Garcia PA, Pancotto T, Rossmeisl JH, Henao-Guerrero N, Gustafson NR, et al. (2011) Non-Thermal Irreversible Electroporation (N-TIRE) and Adjuvant Fractionated Radiotherapeutic Multimodal Therapy for Intracranial Malignant Glioma in a Canine Patient. *Technol Cancer Res Treat* 10: 73-83.
3. Neal RE, 2nd, Rossmeisl JH, Jr., Garcia PA, Lanz OI, Henao-Guerrero N, et al. (2011) Successful Treatment of a Large Soft Tissue Sarcoma With Irreversible Electroporation. *J Clin Oncol*.
4. Li W, Fan QY, Ji ZW, Qiu XC, Li Z (2011) The Effects of Irreversible Electroporation (IRE) on Nerves. *Plos One* 6: e18831.
5. Maor E, Ivorra A, Leor J, Rubinsky B (2007) The effect of irreversible electroporation on blood vessels. *Technol Cancer Res Treat* 6: 307-12.
6. Edd JF, Horowitz L, Davalos RV, Mir LM, Rubinsky B (2006) In vivo results of a new focal tissue ablation technique: irreversible electroporation. *IEEE Trans Biomed Eng* 53: 1409-15.
7. Arena CB, Davalos RV (2012) Advances in Therapeutic Electroporation to Mitigate Muscle Contractions. *J Membra Sci Technol* 2: 1000e102.
8. Arena CB, Sano MB, Rossmeisl JH, Jr., Caldwell JL, Garcia PA, et al. (2011) High-Frequency Irreversible Electroporation (H-FIRE) for Non-thermal Ablation without Muscle Contraction. *Biomed Eng Online* 10.

CHEMOTACTIC LIVE AUTONOMOUS DRUG DELIVERY AGENTS WITH DIFFERENT BODY SHAPES

Ali Sahari¹, Mahama A. Traore², and Bahareh Behkam^{1,2}

1. Virginia Tech, School of Biomedical Engineering and Sciences

2. Virginia Tech, Mechanical Engineering Department

Corresponding Author: Bahareh Behkam, Email: Behkam@vt.edu

INTRODUCTION

Bacteria-based drug delivery carriers are envisioned to significantly improve the targeted delivery of drug molecules and imaging agents to the regions of interest. These autonomous drug carriers if directed by chemical cues can offer novel solutions for targeted drug delivery. DrugBots, the potential drug carriers developed by the authors, are constructed by interfacing various shapes micro/nano-particles with an ensemble of live engineered bacteria with the purpose of using the bacteria for actuation, sensing, communication and control. Non-spherical particles are also recognized to have advantages over their spherical counterparts such as higher margination and adhesion as well as prolonged circulation which make them attractive for drug delivery purposes. Gradients of chemical attractants can be utilized to control the motion of the bacteria (and hence DrugBots with spherical and non-spherical body shapes) towards higher concentrations of chemo-effectors. Semi-solid agar plates, plug-in-pond assays and capillary assays are the mostly used conventional techniques for testing bacterial chemotaxis towards chemo-attractants. However, in order to quantitatively investigate migration of bacteria, and hence the DrugBots, in response to stable and well-controlled concentration gradients of chemo-attractants, only microfluidic technology, and especially flow-free hydrogel-based microfluidic devices, can offer the desired microenvironments. This study focuses on investigating the role of body shape and chemotaxis in the motile behavior of DrugBots. We established a linear gradient of a chemoattractant for bacteria in a hydrogel-based microfluidic device in order to characterize the DrugBot transport for two different morphologies of the DrugBot, sphere and elliptical disks. Disks are fabricated here using a stretching technique [1] and this shape of particles has exhibited longer half-life circulation and higher targeting specificity in mouse models [2] which makes them a good

candidate, along with their spherical counterparts, for chemotaxis experiments.

MATERIALS AND METHODS

PEG-DA hydrogel based Microfluidic device fabrication: A diffusion-based microfluidic device using 700 Da polyethylene glycol diacrylate (PEG-DA) hydrogel was fabricated through a one-step UV polymerization process. Briefly, a PEG-DA solution in PBS (10% w/v) plus a photoinitiator solution, Irgacure 2959 in 70% ethanol (10% w/v), was prepared and they were mixed at a 20:1 ratio. The hydrogel solution was then photopolymerized using UV light. The hydrogel device was assembled before use. The three parallel channels separated by the two hydrogel walls enabled us to establish concentration gradients of chemo-effectors for bacteria (and hence the DrugBots) (See Fig. 1 (a)).

DrugBot Construction: Spherical 6 μm polystyrene (PS) particles were used in the experiments after three washing steps with 30% isopropyl alcohol (IPA). Elliptical disk (ED) shaped PS particles were fabricated using a high throughput particle stretching technique. First, spherical 6 μm particles, from the same stock as above, were embedded in a poly vinyl alcohol (PVA) film and then the film was mounted on a 2D mechanical stretcher, stretched in air and soaked in toluene for 3 hours. The toluene-treated film was allowed to dry overnight at room temperature. The film was cut off the stretcher and dissolved in 30% IPA overnight. The particles were recovered after 5 times of washing with the same IPA solution. Motile sub-populations of *Escherichia coli* (*E. coli*) MG1655 transformed with pHC60 (GFP-expressing plasmid) were grown in Tryptone Broth (supplemented with 10 $\mu\text{g ml}^{-1}$ tetracycline) to $\text{OD}_{600}=0.5$ at 32 °C and incubated with goat polyclonal anti-lipid A LPS antibody labeled with biotin (10 $\mu\text{g/ml}$). The two collections of 6

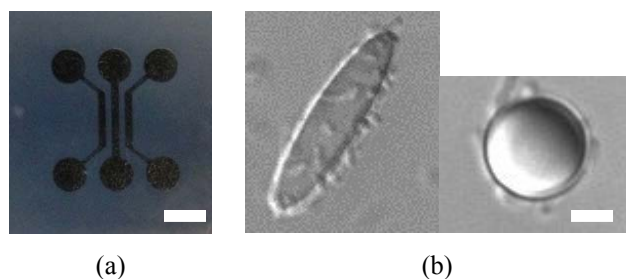


Figure 1: (a) Top view of the PEG-DA hydrogel device before assembly. Scale bar is 3 mm, (b) Representative DrugBots with different body shapes. Scale bar is 2 μm .

μm microparticles (spheres and EDs) were coated with Cy3-streptavidin and were added to the antibody-coated bacteria which produced the DrugBots (See Fig. 1 (b)) utilizing the high affinity between biotin and streptavidin. L-Aspartic acid, a known chemoattractant for *E. coli* bacteria, was selected to control the movement of the DrugBots in the device. Spherical and ED-shaped DrugBots were injected into the chemotaxis observation channel after a concentration gradient of the chemo-effector (0.1 mM/mm) was established. Motile DrugBots were observed using a Zeiss AxioObserver D1 inverted microscope equipped with an AxioCam HS camera plus a 20 \times objective and the captured videos were analyzed using the ImageJ software (NIH, Bethesda, MD). The width of the observation channel was divided into 3 partitions (each partition was $\sim 166 \mu\text{m}$ wide) and the spatial distribution of motile DrugBots was monitored across the width of the channels in order to quantify the migration profiles of the DrugBots.

RESULTS AND DISCUSSION

Quantitative investigation of DrugBot chemotaxis in response to concentration gradients of L-Aspartic acid as well as screening the effect of particle geometry on this chemotactic response is the main purpose of this study. The fabricated PEG-DA microfluidic device generates a well-controlled chemical gradient across the chemotaxis observation channel and allows us to measure the chemotactic response quantitatively. The chemo-attractant gradient reached a steady state after around 60 min and it was replenished by introducing a slow flow through the channels. The fabricated spherical and ED-shaped DrugBots were then introduced into the center channel and every 5 min, 5 second videos were recorded at 20 frames/sec frame rate 1,000 μm down the channel output. In order to quantify the migration profile of the DrugBots, the spatial distribution of the DrugBots in the three partitions across the chemotaxis chamber was calculated using ImageJ software. The number of spherical and ED-shaped DrugBots was counted in the defined partitions along 6 successive sections in the center channel. The results showed that the number of the DrugBots at the

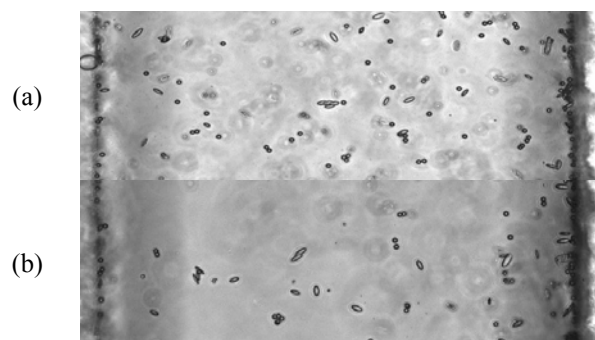


Figure 2: (a) Representative DrugBots in the center channel at $t=0$ min, (b) the DrugBots at $t=10$ min.

chemo-attractant side increases after 10 min implying that there was a distinct bias towards the high concentration of L-aspartic acid for the both types of DrugBots (See Fig. 2). Further data analysis required for comprehensively exploring the chemotactic response of the DrugBots remains to be performed to provide the answer to this critical question: Which one reaches there faster? Spheres or EDs? To ensure that the DrugBot movement is because of the chemo-attractant, a control experiment was conducted with no chemo-attractant and as expected, the distribution of the DrugBots remained unchanged (data not shown). The gradient steepness can also influence the migration of the DrugBots. A steeper gradient is expected to generally yield a stronger chemotaxis response. However, an inhibitory effect might be observed if the high chemo-attractant concentration saturates the bacterial chemotaxis receptors. A thorough study of the effect of a varying gradient steepness on the chemotactic response of the DrugBots remains to be conducted as well.

CONCLUSIONS

Bacteria-based cargo carriers with spherical and ED shapes along with *E. coli* strain MG1655 were constructed here. Chemotaxis was exploited to control the movement of these autonomous drug delivery vehicles introduced into a PEG-DA hydrogel based microfluidic device. Both types of these carriers, called DrugBots, have shown a biased movement towards higher concentrations of L-Aspartic acid. These controllable DrugBots have a great potential to autonomously navigate and carries/deploy a wide variety of cargos such as therapeutics and contrast agents to hard-to-reach diseased areas.

REFERENCES

- [1] Champion, J.A. et al., Making polymeric micro- and nanoparticles of complex shapes, *Proceedings of the National Academy of Sciences*, 104:11901 (2007).
- [2] Muro, S. et al. Control of endothelial targeting and intracellular delivery of therapeutic enzymes by modulating the size and shape of ICAM-1-targeted carriers. *Molecular Therapy*, 16:1450–1458 (2008).

MYO-INOSITOL AS A BIOMARKER IN THE RATS EXPOSED TO BLAST OVERPRESSURE WITH OBSERVED IMPAIRED WORKING MEMORY AND ELEVATED ANXIETY

Sujith Sajja¹, Shane A. Perrine², Farhad Ghoddoussi^{2,3}, Matthew P. Galloway^{2,3}, Pamela J. VandeVord^{1,4}

¹Department of Biomedical Engineering and Sciences, Virginia Polytechnic and State University

²Psychiatry and Behavioral Neurosciences, and ³Anesthesiology, Wayne State University, and

⁴John D. Dingell Veteran's Administration Medical Center, Detroit, MI USA

Corresponding Author: Sujith Sajja, Email:sujits@vt.edu

INTRODUCTION

Impaired working memory (dependent on an intact prefrontal cortex) and anxiety are major clinical symptoms commonly associated with blast overpressure [1-4]. There is a vital need for blast exposure biomarkers to help effectively diagnosis blast-induced neurotrauma (BINT). In this study, we evaluated working memory impairment associated with blast overpressure along with neurochemical assessment in a rat model of blast. We have studied the behavioral changes in animals especially novel object recognition (working memory paradigm) and light and dark (anxiety test) study along with neurochemical changes within the prefrontal cortex and amygdala of blast-exposed animals which are the cognitive centers associated with working memory and anxiety respectively. Temporal evaluation of neurochemical changes was done using ¹H- Magnetic Resonance Spectroscopy (1HMRS). Results suggest that exposure to blast waves has a significant effect on the neurochemical changes eventually leading to elevated anxiety and impaired working memory.

METHODOLOGY

Blast: Male Sprague Dawley rats (~250g) were briefly anesthetized with 3% isoflurane. The animals were positioned so that the rat's head was at 44 inches from the open end of the tube, facing the shock wave frontally. During blast exposure, the pressure-time profile is measured using a piezoelectric sensor (PCB Piezotronics) placed perpendicular to the air flow, Animals were exposed to a 119 kPa (17psi) overpressure for a 7 msec duration; control animals did not experience the overpressure. 3, 24, 48, 72 and 168 hours post blast, animals were sacrificed.

Novel Object Recognition Test: The animals subjected to the testing (72 hours post blast) underwent two tasks with a delay of 20 minutes between each trail for short term memory evaluation. The first task (T1) involves the exposure of animal to identical "familiar" objects for 5 minutes. In the second the task (T2), animals were exposed to a "familiar" object (same object used in the first task) and a novel object with which the animal was never exposed. To eliminate the bias towards the objects, orientation of the animal when placed into the chamber was done such that animals does not get a first look on any of the objects as shown in the figure 1. The tracking of the tasks were done by EthoVision™ tracking software.

The data is collected when the animal "noise point" is facing towards the object with in 1.5x radius of object from the measured from center of the object (arena settings were done EthoVision™ tracking software). The animal that spends more than 75% of its time in T1 at one object was excluded in the study in order to avoid the animal preferences in the one particular location in the experimental chamber

¹H-Magnetic Resonance Spectroscopy (1H-MRS)

Analysis: Anatomically specific hippocampal punches were obtained from 2 mm coronal slices. Intact tissue samples (maintained at 4°C) were analyzed with magic angle spinning 1H-MRS at 11.7 Tesla. Concentrations (nmol/mg tissue) of individual neurochemicals were determined with the LCModel using 27 compounds in the basis set; neurochemical/creatine ratios were also analyzed.

Light and dark box: The apparatus consisted of two equal acrylic compartments, one dark side closed with a lid and one light side. Each rat was tested by placing it in the light area, facing away from the dark one, and was

allowed to explore the novel environment for 5 min. The number of transfers from one compartment to the other along with the time spent in the light and dark side was measured. This test exploited the conflict between the animal's tendency to explore an open environment (non-anxiety like effect) and to stay in a defensive mode (anxiety like effect).

RESULTS

¹H-MRS:

Prefrontal cortex: We observed a significant decrease in glutathione (GSH-15%) and myo-inositol (13%) at 3 hours; decrease in betaine (BET – 20%) and increase in γ - amino butyric acid (GABA – 13%) at 24 hours post; increase in glycerophosphocholine (GPC – 15%), phosphorylethanolamine (PEA – 11%), Glutamate/creatine ratio (Glu/Cre – 5%), Lactate/creatine (Lac/Cre – 7%) ratio at 22 hours post blast; increase in myo-inositol (15%) at 168 hours post blast compared to their respective

Amygdala: We observed a significant decrease in N-acetyl aspartate (NAA -10%) and PEA/Cre ratio (28%), and increase in N-acetyl aspartate glutamate (NAAG – 34%), phospho-choline (Pch – 39%) and BET (37%) at 24 hours post blast exposure; decrease in Glu/Cre (6%) and NAA/cre (9%) at 48 hours post blast exposure.

Behavioral tests: NOR revealed significantly impaired working memory (23%) in blast group compared to shams. Interestingly, working memory in control animals was negatively correlated with myo-inositol levels ($r = -.759$, $p < 0.05$), an association that was absent in blast exposed animals. Light and dark test revealed increased anxiety in blast group compared to their respective shams (latency change – 44%)

Discussion: Our results suggest the hippocampus of rats exposed to blast wave (119KPa) was significantly altered. We found several changes within the neurochemical profile in both prefrontal cortex and amygdala. Behavioral deficit in working memory and elevated anxiety is consistent with clinical symptoms associated with BINT. Although the relationship between early neurochemical changes [viz. in GABA, membrane turnover, glutamate, and lactate] and behavioral deficits at remains to be determined, the observations are consistent with glutamate dysregulation, increased inflammation, and disrupted equipose of energy status.

The major finding of our report is that 7 days after a single exposure to blast overpressure, rats have a deficit in novel object recognition (working memory) and an increase in prefrontal cortex levels of myo-inositol.

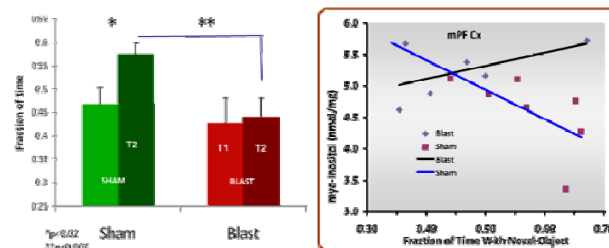


Figure 1: At 7 days in NOR test, blast exposed animals exhibited impaired working memory when compared to sham animals (on left). Correlation of myo-inositol with working memory in animals (on right)

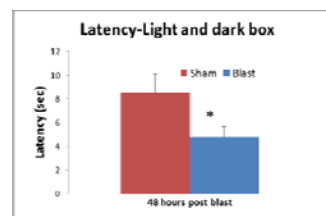


Figure 2: Decreased latency of light and dark box test in blast group compared to sham group indicates elevated anxiety in blast animals

CONCLUSIONS

Although higher-order cognitive aspects of working memory are dependent on recruitment of the prefrontal cortex, a blast-induced damage to loss of the hippocampus integrity may also contribute to the memory deficit. Performance in the NOR paradigm is negatively correlated with prefrontal myo-inositol and this correlation was lost in the animals exposed to blast. Increased myo-inositol may represent tardive glial scarring and contribute to the impaired working memory. Thus myo-inositol could be a potential biomarker for diagnosis of BINT.

REFERENCES

1. Warden DL, French LM, Shupenko L, Fargus J, Riedy G, Erickson ME, et al. Case report of a soldier with primary blast brain injury. *NeuroImage*. 2009;47, Supplement 2:T152-T3.
2. McAllister TW, Stein MB. Effects of psychological and biomechanical trauma on brain and behavior. *Annals of the New York Academy of Sciences*. 2010;1208:46-57.
3. Hicks RR, Fertig SJ, Desrocher RE, Koroshetz WJ, Pancrazio JJ. Neurological Effects of Blast Injury. *The Journal of Trauma*. 2010;68:1257-63
4. Bhattacharjee Y. Shell Shock Revisited: Solving the Puzzle of Blast Trauma. *Science*. 2008;319:406-8.

SKELETAL MUSCLE CONTRACTION AND SYSTEM TRACKING IN FEEDBACK CONTROL

Paola Jaramillo¹, Adam Shoemaker¹, and Alexander Leonessa¹

1. Department of Mechanical Engineering, Virginia Tech

Corresponding Author: Paola Jaramillo, Email: paolajc@vt.edu

INTRODUCTION

Trauma attributed to spinal cord injury (SCI) triggers a cascading effect due to the sudden disruption of axons and damaged blood vessels. Hence, the transmission lines to and from the nervous system cease, which results in the swelling of the spine and lack of blood flow regulation. Secondary outcomes from these responses result in ischaemia and the release of toxic chemicals that harm nearby cells and cause apoptosis. So far, there are approximately 265,000 people living with SCI in the United States at an average cost of treatment between U\$500,000 to 2,000,000 per patient [1,2]. Functional Electrical Stimulation (FES) is a promising approach since it can directly stimulate through electrical current the peripheral nerves and their corresponding motoneurons in order to maintain muscle mass and promote blood flow [3]. A major drawback when applying FES in clinical settings is that most systems employ an open-loop approach. Closed-loop systems, conversely, enable repeatability due to the relationship established through feedback by the input and output of the system. Through this study, two closed-loop FES systems, a Proportional-Integral (PI) controller and a Model Reference Adaptive Control (MRAC) are applied to skeletal muscle *in vitro*. The experiments are position-controlled through predetermined functions such as step and sine trajectories. The controllers are experimentally tested on a muscle-mass-spring setup to capture the dynamics of muscle contraction.

METHODOLOGY

When a muscle is stimulated by an action potential, a twitch is generated as shown in Figure 1. In these experiments, a set frequency at 100 Hz is implemented, which generates a series of twitches. The time to relax between each activation pulse is so short that the twitch

forces summate to yield a tetanic response. For this study, a mouse muscle used is the extensor digitorum longus (EDL), a penniform muscle composed of mainly type II fibers. Relevant characteristics of type II muscle fibers include medium to high peak forces and short rise times.

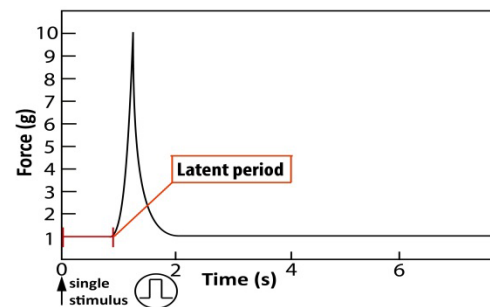


Figure 1: Mechanical muscle response due to a single stimulus causing contraction.

An *in vitro* study using 16 mice (N=8 for each controller) was approved by the Institutional Animal Care and Use Committee (IACUC). The right and left EDL muscles were surgically removed from C57BL6 male mice postmortem. Once removed, the muscle was suspended in a 95%O₂-5%CO₂ physiologic saline solution to maintain a pH of 7.4 under fixed boundary conditions. The EDL muscle was then pre-tensioned to 1g of force that provided optimum length (L_0), prior to initial stimulation. Each EDL muscle extracted was then stimulated using either the PI or MRAC controller.

PI Controller. A PI controller was described by Ogata in [4]. In this model, the user specifies the desired trajectory, $x_d(t)$, as the system input, which is then compared to the current measured state, $x(t)$. This is known as the system error, $e_{PI}(t)$, defined as,

$$e_{PI}(t) \triangleq x(t) - x_d(t). \quad (1)$$

Based on this definition of error, the PI controller then determines the control input, $u_{PI}(t)$, with the control law,

$$u_{PI}(t) = K_P \left(e_{PI}(t) + \frac{1}{T_i} \int_0^t e_{PI}(t) dt \right), \quad (2)$$

where K_P is the proportional gain and T_i , the integral time.

MRAC Controller. A first-order MRAC algorithm based on [7] was used. The control effort is a function of the adaptive gains, reference input and current state. This method assumes the linear structure,

$$\dot{x}(t) = ax(t) - bu_{adp}(t), \quad (3)$$

where $x(t)$ is the system state, a is the unknown system state constant, b is the system input constant with known sign and unknown magnitude, and $u_{adp}(t)$ is the control effort. The MRAC controller forces the system in (3) to converge to the reference model,

$$\dot{x}_r(t) = a_r x_r(t) - b_r r(t), \quad (4)$$

where $x_r(t)$ is the reference model state, a_r is a negative (stable) system constant, b_r is a known input constant, and $r(t)$ is the reference input. Moreover, there are ideal gains driving the system to the reference model,

$$u_{ideal}(t) = \theta_x^* x(t) + \theta_r^* r(t), \quad (5)$$

where $\theta_x^* = \frac{a_r - a}{b}$ and $\theta_r^* = \frac{b_r}{b}$ allows the system to converge to the reference model.

RESULTS

PI Controller Results. The results obtained from the PI controller are displayed in Figures 2 and 3. Tuning was dependent on each muscle. Still, PI controller's tracking enabled the control of the muscles' trajectory.

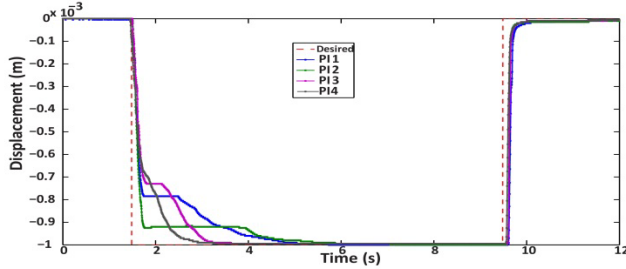


Figure 2: Trajectories from the PI muscle step response.

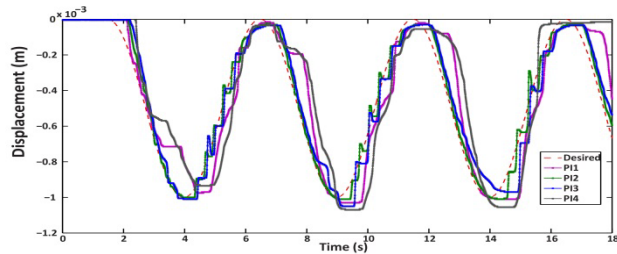


Figure 3: Trajectories from the PI muscle sine response.

MRAC Controller. The challenge to implement this controller relied on specifying the initial six parameters of the system. Nevertheless, stability of the simplified system was observed in Figures 4 and 5.

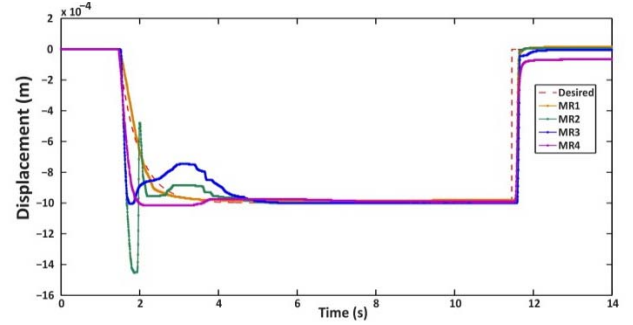


Figure 4: Trajectories of the MRAC muscle step response.

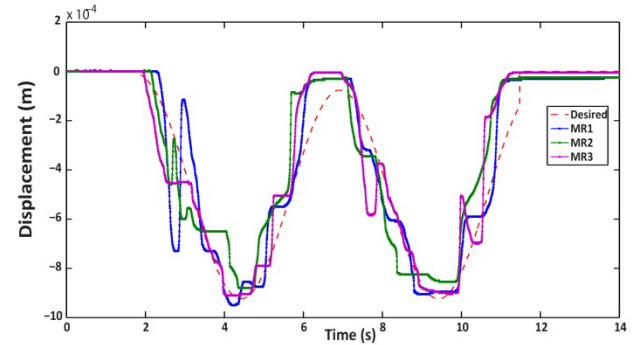


Figure 5: Trajectories of the MRAC muscle sine response.

CONCLUSIONS

The study effectively carried out a simplified setup to implement closed-loop control systems (PI and MRAC), which can experimentally stimulate the EDL muscles. The controllers were able to control the stimulation trajectories set for all the EDL muscles effectively. A major challenge is the time constraint observed when performing a study *in vitro*. Once isolated and extracted, there was muscle decay present which needed to be compensated with the controllers. Nevertheless, a coupling PI-MRAC controller has also been developed so as to improve the system's tracking and minimize instabilities that hinder the muscles' controlled trajectories.

REFERENCES

- [1] J.W. McDonald, C. Sadowsky, "Spinal-cord injury," *Lancet*, vol. 359, Feb 2002, pp. 394-396.
- [2] National Spinal Cord Injury Statistical Center, "Spinal cord facts and figures at a glance," 2011.
- [3] A. Kralj, T. Bajd, "Functional Electrical Stimulation: standing and walking after spinal cord injury," CRC Press, 1989.
- [4] Ogata, K., 2009. *Modern Control Engineering*, 5 ed. Prentice-Hall, Upper Saddle River, NJ.
- [5] Ioannou, P. A., and Sun, J., 1996. *Robust Adaptive Control*. Prentice-Hall, Upper Saddle River, NJ.

ABDOMINAL INJURY BIOMECHANICS

Meghan K. Howes¹ and Warren N. Hardy¹

1. Virginia Tech-Wake Forest University, Center for Injury Biomechanics
Corresponding Author: Meghan K. Howes, Email: mkhowes@vt.edu

INTRODUCTION

Motor vehicle collisions (MVCs) are the leading cause of injury-related deaths in the United States, resulting in approximately 45,000 deaths and 357,000 hospitalizations annually [1]. MVCs are a common cause of blunt abdominal injuries. An estimated 9000 front seat occupants sustain moderate to severe abdominal injuries in frontal MVCs in the United States each year [2]. Injury mitigation for the abdominal organs has become increasingly important in recent years as the overall injury incidence to the other body regions has been reduced with improved occupant restraint systems. This study was conducted to characterize abdominal injuries with the purpose of establishing crash-induced injury mechanisms and thresholds which can be applied to assess and improve occupant protection systems in automobiles.

METHODOLOGY

This study has three primary components that are described herein: in-depth examination of field accident data to investigate the mechanisms of hollow abdominal organ (e.g. intestinal) injury in MVCs, high-rate tissue testing to quantify the material properties and failure thresholds of the abdominal tissues, and impact testing using whole post-mortem human surrogates (PMHS) and high-speed biplane x-ray to quantify the relative kinematics of internal organs in response to blunt loading.

Field Data Analysis. Information regarding the occupant and crash characteristics associated with injury in MVCs is crucial to the development of improved safety systems. To determine these characteristics, an etiological study was conducted using field accident data from the Crash Injury Research and Engineering Network (CIREN). The CIREN database combines field accident data from detailed crash investigations with occupant information from medical examinations and imaging, which allows for

a multidisciplinary analysis of real-world crashes. Cases of hollow abdominal organ injury in the CIREN database were categorized by occupant characteristics, crash characteristics, injury severity, and injury source. Case analysis was used to identify characteristics predisposing occupants to moderate and serious abdominal injuries.

Material Testing. The proper use of seatbelts reduces the risk of serious abdominal injury in MVCs [2]. However, a significant increase in the occurrence of digestive tract injuries exists with seatbelt loading [3]. Limited material property data are available in the literature for the complex anatomical structures of the digestive system. These data were obtained at quasi-static rates not representative of the dynamic loading rates in MVCs. To characterize the biomechanical response of the hollow abdominal organs, stress and strain data were obtained from high-rate, equibiaxial testing to failure.

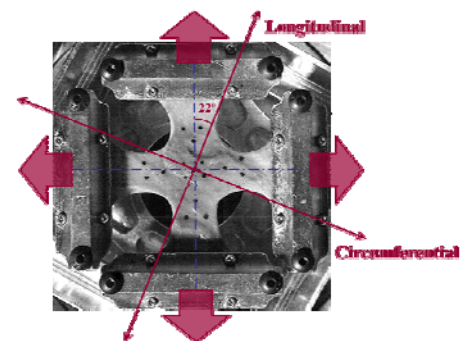


Figure 1: Equibiaxial Tissue Test Setup.

Testing was conducted using a custom dynamic device designed to apply simultaneous equal stretch to a tissue sample in four directions. Stomach, small intestine, and colon samples harvested from four fresh, never-frozen PMHS were tested. A custom stamp was used to cut the tissues into cruciate-shaped samples with four arm

branches converging to form a central region of interest (ROI). The stamp was aligned such that two co-linear arms were oriented with the visible longitudinal fiber direction of the tissue, or offset from the long axis by 22° to ensure failure through the ROI (Figure 1). Each sample was tested to failure at a rate of 100s^{-1} . Load, acceleration, displacement, and sample thickness were obtained to facilitate calculations of stress and strain for each test.

Regional Impact Testing. Full-body finite element models are becoming increasingly more prevalent for the evaluation of occupant protection in MVCs. Internal organ motion and interaction are hypothesized in the process of model development; yet, organ kinematics in response to high-rate loading have not been quantified. In this study, the relative kinematics of the thoracic and abdominal organs were quantified in response to blunt loading using four whole PMHS and impacts simulating the loading expected in MVCs [4]. The PMHS were tested inverted, perfused, and ventilated to simulate physiologic conditions. The position and displacement of radiopaque markers implanted in the thoracic and abdominal organs of each PMHS were recorded for the duration of the impacts using high-speed biplane x-ray (1000fps). Marker displacement was tracked using motion analysis software and projected into calibrated three-dimensional coordinates to obtain each marker trajectory.

RESULTS & DISCUSSION

Field Data Analysis. Results showed an association between hollow abdominal organ injury and seating position, increased interaction with the restraint system, and increased crash severity ($>50\text{kmph}$). Classification of the environment in which these injuries occur is being applied to design controlled experiments to investigate injury mechanisms and evaluate safety technologies.

Material Testing. Results of this study showed regional and directional differences in material response for the stomach, small intestine, and colon [5]. For the colon, the difference in stress and strain in each direction indicated increased stiffness in the axial direction and for all regions except the descending colon (Figure 2).

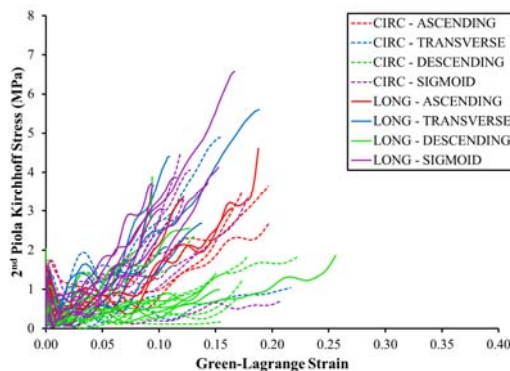


Figure 2: Stress-Strain Response for the Colon.

Material response and failure thresholds quantified in this study can be used to assess organ failure in finite element simulations designed to evaluate crash-induced injury.

Regional Impact Testing. The internal organ kinematics data quantified in this study compliment available regional response data and can be used to investigate injury with a better understanding of the interaction of anatomical structures that occurs during impact (Figure 3). These data can be applied to validate internal organ motion generated in human body finite element model simulations, which are used to assess occupant safety.

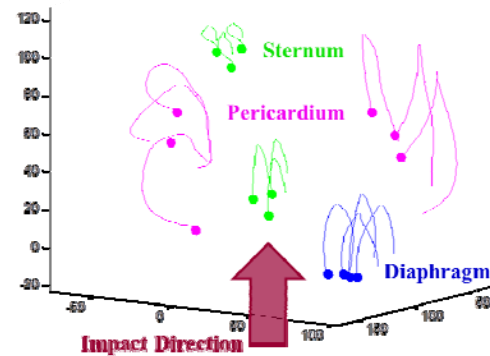


Figure 3: Example Kinematics Data [mm].

CONCLUSION

An etiological study was conducted to characterize hollow abdominal organ injury in MVCs, soft tissue testing was used to define the material properties of these tissues, and the motion and interaction of the abdominal organs in response to blunt impact was quantified. Each aspect of this research delivers novel injury biomechanics data for use in modeling applications, with the ultimate goal of abdominal organ injury mitigation in MVCs.

ACKNOWLEDGMENTS

This work was funded by the Global Human Body Models Consortium, LLC, the Toyota Motor Corporation, and the Toyota Collaborative Safety Research Center.

REFERENCES

- [1] MacKenzie, EJ, and Fowler, CJ. "Epidemiology," *Trauma, 6th Edition* (Feliciano, DV, Mattox, KL, and Moore, EE, ed.). New York: The McGraw-Hill Companies, Inc., 2008.
- [2] Klinich, KD et al., "Factors Associated with Abdominal Injury in Frontal, Farside, and Nearside Crashes," *Stapp Car Crash J*, 54, 73-91, 2010.
- [3] Rutledge, R et al., "The Spectrum of Abdominal Injuries Associated with the Use of Seat Belts," *J Trauma*, 31, 820-825, 1991.
- [4] Howes, MK et al., "Kinematics of the Thoracoabdominal Contents under Various Loading Scenarios," *Stapp Car Crash J*, 56, 1-48, 2012.
- [5] Howes, MK, and Hardy, WN. "Material Properties of the Post-Mortem Colon in High-Rate Equibiaxial Elongation," *Biomed Sci Instrum*, 48, 171-178, 2012.

KERATEINE BIOMATERIALS BRIDGE CRITICALLY-SIZED RAT MANDIBULAR DEFECTS WITH MINIMAL ECTOPIC BONE GROWTH THROUGH CONTROLLED RELEASE OF BONE MORPHOGENIC PROTEIN-2

Christine Kowalczewski^{1,2}; Seth Tombyln³; David Wasnick²; Mary Ellenburg³; Michael Callahan⁴; Thomas Smith⁴; Mark Van Dyke⁴; Luke Burnett³; Justin Saul²

1. Virginia Tech – Wake Forest University (School of Biomedical Engineering and Sciences, Tissue Engineering)
 2. Miami University (School of Engineering, Paper and Chemical Engineering)
 3. KeraNetics, LLC
 4. Wake Forest University School of Medicine (Orthopaedic Surgery)
- Corresponding Author: C. Kowalczewski, kowalcc@miamioh.edu

INTRODUCTION

Combination products of biomaterials and protein growth factors such as recombinant human bone morphogenetic protein 2 (rhBMP-2) are proving to be a successful clinical alternative to autografts in promoting bone regeneration. While collagen rhBMP-2 carriers (Medtronic's Infuse®) have shown robust regenerative capabilities, adverse side effects such as ectopic growth have limited their use to several specific conditions.¹ Kerateine biomaterial carriers for rhBMP-2 offer potential advantages compared to collagen including controlled rates of degradation *in vivo* (due to lack of keratin-degrading enzymes), flexible material properties, and tunable rates of delivery. In this work, we describe the application of kerateine carriers of rhBMP-2 including their application to a critically-sized rat mandibular defect.

METHODOLOGY

Kerateine, the reductive form of keratin, powder was reconstituted in water with or without 100µg/ml rhBMP-2 and was incubated overnight at 37°C to make homogenous gels. In some cases, kerateine scaffolds were formed by freeze drying the hydrogels. Material properties of kerateine gels were determined by parallel plate rheology. Quantification of kerateine material degradation and rhBMP-2 release was measured by DC protein assay and rhBMP-2 ELISA, respectively. A bilateral 5mm circular critically-sized mandibular defect model was generated under aseptic technique on anesthetized 350g male Sprague Dawley rats (n=5). Kerateine hydrogels or scaffolds containing a total of 5 µg of rhBMP-2 were used as treatments and were compared to no treatment and Infuse® controls. Infuse® was prepared using manufacturer's recommend methods with

the exception that the final dose was 5 µg total rhBMP-2 in the 5mm defect. *In vivo* bone regeneration was determined by µCT scans at 8 and 16-week time points post-surgery. At 16 weeks animals were humanely euthanized and mandibles were harvested. Defect volume and volume of ectopic bone growth were quantified from µ-CT scans by using Osirix 3D Imaging Software. Bone mineral density was determined in ImageJ by comparison to known standards. One-way ANOVA was used to determine statistical significance between experimental groups.

RESULTS

Material, degradation, and rhBMP-2 release properties were controlled by varying weight percent and alpha to gamma protein fraction of kerateine. *In vitro* release studies indicate that rhBMP-2 release correlates with kerateine degradation. Approximately 15% of rhBMP-2 was released over the course of 8 weeks. *In vivo*, 3D rendering of µ-CT images indicated that untreated rat mandibles as well as those treated with kerateine gels or scaffolds without rhBMP-2 did not spontaneously heal by 16 weeks, highlighting the critical-sized nature of the defect. In contrast, Infuse®, kerateine gels with rhBMP-2, and kerateine scaffolds with rhBMP-2 achieved complete closure of the mandibular defect by 8 weeks (Figure 1). At 8 and 16 weeks significantly increased levels of bone mineral density compared to carriers without rhBMP-2 was observed. At 8 weeks there was no significant difference between Infuse and rhBMP-2 loaded kerateine gels but by 16 weeks rhBMP-2 kerateine gels had significantly higher bone mineral density. Both Infuse and rhBMP-2 kerateine gels showed significantly less bone mineral density compared to rhBMP-2 loaded kerateine scaffolds and normal bone which were statistically comparable by 16 weeks. Ectopic growth

was observed in all rhBMP-2 treatment groups, but quantitative volume measurements found significantly reduced levels of ectopic growth in kerateine gels and scaffolds loaded with rhBMP-2 than from Infuse® with the same dosage of rhBMP-2.

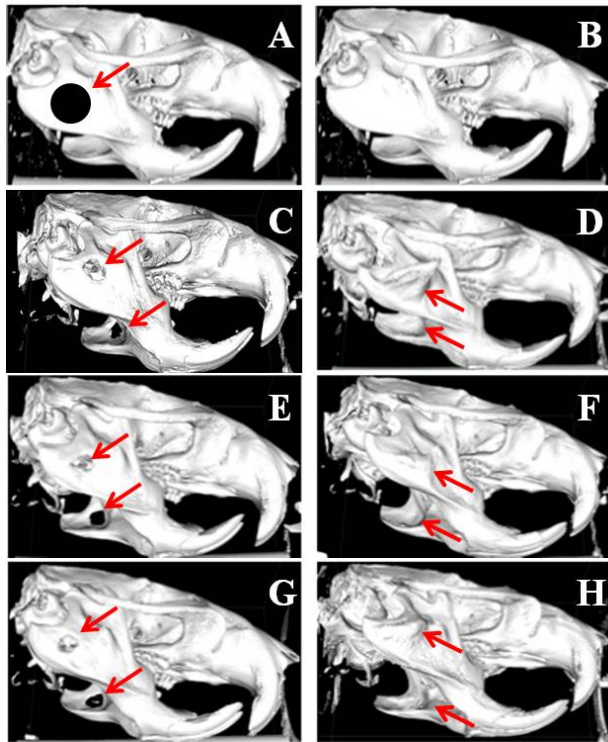


Figure 1: Representative uCT images of bone regeneration sixteen weeks after surgical creation of bilateral 5mm critically-sized circular mandibular defect. Illustration of initial 5mm defect size and location (A) imposed on a normal rat mandible (B). Animals which recieved no treatment (C), kerateine gel (E), or kerateine scaffold (G) without rhBMP-2 were unable to bridge the defect (arrow). Administrations of Infuse (D), kerateine gel (F), or kerateine scaffold (H) loaded with 5ug rhBMP-2 were able to close the defect with varying degrees of adverse ectopic bone growth (arrows).

DISCUSSION

Kerateine biomaterials are an interesting alternative to collagen-based carriers for several reasons. The fact that there are no keratin enzymes found in the human body allows kerateine to remain stable *in vivo* to serve as a matrix for cell infiltration in the regenerative microenvironment. The strong correlation between kerateine degradation and rhBMP-2 release profiles suggests that rhBMP-2 delivery can be controlled by modulating the rate of kerateine degradation. Kerateine-based carrier hydrogels of rhBMP-2 achieved the same levels of bone regeneration as Infuse® while kerateine

rhBMP-2 loaded scaffolds at the same dosage achieved statistical equivalence to normal bone, as quantified by several measures including healing volume and bone mineral density. Given the challenges related to ectopic bone formation observed with collagen-based scaffolds such as Infuse®, the analogous healing profiles and reduction in ectopic bone formation observed with kerateine-based carriers highlight the potential clinical utility of these materials in craniofacial bone regeneration.

CONCLUSIONS

Clinical collagen-based systems for delivery of rhBMP-2 such as Medtronic's Infuse® have been associated with adverse side effects such as ectopic bone growth. Kerateine biomaterials offer a naturally-based polymeric system that can provide tailored rhBMP-2 release profiles, significantly reduce ectopic bone growth, and achieve comparable (in the case of rhBMP-2 loaded kerateine gels) or physiologically relevant (in the case of rhBMP-2 kerateine scaffolds) levels of bone healing to existing collagen-based clinical alternatives for mandible injury.

ACKNOWLEDGMENTS

This work is supported by the US Army Medical Research and Materiel Command under Contract No.W81XWH-10-C-0165. In conducting research using animals, the investigator(s) adhered to the Animal Welfare Act Regulations and other Federal statutes relating to animals and experiments involving animals and the principles set forth in the current version of the Guide for Care and Use of Laboratory Animals, National Research Council. Thanks to Dr. Lindquist, Dr. Pratt, and John Pearce for their assistance with microCT scans (Cincinnati Children's Hospital). Thanks for technical support to Dr deGuzman (Virginia Tech), Cathy Mathis (Wake Forest Institute for Regenerative Medicine), Judy Bohnert (Miami Univeristy), and Linda Zehler (Miami University).

REFERENCES

1. Mckay, W. F., Peckham, S. M. & Badura, J. M. A comprehensive clinical review of recombinant human bone morphogenetic protein-2 (INFUSE ® Bone Graft). *International Orthopaedics* **2**, 729–734 (2007).

SMARTER CARS: INJURY AND FATALITY REDUCTIONS OF COLLISION AVOIDANCE TECHNOLOGIES

Kristofer D. Kusano¹ and Hampton C. Gabler²

1. Mechanical Engineering, Virginia Tech

2. School of Biomedical Engineering and Sciences, Virginia Tech

Corresponding Author: Kristofer D. Kusano, Email: kdkusano@vt.edu

INTRODUCTION

Societal costs from traffic crashes are a substantial burden to the world and U.S. economies. Worldwide there are an estimated 1.2 million road fatalities per year [1]. In the U.S. there were 33,808 fatalities and approximately 2,217,000 injuries in 2009 [2]. The monetary cost of crashes in the U.S. is estimated at upwards of \$500 billion per year [3]. Engineering innovations, such as seat belts and airbags, have led to the lowest number of fatal crashes since data was first collected in 1966. These and other vehicle design initiatives are known as passive safety systems because they mitigate consequences after a crash occurs.

Although passive safety has been very effective in reducing crash injuries, many researchers have recognized that in order to further reduce the societal costs of crashes, systems must be developed that prevent crashes from ever happening. Systems are being developed and introduced by automakers today that are known as active safety systems, which focus on crash prevention. An example of a system available on vehicles today is Forward Collision Avoidance Systems (FCAS), shown in Figure 1. Rear-end collisions, where one vehicle strikes another going in the

same direction, are the type of crash FCAS may be most effective in mitigating.

Adoption of active safety systems is in the early stages and as a result both policymakers and automakers are motivated to predict the societal benefits of proposed active safety systems. These systems are almost exclusively available on luxury vehicles and are not currently mandated on new vehicles like seat belts and airbags. Automakers need research to justify developing these expensive systems on non-luxury vehicles. Regulatory agencies, such as the U.S. Department of Transportation, need research to make a decision on which systems to require.

OBJECTIVE

The research question for this study is: If all vehicles were equipped with a proposed active safety system, how many crashes and injuries would be prevented each year?

Although the methodology developed in this research can be generally applied to different systems, we focused on FCAS as an example application.

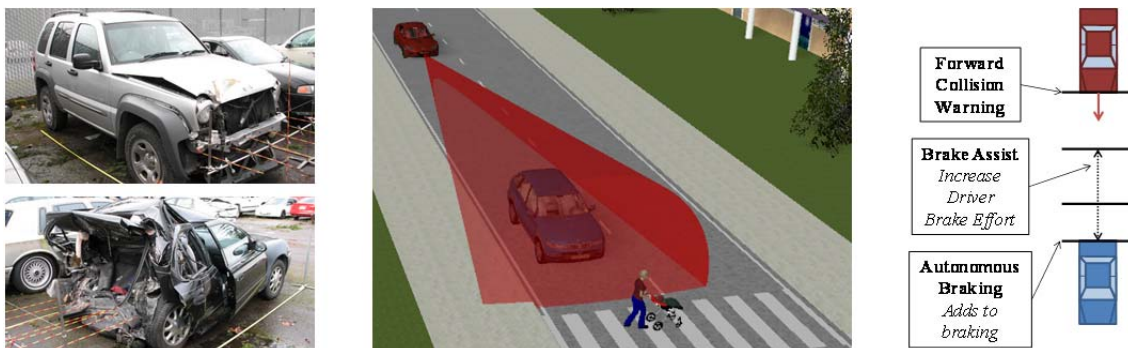


Figure 1. Active safety systems aim to prevent crashes, like the fatal rear-end shown to the left. FCAS use radar (middle) and have several components that assist the driver in avoiding frontal collisions (right).

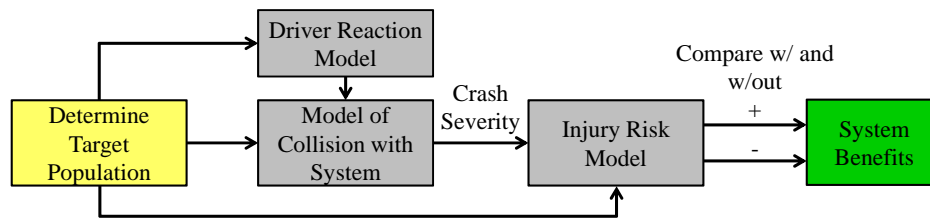


Figure 2. Method for Predicting Active Safety System Benefits using Real-world Data

METHODOLOGY

Figure 2 summarizes the overall approach for this research. First, the target population is the number of crashes that could be potentially mitigated by the proposed technology. Next, using this population, a model of the driver’s reaction to the system and of the collision with the proposed system active was developed. The result of these models is to predict the crash severity, i.e. change in velocity during the crash, given the proposed system is active. Next, the risk for injury in each simulated crash was estimated using statistical injury risk models. The crash database used for this study was a U.S. government sponsored database and an industry-standard data source for safety information.

The main challenge of using real-world crash databases is that every driver is different. The crash databases do not give information on reaction times or brake forces a driver would apply with a FCAS. The total number of injuries simulated with the system is

$$\# \text{ Injuries with system} = \sum_{i=1}^N \sum_{j=1}^M w_i w_j g(\theta_i, \gamma_j), \quad (1)$$

where N is the total number of crashes in the data and M is the total number of simulated drivers. For this study we simulated up to 12 different driver reactions to the system for each crash. Each driver modified the risk of injury, $g(\cdot)$, as a function of the crash parameters, θ_i , and crash severity for the simulated driver, γ_j . To make the sample representative, we used weights for the case, w_i , and driver, w_j , based on the likelihood of the event occurring in the crash population.

RESULTS

To derive the benefits for FCAS, we simulated 1,396 rear-end collisions as if it had an FCAS. We found that different combinations of FCAS components could reduce the number of moderately to fatally injured drivers of between 29% and 50% [4]. These injury reduction benefits for this system are comparable to those of wearing seat belts, known to be one of the most effective injury countermeasures [5].

CONCLUSIONS

Although the crash database used in this study is a ubiquitous source for research in the crash safety field, the methodology developed for this study was almost entirely novel. The methods fused multidisciplinary approaches, i.e. biomechanics, statistics, human factors, crash reconstruction, to answer the fundamental research question. The study is one of the most comprehensive investigations into FCAS benefits to date and is immediately applicable to policy-making and product development decisions.

ACKNOWLEDGMENTS

The authors would like to acknowledge Toyota Motor Corporation, Toyota Engineering & Manufacturing North America, Inc., and the Toyota Collaborative Safety Research Center for funding this study.

REFERENCES

1. “Global Status Report on Road Safety.” World Health Organization, Geneva, Switzerland, 2009.
2. “Traffic Safety Facts 2009.” National Highway Traffic Safety Administration, Washington, D.C., Report Number DOT HS 811 402, 2011.
3. Miller, T. R., Bhattacharya, S., Zaloshnja, E., Taylor, D., Bahar, G., Iuliana, D. “Costs of Crashes to Government, United States, 2008.” *Annals of the Advancement of Automotive Medicine*, Vol. 55, pp. 347-35, 2011.
4. Kusano, K. D., Gabler, H. C., “Safety Benefits for Vehicles Equipped with Forward Collision Warning, Brake Assist, and Autonomous Braking Systems in Rear-end Collisions,” *IEEE Transaction on Intelligent Transportation Systems*, Vol. 13, No. 4, 2012, pp. 1546-1555.
5. Cummings, P., Wells, J. D., Rivara, F. P., “Estimating Seat Belt Effectiveness using Matched-pair Cohort Methods,” *Accident Analysis and Prevention*, Vol. 35, 2003, pp. 143-149.

DEVELOPMENT OF MECHANICAL OPTICAL CLEARING DEVICES FOR IMPROVED LIGHT DELIVERY IN OPTICAL DIAGNOSTICS

William C. Vogt¹, Christopher G. Rylander^{1,2}

1. School of Biomedical Engineering and Sciences, Virginia Tech, Blacksburg, VA 24061
 2. Department of Mechanical Engineering, Virginia Tech Blacksburg, VA 24061
- Corresponding Author: Christopher G. Rylander, Email: cgr@vt.edu

INTRODUCTION

Light delivery for detecting and treating disease has become a major paradigm of medical research since the development of the first laser. However, the efficacy of light-based diagnostic and therapeutic procedures is severely limited by low optical penetration depth in tissue due to attenuation by absorption and scattering, caused primarily by water and blood [1]. Mechanical optical clearing (MOC) is a novel technique that utilizes mechanical loading to reversibly modify tissue optical properties, making tissues more transparent and enabling deeper light delivery (see Fig. 1) [2]. However, this technique has not been fully characterized, nor is the underlying mechanism understood. The focus of my work has been determining the mechanism behind MOC, and using this knowledge to apply MOC to optical spectroscopic methods for diagnosing disease.

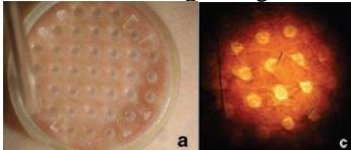


Figure 1. prototypical MOC device [2].

DIFFUSE REFLECTANCE SPECTROSCOPY

Diffuse Reflectance Spectroscopy (DRS) is a mature optical diagnostic technique, with broad applications, including cancer detection, muscle oximetry, and cognitive neuroscience. DRS is typically performed using fiberoptics, where a source fiber emits broadband light to the tissue, while an adjacent fiber collects a remitted fraction of photons to be analyzed by a spectrometer. To characterize the effects of MOC on tissue optical response, a custom-built DRS system was used to capture diffuse reflectance spectra from ex vivo porcine skin samples undergoing indentation. The two-fiber DRS probe was designed to perform both optical sensing and tissue indentation. A mechanical load frame was used to dynamically control probe displacement and

resultant specimen thickness change while recording applied force (Fig. 2). Diffuse reflectance spectra and light transmission were recorded during stress relaxation tests. Tissue optical properties were extracted from reflectance spectra using a look-up table approach developed by others [3]. Results showed that indentation could reduce tissue scattering by up to ~35% at ~70% compressive strain, and that transmission increases were due to both optical property changes and tissue thinning, and not tissue thinning alone.

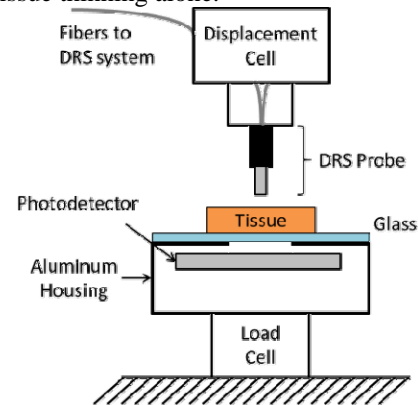


Figure 2. Combined mechanical and optical tissue interrogation.

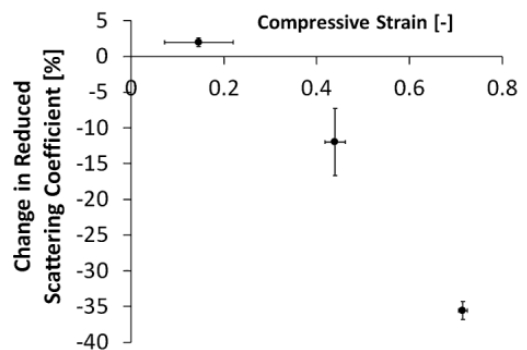


Figure 3. Tissue scattering decreased with high strain.

SIMULATION OF OPTICAL CLEARING

Biological tissues may be considered biphasic materials, with a solid phase (e.g. protein matrix) and a liquid phase (e.g. water, blood). Since DRS data showed that optical property change is significant, we hypothesized that mechanical compression of soft tissues causes interstitial movement of water and blood away from the indented region, reducing relative liquid fraction and lowering optical attenuation. The goal of this study was to demonstrate that a novel multidomain simulation of coupled tissue mechanical deformation and light transport can predict mechanical and optical signals. Poroviscoelastic properties of porcine skin (e.g. permeability, hyperelastic modulus) were determined using mechanical testing, while tissue absorption and scattering coefficients were determined as functions of water volume fraction using spectrophotometry. Finite element analysis (FEA) using these data enabled simulation of dynamically changing optical property distributions (Fig. 4 shows spatial variations in scattering coefficient during indentation). Optical Monte Carlo simulations using these distributions and FEA-predicted tissue deformation enabled simulation of dynamic light transmission. Model outputs were compared to data acquired during indentation tests using a light-emitting indenter. Results (Fig. 5) indicated that model output (red) agreed with measured data (blue) in both mechanical and optical domains, supporting the hypothesis that interstitial fluid transport changes optical response.

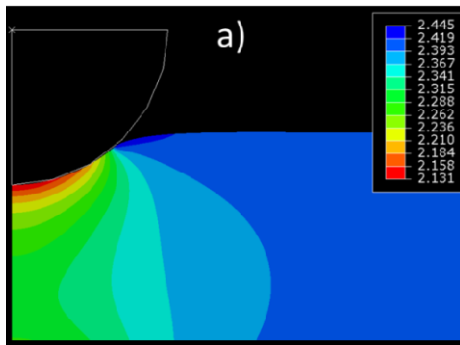


Figure 4. Optical scattering coefficient varies spatially and temporally during indentation.

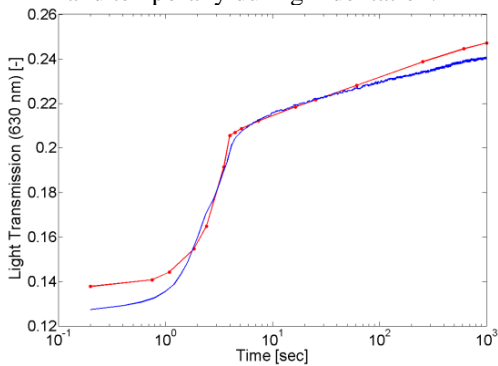


Figure 5. Model output (red points) predicts light transmission data (blue line)

FUNCTIONAL BRAIN IMAGING

Functional near-infrared spectroscopy (fNIRS) uses DRS concepts to measure changes in cerebral oxygenation, which can be used to study cognitive activation of different regions of the brain for both neuroscience and neuropathology applications. But like DRS, fNIRS is also limited by light attenuation in overlying scalp/skull tissues, and by scalp blood perfusion which biases cerebral blood signals. MOC is an ideal solution for improving sensing of cerebral oxygenation by reducing scalp water attenuation (significant in the NIR range) as well as removing confounding signals created by scalp blood flow. We developed a MOC-fNIRS device that combines a commercial fNIRS sensor headband and an array of lenses that are loaded to compress the scalp (Fig. 6). In a breath-holding study, human volunteers were asked to breath normally for 15 sec., hold their breath for 15 sec., and repeat for 6 cycles. Breath holding causes hypercapnia, leading to changes in hemoglobin (HHb) concentrations. Fig. 7 shows HHb concentrations with a) fNIRS and b) MOC-fNIRS, with MOC-fNIRS showing drastically improved signal quality and inter-channel agreement. Results suggest that MOC may improve fNIRS sensing and enable deeper sensing than previously possible.

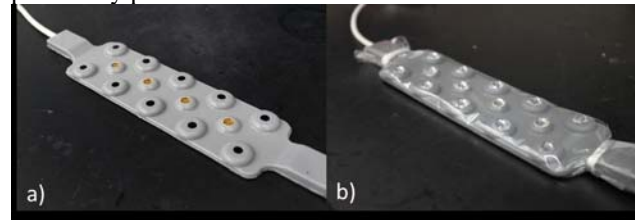


Figure 6. a) commercial fNIRS device. b) MOC-fNIRS device with array of transparent indenters.

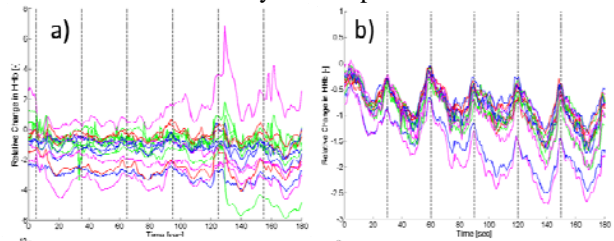


Figure 7. 16-channel hemoglobin measurements using a) standard fNIRS, and b) using MOC-fNIRS.

ACKNOWLEDGMENTS

William C. Vogt is supported by the Institute for Critical Technology and Applied Science (ICTAS).

CONCLUSIONS

MOC is now a well-characterized technique that is caused by biphasic transport through soft tissues. MOC has been demonstrated to be a promising tool for improving optical diagnostic technologies.

REFERENCES

- [1] Tuchin. *J. Phys. D: Appl. Phys.* 38 (2005) 2497–2518.
- [2] Rylander, *et al. Laser Surg Med* 2008;40(10):688–694.
- [3] Rajaram, *et al. Applied Optics*, 2010; 49(2): 142–152.

DEVELOPMENT OF METHODOLOGIES FOR HIGH ACCURACY WALL SHEAR STRESS ESTIMATIONS IN MEDICAL DEVICES

Jaime S. Raben¹, Pavlos P. Vlachos^{1,2}

1. School of Biomedical Engineering and Sciences, Virginia Tech

2. Mechanical Engineering, Virginia Tech

Corresponding Author: Jaime Raben, Email: jschmieg@vt.edu

INTRODUCTION

Accurate estimation of wall shear stresses and Reynolds stresses is a challenging yet vital step while evaluating medical devices. Specifically, abnormally high or low shear stresses are causes of concern in blood-contacting medical devices due to the damage of red blood cells seen in high-stress environments as well as the response of endothelial cells in low shear regions. This work is an extension of previous studies¹ aimed at improving upon experimental methods to accurately measure/estimate hydrodynamic quantities including velocity, shear stress and Reynolds stresses using Particle Image Velocimetry (PIV). In doing so, PIV can provide a detailed description of local flow environments in addition to serving as a validation tool for computational fluid dynamics (CFD) models commonly used evaluate medical devices.

METHODOLOGY

Particle Image Velocimetry was performed in conjunction with pressure measurements to evaluate the hydrodynamics in the acrylic FDA benchmark nozzle model (Fig. 1). The model consists of several geometries that mimic those of medical devices. These include sudden expansion/contraction as well as conical contraction/diffusion. Relevant Reynolds numbers of 500, 2,000, 5,000, and 8,000, calculated using the throat diameter (0.004m), were chosen for investigation to include laminar as well as fully turbulent regimes capable of causing blood damage.

A flow loop was constructed and flow was provided using two computer controlled gear pumps run in parallel, each capable of 5L/min. Using these pumps, the working fluid is pumped out of a reservoir through a stagnation chamber/flow straightener. Stainless steel tubing is used for entrance and exit lengths that were

approximately 150 and 60 diameters respectively. Flow rates are measured using an ultrasonic flow meter (Transonic systems T110) downstream of the nozzle model.

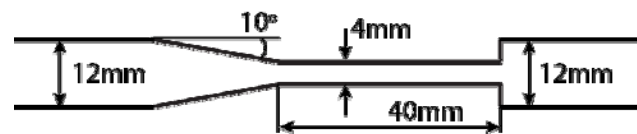


Figure. 1: FDA benchmark nozzle model.

The blood analog fluid used in this experiment was composed of 50 wt % saturated aqueous sodium iodide (NaI), 20 wt % glycerin and 30 wt % water and was measured/adjusted each day to match viscosity of blood and the refractive index of the acrylic model. The resulting viscosity and refractive index were 3.2 cP and 1.49, respectively. A small amount of saturated solution of Sodium Thiosulfate was added to the mixture to prevent oxidation of the NaI and remove discoloration.

The pressure was measured at ten counter-bored pressure tap locations along the length of the acrylic model during PIV data acquisition. Differential pressure transducers (Setra 230 0-2 psig) were used for pressure monitoring.

PIV parameters were chosen to achieve high temporal and spatial resolution resulting at a frame rate of 500 fps and spatial resolution of 15.1 microns/pix with a field of view (FOV) of approximately 12.5mm x 29mm. This extended FOV permits five overlapping data acquisition locations.

A high speed Nd:YAG laser and IDT XS-5i intensified cameras were used for data acquisition and were controlled by a pulse generator (Berkeley Nucleonics model 565). Although this experiment investigated steady flow conditions, time-resolved PIV measurements are beneficial in order to quantify

turbulence statistics, confirm the steadiness of the flow, as well as to set a protocol for future experiments that may use PIV to investigate unsteady flow environments. Furthermore, when adequate temporal resolution is available, the use of multiframe (dynamic range enhancement) PIV can be performed in flow environments with high dynamic range to simultaneously resolve large and small particle displacements.

PIV images were processed with Robust Phase Correlation (RPC) ensemble correlation using an iterative deformation scheme²⁻⁵. The RPC method utilizes a PIV spectral filter applied to the cross-correlation in the phase space to increase correlation signal-to-noise ratios and accuracy. Processing included two passes starting with a 64 x 16 pixel window resolution and 16 x 8 pixel grid resolution which was reduced to 16 x 8 pixel window resolution and 4 x 4 pixel grid resolution for the second pass. Two iterations were performed on the first pass and three iterations were performed on the second pass. Multiple iterations are typically performed for iterative deformation schemes in PIV to ensure measurements have converged prior to image transformations. PIV validation was performed using the Universal Outlier Detection⁵ with 5x7 pixel neighborhoods.

RESULTS

The resulting velocity field at the sudden expansion location is shown in Fig. 2 for Re = 500. Measurements were emitted from the location just upstream from the sudden expansion due to a loss in clarity in the acrylic model. The Velocity field indicates a strong jetting region after the expansion with low velocity regions outside of the jet. These outer regions contain recirculating flows due to the backward facing step geometry.

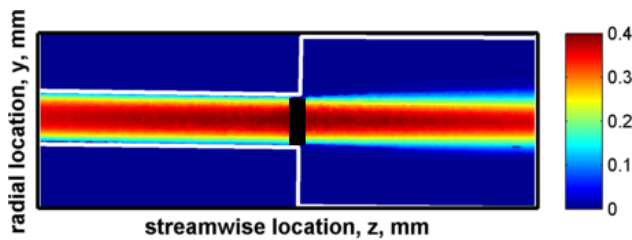


Figure. 2: Ensemble averaged velocity field for Re = 500. Wall locations are indicated by white lines. Colorbar values are in units of m/s.

Additionally, axial velocity profiles normalized by the inlet average velocity at 8 mm upstream and downstream of the sudden expansion are shown in Figures 3 and 4 for Reynolds numbers 500, 2000, 5000 and 8000. A Poiseuille velocity profile is observed for the laminar case (Re = 500) at the upstream location (Fig.3). As Reynolds number increases, velocity profiles begin to resemble plug flow. Recirculating regions are

visible outside of the jet downstream of the expansion (Fig4).

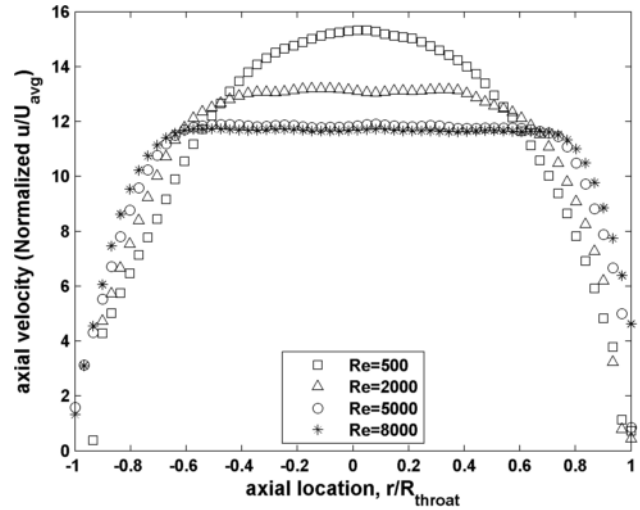


Figure 3. Normalized axial velocity at 8 mm upstream of the sudden expansion.

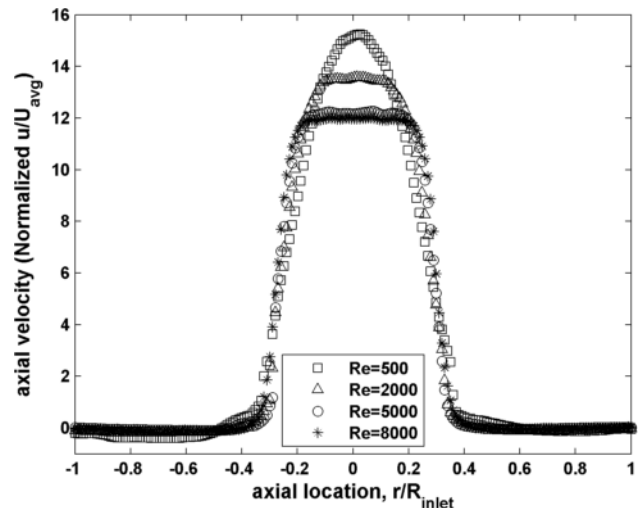


Figure 4. Normalized axial velocity at 8 mm down stream of the sudden expansion.

CITATIONS

1. Hariharan et al. "Multilaboratory Particle Image Velocimetry Analysis of the FDA Benchmark Nozzle Model to Support Validation of Computational Fluid Dynamics Simulations." *Journal of Biomechanical Engineering*. 133. (2011).
2. Eckstein and Vlachos. "Digital Particle Image Velocimetry (DPIV) Robust Phase Correlation." *Meas. Sci. Technol.* 20. (2009).
3. Meinhart et al. "PIV measurements of a microchannel flow." *Experiments in Fluids* 27 (5): 414-419. 1999.
4. Santiago et al. "A particle image velocimetry system for microfluidics." *Experiments in Fluids* 25 (4):316-319. 1998.
5. Scarano et al. "Iterative image deformation methods in PIV." *Meas. Sci. Technol.* 13. (2002).

DETECTING BURN SEVERITY AND THE ASSOCIATED INFLAMMATION RESPONSES USING THERMAL MEASUREMENTS IN LIVING TISSUE - MODELING AND EXPERIMENTAL APPROACHES

Abdusalam I. K. Al-Khwaji¹, Tom Diller¹, and Brian Vick¹

1. Virginia Tech, ME

Corresponding Author: Abdusalam Al-Khwaji, Email: alkhwaji@vt.edu

INTRODUCTION

Monitoring the healing process of a burn wound during the treatment or diagnosing the severity of the burn to get the right treatment requires an accurate evaluation technique. Early detection of burn severity is important to determine the best treatment and if skin grafting is required. The existing burn-detection methods rely heavily on the surgeon's physical observations. The proposed technique is intended to supplement this evaluation with quantifiable measurements.

The process of transporting heat and perfusion through burnt tissue region is modeled in this research work using Green's function based analytical solution along with new efficient parameter estimation code. The measurements are collected from the perfusion-thermal-resistance-probe which operates by imposing a thermal event on the tissue surface and directly measuring the thermal response of the tissue with a small sensor. The hypothesis of this proposed effort is that the new approach of simultaneous measurement of temperature and heat flux can be successfully used for practical burn characterization of depth and severity or to study inflammation associated with burn wound. Although the sensor is in light contact with the tissue, it is encased in a thin layer of plastic and can easily be sterilized. Because it operates by cooling rather than heating, it is inherently safe for any patient application. Previous work has demonstrated the ability of the system to quantify the thickness of non-perfused layers over perfused layers, such as tissue. The present work presents the results detecting third degree burn and analyzing inflammation associated with four different burn severities at four different monitoring times with actual living tissue.

MATERIAL & METHODS

The perfusion-thermal-resistance probe imposes a short thermal cooling event on the surface of tissue through a combination heat flux and temperature sensor. After the probe is placed on the tissue and reaches thermal equilibrium with the tissue, compressed air is turned on through an array of impinging jets onto the back side of the sensor opposite the tissue. The room temperature air cools the tissue for the duration of the sixty-second test. The resulting surface temperature and heat flux measurements are processed analytically as a function of time using an analytical model to estimate blood perfusion (w_b), thermal contact resistance (R'') and core temperature. Figure 1 illustrates the three parameters inside the 1D-Pennes equation and the boundary conditions which were used to derive the Green's function analytical solution [1-2].

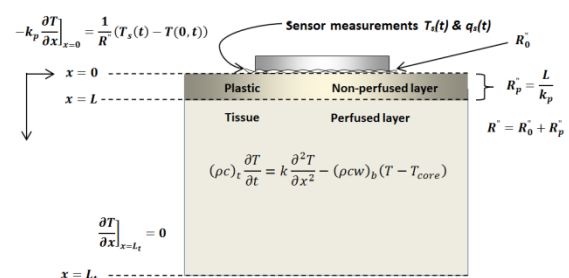


Figure 1 Mathematical burn modelling

For the experiments a series of burns with varying severity were created on two pigs by putting a 100°C brass cylinder on the skin for four specified lengths of time. The severity of the burn increased as the length of time the cylinder was in contact with the tissue increased from three seconds to seventy-five seconds. The thermal perfusion probe was then used to measure the thermal

response of the tissue at times from one hour to five days following the imposition of the burn [3].

RESULTS

The damage function was used with a finite-difference model to specify the depth from each burn time which cause third degree burn

$$\Omega(x, t_{burn}) = \int_{t_0}^{t_{burn}} A e^{-G/R T(x,t)} dt \geq 10^4$$

where burn time $t_{burn} = \{ 3, 12, 20, 75 \text{ seconds} \}$. Only 20 and 75 seconds were proved to cause third degree burn. Figure 2 illustrates the two burn times which cause third degree burn. Figure 3 illustrates the estimated burn depth in mm related to 20 and 75 seconds burns, while monitoring them for four different monitoring times $\{ 1, 24, 72, 120 \text{ hours} \}$. Results show the ability of the model in detecting third degree burn and that the third degree burn has the lowest inflammation response after 24 hours since tissue starts to dry and it becomes full non-perfused layer clearly around 72 hours.

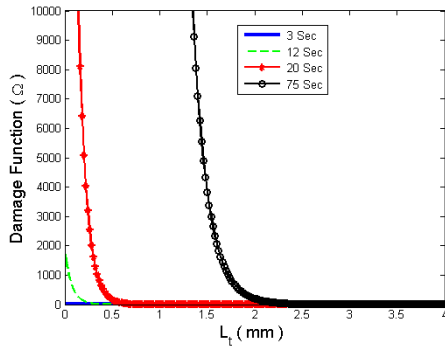


Figure 2 Damage function specifies 3rd degree burn

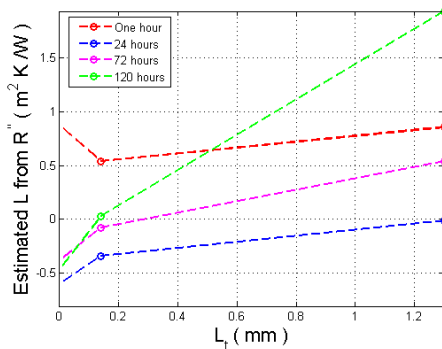


Figure 3 Estimating burn depths from pig experiments

Figure 4 illustrates burn factor concept which we develop it to monitor the inflammation response related to the burn wound. It indicates that as the burn severities increase as the inflammation responses decrease and vice versa. Overall, observation of the three graphs is that

detecting burn severity is possible before the standard known time which is 5 days and also that burn times above 20 seconds causes third degree burn. Also the burn factor combines perfusion and thickness of burnt layers, which is useful in many clinical applications.

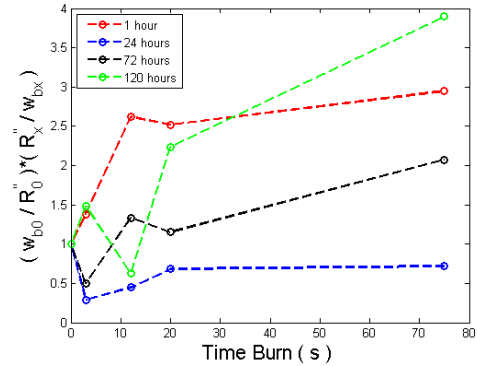


Figure 4 Burn factor for different burn severities

CONCLUSIONS

After analyzing four different burn severities, we show that our system of thermal measurements can be used to identify the status of burns as indicated by the blood perfusion and thermal resistance of the tissue and monitoring the inflammation associated with the healing process.

ACKNOWLEDGMENTS

The Libyan-North American Scholarship program (CBIE), and Omar Almkhatar University/ Elbeida-Libya

REFERENCES

- (1). Abdulalam Alkhawji, Brian Vick, and Tom Diller, "New Mathematical Model to Estimate Tissue Blood Perfusion, Thermal Contact Resistance and Core Temperature", *Journal of Biomechanical Engineering*, Vol.134, 2012, 081004, pp. 1-8.
- (2). Abdulalam Alkhawji, Brian Vick, Tom Diller, "Modelling and Estimating Simulated Burn Depth Using the Perfusion and Thermal Resistance Probe," *Journal of Medical Device*, in press.
- (3). Abdulalam Alkhawji, Brian Vick, Tom Diller "Thermal measurements for quantifying burn severity in living tissue", the Annual Meeting of the Biomedical Engineering Society, October 24-27, 2012, Atlanta, USA

INFLUENCE OF FREEZE-THAWED EFFECT ON THE STRESS-STRAIN CURVES OF BOVINE LIVER TISSUES

Yuan-Chiao Lu¹, Costin D. Untaroiu¹

1. Virginia Tech-Wake Forest University Center for Injury Biomechanics
 Corresponding Author: Yuan-Chiao Lu, Email: yclu@vt.edu

INTRODUCTION

Cadaveric and human numerical models are playing an important role in the assessment and optimization of advanced restraint systems for reducing the abdominal injuries⁶. While the material properties of the liver were recently investigated, most of these studies^{2, 4} tested only fresh human or porcine livers. Since the majority of abdominal tests used to develop injury criteria were done with preserved cadavers⁶, there is a need to better understand possible changes to the material properties of the liver caused by preservation methods.

The scope of this study was to investigate the influence of storage method on the biomechanical responses of the liver, by examining the failure properties of the tissue. The hypothesis in this study was that the failure properties of the bovine liver change over time (fresh vs. 30-day and 60-day frozen preserved specimens).

METHODOLOGY

Uniaxial tensile tests were conducted on the parenchyma of 10 fresh bovine livers obtained from Animal Technologies (Tyler, Texas, USA). Specimens from each liver were equally divided into three groups: fresh, 30-day frozen storage, and 60-day frozen storage. All preserved specimens were stored at -12°C . Preserved tissues were tested under the same testing condition as fresh samples after thawing for 12 hours. The coupon specimens (Fig. 1a) were cut from both fresh and thawed livers using a custom stamp⁴. The Dulbecco's Modified Eagle's Medium was utilized to maintain specimen hydration until test for all samples. Each specimen from every group (fresh, Day 30, and Day 60) was randomly assigned to one of the three strain rates: 0.01 s^{-1} (Rate 1), 0.1 s^{-1} (Rate 2), and 1.0 s^{-1} (Rate 3). The tensile experimental setup is shown in Fig. 1b.

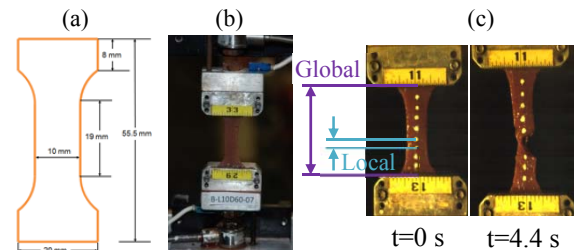


Figure 1. Experimental setup and video stills.

Each specimen was stretched at the two ends, and tested until failure at normal room temperature (24°C). The force and acceleration were measured at the clamps in each tensile test. A typical uniaxial tensile test at initial and failure states is shown in Fig. 1c.

The 2nd Piola-Kirchhoff (PK) stress (S) and the Green-Lagrangian (GL) strain (ε) were calculated using inertially compensated force, the initial cross-sectional area, and the stretch ratio⁴. The stretch ratios were measured at the tear site (local) and along the entire specimen (global) (Fig. 1c). To calculate the local stretch ratio, the optical markers adjacent to the tear location were tracked until the time of failure using motion analysis software (TEMA v. 2.6, Linköping, Sweden). To calculate the global stretch ratio, the clamp displacements of two motor driven linear stages were recorded. The initial cross-sectional area (A_0) used for the stress calculation was determined from the pre-test pictures at the tear site (local) and at the middle of the specimen (global). The failure stress and failure strain were determined as the maximum of the 2nd PK stress and the GL strain which occurs at the same time when the peak force was observed.

The two-sample Mann-Whitney tests were performed to evaluate the statistical significance ($\alpha=0.05$) of failure stress and failure strain between storage times and

between strain rates. Furthermore, the characteristic average and elliptical response corridor were determined for each loading rate by storage time (fresh, Day 30, Day 60)¹. In addition, the paired two sample t-test was employed to compare the failure properties between local and global data sets ($\alpha=0.05$).

RESULTS

For both local and global data (Table 1), the failure stresses significantly increased and failure strain significantly decreased when strain rate increased for preserved bovine livers (Day 30 and Day 60) ($p<0.05$). While the same trend was observed for fresh samples, significant differences were not found.

Table 1. Failure stress and failure strain by loading rate.

Rate (# of Specimens)	Local Failure Properties		Global Failure Properties	
	Stress (kPa)	Strain	Stress (kPa)	Strain
Fresh				
Rate 1 (14)	44.6 (± 16.4)	0.35 (± 0.08)	42.9 (± 15.1)	0.42 (± 0.08)
Rate 2 (11)	50.0 (± 14.8)	0.34 (± 0.13)	48.1 (± 14.8)	0.41 (± 0.12)
Rate 3 (11)	55.8 (± 24.4)	0.29 (± 0.07)	52.9 (± 21.7)	0.35 (± 0.07)
Day 30				
Rate 1 (12)	45.7 (± 10.9)	0.28 (± 0.09)	43.5 (± 9.7)	0.35 (± 0.08)
Rate 2 (13)	53.3 (± 19.1)	0.24 (± 0.09)	50.3 (± 17.0)	0.32 (± 0.09)
Rate 3 (12)	64.7 (± 18.9)	0.23 (± 0.05)	62.7 (± 18.8)	0.28 (± 0.04)
Day 60				
Rate 1 (12)	46.6 (± 20.4)	0.26 (± 0.08)	44.3 (± 18.8)	0.33 (± 0.05)
Rate 2 (11)	54.1 (± 13.8)	0.22 (± 0.07)	52.0 (± 12.9)	0.29 (± 0.05)
Rate 3 (11)	65.8 (± 15.4)	0.21 (± 0.05)	63.5 (± 15.4)	0.27 (± 0.07)

The characteristic averages and elliptical response corridors (± 1 SD) of stress-strain curves by loading rate for fresh and preserved specimens are shown in Fig. 2. The average failure strains significantly decreased between fresh and Day 30 specimens ($p<0.05$) and between fresh and Day 60 specimens ($p<0.05$) for both local and global data. Contrarily, the average failure stresses increased between fresh and preserved tissues for both local and global data, but the changes were not statistically significant ($p>0.05$).

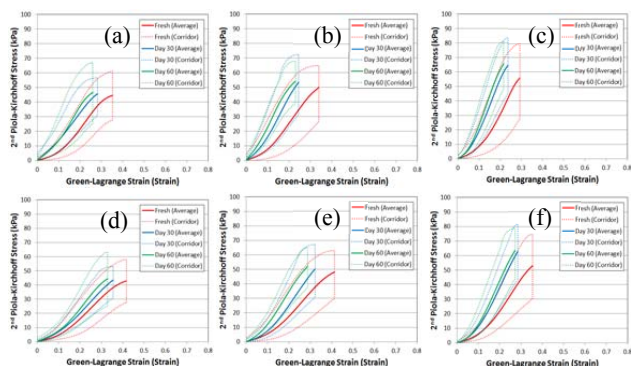


Figure 2. Average curves and elliptical response corridors. (a)-(c): Rate 1-3 for local data; (d)-(f): Rate 1-3 for global data.

The paired two-sample t-tests showed that both failure stress and failure strain were significantly different

between local and global data sets for all three loading rates ($p<0.05$).

DISCUSSION

The current study quantifies the tensile responses of bovine liver parenchyma at various loading rates for fresh and preserved tissues. It was shown that the liver preservation by freezing affects both the biomechanical and failure responses under tensile loading. These stiffness changes could be caused by the damage of the liver cell structure as a result of the freezing and thawing processes⁵. No significant differences of the failure properties were found between fresh bovine livers from this study and fresh human livers⁴ ($p>0.05$), which suggest a mechanical similarity between human and bovine livers. One limitation in this study is the assumption of the constant cross-sectional area used for the stress-strain calculation. A finite element based approach could be attempted to obtain stress-strain behaviors using the exact shape of the specimens³.

CONCLUSIONS

Significant changes in the biomechanical and injury responses of frozen preserved liver samples relative to fresh samples were demonstrated at both global and local levels in this study. In addition, nonlinear, viscoelastic characteristics, and rate dependency of the liver parenchyma were observed in tension for both fresh and preserved samples. Human models assigned with accurate material models could help in better understanding the injury mechanism of liver and in development of injury countermeasures.

ACKNOWLEDGMENTS

Dr. Andrew Kemper for assisting the setup of the tensile testing device.

REFERENCES

- 1 J. H. Ash, D. J. Lessley, J. L. Forman, Q. Zhang, C. G. Shaw, and J. R. Crandall, 'Whole-Body Kinematics: Response Corridors for Restrained Pmhs in Frontal Impacts', in *IRCOBI* (2012).
- 2 A. Brunon, K. Bruyere-Garnier, and M. Coret, 'Mechanical Characterization of Liver Capsule through Uniaxial Quasi-Static Tensile Tests until Failure', *J Biomech*, 43 (2010), 2221-7.
- 3 J. Hu, K. D. Klinich, C. S. Miller, G. Nazmi, M. D. Pearlman, L. W. Schneider, and J. D. Rupp, 'Quantifying Dynamic Mechanical Properties of Human Placenta Tissue Using Optimization Techniques with Specimen-Specific Finite-Element Models', *J Biomech*, 42 (2009), 2528-34.
- 4 A. R. Kemper, A. C. Santago, J. D. Stitzel, J. L. Sparks, and S. M. Duma, 'Biomechanical Response of Human Liver in Tensile Loading', *Ann Adv Automot Med*, 54 (2010), 15-26.
- 5 S. Ocal, M. U. Ozcan, I. Basdogan, and C. Basdogan, 'Effect of Preservation Period on the Viscoelastic Material Properties of Soft Tissues with Implications for Liver Transplantation', *J Biomech Eng*, 132 (2010), 101007.
- 6 C. D. Untaroiu, D. Bose, Y. C. Lu, P. Riley, D. Lessley, and M. Sochor, 'Effect of Seat Belt Pretensioners on Human Abdomen and Thorax: Biomechanical Response and Risk of Injuries', *J Trauma Acute Care Surg*, 72 (2012), 1304-15.

INJURY RISK IN SIDE IMPACT OF NON-TRACKING VEHICLES INTO GUARDRAIL

Nicholas S. Johnson¹ and Hampton C. Gabler¹

1. Virginia Tech, School of Biomedical Engineering and Sciences

Corresponding Author: Nicholas S. Johnson, Email: johnso5a@vt.edu

INTRODUCTION

Side crashes are one of the most dangerous types of guardrail crash. Of particular concern is when a non-tracking vehicle slides sideways into a guardrail end treatment. Modern guardrail end treatments are designed to break away or absorb energy under the loads which are typical of a frontal impact. Because the side of a vehicle, unlike the front, has so little structure to protect an occupant, side impacts to end treatments carry a higher injury risk than frontal impacts to end treatments. The concentrated load on the side door structure seen in end treatment side impacts frequently results in deep intrusion of door structure into the occupant compartment. In extreme cases, the guardrail itself may even penetrate the occupant compartment directly, resulting in a very high probability of serious occupant injury or death.

METHODOLOGY

This analysis examined National Automotive Sampling System / Crashworthiness Data System (NASS/CDS) data from case years 1997 to 2008 (inclusive). CDS vehicles for which the highest- ΔV (delta-V; i.e., highest-severity) impact was a non-oblique side impact with a guardrail were included in the analysis. Vehicle occupants were considered “injured” if their maximum Abbreviated Injury Scale (MAIS) score was 3 or greater, or if they died within one month of the crash date due to crash-related injuries. In order to simplify the analysis, only drivers were considered, as drivers comprise approximately 70% of all occupants in vehicles which strike guardrail. NASS/CDS does not distinguish guardrail Length of Need (LON) from guardrail end terminals, so the area impacted was identified through manual inspection of NASS/CDS case photos.

All analysis was performed in SAS 9.2 using NASS case weights and, if necessary, clustering and stratification variables to obtain results representative of all U.S. crashes. All cases with statistical weights of zero or less were excluded prior to analysis (7 in total). Odds ratios comparing relative injury risk between different categories (and associated confidence intervals) were computed using PROC SURVEYLOGISTIC.

RESULTS

The analyzed dataset contained 142 side guardrail crashes. 55 cases were identified as tracking impacts and were excluded. 12 cases were excluded because the struck object was actually a concrete barrier, rail junction with a concrete barrier or crash cushion, 4 were excluded for having unknown driver injury levels and another 7 were excluded for having NASS weights of zero or less. Left and right (driver and passenger) side crashes were split about 40%-60%. Cars made up about 80% of all side guardrail crashes, with the remaining 20% being LTVs. The majority of studied crashes had less than 4 total impacts, and about 60% were LON crashes. Each examined NASS case year was well represented in the sample.

Figure 1 divides cases guardrail area impacted. It appears that contact with the end terminal is substantially more hazardous than LON contact. Terminal side crashes are observed to be 8.33 times more likely than LON side crashes to produce injury (95% CI: 2.96 – 23.4). LON impacts represent 75.5% of all non-tracking guardrail side crashes, yet only 28.9% of the resulting injuries; the remaining 24.5% of crashes with end terminals causes 71.1% of the injuries.

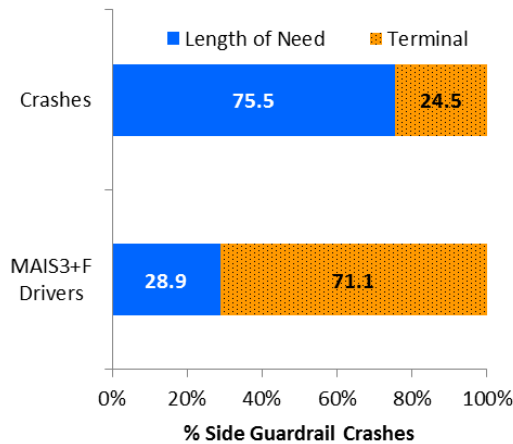


Figure 1: Crashes and injuries by area of rail system contacted.

Figure 2 breaks down terminal crashes and associated injuries by the type of the terminal system. Designs not compliant with NCHRP Report 350 criteria (1, 2) were observed to pose an injury risk 5.11 times as great as compliant designs, but the difference was not statistically significant (95% CI: 0.629 – 41.5). The p-value for this difference is only 0.171; it is very likely that a larger sample would yield a statistically significant difference between compliant and non-compliant terminals. Striking any narrow fixed object with the side of a vehicle is inherently very dangerous, so the difference between terminal types may appear somewhat subdued as a result. Note that this assessment does not qualitatively change even if all terminals of unknown type are assumed to be non-compliant.

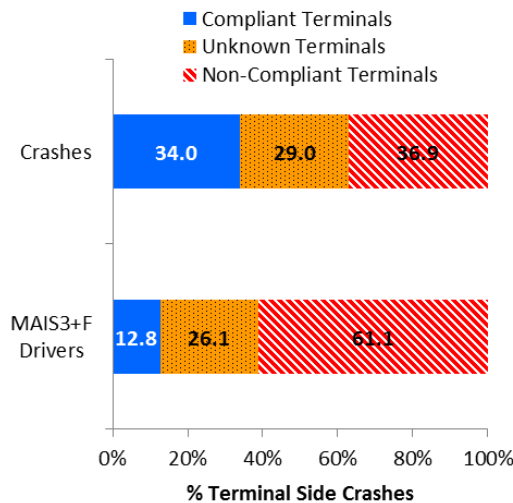


Figure 2: Effect of terminal crashworthiness on injury risk (terminal side crashes only).

CONCLUSIONS

Any contact with an end terminal is highly over-represented in terms of driver injury. Although terminal crashes represent only about 25% of guardrail side crashes, they account for more than 70% of the injuries sustained in such crashes. Terminals compliant with NCHRP-350 may be about five times as safe as non-compliant designs, but the difference appears to be overshadowed by the high degree of risk involved in striking any narrow fixed object with the side of the vehicle. A somewhat larger sample appears necessary to make this finding significant at the 95% confidence level.

ACKNOWLEDGMENTS

The authors would like to thank the Transportation Research Board for their support of this research under National Cooperative Highway Research Program Project 17-43.

REFERENCES

1. Ross HE Jr., Sicking DL, Zimmer RA and Michie JD, "Recommended Procedures for the Safety Performance Evaluation of Highway Features", NCHRP Report 350, Transportation Research Board (1993).
2. AASHTO, "Roadside Design Guide, 4th Edition", American Association of State Highway and Transportation Officials (2011).

NON-DESTRUCTIVE IMAGING AND CHARACTERIZATION OF TISSUE-ENGINEERED BLOOD VESSEL GROWTH WITHIN A BIOREACTOR USING OCT

Abhijit A. Gurjarpadhye¹ and Christopher G. Rylander, PhD^{1,2}

¹School of Biomedical Engineering and Sciences, Virginia Tech, Blacksburg, VA

²Mechanical Engineering Department, Virginia Tech, Blacksburg, VA

Corresponding Author: Abhijit A. Gurjarpadhye, Email: abhijitg@vt.edu

INTRODUCTION

Cardiovascular disease is one of the leading causes of death in the western world [1]. Coronary artery disease (CAD) is the most common form of heart disease, which includes occlusion of the coronary artery due to atherosclerotic plaque buildup, leading to myocardial infarction. This vascular condition is commonly treated with a coronary artery bypass graft, where a healthy native blood vessel from the patient's body is used to create a bypass around the atherosclerotic region in the artery. However, removing healthy blood vessels from the vasculature is less than desirable and in some cases not possible [2].

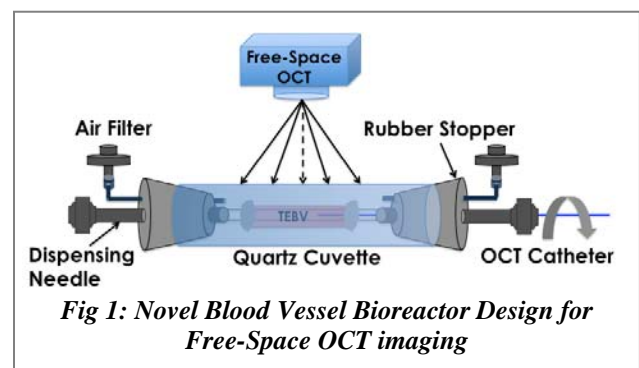
Vascular tissue engineering has emerged as a key technology for replacement of damaged or diseased blood vessels. However, despite the huge potential to "manufacture" histocompatible blood vessels and other tissue/organs, regenerative medicine faces some major challenges such as monitoring this dynamic and complex biological process in real-time, making control and optimization extremely difficult. Histology, the gold standard used for tissue structural assessment, is a static technique that only provides a "snapshot" of the specimen and requires the specimen to be sacrificed. This inefficiency severely limits our understanding of the biological processes associated with tissue growth during the *in vitro* pre-conditioning phase. Optical Coherence Tomography (OCT) enables imaging of cross sectional structure in biological tissues by measuring the echo time delay of backreflected light [3]. OCT has recently emerged as an important method to assess the structures of physiological, pathological as well as tissue engineered blood vessels [4]. The goal of the present study is to develop OCT-based imaging system for non-destructive

imaging of tissue-engineered blood vessels (TEBV) developing within a bioreactor.

METHODOLOGY

A swept-source OCT imaging system, which comprises a 20 kHz tunable laser (Santec HSL2000) with 1300 nm central wavelength and 110 nm FWHM bandwidth was used for imaging. This system is capable of acquiring cross-sectional 2D images of a sample with an axial (in-depth) resolution of ~13 μ m.

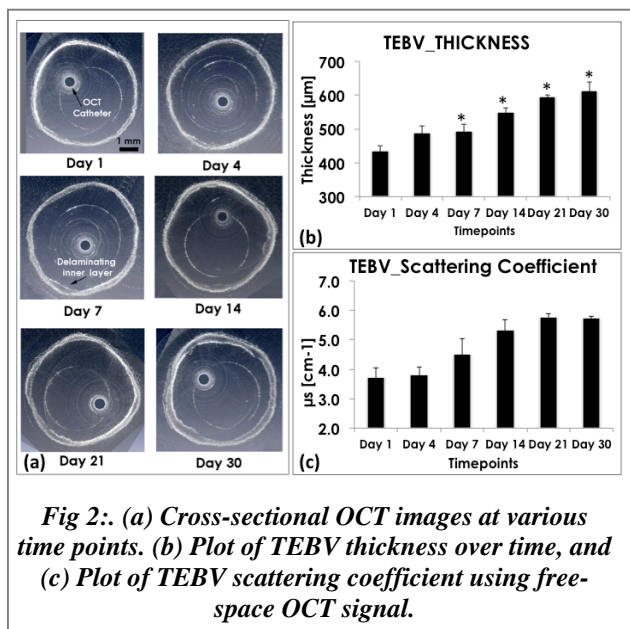
A novel blood vessel bioreactor utilizing a quartz cuvette conducive to free-space OCT imaging was constructed (Fig 1). The quartz cuvette permits free-space OCT imaging of the blood vessel over 360 degrees.



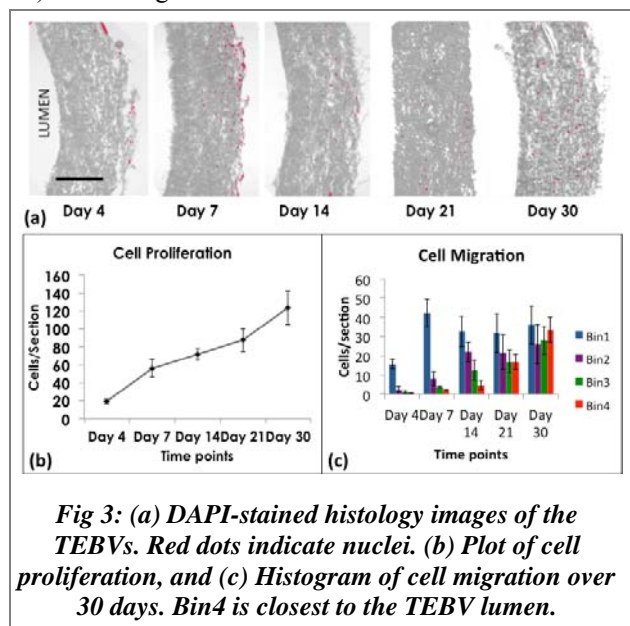
Biodegradable scaffolds (15% PCL/collagen, ~300 micron thick) were seeded with CH3 10t1/2 mesenchymal pluripotent cells to develop bioengineered blood vessels. OCT images of these blood vessels were obtained in free space (catheter free) as well as using a vascular OCT catheter at days 1, 4, 7, 14, 21 and 30. Free-space OCT images were co-registered with endoscopic OCT images

to determine the vessel wall thickness. Additionally, small segments of a control vessel were extracted and stained with DAPI to quantify cellular infiltration. Non-linear curve fitting of free-space OCT data to the extended Huygen-Fresnel model was performed to determine optical scattering properties.

RESULTS



The vessel wall thickness, determined using co-registered OCT images shown in Fig. 2a, increased from $435 \pm 15 \mu\text{m}$ to $610 \pm 27 \mu\text{m}$ and the scattering coefficient increased from $3.73 \pm 0.32 \text{cm}^{-1}$ to $5.74 \pm 0.06 \text{cm}^{-1}$ over 30 days (Fig. 2b). Scattering coefficients of the TEBVs increased from



$\mu_s = 3.733 \pm 0.318 \text{cm}^{-1}$ on day 1 to $\mu_s = 5.737 \pm 0.061 \text{cm}^{-1}$ on day 30 (Fig. 2c).

Histology showed that the smooth muscle cells penetrated the scaffold and migrated toward the lumen, thus populating the full thickness of the scaffold (Fig. 3a). Cell migration histograms (Fig. 3c) indicated that while the cells populated only the outer (abluminal) sections of the scaffold thickness at early time points, they proliferated and infiltrated the entire thickness of the scaffold toward the end of the study.

DISCUSSION

Our results showed that the high-resolution, cross-sectional imaging potential of optical coherence tomography could be utilized for non-destructive imaging of tissue-engineered constructs without compromising the sterile environment of the vessel.

CONCLUSION

This study suggests that combination of free-space and catheter based OCT for blood vessel imaging provides accurate structural information of the developing blood vessel. In this study, we determined that free-space OCT images could be co-registered with catheter-based OCT images to monitor structural features such as wall thickness or delamination of the developing tissue-engineered blood vessel within a bioreactor. Structural parameters and optical properties obtained from OCT imaging correlate with histological sections of the blood vessel and could potentially be used as markers to non-invasively and non-destructively assess regeneration of engineered tissues in real time. This novel method of OCT imaging could be utilized to study physiological as well as pathological development and tissue structure of bioengineered tissue in real time.

ACKNOWLEDGMENTS

This study was funded by a grant from the NIH/NHLBI (R01 HL098912).

REFERENCES

1. Patnaik JL, Byers T, DiGuseppi C, Dabelea D, Denberg TD.. Breast Cancer Res 2011; 13(3):R64.
2. Sybrandy JE, Wittens CH. Journal of vascular surgery, North American Chapter 2002; 36(6):1207-1212.
3. Huang D et al. Optical coherence tomography. Science 1991; 254(5035):1178-1181.
4. Bonnema GT, Cardinal KO, McNally JB, Williams SK, Barton JK.. J Biomed Opt 2007; 12(2):024018.

ANALYSIS OF EVENT DATA RECORDER SURVIVABILITY IN CRASHES WITH FIRE, IMMERSION, AND HIGH DELTA-V

Ada H. Tsoi¹, John C. Hinch, and Hampton C. Gabler¹

1. Virginia Tech, Biomedical Engineering

Corresponding Author: Ada H. Tsoi, Email: atsoi@vt.edu

INTRODUCTION

Event Data Recorders (EDRs), the ‘black boxes’ now installed in over 90% of model passenger vehicles, offer a unique opportunity to understand the biomechanics of crash injury. These devices are capable of recording the characteristics of a crash and as a result, EDR data has become an invaluable tool for law enforcement, researchers, and government agencies.

In late 2012, NHTSA issued a regulation (49 CFR 563) which imposed survivability requirements on EDR data for the first time. Part 563 requires EDR functionality during and after compliance crash tests as specified in Federal Motor Vehicle Safety Standard (FMVSS) 208 and FMVSS 214. These tests are representative of a major proportion of U.S. highway crashes; however, there are undeniably crashes that fall beyond the scope of these tests. In particular, concerns have been expressed over EDR operation after crashes involving fire, immersion, or high changes in velocity (ΔV) as little is known about whether EDRs, or the data they store, are capable of surviving these events. In addition, a study is needed to address whether these events are sufficiently common to justify the expense of hardening the EDRs.



Figure 1. Can the Event Data Recorder (EDR) information of a submerged vehicle be read?

The goal of this study was to investigate the survivability of light vehicle EDRs in real world fire, immersion, and high severity cases. The two objectives were to determine the frequency of these crashes and to determine whether EDR data could be downloaded after these events.

METHODOLOGY

Analyses indicate each of these scenarios represents about 1% of the crash problem. To refine these measurements, a case level study was performed using 3 databases. The Fatality Analysis Reporting System (FARS) database contains a U.S. census of all fatal crashes. The National Automotive Sampling System Crashworthiness Data System (NASS-CDS) is an annually tabulated, random sample of nationally representative crashes from which crash investigators analyze and collect data. Similarly, the National Motor Vehicle Crash Causation Survey (NMVCCS) is a nationally representative collection of crashes; however, the crash investigators were present at the crash location as soon as possible after the crash occurred.

Cases were limited to General Motors (GM) vehicles of model year 1995 and greater to ensure EDRs in our dataset could be read by the publicly available Bosch Crash Data Retrieval tool at the time of the crash.

Frequency of Fire, Immersion, and High ΔV Crashes

Our frequency analysis was limited to the years 2009 and 2010 for FARS, 2005-2008 for NASS-CDS, and all years (2005-2007) for NMVCCS. Presence of vehicle fire was indicated as a variable in all three databases and nationally representative values are reported for NASS-CDS and NMVCCS.

Cases indicating vehicle immersion were available in FARS as a variable. Crash narratives from NMVCCS

were examined for terms indicative of sources of water and manually perused for relevance. These NMVCCS cases were reported as nationally representative values.

For the high ΔV frequency assessment, cases were divided by their crash orientation. For side crashes, severe ΔV was defined to be greater than 21 mph, as dictated by the side crash test FMVSS 214. The threshold for frontal crashes was 35 mph, as dictated by FMVSS 208. Estimates of ΔV were only provided by NASS-CDS and reported as nationally representative values.

Recoverability of EDR Data

Our recoverability analysis included vehicle fire and high ΔV case extraction from NASS-CDS (2005-2010). Vehicle immersion cases were drawn from NMVCCS (2005-2007). These cases were identified identically to the frequency analysis; however, cases were not extrapolated to national values. In addition, photographs of fire and immersion cases were extracted from the electronic case viewer [1,2], scrutinized, and categorized by damage. Both databases additionally include the success of EDR information download. For vehicles where EDR information was not obtained, the investigator's reason for not downloading the EDR was tabulated.

RESULTS

Frequency of Fire, Immersion, and High ΔV Crashes

Vehicle fire was found to be exceedingly rare, only occurring in 0.5% of FARS cases. Similarly, only 0.2% of NASS-CDS cases and 0.7% of NMVCCS cases indicated involved fire. Vehicle immersion was also a rare event in our sample, where 0.5% of FARS cases experienced this event and only 0.1% NMVCCS cases were exposed to a source of water. NASS-CDS indicated that less than 1% of frontal crashes involve a ΔV exceeding 35 mph and less than 5% of side crashes experience a ΔV exceeding 21 mph.

Recoverability of EDR Data

Vehicle fire was identified in 70 of 11,944 NASS-CDS cases. There were 7 EDRs that were successfully read; however only 1 vehicle indicated visible fire damage in the occupant compartment. Of the remaining 63 cases, 45 cited vehicle damage as the reason for not obtaining the EDR data, most of which coincided with visible fire damage in the occupant compartment.

Vehicle immersion was identified in 9 of 2,759 NMVCCS cases. Two EDRs were successfully downloaded, one of which was completely submerged. Of the remaining 7 cases, only 2 indicated vehicle damage as the reason preventing download.

Of the 11,944 NASS-CDS cases, high ΔV was indicated in 141 frontal crashes, where 32 were read and 51 were not read due to damage. High severity was indicated in 243 side crashes, where 71 were read and 75 were not read due to damage.

LIMITATIONS

Our study was limited to GM vehicles which could have been downloaded during the various data collection periods. We do not know if our findings on EDR survivability can be generalized to the EDRs of other automakers. However, we conjecture that as EDR packaging differs very little from OEM to OEM that there would be little difference in EDR survivability.

Another limitation of this study is that the "EDR information not obtained" designation is imprecise. The designator does not specify whether the EDR could not be physically read, or whether the investigator chose to not download the EDR for other non-damage related reasons. Our analysis also showed that the designator "Vehicle not equipped with EDR" was miscoded in some cases. Our dataset contained 3 Bosch-readable EDRs with this annotation which were in actuality readable with the Bosch CDR tool.

The EDRs explored in this study were developed many years ago, generally before the first rulemaking activity associated with Part 563. The performance of the EDRs and preservation of their data in crashes was the result of then-current industry practices. The findings of this analysis may or may not be relevant to EDRs that are currently being designed and manufactured to be compliant to Part 563.

CONCLUSION

Vehicle fire and immersion were each found to constitute less than 1% of all crashes. High ΔV crashes made up less than 1% of frontal crashes and less than 5% in side crashes. There is anecdotal evidence that supports the survivability of GM EDRs in real world crashes involving fire, immersion, or high ΔV ; however, this is accompanied by EDRs that could not be downloaded due to crash damage. While these EDRs could be hardened to higher standards, the rare occurrence of these events in crashes indicates that survivability requirements beyond those currently in place may not be cost beneficial.

REFERENCES

- [1] NHTSA, "National Motor Vehicle Crash Causation Survey SearchForm," <http://www-nass.nhtsa.dot.gov/nass/nmvccs/SearchForm.aspx>, accessed 3/31/12.
- [2] NHTSA, "National Automotive Sampling System CDS XML Case Viewer" <http://www-nass.nhtsa.dot.gov/nass/cds/SearchForm.aspx>, accessed 3/31/12.

THE INFLUENCE OF COMBINATORIAL SHEAR AND THERMAL STRESS ON PRE-OSTEOBLASTS FOR BONE REGENERATION

Alana Sampson¹ and Nichole Rylander^{1,2}

1. School of Biomedical Engineering and Sciences, Virginia Tech

2. Department of Mechanical Engineering, Virginia Tech

Corresponding Author: Alana Sampson, Email: asampson@vt.edu

INTRODUCTION

Bone possesses the intrinsic ability to regenerate, however critical-sized bone defects have minimal capacity to heal on their own¹. Tissue engineered scaffolds provide a platform for tissue growth and have great potential to facilitate bone regeneration. Despite advances in tissue engineering, there has been limited success in maturation and integration of these scaffolds *in vivo* to provide efficient bone regeneration. The use of external stimuli to condition cells within a scaffold has been investigated as a method to produce bone-like constructs. Previous studies have shown that hydrodynamic shear stress can direct cell behavior through the activation of different signaling cascades, stimulating the synthesis of proteins essential for bone development². These stresses can influence cell proliferation, ECM deposition, and scaffold maturation. In addition, our prior work has shown that thermal stress has similar potential to induce osteogenic effects³. Although ample research has been conducted on the effect of individual stress on cells, there is little focus on cellular response to a combination of stresses. The application of multiple stimuli on cells may have a synergistic effect on protein upregulation through the activation and integration of several signaling pathways. This combinatorial signal transduction may initiate a cellular response that leads to enhanced osteogenesis. Therefore, we aim to determine the osteogenic-inducing effects of combined thermal and shear stress on pre-osteoblastic cells through *in vitro* analysis of protein expression and secretion.

METHODOLOGY

MC3T3-E1 (ATCC) murine pre-osteoblastic cells were seeded onto tissue culture treated slides and cultured in

osteogenic differentiation media (α -modified Eagles Medium (Invitrogen) supplemented with 10% Fetal Bovine Serum (FBS), 1% Penicillin-Streptomycin (PS), β -glycerol phosphate, and ascorbic acid). After 2 days, cells were exposed to the following stress treatment condition: no stress (control), shear stress, thermal stress, or a combination of shear and thermal stress. Thermal stress was applied by replacing the media with pre-warmed media at 41°C, then placing cells in an incubator set to 41°C for 1 hour. Shear stress was applied using a parallel plate flow chamber (PPFC), as shown in Figure 1. Media at 37°C was pumped at a continuous flowrate of 100ml/min across the cell monolayer for 30 minutes. For combined shear and thermal stress, the PPFC system was placed in a 41°C incubator for 30 min. Cells were allowed to recover in an incubator set to 37°C for 48 hours, then stress protocols were repeated on Day 4.

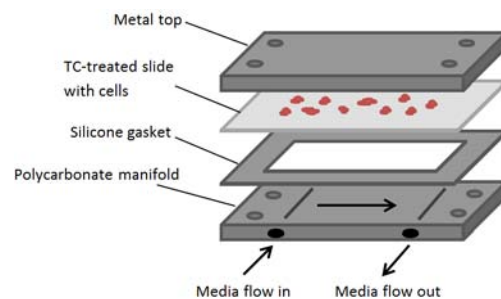


Figure 1: Schematic of parallel plate flow chamber

After stress conditioning the cells, HSP70 protein expression was analyzed using immunofluorescent (IF) staining. Fifteen hours post-stress, cells were fixed with Histochoice MB Fixative, permeabilized with Triton X-100 solution, and non-specific binding was blocked with a 2% BSA solution. An anti-HSP70 antibody conjugated to Dylight 488 was used to visualize HSP70 expression and

DAPI was used to stain the cell nuclei. On Day 6, alkaline phosphatase (ALP) activity was measured using a colorimetric assay. The conversion of p-nitrophenyl phosphate to a colored product was measured with endpoint absorbance readings at 405nm using a spectrophotometer.

RESULTS AND DISCUSSION

Fifteen hours after stress, IF images showed significant increase in HSP-70 expression (Fig. 2) in all stressed samples compared to the control. The combined thermal and shear stress samples had a slightly higher HSP70 expression than that of single stress samples. The amount of HSP70 expression correlates to the degree of stress cells experience, showing that combined stress treatments have a greater effect on cells. Due to the role of HSP-70 in protein re-folding, apoptosis inhibition, and cell survival after stress exposure, the data suggests the importance of HSP-70 in protecting cells after stress conditioning.

On Day 6, all stressed samples had higher levels of ALP activity than the control (Fig. 3). Cells exposed to combined thermal and shear stress had a slightly higher ALP activity than individually stressed samples. Since ALP is an early stage marker for osteoblastic differentiation and an important enzyme involved in bone development, this suggests an improved osteogenic response from cells.

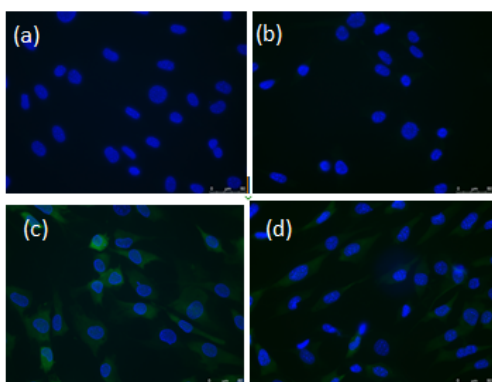


Figure 2: Immunofluorescent staining of HSP70 expression 15 hr after (a) no stress, (b) thermal stress, (c) shear stress, and (d) combined shear and thermal stress. Cell nuclei stained with DAPI (blue) and HSP70 stained with Dylight 488 (scale bar = 50um).

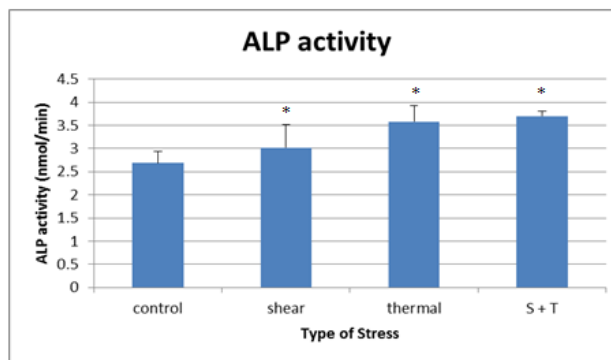


Figure 3: ALP activity on day 6 of culture after cells were exposed to stress conditioning. Asterisk (*) indicates significance difference between control and stressed groups.

CONCLUSIONS

This study investigates whether conditioning cells with a combination of shear and thermal stress may lead to an enhanced osteogenic response. Thermal and shear stress caused an increase in HSP70 production, with slightly higher expression seen with combined stress treatments. HSP70 is an important protein involved in repairing cells after exposure to sub-lethal stress and is important in regulating cell proliferation, ECM production, and cell survival. Combined stress slightly increased ALP activity compared to individual stress. This data suggests the potential of combinatorial thermal and shear stress treatments to stimulate an enhanced osteogenic response. With further investigation, this study will be useful in developing combined stress preconditioning protocols that can produce suitable bone tissue engineered constructs capable of improving bone regeneration in bone defects.

ACKNOWLEDGMENTS

The authors would like to thank the National Science Foundation (CBET 0966546) for funding.

REFERENCES

- [1] Dimitriou R et al (2011) "Bone regeneration: current concepts and future directions." *BMC Medicine* 9:66.
- [2] Kreke et al. (2008) "Effect of Intermittent shear stress on mechanotransductive signaling and osteoblastic differentiation of bone marrow stromal cells." *Tissue Engineering, Part A* 14, 529-537.
- [3] Chung E et al (2011) "Response of preosteoblasts to thermal stress conditioning and osteoinductive growth factors." *Cell Stress and Chaperones* 16 (6).

MECHANICS OF COLLAGEN TYPE I AND ITS CROSSLINKS

Albert L. Kwansa¹, Raffaella De Vita^{1,2}, and Joseph W. Freeman³

1. Virginia Tech-Wake Forest University, School of Biomedical Engineering and Sciences
 2. Virginia Polytechnic Institute and State University, Dept. of Engineering Science and Mechanics
 3. Rutgers University, Dept. of Biomedical Engineering
- Corresponding Author: Albert L. Kwansa, Email: alkwansa@vt.edu

INTRODUCTION

Collagens are extracellular matrix (ECM) proteins found in vertebrates and invertebrates. Collagens are especially abundant in mammals, often comprising up to one-third of total body protein (Williams, 1978). There are ~27 different types of collagens that have been identified; they are often categorized as fibril-forming, network-forming, and fibril-associated collagens (von der Mark, 2006).

Type I collagen is the most prevalent; it is a fibril-forming collagen found in tissues such as tendon, ligament, bone, and skin. Type I collagen functions to provide tensile strength, and it serves as a biological scaffold for cells and other ECM components (Sweeney *et al.*, 2008). The strength of type I collagen and other fibrillar collagens has been attributed to their molecular structure (~300-nm-long molecule composed of three amino acid chains twisted into a right-handed triple helix), their assembly into fibrillar structures, and their inter-molecular covalent bonds called crosslinks. There are several types of collagen crosslinks, and their prevalence is tissue-specific and dependent upon factors such as age, nutrition, and health. These crosslinks are often classified as divalent or trivalent (i.e., joining two or three amino acids, respectively) (Eyre & Wu, 2005).

There are certain connective tissue disorders that have been associated with improper crosslinking, namely, Ehlers-Danlos syndrome (EDS) type 6A, Bruck syndrome type 2, Cutis laxa type 4, and scleroderma. Most of these disorders appear to have a genetic basis leading to an altered expression or activity of enzymes that are directly or indirectly involved in the formation of collagen crosslinks. These disorders can cause symptoms such as fragile skin and eyes (EDS), brittle bones and stiff joints (Bruck syndrome), loose and inelastic skin (Cutis laxa),

and overly stiff skin (scleroderma) (Eyre *et al.*, 1984; Ishikawa *et al.*, 1998; van der Slot *et al.*, 2003).

Techniques and models have been developed within the last ~10 years to characterize and model collagen molecules (e.g., optical tweezers and molecular dynamics (MD)); to model microfibrils (e.g., MD and finite element models); and to characterize and model single fibrils (e.g., atomic force microscopy (AFM), microelectromechanical systems (MEMS), Kelvin-Voigt models, and mesoscopic models). However, models of crosslinked collagen type I have, thus far, treated the crosslinks generally (i.e., without distinguishing between crosslink types). Thus, we sought to model different crosslink types and to develop a model to predict the mechanical behavior of a single fibril while accounting for different crosslink types.

METHODOLOGY

Atomistic molecular models of microfibril units (~65-nm-long) were constructed, using the computer programs VMD (Humphrey *et al.*, 1996) and Discovery Studio (Accelrys Software, Inc., 2011), based on x-ray diffraction literature data (Berisio *et al.*, 2002; Fraser *et al.*, 1983; Orgel *et al.*, 2006). The NAMD code (Phillips *et al.*, 2005) was then used with the CHARMM all-atom force field (Accelrys Software, Inc., 2011) to conduct energy minimization, heating to 293.15 K, and equilibration at this simulated temperature for 10 ns.

A technique called moving constraints was used to fix 12 or three alpha carbon ($C\alpha$) atoms at one side (e.g., C- or N-end) and to pull 12 $C\alpha$ atoms at the opposite side at a constant velocity (100 down to 6.25 m/s). The resulting strain energy-extension data, at 6.25 m/s, were used to derive nominal stress-strain data for making predictions at the fibril level by modeling microfibril units in series into sub-fibrils and sub-fibrils in parallel into a fibril. Nominal strain was defined as the change in length over the initial

length; and nominal stress as the derivative of strain energy (i.e., force) over the initial cross-sectional area. Then low- and high-strain tensile moduli were calculated.

RESULTS

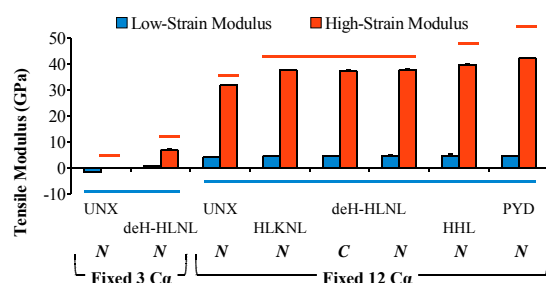


Figure 1: Low- and high-strain tensile moduli for our microfibril unit molecular models (mean + s.d., $n = 3$). “N” and “C” denote the pulling directions. The horizontal bars indicate results from Student's t-tests with Bonferroni correction using $\alpha = 0.0018$ (0.05 divided by 28 t-tests).

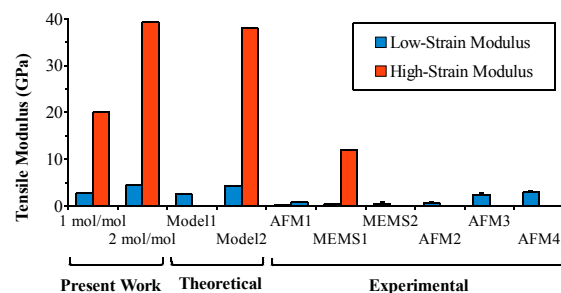


Figure 2: Low- and high-strain tensile moduli for our fibril model (at 1 and 2 moles of crosslink per mole of collagen) with literature data, which includes Model1 (Kelvin-Voigt model), Model2 (2-D mesoscopic model at 2 mol/mol), AFM1 and AFM2 (bovine Achilles tendon), MEMS1 and MEMS2 (sea cucumber dermis), AFM3 (deer antler bone), and AFM4 (human patellar tendon).

DISCUSSION

Fig. 1 shows that crosslink type affected the high-strain moduli, but not the low-strain moduli. The uncrosslinked (UNX) model displayed the lowest high-strain modulus, followed by the divalent crosslinks (HLKLN and deH-HLNL), the trivalent HHL crosslink, and the trivalent PYD crosslink; these differences are likely due to their chemical structures. HLKLN and deH-HLNL involve the joining of two amino acids leading to a carbon-nitrogen single bond and double bond, respectively (i.e., both are linear, unbranched crosslinks). The trivalent HHL crosslink involves the addition of a third amino acid to deH-HLNL leading to a branched crosslink with single bonds around an sp^3 carbon, while the trivalent PYD crosslink involves the addition of a third amino acid to HLKLN leading to a six-membered, aromatic ring structure (i.e., a more stable, branched crosslink with

several partial double bonds). It is interesting to note that HHL is found in skin and cornea, while PYD is present in stiffer tissues such as bone, tendon, and ligament.

Fig. 2 shows our fibril data. Experimental literature data shows low-strain moduli in the range of 0.25 to 2.89 GPa; our data at 1 mol/mol (2.74 GPa) and 2 mol/mol (4.49 GPa) are ~1 to 11x and 1.6 to 18x greater. Literature data shows high-strain moduli at 12 GPa (experimental) and 38 GPa (theoretical), while our model predicts 20 and 39 GPa at 1 and 2 mol/mol, respectively. Thus, our data is in good agreement with some literature data, but exceeds other literature data by up to an order of magnitude.

CONCLUSIONS

Only the tensile modulus was predicted and compared here; other deformations were not considered. Further, our model is not yet able to account for covalent bond failure and is thus unable to model yield and failure. There are several assumptions that can be addressed, in future work, to refine and expand the model. This model could then aid the prediction of fibril mechanics while accounting for the density of specific crosslink types.

ACKNOWLEDGMENTS

We acknowledge the Virginia Tech ESM Dept. and VT-ARC for granting access to their computing clusters; the NASA JPPF and NIH VT-IMSD programs for graduate support; and the NSF's CBET for research funding.

REFERENCES

- Accelrys Software, Inc. 2011. Discovery Studio.
- Berisio, R. *et al.* 2002. *Protein Sci*, **11**:p 262.
- Eyre, D.R. *et al.* 1984. *Ann Rev Biochem*, **53**:p 717.
- Eyre, D.R. & Wu, J.-J. 2005. In *Collagen* (editors: J. Brinckmann *et al.*). **247**:p 207.
- Fraser, R.D. *et al.* 1983. *J Mol Biol*, **167**:p 497.
- Humphrey, W. *et al.* 1996. *J Mol Graphics*, **25**:p 33.
- Ishikawa, O. *et al.* 1998. *Arthritis Rheum*, **41**:p 376.
- Orgel, J.P. *et al.* 2006. *PNAS*, **103**:p 9001.
- Phillips, J.C. *et al.* 2005. *J Comput Chem*, **26**:p 1781.
- Sweeney, S.M. *et al.* 2008. *J Biol Chem*, **283**:p 21187.
- van der Slot, A.J. *et al.* 2003. *J Biol Chem*, **278**:p 40967.
- von der Mark, K. 2006. In *Dynamics of Bone and Cartilage Metabolism* (editors: M.J. Seibel *et al.*). p 4.
- Williams, A.P. 1978. *J Agr Sci*, **90**:p 617.
- Fig. 2** (Model1-2, MEMS1-2, and AFM1-4):
- Gautieri, A. *et al.* 2012. *Matrix Biol*, **31**:p 141.
- Buehler, M.J. 2008. *J Mech Behav Biomed*, **1**:p 59.
- Eppell, S.J. *et al.* 2006. *J R Soc Interface*, **3**:p 117.
- Shen, Z.L. *et al.* 2010. *Biophys J*, **99**:p 1986.
- van der Rijt, J.A.J. *et al.* 2006. *Macromol Biosci*, **6**:p 697.
- Yang, L. *et al.* 2012. *J Mech Behav Biomed*, **6**:p 148.
- Hang, F. & Barber A.H., 2011. *J R Soc Interface*, **8**:p 500.
- Svensson, R.B. *et al.* 2010. *Biophys J*, **99**:p 4020.

THREE DIMENSIONAL *IN VITRO* TUMOR MODEL TO STUDY FOLIC ACID CONJUGATED CELLULOSE NANOCRYSTALS BINDING AND UPTAKE ABILITY TO FOLATE RECEPTOR POSITIVE CANCER CELLS

Alexander L. Callo¹, Katelyn R. Colacino², Shuping Dong³, Maren Roman³, Yong Woo Lee^{2,4}

1. Virginia Tech, Department of Biology and Biochemistry, Blacksburg, VA 24061
 2. Virginia Tech-Wake Forest University, School of Biomedical Engineering and Sciences, Blacksburg, VA 24061
 3. Virginia Tech, Macromolecules and Interfaces Institute and Department of Sustainable Biomaterials, Blacksburg, VA 24061
 4. Virginia Tech, Department of Biomedical Sciences and Pathobiology, Blacksburg, VA 24061
- Corresponding Author: Katelyn R. Colacino, colacino@vt.edu

INTRODUCTION

Type I collagen hydrogels are currently used as effective biomimetic scaffolds for tumor growth and proliferation. Their accessibility, biocompatibility, and non-toxicity render them appropriate as representations of the tumor extracellular matrix¹. In addition to their compatibility with cancer cells, collagen hydrogels also accurately depict the pre-vascularized tumor matrix with regards to stiffness, structure, and remodeling potential leading to proliferation, migration, and infiltration². Their biggest attraction is the fact that they present 3-D *in vitro* models, better depicting cell growth and response to external stimuli³.

Prior studies have noted that cellulose nanocrystals (CNCs) conjugated with folic acid (CNC-FA) potentiate irreversible electroporation (IRE) in cell monolayers (i.e. 2-D tumor models), causing greater cell death after exposure to an electric field (publication in review). The present study is designed to optimize various parameters such that the hydrogels best mimic the tumor microenvironment, while also testing CNC-FA diffusion across the hydrogel such that we can ensure CNC binding/uptake to cells for future IRE treatments.

METHODOLOGY

Folate receptor (FR) positive MDA-MB-468 breast cancer cells were purchased from American Type Culture Collection (ATCC) and were cultured in folate free RPMI 1640 growth medium. Collagen was extracted from frozen rat tails and isolated using acid separation,

lyophilization, and chloroform sterilization. Lastly, CNCs were isolated from wood pulp using sulfuric acid hydrolysis, and then followed by folic acid and FITC conjugation⁴. The hydrogel concentrations were 5 mg/mL, prepared with appropriate amounts of Dulbecco's Modified Eagle Medium (DMEM), distilled water, and sodium hydroxide³. Cell containing hydrogels were incubated at 37°C, in 5% CO₂ with folate-free RPMI 1640 growth media. Parameters optimized included hydrogel thickness, cell density, and cell incubation time. To optimize hydrogel thickness, the diameter of each hydrogel was fixed to 5 mm and four volumes were tested: 150, 185, 200, and 235 μ L. After 3 days, the hydrogels were fixed and stained with cleaved caspase-3 to determine percentage of cell apoptosis. Nuclei were stained with ProLong Gold Antifade Reagent with DAPI. Hydrogels were viewed in layers using a Leica DMI 6000 fluorescent microscope. Three cell densities were tested: 5, 10, and 20 million cells/mL. After 1 day, each of the 200 μ L hydrogels were fixed and embedded in paraffin. 10 μ m cross sections of the hydrogels were stained for cleaved caspase-3, mounted with mounting medium containing DAPI, and imaged under the Leica DMI 6000 fluorescent microscope. The third parameter optimized was the incubation period, in which cells were incubated within 200 μ L hydrogel solutions for 1, 2, and 3 days in a 10 million cells/mL density. The hydrogel was fixed, paraffin embedded, and cross-sectioned. Sections were stained for cleaved caspase-3, mounted with mounting medium containing DAPI, and imaged in the abovementioned manner. Lastly, MDA-MB-468 containing hydrogels were treated with 10 μ g/mL of

FITC-CNC-FA (suspended in folate-free RPMI growth media). These particles were synthesized as previously described by the sulfuric acid hydrolysis of wood pulp, followed by conjugation with folic acid and FITC conjugation steps. After a three day incubation period, the hydrogels were fixed, paraffin embedded, cross-sectioned, stained with Concanavalin A (AlexaFluor) and mounted in mounting medium containing DAPI. Sections were imaged as previously described.

RESULTS AND DISCUSSION

With respect to the hydrogel volume/thickness optimizations, it was noted that the hydrogel with 200 μ L of solution clearly contained the most viable cells with the most notable proliferative properties. A ten-million cell/mL density was also seen as ideal, both in terms of confluency within the hydrogel and with the smallest ratio of cell death/life. In regards to incubation period, the 3-day option was chosen, seeing as cell-to-cell adhesion and more a natural proliferation were observed, thus better

mimicking the tumor microenvironment. After optimizing the nanoparticle-independent parameters, FITC-CNC-FA diffusion through the gel was imaged, and its binding to the folate-receptor rich cells was overlaid onto the DAPI nucleus staining Figure 1.

CONCLUSIONS

Future studies involving cancer cell manipulation on a collagen type 1 based hydrogel can now be performed. By optimizing cell density, hydrogel width, and incubation period of the cells on the 3-D tumor model, the cells' properties are now more reflective of *in vivo* characteristics, leading to more effective observational studies and drug development. Combining these parameter optimizations with the fact that CNC-FA is noted to freely diffuse through the hydrogels, our lab can now move forward in observing the potentiating effect of irreversible electroporation (IRE) on cells incubated with CNC-FA while seeded on a 3-D hydrogel scaffold.

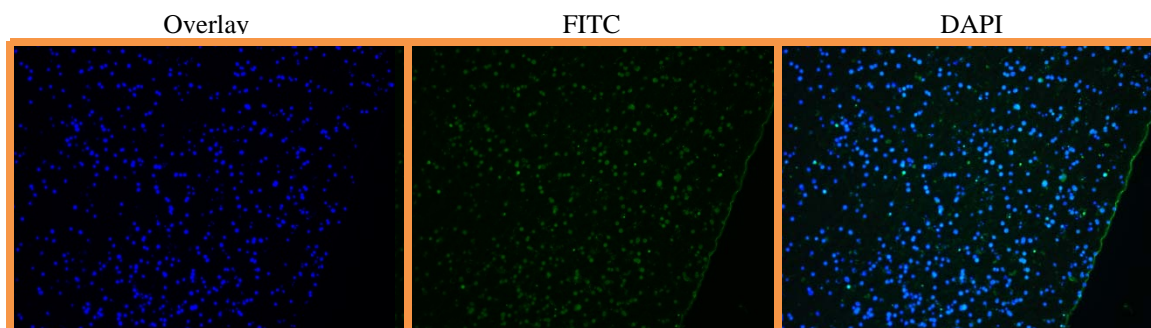


Figure 1: Uptake/binding of FITC-CNC-FA to MDA-MB-468 cells in 3-D hydrogel tumor model.

ACKNOWLEDGEMENTS

This work was supported by Virginia Tech's Institute for Critical Technology and Applied Science (ICTAS) and the National Science Foundation (DMR0907567). Another special thanks to Katherine Prokop for isolating the collagen.

REFERENCES

1. Raeber, G.P., et al., *Biophys J*, 2005. **89**(2)
2. Lee, C.H., et al., *Int J Pharm*, 2001. **221**(1-2)
3. Szot, C.S., et al., *Biomaterials*, 2011. **32**(31)
4. Roman, M., et al., *Cellulose Nanocrystals for Drug Delivery*. 2009. p. 81-89.

AGE-RELATED CHANGES TO SHOULDER MUSCULATURE IN A VERVET MONKEY MODEL

Anthony C. Santago II^{1,2}, Johannes F. Plate¹, Thomas L. Smith¹, Katherine R. Saul^{1,2}

1. Wake Forest School of Medicine, Winston-Salem, NC

2. Virginia Tech – Wake Forest School of Biomedical Engineering and Sciences

Corresponding Author: Anthony C. Santago, Email: asantag@wakehealth.edu

INTRODUCTION

Age-related changes to muscle tissue are well documented and include losses of mass and force as well as slowed shortening velocity [1]. In the upper limb, aging is also associated with reduced strength [2], rotator cuff tears, and arthritic changes. Characterizing the pathophysiology and progression of age-related changes to the upper extremity would help advance orthopaedic treatments to retain and improve function. An animal model of aging in the upper extremity would allow for longitudinal studies of musculoskeletal degradation that are difficult or expensive to perform in a human population. Additionally, animals are housed in a well-regulated environment, are more homogenous, and are easier to control than humans [3].

Non-human primates may be superior to other large animal models because their anatomical shoulder structure and functional use of the arm are more similar to those of humans [4]. Previous work in elderly vervet monkeys (*Chlorocebus pygerythrus*) demonstrated degenerative changes of the glenoid and more retroversion similar to changes observed in an older adult human population [5]. Additionally, the supraspinatus demonstrated decreased muscle fiber cross-sectional area which is consistent with aging humans. [5]. However, age-related changes in muscle architecture have not been studied in vervet monkeys. Therefore, the purpose of this pilot study was to quantify age-related changes to the rotator cuff and deltoid muscle architecture in a group of vervet monkeys.

METHODOLOGY

The right upper limb of two middle aged vervets, MA1 and MA2, (11.6 and 9.3 years; approximately 44 and 35 human years, respectively) and two older adult vervets,

OA1 and OA2 (21.3 and 25.6 years; approximately 80 and 96 human years, respectively) were obtained from a previously-studied population of vervets [5]. Each limb was thawed, skinned, and fixed in 10% phosphate buffered formalin for 24 hours in a neutral shoulder and wrist posture with 90° of elbow flexion. The limb was then removed from formalin and placed in a 70% ethanol solution for a minimum of 24 hours to preserve the fixation and remove any excess formalin. The four rotator cuff muscles (supraspinatus, infraspinatus, subscapularis, teres minor) and the deltoid were dissected from the shoulder. Muscle belly length was measured using calipers from the most proximal end of the muscle fibers to the most distal end of the muscle fibers. Muscle volume was measured by placing the muscles in ethanol and measuring the displacement. Care was taken to remove all fascia and tendinous structures prior to volume and mass measurements. Infraspinatus, subscapularis, and deltoid were divided into subsections for mass, volume, and length measurements according to previous descriptions of muscle architecture [6]. For the muscles with multiple subsections, total volume was determined by adding the volume of the subsections, and average muscle belly length was calculated as the mean of the lengths of each subsection. A representative cross-sectional area of each muscle was determined by dividing volume by muscle belly length [7]. To determine muscle volume distribution, the volume fraction of the rotator cuff muscles and deltoid were calculated as a percentage of the total rotator cuff volume.

RESULTS AND DISCUSSION

The total mass of the rotator cuff muscles in the middle aged vervets, MA1 and MA2, was 42.24 and 32.10 grams, respectively; by comparison, the total rotator cuff mass of the older adult vervets, OA1 and OA2, was lower, at 30.89 and 26.92 grams, respectively. No evidence of

rotator cuff tears was found during dissection for any of the vervet upper extremities, consistent with a previous study of the contralateral shoulders of these same animals [5].

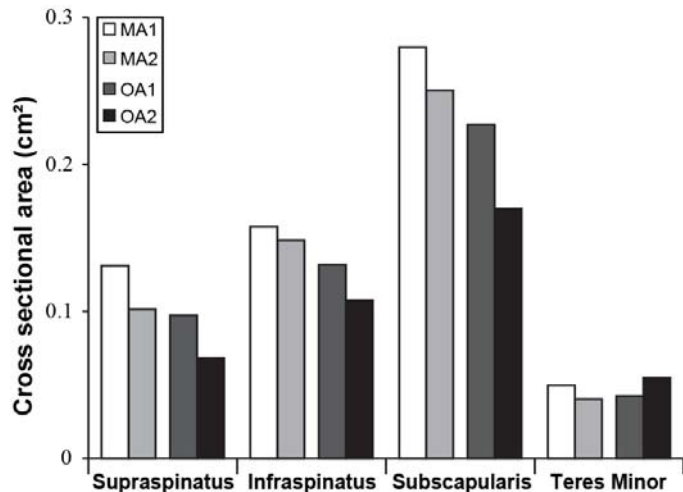


Figure 1: Cross-sectional area of rotator cuff muscles. The middle aged vervets had a larger cross-sectional area than the older adult vervets in the supraspinatus, infraspinatus and subscapularis.

With the exception of teres minor, the rotator cuff muscles of the older adult vervets had a smaller average cross-sectional area (Figure 1). Cross-sectional area is correlated with strength in human subjects and decreases with increasing age [10]. The observed reduced mass and cross-section in the older vervets warrants confirmation in a larger cohort of vervets.

Although our data set is small, our preliminary findings indicated similar muscle volume distributions in both middle-aged and old vervets (Figure 2). These findings are consistent with human data that demonstrated no difference in rotator cuff muscle volume distribution between young adult and older adult humans [2, 7]. However, the supraspinatus volume fraction is smaller in humans than in this vervet group. Additionally, the deltoid volume fraction is larger in humans than in this vervet group. The supraspinatus acts a dynamic stabilizer in both humans and vervets [9], while the deltoid, an abductor, can contribute to superior translation of the humeral head and increase load on the supraspinatus [8]. Therefore, the relatively smaller deltoid and larger supraspinatus in these vervets may be associated with reduced loads on the supraspinatus muscle-tendon unit, which could explain the lack of rotator cuff tears seen in these vervets.

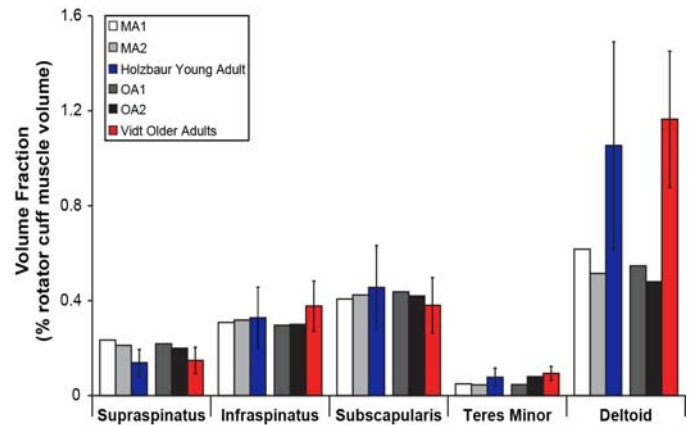


Figure 2: Volume fractions of the rotator cuff muscles and deltoid. Volume fractions of the supraspinatus and deltoid are smaller and larger, respectively, in humans than in the vervet subjects.

CONCLUSIONS

Our pilot data indicate that rotator cuff and deltoid muscles in vervet monkeys have reduced mass and cross-sectional area with increasing age. Additionally, our preliminary data did not provide evidence that the distribution of muscle mass in the rotator cuff and deltoid muscles change with age, which is consistent with aging in the human shoulder. However, the relative size differences between the supraspinatus and deltoid in humans and vervets may limit the vervet as a model to study rotator cuff tears. Future work will evaluate these and other structural parameters (such as optimal fiber length and PCSA) in a larger cohort of vervet monkeys, and will include analysis of the biceps, triceps, coracobrachialis, and teres major muscles.

REFERENCES

1. Choi S, et al. *J Gerontol A Biol Sci Med Sci*, **68**, 258-67, 2013.
2. Vidt M, et al. *J Biomech*, **45**, 334-41, 2012.
3. Lui PP, et al. *Scan J Med Sci Sports*, **21**, 3-17, 2011
4. Mannava S and Plate J, et al. *KSSTA*, doi:10.1007/s00167-012-2145-9.
5. Plate J, et al. *J Shoulder Elbow Surg*, doi: 10.1016/j.jse.2012.11.004.
6. Langenderfer J, et al. *Clin Biom*, **19**, 664-70, 2004.
7. Holzbaur K, et al. *J Biomech*, **40**, 742-49, 2007.
8. Potau J, et al. *Int J Primatol*, **30**, 697-708, 2009.
9. Larson S and Stern J, *Am J Phys Anthropol*, **79**, 369-77, 1989.
10. Hakkinen A and Hakkinen K. *Eur J Appl Physiol*, **62**, 410-14, 1991.

FEA SIMULATION COMPARISON FOR CRASH TEST MODELING OF FRONTAL IMPACTS USING HYBRID-III ATD

Caitlin M. Weaver¹, Kerry A. Danelson¹, Adam J. Golman¹, and Joel D. Stitzel¹

1. Wake Forest University, School of Biomedical Engineering and Sciences

Corresponding Author: Caitlin M. Weaver, Email: cweaver@wakehealth.edu

INTRODUCTION

Unintentional injuries are the fifth leading cause of death in the United States (U.S.) and motor vehicle crashes are the leading cause of unintentional injury-related death. The human and capital costs of motor vehicle crashes are substantial. In 2009, motor vehicle crashes accounted for approximately 36,000 deaths and 3.5 billion injuries in the U.S. The estimated cost of these injuries was \$244.7 billion.

The purpose of this study is to compare anthropomorphic test device (ATD) data from a real world vehicle crash test to a finite element analysis (FEA) simulation using a FE ATD in a reduced vehicle configuration. The hypothesis was that a reduced vehicle configuration could be created that resulted in comparable occupant kinematics to a full scale crash test. Once a reduced sled development methodology is established, the ATD can be replaced with a human body model and a similar real world crash can be simulated to better understand injury mechanisms.

METHODOLOGY

This analysis uses data from the National Highway Traffic Safety Administration (NHTSA) New Car Assessment Program (NCAP) test number 6750 for a 2010 Toyota Camry. A generic sled buck configuration was used to model the vehicle in the FEA program LS-DYNA (LSTC, Livermore, CA). The ATD used in test 6750 and the FEA ATD model is the 50th percentile male Hybrid-III dummy developed by Humanetics.

The generic sled buck vehicle model used in the FEA is a reduced version of the 2001 Ford Taurus developed by the National Crash Analysis Center (NCAC). The inside

of the vehicle is modeled using a rigid metal floor pan, a simplified instrument panel, the existing driver's seat, the NCAC frontal airbag model, and a foam pad to represent a knee bolster air bag. The seat belt material properties are generic belt properties provided by a belt manufacturer.

To evaluate whether the generic sled buck vehicle model is performing similarly to the vehicle used in the NCAP test, the test ATD and FEA ATD instrumentation outputs for the head, chest and pelvis were compared to evaluate occupant response to the crash. Additionally, the steering column stroke and the seatbelt loads were also measured and compared between the test and the FEA. The sled buck properties modified to match the experimental to the simulation results using a variation study were the seatbelt, frontal airbag, steering column, and knee bolster air bag properties. These parameters were selected because they could not be determined from the existing test data; therefore, they were varied over a range of values until the two occupant response curves matched in phase and magnitude.

RESULTS

As hypothesized, a reduced vehicle configuration was created that resulted in similar occupant loading in the crash test and the simulation. The shoulder and lap belt curves from the simulation have similar phase and magnitude profiles as the curves produced by the seat belt sensor data measured in the test. The curves from the head, chest and pelvis accelerometers in the simulation also showed similar phase and magnitude profiles as the curves measured by the accelerometers in the Hybrid-III used in the test. Figure 1 shows the comparison of measured and simulated head acceleration data. Future work will compare these results to actual vehicle material

properties to validate the reduced sled configuration method proposed.

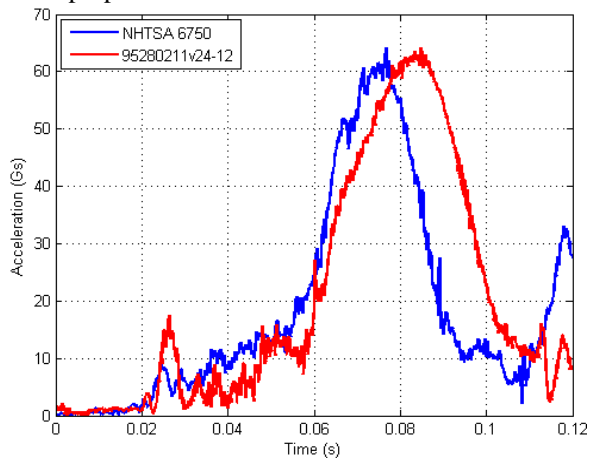


Figure 1. Comparison of test 6750 (in blue) and FEA head accelerations (in red).

CONCLUSIONS

ATD vehicle crash tests are a commonly used method to evaluate vehicle performance. The results of this study demonstrate that the FEA reduced buck configuration could reproduce the results of the real world crash test. The next step will be to use the reduced vehicle configuration with the human body model in a real world crash to better predict the injuries sustained by the human body.

ACKNOWLEDGMENTS

Thank you to Toyota for sponsoring the research conducted in this paper.

REFERENCES

- Injury Facts. National Injury Safety Council. 2011 Edition.
- Hollowell, W.T. et. al. Updated Review of Potential Test Procedures for FMVSS No. 208. Office of Vehicle Safety Research. NHTSA. October 1999.
- NHTSA. Databases and Software. <http://www.nhtsa.gov/Research/Databases+and+Software>

3D INTEGRATED ORGAN PRINTING FOR EAR RECONSTRUCTION

Carlos Kengla^{1,2}, Hyun-Wook Kang¹, Sang Jin Lee^{1,2}

1. Wake Forest Institute for Regenerative Medicine, Winston Salem, NC
 2. School of Biomedical Engineering and Sciences, Wake Forest University and Virginia Tech
- Corresponding Author: Carlos Kengla, Email: ckengla@wakehealth.edu

INTRODUCTION

The elastic auricular cartilage of the outer ear is composed of chondrocytes embedded in an extracellular matrix (ECM) predominated by collagen (type II), elastin, and various glycosaminoglycan macromolecules. Tissue engineered cartilage for outer ear reconstruction has been a pursuit for more than two decades¹. The major hurdle has been the deterioration of any molded shape as the developing tissue contracts and succumbs to surrounding forces². This mode of failure also plagues the standard means of surgical repair, which harvests costal cartilage from the ribs, shapes the pieces, and implants them in place of the ear. The reconstructed ear has several disadvantages including fibrocartilage instead of elastic cartilage and weak structural integrity.

This study seeks to demonstrate the feasibility of using the Integrated Organ Printing platform, developed at the Wake Forest University Institute for Regenerative Medicine, to fabricate a construct able to develop cartilage tissue in a stable 3D shape.

METHODOLOGY

Primary rabbit chondrocytes were isolated from New Zealand White rabbits. Auricular cartilage biopsies were stripped of perichondrium, minced, and serially digested with 0.5mg/ml pronase followed by 3% (v/v) collagenase. Cells were plated and expanded up to passage 2 using growth media composed of DMEM:F12, 10% FBS and 2% antibiotic/antimycotic (A/A).

In vitro constructs consisted of overlapping chondrocyte-laden hydrogel and PCL patterns. The hydrogel consisted of gelatin (30mg/ml), fibrinogen (30mg/ml), hyaluronic acid (3mg/ml), and glycerol (10%v/v) in High Glucose

DMEM with a chondrocyte density of 40M cells/ml. The PCL had a molecular weight of 43-50kDa (Polysciences, Inc). Constructs were printed with the IOP system with either a porous pattern or nonporous pattern. After printing, the fibrinogen was converted to fibrin by thrombin cross-linking with 20u/ml thrombin in PBS for 10 minutes and cultured for one month at 37°C and 5% CO₂ in chondrogenic differentiation media. Chondrogenic media consists of DMEM/F-12 1:1 Modified, TGF-β₃ (10ng/ml), ITS, dexamethasone (10⁻⁷ M), ascorbic acid 2-phosphate (5μg/ml), 1% aprotinin, 1%A/A1.

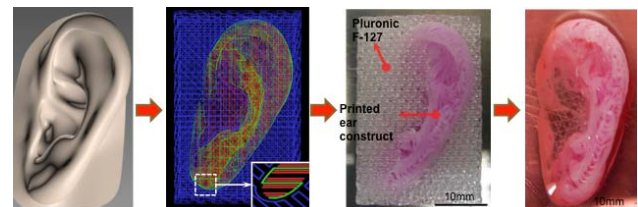


Figure 1: Fabrication process takes 3D imaging data, converts to tool paths for layer-by-layer printing, and produces a cell-laden construct ready for implantation.

In vivo constructs consisted of overlapping chondrocyte-laden hydrogel and PCL patterns. The hydrogel consisted of gelatin (47mg/ml), fibrinogen (30mg/ml), hyaluronic acid (3mg/ml), and glycerol (10%v/v) in High Glucose DMEM with a chondrocyte density of 40M cells/ml. The PCL had a molecular weight of 43-50kDa (Polysciences, Inc). Constructs were printed with the IOP system with a porous pattern. After printing, the fibrinogen was converted to fibrin by thrombin cross-linking with 20u/ml thrombin in PBS for 10 minutes and incubated overnight at 37°C and 5% CO₂ in growth media before implantation.

Dorsal subcutaneous implantation in nude athymic mice followed protocol approved by the Animal Care and Use Committee at Wake Forest Baptist Medical Center. A small subcutaneous pocket was formed through a small incision and two small constructs were implanted or one ear shaped implant was inserted. The incision was closed with sutures, and implants remained for one or two months. Animals were euthanized according to protocol by CO2 asphyxiation followed by cervical dislocation.

RESULTS

Constructs printed for *in vitro* culture were analyzed with Safranin O, Alcian Blue and immunohistochemistry labeling Type II collagen after 1 month of culture in chondrogenic media. The porous construct design demonstrated positive staining for cartilage formation throughout the growing tissue (see Figure 2) while the nonporous design only stained for positive cartilage formation on the construct surface in contact with the media.

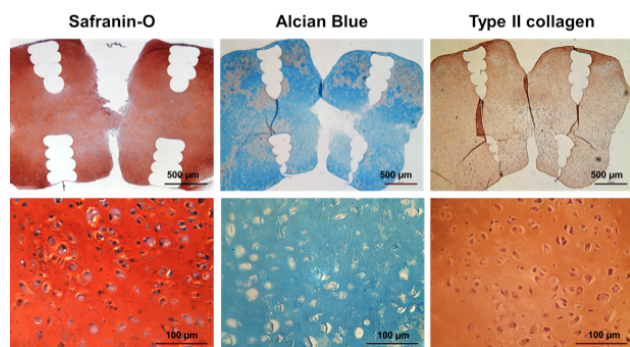


Figure 2: Histological stains show cartilage tissue formation after 1 month *in vitro*. Top: 5x. Bottom: 20x.

Constructs implanted *in vivo* were harvested after one month for analysis by histological staining, immunohistochemistry, and biochemical analysis. Histology demonstrates positive staining by Safranin O and Alcian Blue (see Figure 3), which stain positively charged polysaccharides like aggrecan and chondroitin. Negative controls consisted of polycaprolactone structure alone. Harvested negative control samples showed host tissue infiltration.

Samples were also analyzed with biochemical assay for total concentration of glycosaminoglycans (GAGs). After one month *in vivo*, the GAG concentration approached 50% that of native rabbit auricular cartilage.

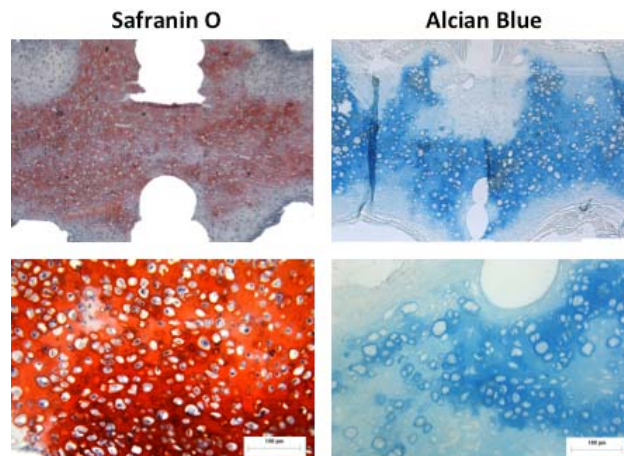


Figure 3: Constructs after 1 month *in vivo* demonstrate positive staining characteristic of cartilage tissue.

CONCLUSIONS

Based on histological findings, this study shows that the IOP platform does indeed allow for the printing of living and productive chondrocytes resulting in the production of cartilaginous tissue. The constructs can be printed in 3D shapes including that of the outer ear.

Future development can optimize the processes for chondrocyte isolation and printing. Important aspects for successful clinical translation will be the optimization of construct architecture, polymeric biomaterial for appropriate degradation time/rate, and reliable cell sources and combinations for cartilage and perichondrium regeneration.

ACKNOWLEDGMENTS

Thanks are due Denethia Green and Cristina Velasquillo for assistance with cell culture and analysis work.

REFERENCES

1. Cao, Y., Vacanti, J. P., Paige, K. T., Upton, J. & Vacanti, C. A. Transplantation of chondrocytes utilizing a polymer-cell construct to produce tissue-engineered cartilage in the shape of a human ear. *Plast. Reconstr. Surg.* **100**, 297–302; discussion 303–304 (1997).
2. Xu, T. *et al.* Hybrid printing of mechanically and biologically improved constructs for cartilage tissue engineering applications. *Biofabrication* **5**, 015001 (2013).

ELECTROPORATION-DELIVERED PROTEIN BIOSENSORS FOR STUDY OF MOLECULAR ACTIVITY

Chen Sun¹, Yi Wang², Yingxiao Wang² and Chang Lu^{1,3}

1. Virginia Tech-Wake Forest University, School of Biomedical Engineering and Sciences

2. University of California, San Diego, Department of Bioengineering

3. Virginia Tech, Department of Chemical Engineering

Corresponding Author: Chang Lu, Email: changlu@vt.edu

INTRODUCTION

Fluorescence resonance energy transfer (FRET) is a mechanism describing energy transfer between two chromophores. FRET-based biosensors have been widely used for visualization of molecular activities in live cells in real time with high spatiotemporal resolution [1, 2]. However, their use is currently limited to genetically modified cell lines created by delivering a plasmid form of biosensor. The genetic encoding requires a sizable cell population for successful transfection and high cell viability and functionality after the procedure for strong gene expression. Besides, the lack of long term and stable expression of FRET biosensor also restricts its use. Such limitations render the application of protein biosensors to rare primary cells impractical [3].

One possible solution to this problem is to deliver biosensor in its protein form into cells via electroporation [4]. Electroporation is the use of an externally electrical field to increase electrical conductivity and permeability of the cell plasma membrane, thus permitting cellular uptake of particles. Electroporation is most commonly used for gene transfer and drug delivery in vitro and in vivo, and several studies also demonstrated its use in protein delivery [5].

In our study, ECPF/YPet paired Src biosensor in its protein form was first produced and then was loaded into cells by electroporation. Src reporter is composed of enhanced cyan fluorescent protein (ECFP), a flexible linker and a variant of yellow fluorescent protein (YPet). FRET effect of the Src reporter can be viewed upon the actions of Src kinase or phosphatase[2]. We were able to monitor Src activity in the cytoplasm with very similar sensitivity and spatial resolution to that obtained with genetic encoding. Src is a protein tyrosine kinase which

plays critical roles in a variety of cellular activities, including cell adhesion, migration and cancer invasion and metastasis [6]. We envision that our biosensor approach will be useful for examining primary cell samples.

METHODOLOGY

PDMS microfluidic channels were fabricated. Mouse embryonic fibroblasts (MEF) or Src/Yes/Fyn triple-knockout (SYF^{-/-}) cells were suspended in electroporation buffer solutions (8 mM Na₂HPO₄, 2mM KH₂PO₄, 1 mM MgSO₄·7H₂O and 250 mM sucrose, pH=7.4). Src reporter (in protein form) was then added into them, followed by pipetting the cell suspension into the reservoir of fibronectin pretreated microfluidic channel. Cells entered the channel due to the gravity and began to settle down on the channel bottom after 10 min. Electroporation was carried out via two platinum electrodes, which were connected to a pulse generator controlled by Labview software (Figure.1). After electroporation, fresh 0.5% FBS cell culture media was then flowed through the devices to wash away excessive

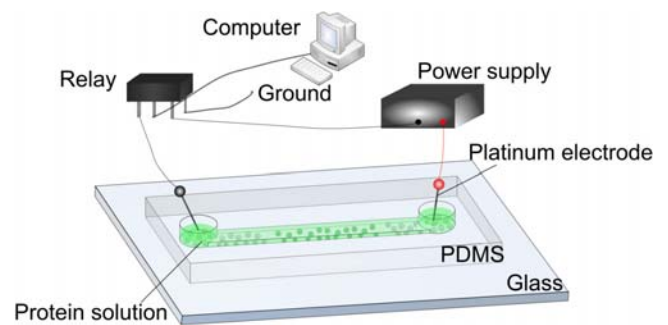


Figure 1: The setup for electroporation-based Src reporter delivery

src reporter and supply nutrients for the cells. Incubate the devices into a humidified, 5% CO₂, 37 °C incubator for 36h before stimulation and observation of the cells using fluorescence microscopy.

RESULTS

As shown in the image of Figure 2, Src reporters have been delivered into cells and significant FRET signal change before and after the treatment of tyrosine phosphatase inhibitor, pervanadate (PVD) has been observed in MEF cells, while no change in SYF^{-/-} cells (with Src knockout). This suggests that electroporation delivered Src reporter (in protein form) closely reflects Src kinase activity in Src⁺ cells. It also indicates the specificity of the Src reporter toward Src in live cells. We studied the ECFP/YPet ratio time course of Src biosensor and found that it had a quick response to stimulation within several minutes and the FRET effect was very stable. We also investigated the dependence of the Src reporter delivery on electroporation parameters. We found that more delivery of Src reporter and lower cell viability occurred with longer duration and stronger field strength. It has also been confirmed that higher delivery efficiency associated with higher concentration of Src reporter in electroporation solution.

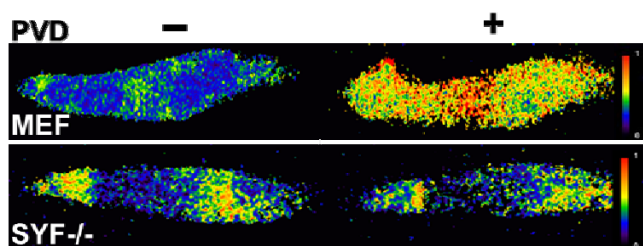


Figure 2: The ECFP/YPet emission ratio images of Src biosensors before and after PVD treatment in MEF and SYF^{-/-} cells.

DISCUSSION

During electroporation the electrical field opens nanoscale pores (or creates instability) in the cell membrane that permit cell uptake of nanoparticles, including proteins. Src reporters enter cells by electroporation and distributed within cytoplasm. The design of the Src reporter allows the juxtaposition of ECFP and YPet to yield a high FRET, so that it emits yellow fluorescence. Upon PVD stimulation, the Src reporter is phosphorylated by Src in vitro, which separates YPet from ECFP and induce the loss of FRET, hence cyan fluorescence increased at the expense of yellow fluorescence protein emission. In this way, the activity of Src within cells can be analyzed by monitoring the fluorescence.

CONCLUSIONS

We successfully delivered Src reporters in their protein form into cells by electroporation, and these Src reporters in Src⁺ cells reveal Src activity in response to PVD stimulation. We also demonstrated that microfluidic platform offers a convenient format for integrating electroporation and fluorescence imaging. Our approach circumvents issues associated with genetic encoding that is typically involved in protein biosensor study.

ACKNOWLEDGMENTS

This work was supported by NSF grants CBET 1016547 and 0967069 (to C.L.) and NIH AI35098 (to A.S.B.).

REFERENCES

1. Wang YX, Botvinick EL, Zhao YH, Berns MW, Usami S, Tsien RY, Chien S: **Visualizing the mechanical activation of Src.** *Nature* 2005, **434**(7036):1040-1045.
2. Ouyang MX, Sun J, Chien S, Wang YX: **Determination of hierarchical relationship of Src and Rac at subcellular locations with FRET biosensors.** *Proceedings of the National Academy of Sciences of the United States of America* 2008, **105**(38):14353-14358.
3. Aoki K, Komatsu N, Hirata E, Kamioka Y, Matsuda M: **Stable expression of FRET biosensors: A new light in cancer research.** *Cancer Science* 2012, **103**(4):614-619.
4. Hahn LHFSK: **Biosensors for Characterizing the Dynamics of Rho Family GTPases in Living Cells.** *Curr Protoc Cell Biol* 2010, **14**(14):1-24.
5. Geng T, Zhan YH, Wang HY, Witting SR, Cornetta KG, Lu C: **Flow-through electroporation based on constant voltage for large-volume transfection of cells.** *J Control Release* 2010, **144**(1):91-100.
6. Martin GS: **The hunting of the Src.** *Nature Reviews Molecular Cell Biology* 2001, **2**(6):467-475.

ANKLE AND KNEE MECHANICS DURING ATHLETIC MANEUVERS IN ADULTS WITH AND WITHOUT ANKLE INSTABILITY

Courtney A. (Haynes) Webster¹, Maury A. Nussbaum, PhD^{1,2}

1. School of Biomedical Engineering and Sciences (Virginia Tech)
2. Grado Department of Industrial and Systems Engineering (Virginia Tech)

Corresponding Author: Courtney A. Webster, Email: chaynes7@vt.edu

INTRODUCTION

Ankle sprains account for nearly 50% of all sports injuries¹ and are the most common injury in running and jumping sports^{1,2}. Of those who sustain an initial sprain injury, ~30-40% will develop chronic ankle instability (CAI)³ which is characterized by repeated sprains to a previously injured ankle and sensations of the ankle “giving way” during activity⁴.

Inversion ankle sprains occur when the ankle is oriented with either excessive plantarflexion or inversion, and the rapid loading caused by ground contact creates an inversion moment about the ankle. If this inversion moment is not sufficiently detected or controlled through voluntary and reflexive actions, sprain injury will result. It is thought that adults with CAI have motor control deficits that impair the ability to recover from and inversion moment resulting in repetitive sprains.

Several studies have employed non-weight bearing or quasi-static methods to investigate the specific deficits responsible for frequent sprains in adults with CAI. Considerably fewer studies, however, have quantified motor control during dynamic or simulated sporting tasks. Additionally, it is well-accepted that running speed directly influences ground reaction force and joint kinematics⁵. Given the relevance of these parameters to ankle sprain injury, it would seem that quantifying kinetics and kinematics could reveal important motor deficits that can't be identified through quasi-static evaluations.

To that end, the goal of this research was to quantify joint mechanics of adults with and without ankle instability during the performance of dynamic athletic maneuvers. It was hypothesized that adults with CAI would exhibit

significant differences in joint kinetics and kinematics that may help to explain their recurrent sprain tendency. Further, these dynamic maneuvers were performed at different speeds to determine whether speed-dependent changes in joint mechanics were consistent between groups.

METHODOLOGY

Participants. Thirteen adults (6 males, 7 females) with a history of ankle sprains and a self-reported perception of ankle instability were recruited to form an unstable (U) ankle test group. Another 13 participants with no history of ankle sprains were recruited to serve as controls (C). Each of the controls was selected to match, at the individual level, to one of the individuals in the U group in terms of age, gender, stature, and body mass. All participants were active (exercising at least 2-3 times/week) and, aside from a history of ankle sprains in the U group, had no current or chronic musculoskeletal problems and no history of lower limb joint surgeries, neuropathies, muscle weakness, or balance disorders. Participants were excluded if they were currently completing physical rehabilitation or if they regularly used ankle tape or bracing. All protocols were reviewed and approved by the Virginia Tech Institutional Review Board, and verbal and written consent were obtained from all participants before completing the study.

Protocols. All participants completed a series of dynamic athletic maneuvers including running strides (Run), jump stops (JS), cut steps (Cut), and shuttle runs (Shuttle) at each of two running speeds: 2.5 m/s and 3.6 m/s. Trials were completed on a linear walkway equipped with a force platform (Model #K20102, Bertec Corp., Columbus, OH). A set of reflective markers were attached to specific anatomical landmarks, and a 6-camera motion capture

system (Vicon MX 1.7.1, Vicon, Oxford, UK) was used to simultaneously collect kinetic and kinematic data for each trial at rates of 2500 and 500 Hz, respectively. After sufficient practice, participants completed 5 trials of each athletic maneuver at each of the two test speeds. A motor-driven belt and pulley system running parallel to the walkway provided visual cues to help control running speed. The sequence in which the running speeds and athletic maneuvers were performed was randomized. All participants wore a standardized model of athletic shoe for all trials.

Dependent Measures. Kinetic and kinematic data were processed and filtered using 4th-order, zero-lag Butterworth filters with cutoff frequencies of 50 and 20 Hz, respectively. Custom Matlab® programs (Math Works, Inc., Natick, MA) were developed to complete 3D inverse dynamics with the filtered kinetic and kinematic data. Specific dependent measures included 3D ankle and knee joint angles at the instant of ground contact (GC) and joint angles, moments, and powers during the landing phase (first 100 ms)⁶ following GC.

Statistical Analyses. Statistics were completed using JMP 10.0 software (SAS Institute Inc., Cary NC). Analyses involved separate 2x2 (group x speed) mixed model ANOVAs for each of the dynamic maneuvers. The restricted maximum likelihood (REML) technique was used for error estimations, and significance was concluded when $p < 0.05$. Where relevant, post-hoc paired comparisons were done using Tukey's Honestly Significant Difference (HSD) and simple effects tests.

RESULTS

Significant group and group x speed interaction effects were obtained for many measures within each maneuver type. A subset of results from the Run and Cut maneuvers are presented here.

Run. There was a significant group x speed interaction effect ($F_{(1,125)} = 4.24, p = 0.04$) on knee flexion angle at GC. At the faster running speed, knee flexion at GC increased by 6.4 deg (~62%) in the U group, but increased by only 4.2° (~44%) in the C group. The U group also showed a small but significant increase ($F_{(1,125)} = 8.91, p = 0.003$) in peak knee flexion angle (2.7°, ~6%) during the landing phase as speed increased.

Cut Step. During the landing phase, the U group coped with the faster running speed by increasing peak knee abduction angle ($F_{(1,121)} = 10.81, p = 0.001$) by 2.5° (~24%) while the C group instead employed more knee external rotation ($F_{(1,121)} = 4.06, p = 0.04$; 3.2°, 26%). As speed increased, peak ankle eversion for the C group remained nearly constant while the U group increased 3-fold ($F_{(1,121)} = 5.05, p = 0.02$) to match the

magnitude of the C group. A similar result was observed at the knee. At the higher speed, the U group increased peak knee abduction moment by 0.88 Nm/kg, to a value comparable to that of the C group. Instead, the C group increased peak knee internal rotation moment ($F_{(1,121)} = 7.02, p = 0.009$; 0.6 Nm/kg, ~55%) as speed increased.

DISCUSSION/CONCLUSIONS

The results of this study support the hypothesis that dynamic maneuvers can be used to identify important group differences in landing mechanics relevant to sprain injury. Regarding the Run trials, the U group exhibited greater knee flexion at GC and deeper peak knee flexion. Increasing knee flexion is thought to be a technique to lessen the impact sustained by the ankle. Additionally, group differences in dorsiflexion moments seem to suggest that, at least at the slower speed, the C group exerted more control over ankle motion than the U group, perhaps to control "foot slap" at the time of ground contact. The cut step maneuver was perhaps the most revealing. Results suggest that adults in the C and U groups address increases in running speed differently. As speed increases, the C group engages more control in the transverse plane as evidenced by increases in knee external rotation angle and knee internal rotation moment. The U group, however, dealt with an increase in speed by increasing knee abduction angle, knee abduction moment, and ankle eversion moments. While these measures at the faster speed are not different than those of the C group, it may be that adults in the U group fail to employ adequate frontal plane control until relatively faster running speeds are reached.

ACKNOWLEDGMENTS

Many thanks to my advisor, Dr. Maury Nussbaum, for all his guidance and helpful feedback in completing this research. Thanks also to Dr. Michael Agnew for his assistance in developing the 3D inverse dynamics analysis programs. Finally, thank you to Dr. Michael Madigan and the students of the Kevin P. Granata Musculoskeletal Biomechanics lab for the use of their lab and their support in my data collection.

REFERENCES

- ¹Waterman BR, et al. (2010) Am J Sports Med 38(4): 197-205.
- ²Hootman JM, et al. (2007) J Athl Train 42(2): 311-319.
- ³Peters JW, et al. (1991) Foot Ankle 12(3): 182-191.
- ⁴Freeman MA. (1965) J Bone Joint Surg Br 47(4): 669-77.
- ⁵Novacheck TF. (1998) Gait Posture 7(1): 77-95.
- ⁶Decker MJ, et al. (2003) Clin Biomech 18(7): 622-669.

SENSITIVITY OF SHOULDER JOINT FORCES TO MUSCLE CHANGES ASSOCIATED WITH BRACHIAL PLEXUS BIRTH PALSY

Dustin L. Crouch¹, Johannes F. Plate¹, Zhongyu Li¹, and Katherine R. Saul²

1. Virginia Tech-Wake Forest School of Biomedical Engineering and Sciences

2. Wake Forest School of Medicine, Department of Biomedical Engineering

3. Wake Forest School of Medicine, Department of Orthopaedic Surgery

Corresponding Author: Dustin L. Crouch, Email: dcrouch@wakehealth.edu

INTRODUCTION

Nearly 1 in 3 children with brachial plexus birth palsy (BPBP) develop shoulder deformity secondary to muscle paralysis [1]. Researchers posit that muscles crossing the shoulder impart a posteriorly-directed force on the glenoid and high shoulder joint moments, leading to posterior humeral head subluxation, glenoid retroversion, and limited abduction and external rotation range of motion (ROM) at the glenohumeral (GH) joint. Muscles may produce these abnormal shoulder forces through two possible mechanisms that have been observed clinically or in models of BPBP. The first mechanism, impaired longitudinal muscle growth, affects paralyzed muscles [2]. Active forces produced by non-paralyzed or reinnervated muscles that oppose paralyzed muscles are thought to contribute to strength imbalance, the second possible mechanism of deformity [3]. However, the extent to which these observed mechanisms occur in muscles crossing the shoulder and are able to alter shoulder forces and produce deformity remains unknown. In this study, we performed a sensitivity analysis to determine which muscles and mechanisms could produce shoulder forces consistent with the progression to deformity following BPBP.

METHODOLOGY

We used a well-tested upper limb musculoskeletal computer model [4] implemented for dynamic simulation [5] in OpenSim [6]. The model was simplified to include five degrees of freedom at the shoulder, elbow, and forearm. Thirty-two linear Hill-type muscle-tendon actuators represented muscles and muscle compartments crossing the shoulder and elbow.

In the model, we simulated impaired longitudinal muscle growth and strength imbalance, two possible mechanisms of shoulder deformity, to determine their potential to produce shoulder forces that are thought to contribute to deformity following BPBP. We simulated impaired longitudinal muscle growth by reducing the optimal fiber length of each muscle crossing the shoulder iteratively by 30%. All muscles were inactive and could generate passive forces only. To simulate strength imbalance, each muscle crossing the shoulder was iteratively activated at 10% of its maximum activation level without changing other muscle properties; all other muscles were inactive and could generate passive forces only.

We evaluated the effect of each iteratively-applied muscle change on shoulder forces. First, we calculated the change in GH bone-on-bone joint force from baseline due to the simulated deformity mechanisms. Muscle forces used to compute GH joint force were calculated with the arm fixed in a neutral posture: full adduction and neutral internal/external shoulder rotation. GH joint force changes were computed in the axial plane, since shoulder deformity occurs in this plane. Additionally, GH joint force changes were normalized to the resting GH joint force of the baseline model. We identified muscles that increased posteriorly-directed GH joint force and thus could contribute to bone deformity following BPBP.

Second, we determined whether deformity mechanisms reduced the ROM of the shoulder. Physiologically, at the limit of ROM, further joint rotation is resisted by opposing joint moments generated by soft tissues surrounding a joint. Therefore, we computed the net muscle-generated shoulder joint moments along three directions of movement: abduction in the frontal plane, external rotation in adduction (elbow flexed to 90°), and passive external rotation in 90° abduction (elbow flexed

to 90°). The ROM limit was the joint angle at which muscle generated joint moments opposed a 34.3 N force applied at the wrist [7]. ROM limits were normalized to the baseline model ROM limits. We identified muscles capable of limiting shoulder abduction and external rotation ROM.

RESULTS

At reduced optimal fiber length, the subscapularis, infraspinatus, and long head of biceps increased GH joint force in the posterior direction (Figure 1). At 10% muscle activation, the infraspinatus, subscapularis, latissimus dorsi, and long head of biceps muscles increased GH joint force in the posterior direction (Figure 2).

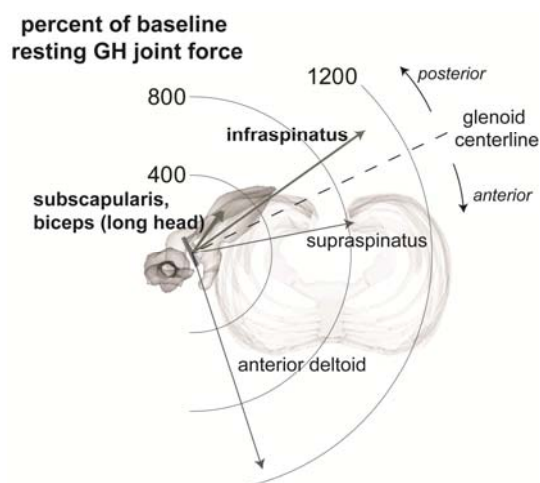


Figure 1: Superior view of the GH joint, superimposed with vectors representing normalized GH joint force changes generated passively by muscles at 30% reduced optimal fiber length.

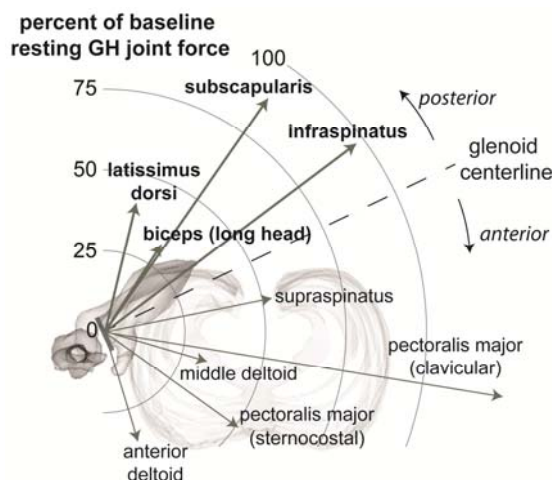


Figure 2: Superior view of the GH joint, superimposed with vectors representing normalized GH joint force changes generated by muscles at 10% activation.

At reduced optimal fiber length, the long head of triceps, anterior deltoid, and subscapularis muscles limited shoulder ROM (Figure 3). Muscles at 10% activation did not limit shoulder ROM.

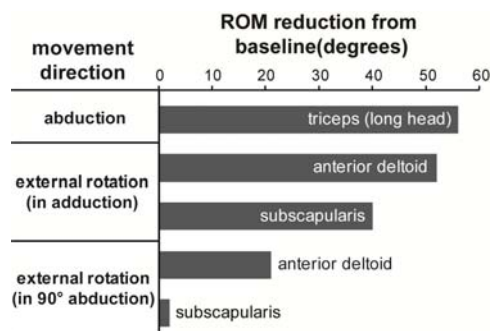


Figure 3: Magnitude of shoulder ROM reduction (in degrees) by muscles at 30% reduced optimal fiber length.

DISCUSSION

When at reduced optimal fiber length, the subscapularis, infraspinatus, long head of biceps, long head of triceps, and anterior deltoid muscles produced GH joint forces that could contribute to shoulder deformity. These muscles are paralyzed in most cases of BPBP [8]; furthermore, the subscapularis and long head of biceps have exhibited impaired longitudinal growth in a murine model of BPBP [2]. When activated, the latissimus dorsi, long head of biceps, subscapularis, and infraspinatus muscles produced GH joint forces that could contribute to shoulder deformity. Whether muscles crossing the shoulder can be activated in children with BPBP depends on the extent of injury and neuromuscular recovery. However, strength imbalance conditions did not progress to shoulder deformity in a murine BPBP model [2].

CONCLUSIONS

Muscles capable of producing shoulder forces consistent with deformity following BPBP may be potentially critical targets for treatments to prevent or alleviate shoulder deformity. Future studies should determine the extent to which the simulated deformity mechanisms occur clinically in patients with BPBP.

REFERENCES

1. Hoeksma AF, et al. *J Bone Joint Surg* **85A**, 316-322, 2003.
2. Nikolaou S, et al. *J Bone Joint Surg* **95A**, 461-470, 2011.
3. Waters PM, et al. *J Bone Joint Surg* **91A**, 2367-2375, 2009.
4. Holzbaur KRS, et al. *Ann Biomed Eng* **33**, 829-840.
5. Daly M. *WFU Graduate School*, Winston-Salem, NC, 2011.
6. Delp SL, et al. *IEEE Trans Biomed Eng* **54**, 1940-1950, 2007.
7. Osbahr DC, et al. *Am J Sports Med* **30**, 347-353, 2002.
8. Lagerkvist, et al. *Dev Med Child Neurol* **52**, 529-534, 2010.

TUBULAR ESOPHAGEAL TISSUE CONSTRUCT BIOENGINEERED FROM ISOLATED ESOPHAGEAL CIRCULAR SMOOTH MUSCLE CELLS

Elie Zakhem^{1,2} and Khalil N. Bitar^{1,2}

1. Wake Forest Institute for Regenerative Medicine, Wake Forest School of Medicine, Winston-Salem NC 27101
 2. Virginia Tech-Wake Forest School of Biomedical Engineering and Sciences, Winston-Salem NC 27101
- Corresponding Author: Khalil N. Bitar, Email: kbitar@wakehealth.edu

INTRODUCTION

The esophagus is a long muscular tube extending from the pharynx to the stomach. It mediates the transport of food to the stomach via a series of coordinated rhythmic peristaltic waves.

Impaired peristaltic function results in esophageal stricture and gastroesophageal reflux disease (GERD). Other forms of disorders include esophageal cancer which is associated with high impact on the quality of life. Treatment of these conditions requires restoration of the gravitational characteristic and the coordinated rhythmic activity of the esophagus.

Current treatments include surgical resection of large parts of the esophagus. This has led to lack of peristalsis followed by dysmotility.

Our objective was to tissue-engineer a tubular esophageal tissue that mimicks the mechanical and physiological function of a native esophagus.

METHODOLOGY

- (1) A 2.5 cm long hollow composite chitosan-collagen scaffold was manufactured using freeze-drying method.
- (2) Cross sections of the lyophilized scaffold were characterized using scanning electron microscopy.
- (3) Several concentrically aligned esophageal circular smooth muscle tissue constructs were bioengineered using collagen hydrogel.
- (4) The bioengineered muscle constructs were placed the composite chitosan scaffold.
- (5) Biodegradable surgical glue was applied between the smooth muscle constructs and along their circumference.

The constructs were maintained around the scaffold in culture.

(6) Liquid and semi-solid materials were pipetted through the lumen of the tube to check for flow, leakage and muscle integrity.

(7) The constructs were taken off and tested for the ability to contract in response to Acetylcholine (Ach) and relax in response to vasoactive intestinal peptide (VIP).

RESULTS

Esophageal smooth muscle cells were cultured on coverslips and supplied with growth medium every other day. The cells were evaluated by immunofluorescence using antibodies to both α -smooth muscle actin and smooth muscle specific heavy caldesmon. Cells stained positive for both markers indicating a population of smooth muscle.

Tubular chitosan scaffolds were synthesized using the freeze-drying method. Chitosan-collagen solution was poured into a cylindrical mold and frozen for 3 hours. The scaffolds were then lyophilized overnight. Scanning electron microscopy of a cross section of the chitosan-collagen scaffold revealed a porous structure with interconnected pores.

Bioengineered circumferential smooth muscle constructs were seeded into collagen gel the cells aligned circumferentially around the post in the center of the plate. At day 7, the bioengineered constructs were placed around the chitosan-collagen tubular scaffold (Figure 1). Surgical glue was applied. The bioengineered 2 cm-long esophageal tube construct, maintained its luminal patency and its structural integrity in vitro for over 1 month.

One end of the scaffold was clamped while the other was left intact. The scaffold, with the tissue constructs around it, expanded while pipetting a liquid then a semi-solid solution through their lumen. The construct was able to restore its original dimensions once the solution was cleared through. No signs of leakage were observed and the tissue constructs did not disrupt due to pressure applied from the semi-solid bolus.

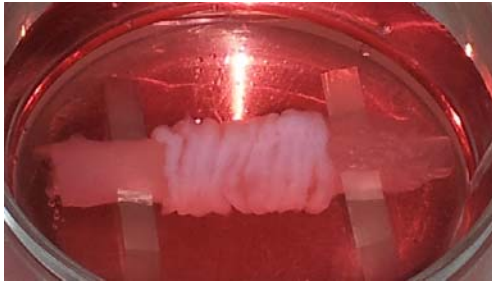


Figure 1: Bioengineered esophageal circular smooth muscle constructs placed around composite chitosan scaffold. Surgical glue was applied between the smooth muscle constructs and along their circumference.

The bioengineered smooth muscle constructs were separated and taken off the scaffold at the end of the study. The construct was immersed in a warm tissue bath and real time force generation was evaluated using force transducer set up. Pharmacologic studies were conducted to test the contractility and relaxation of the constructs.

As the construct established baseline, addition of $1 \mu\text{M}$ of Ach caused a sustained contraction of $45 \mu\text{N}$, after which the construct recovered back to its baseline. The construct was then washed with fresh buffer. As the construct established baseline, treatment with $1 \mu\text{M}$ of VIP caused a relaxation of $-35 \mu\text{N}$. The construct recovered back to its baseline.

CONCLUSIONS

We successfully bioengineered a continuous esophageal tissue construct using a combination of primary isolated circular smooth muscle cells and a biodegradable chitosan scaffold. The smooth muscle constructs were concentrically bioengineered to mimic the alignment of the native circular smooth muscle layer in the esophagus. Alignment of smooth muscle cells is essential for muscle peristaltic function and therefore for the coordination of motility.

The bioengineered tubular construct was able to withstand the pressure of liquid and semi-solid materials pushed through its lumen. The semi-solid material mimicked the texture of a food bolus. This construct could be suitable for esophageal reconstruction.

Our model suggests the potential use of chitosan as a biomaterial. Chitosan can easily form a porous tubular scaffold that can serve as a temporary support for physiologically functional smooth muscle constructs.

ACKNOWLEDGMENTS

This work was supported by NIH/NIDDK RO1 DK042876.

META-ICA REVEALS MEG NETWORKS IN PEDIATRIC SUBJECTS

Elizabeth M. Davenport^{1,2}, Christopher T. Whitlow^{1,3,4}, Alexander K. Powers^{1,5}, Justin B. Rawley^{1,6}, Inna V. McGowin^{1,7}, Greg Alberto¹, Tayler Bungo¹, Dwayne W. Godwin^{1,6}, Megan M. Thompson¹, Jillian E. Urban^{1,2}, Joel D. Stitzel^{1,2}, Joseph A. Maldjian^{1,3}

1. Wake Forest University School of Medicine, Virginia Tech – Wake Forest University School of Biomedical Engineering and Sciences
 2. Wake Forest University School of Medicine, Department of Radiology
 3. Wake Forest University School of Medicine, Translational Science Institute
 4. Wake Forest University School of Medicine, Department of Neurosurgery
 5. Wake Forest University School of Medicine, Department of Neurobiology and Anatomy
 6. Wake Forest University School of Medicine, Department of Physics
- Corresponding Author: Elizabeth M. Davenport, Email: edavenpo@wakehealth.edu

INTRODUCTION

Independent Component Analysis (ICA) can be used to decompose the mixture of signals from recorded Magnetoencephalography (MEG) data into multiple independent components representing networks¹. Meta-ICA is a newly described method to extract networks common across all spectral bands². The purpose of this study is to use Meta-ICA to identify common MEG networks across spectral bands in a group of pediatric subjects.

METHODOLOGY

An institutional ethics committee approved this study. Eight minutes of, eyes open, resting-state MEG data were acquired in 18 normal male subjects aged 16-18 using a 275 channel CTF whole-head system. Structural MRI data for coregistration was obtained on a 3T Siemens Skyra MRI scanner. Using an in-house automated pipeline,

MEG data were baseline corrected, filtered for 60Hz line noise, down-sampled to 100Hz, and band-pass filtered into 5 frequency bands (δ : 0-4Hz, θ : 4-8Hz, α : 8-13Hz, β : 13-30Hz, γ : 30-50Hz). Artifacts from head motion, and muscles were also removed. MEG data was then projected into source space at 5mm resolution using a scalar beamformer with leadfield correction for noise normalization. The Hilbert envelope was computed, and data was down-sampled to 1Hz. This data was then used as the input for Meta-ICA. For each frequency band, the data from each subject was concatenated into a matrix, X, where each row represented a timecourse for a single voxel across all subjects. 25 independent components, S, for each frequency range were estimated from this matrix using FastICA. The 25 estimated components for each frequency range were then concatenated into a matrix where each column represented a single timepoint across all bands and components. 10 independent components, G, were estimated from this matrix using FastICA.

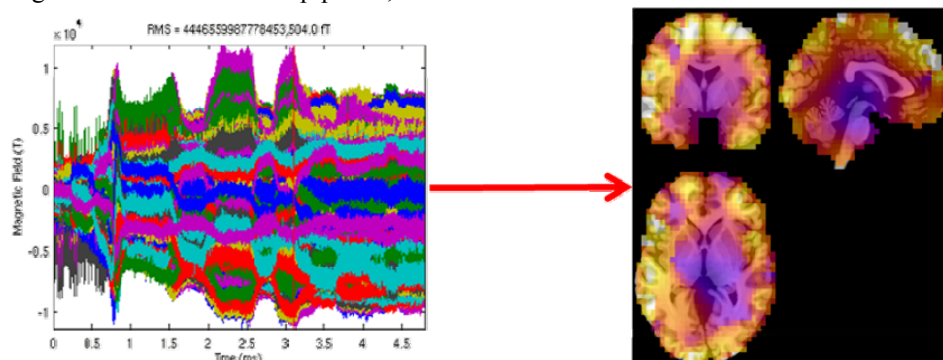


Figure 1: MEG pipeline input (raw data in sensor space) and output (filtered data in MNI space)

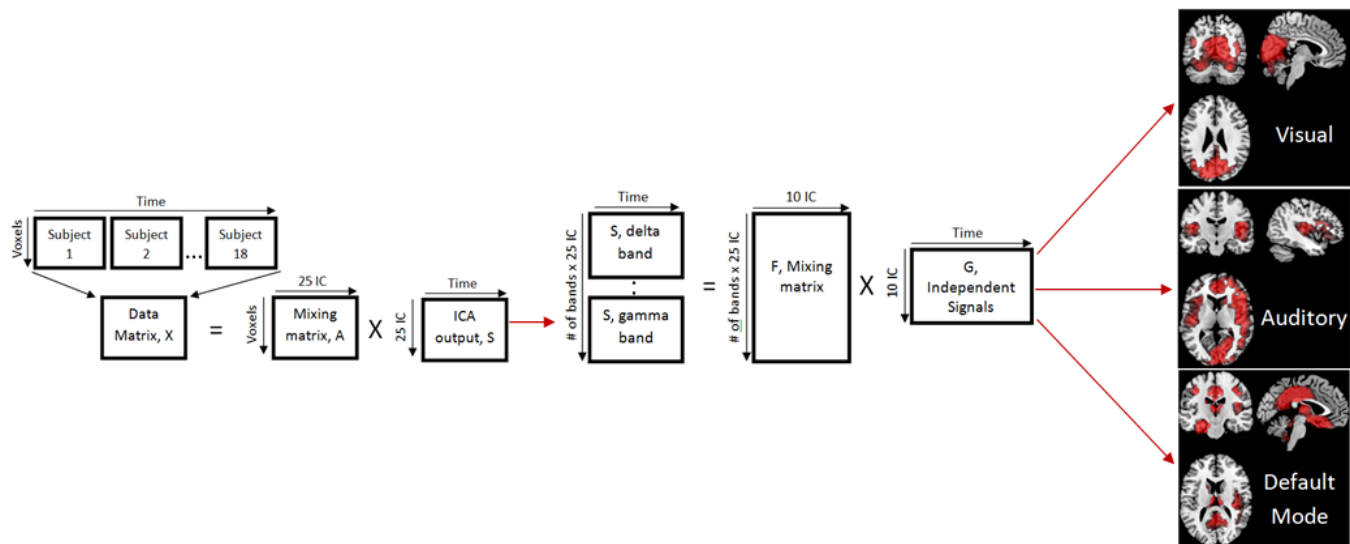


Figure2: Illustration of Meta-ICA pipeline and 3 examples of the 10 output components

RESULTS

Figure 2 demonstrates the spatial representation of 3 of these 10 components, which are representative of all subjects across all bands and time. The components appear to represent portions of the visual, auditory, and default mode networks, in addition to other regions common across spectral bands.

CONCLUSIONS

The application of Meta-ICA analysis to MEG data from pediatric subjects revealed specific networks bearing similarity with those found in other studies of network connectivity. The data demonstrates the utility of Meta-ICA when analyzing MEG data to compare networks in pediatric subjects across spectral bands.

ACKNOWLEDGMENTS

We would like to thank the Childress Institute for Pediatric Trauma and the NSF Graduate Research Fellowship Program for supporting this study and study personnel.

REFERENCES

1. Hyvärinen A, Oja E. Independent component analysis: algorithms and applications. *Neural Netw* 2000;13:411-430
2. Brookes MJ, Liddle EB, Hale JR, et al. Task induced modulation of neural oscillations in electrophysiological brain networks. *NeuroImage* 2012;63:1918-1930

EFFECT OF MULTI-WALLED CARBON NANOTUBES ON BREAST CANCER ADHESION

Elizabeth G. Graham^{1,2} and Nicole H. Levi-Polyachenko²

1. Virginia Tech – Wake Forest School of Biomedical Engineering and Science
 2. Wake Forest Baptist Medical Center, Department of Plastic and Reconstructive Surgery
- Corresponding Author: Elizabeth Graham, Email: elgraham@wakehealth.edu

INTRODUCTION

According to the American Cancer Society, breast cancer is the second leading cause of cancer death in the US. Multi-walled carbon nanotubes (MWNTs) are a unique nanomaterial with interesting electronic and mechanical properties often used for photothermal therapy to eradicate tumors [1]. However, it is known that nanomaterials can affect adhesion, migration, and development of cells [2-4]. Intercellular adhesion determines polarity of cells and allows maintenance of normal tissue architecture and as such, cell adhesion molecules play a significant role in cancer progression and metastasis. It has been extensively documented that downregulation or loss of E-cadherin is correlated with cancer progression and invasiveness [5].

We hypothesize that MWNT will increase adhesion in breast cancer cell lines and offer a secondary mode of cancer treatment in addition to photothermal therapy.

METHODOLOGY

Oxidized MWNTs were added to dilute rat tail collagen type I to create a collagen-MWNT coating with final concentrations of [0, 5, 10, 20, 25, 30, 50, 100] μg MWNT per mL. MCF7, MDA-MB-231, and MCF10A cells were plated and allowed to grow until about 80% confluent. Plates were then sealed and centrifuged upside down for 5 minutes at 50 Gs as described in reference 6. Wells were washed once with phosphate buffered solution and cell viability was then quantified by MTS colorimetric assay. The absorbance values were normalized for the 0 $\mu\text{g}/\text{mL}$ MWNT-collagen control to assess increase in adhesion. Cell viability was also quantified by MTS to investigate cytotoxicity and effect of MWNT-collagen coating on cell proliferation. Western

blot was used to investigate expression of E-cadherin. Statistical analysis was performed by Welch's t-test.

RESULTS AND DISCUSSION

We have found that MWNT-collagen coating increases cell adhesion in breast cancer cell lines, MCF7 and MDA-MB-231, but not in non-cancerous cell line MCF10A. Interestingly, this increase in adhesion appears to peak for both cell lines at 25 $\mu\text{g}/\text{mL}$ (Figure 1). MWNT-collagen does not affect cell viability or proliferation. Western blot demonstrated an increase in E-cadherin that correlates with increased adhesion. As expected, there was no change in expression of E-cadherin across MWNT-collagen coating in MCF10A.

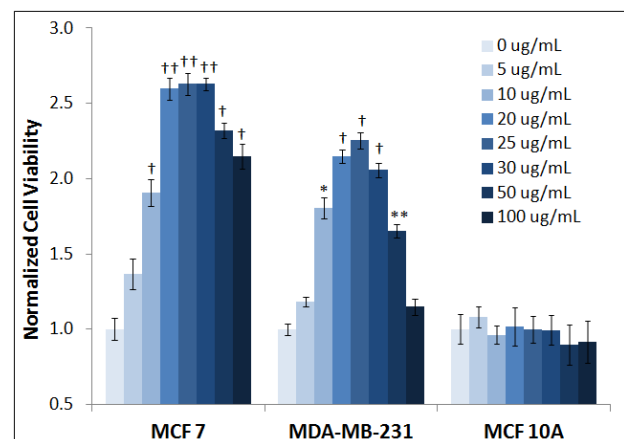


Figure 1: Normalized cell viability visualized by MTS assay after adhesion assay. An increase is seen for both breast cancer cell lines, MCF7 and MDA-MB-231. This increase is not observed for non-cancerous cell line MCF10A. * $p < 0.05$, ** $p < 0.02$, † $p < 0.01$, †† $p < 0.001$

CONCLUSIONS

Breast cancer cells grown on MWNT-collagen coated surface display increased adhesion and increased E-cadherin. This suggests an alternative modality of cancer treatment for MWNTs by inhibiting cancer cell mobility.

ACKNOWLEDGMENTS

I would like to thank Wake Forest's Department of Plastic and Reconstructive Surgery for the generous funding and resources made available for this research.

REFERENCES

1. Burke, A., et al., *PNAS*, 2009. 106(31): p. 12897-12902.
2. Jin, G.Z., et al., *Cell Biol Int*, 2011. 35(7): p. 741-745.
3. Jin, G.Z., et al., *Neurosci Lett*, 2011. 501(1): p. 10-4.
4. Beduer, A., et al., *Langmuir*, 2012. 28(50): p. 17363-17371.
5. Cowin, P., et al., *Curr Opin Cell Biol*, 2005. 17(5): p. 499-508.
6. Reyes, C.D., et al., *J Biomed Mater Res A*, 2003. 67(1): p. 328-333.

ESTIMATION OF SKULL TABLE THICKNESS FROM CLINICAL CT

Elizabeth M. Lillie^{1,2}, Jillian E. Urban^{1,2}, Ashley A. Weaver^{1,2}, and Joel D. Stitzel^{1,2}

1. Wake Forest University School of Medicine, Medical Center Blvd, Winston-Salem, NC 27157
 2. Virginia Tech - Wake Forest University Center for Injury Biomechanics
- Corresponding Author: Elizabeth Lillie, Email: elillie@wakehealth.edu

INTRODUCTION

In the United States traumatic brain injuries contributed to 30.5% of all injury related deaths from 2002 to 2006 [1]. The human cranial vault serves as the main mechanism of protection for the brain from these contact injuries. Despite the important role the skull plays in protecting the cranium, more needs to be known about its anatomy. Cortical thickness of bone is difficult to quantify due to the resolution limitation on clinical computed tomography (CT) scans. Thickness measurements of structures thinner than 3 mm are overestimated using the standard full width half max (FWHM) technique [2]. A better understanding of the physical properties of the skull would provide further insight into the mechanism of head injury. In this paper we present a technique that has been adapted from Treece et al to accurately interpret cranial vault cortical thickness from clinical CT scans [3]. With a large repository of clinical CT scans it would be advantageous to be able to evaluate thickness variations across the population by age and skull location.

METHODOLOGY

Two male cadavers (age 49 and 56) were used to evaluate the cortical thickness of the skull. Clinical CT scans of the head were collected at 0.625 mm isometric resolution for both specimens (GE 64-slice PET/CT Discovery VCT Scanner, Center for Biomolecular Imaging, Wake Forest University). The skulls were removed using a surgical saw at the base of the foramen magnum and cleaned by removing all skin and soft tissue.

One inch diameter sections of the skull were collected using neurosurgical equipment. These samples were then scanned using a GE CT-120 CT scanner (Biomedical Research Imaging Center, University of North Carolina at

Chapel Hill) to evaluate the actual cortical thickness. The scans were collected at 25 micron resolution with isometric voxels and reconstructed at a 50 micron resolution. The FWHM technique was used to evaluate the actual cortical thickness from the microCT.

The software program Stradwin was used to estimate the cortical thickness of the skull from clinical CT scans [3]. Stradwin evaluated cortical density based on an analysis of both in-plane and out-of-plane point spread functions and used the optimized cortical density to interpret cortical thickness. The determined cortical thickness estimates were then mapped over a 3 dimensional (3D) surface of the bone [3, 4]. The location sampled for microCT was identified on the 3D reconstruction of the skull and the skull was then cropped to the appropriate size of the sample. Three dimensional volumes were calculated for both the microCT and the cropped clinical CT. The clinical CT was aligned to the microCT using both Geomagic Studio (Geomagic, Research Triangle Park, NC) and 3D Slicer (National Alliance for Medical Image Computing). The 3D volume from the clinical CT scan was converted to a point cloud and sub-selected to only contain points in contact with the inner and outer tables of the microCT volume. The transforms created from the alignment were used to match the cortical thickness measurements from Stradwin between the clinical CT and the microCT. The thickness measurements corresponding with the surface label map of the clinical CT were then compared to the nearest thickness measurement from the microCT.

RESULTS

A sample from the frontal bone of the 46 year old cadaver was selected for the validation of Stradwin for the skull. This sample contained the frontal suture which can be

identified as a section of continuous cortical bone from the outer to inner cortex without the presence of a diploic layer. The actual thickness measurements for the outer table of the frontal bone are qualitatively shown in Figure 1A. The suture was determined to exceed 4 mm while much of the outer table fell between 1.5 to 2 mm. The thickness measurements calculated from the clinical CT scans are presented in Figure 1B. Qualitatively the thickness measurements between the microCT and the clinical CT were comparable (Figure 1C).

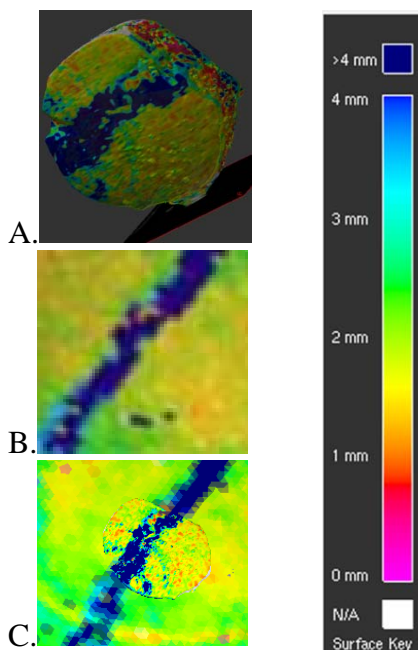


Figure 1: Thickness measurements from Stradwin represented as color maps over the 3D volume's outer surface for A) microCT, B) clinical CT, and C) microCT aligned with the clinical CT. The thickness scale is located on the right.

For a more quantitative analysis the thickness, calculations from the clinical CT that were associated with points on the surface label map were compared to the thickness of the nearest landmark on the microCT. In evaluating the difference in matched thickness calculations, 96% of all selected points fell within ± 0.9 mm (Figure 2). The clinical CT thickness measurement overestimated actual thickness on average only 0.25 mm where the median actual thickness was 1.55 mm.

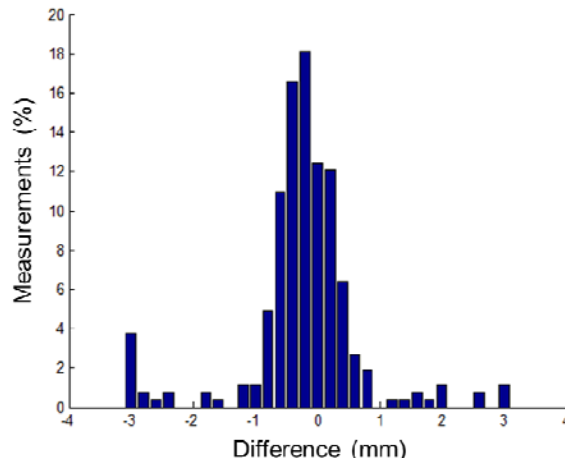


Figure 2: Distribution of difference in thickness measurements between the clinical CT and the thickness of the microCT.

CONCLUSIONS

With the exception of the suture within the sample, cortical thickness measurements on the skull were well below 3 mm and accurate thickness could not be calculated using FWHM on a clinical CT scan. The actual thickness of the skull has been shown to be more accurately determined from clinical CT scans using a cortical density based approach, facilitating the study of populations to assess skull table thickness by age and anatomical location.

ACKNOWLEDGMENTS

Funding was provided by the National Highway Traffic Safety Administration under Cooperative Agreement Number DTN22-09-H-00242. Views expressed are those of the authors and do not represent the views of NHTSA.

REFERENCES

1. Faul M. *Centers for Disease Control and Prevention*, Atlanta, GA, 2010.
2. Newman DL. *Physics in Medicine and Biology* 43, 619-626, 1998.
3. Treece GM. *Med Image Anal* 14, 276-290, 2010.
4. Treece GM. *Med Image Anal* 16, 952-965, 2012.

INHIBITION OF COLLAGEN GEL CONTRACTION BY FIBROBLASTS USING CARBON NANOTUBES

Elizabeth Wailes^{1,2}, Nicole Levi-Polyachenko^{1,2}

1. Wake Forest University Health Sciences, Department of Plastic and Reconstructive Surgery
 2. Virginia Tech - Wake Forest School of Biomedical Engineering and Sciences
- Corresponding Author: Elizabeth Wailes, email: ewailes@wakehealth.edu

INTRODUCTION

There are nearly half a million burn injuries in the US annually.¹ These injuries have a high complication rate and can severely impact a patient's quality of life. Nearly 40 percent of burns develop a scar contracture due to fibrosis.² If the wound is near a joint, the stiff scar tissue can inhibit extension of the joint and severely limit its range of motion, as shown at right.³

Current treatments focus on keeping the skin moist, but no therapy exists to treat the underlying cause of fibrosis.

This work approaches the prevention of scar contracture in a novel way

so as to deliver better therapeutic resources to physicians.



Figure 1: Scar contracture immobilizing the toes

Fibroblasts are the primary cells responsible for skin contraction during wound healing, but they act differently on various substrates. We hypothesize that the use of rod-shaped carbon nanoparticles such as multi-wall carbon nanotubes (MWNT) or single-wall carbon nanotubes (SWNT) may be able to inhibit fibroblast contraction, which would in turn decrease pathological scarring. We then validated the importance of using a rod-shaped particle by using the spherical nanoparticle carbon black (CB) as a control.

METHODOLOGY

Collagen gels were formed in 12 well plates by adding the following solutions in order and then gently mixing:

- 100 μ L 10X Phosphate buffered saline (PBS)

- 20 μ L 1 M NaOH
- 130 μ L cold 1X PBS with 1 mg/mL Pluronic F-127, with or without MWNT, SWNT, or CB
- 800 μ L cold collagen type I from rat tail (5 mg/ml)
- 250 μ L room temperature media or cell solution

Serially diluted solutions of 100 μ g/mL, 10 μ g/mL, and 1 μ g/mL of MWNT, SWNT, or CB in cold 1X PBS and 1 mg/mL Pluronic F-127 were used for the 1%, 0.1%, and 0.01% MWNT, SWNT, or CB gels, respectively.

Each gel contained 10^6 HEPM fibroblasts. The gels were photographed against millimeter-square graph paper each day for 7 days and their area was counted. A two-way ANOVA and Holm-Sidak post-hoc testing were used to determine significance. Viability of the fibroblasts was evaluated using trypan blue exclusion counting after 7 days of incubation. Differences in cytoskeletal actin were investigated with quantitative immunochemistry. The antioxidant abilities of the nanoparticles were measured with a hypoxanthine/xanthine oxidase assay. The mechanical properties of the gels were also evaluated with a Bose ElectroForce mechanical tester. The effect of proliferation was assessed by adding the anti-proliferative but non-cytotoxic chemical Ara-C. 10 μ L of 200 μ g/mL Ara-C was added to the gel solution before mixing and gelation. Viability and contraction were measured for this assay in the same manner as for the original assay. A one-way ANOVA with Holm-Sidak post-hoc testing was used to analyze the data from the proliferation assay.

RESULTS & DISCUSSION

The MWNT and SWNT significantly inhibited contraction at every concentration tested, while carbon black did not differ from the control at any concentration.

A viability assay proved that this effect was not due to cytotoxicity; in fact, the nanotubes greatly increased viability. However, this increase was only observed at the highest concentration of nanotubes tested.

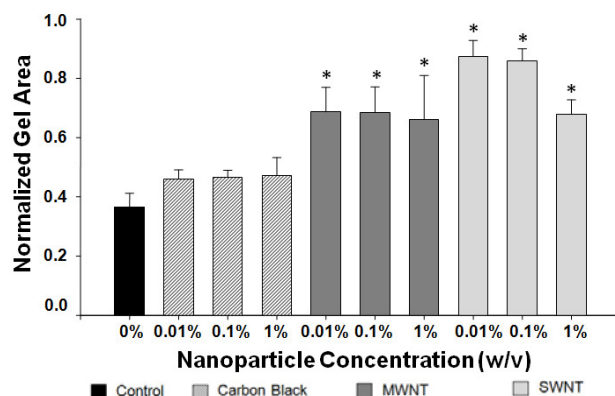


Figure 2: Area of gels with cells at day 7 normalized by the area of otherwise identical gels without cells. An asterisk denotes significance as compared to the control group containing no nanoparticles (0%).

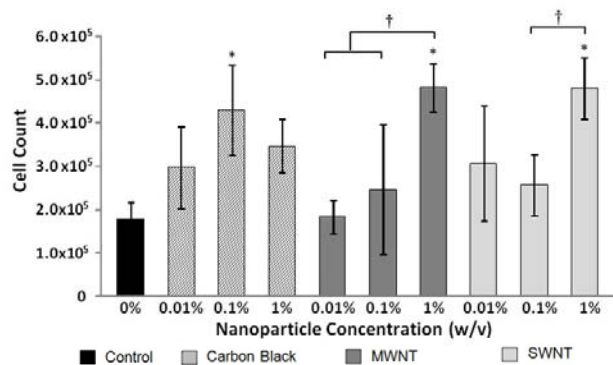


Figure 3: Viability of cells encapsulated in different concentrations of each gel type for one week.

We investigated several mechanisms that might explain these data. However, there were no differences from the control for any gel type in either the cytoskeletal actin content or the mechanical properties of the gels. We did find that the MWNT have an antioxidant ability, which means that they can scavenge pro-inflammatory, pro-fibrotic signaling molecules known as reactive oxygen species. This feature should partially explain the effect of the MWNT on cells. However, we found no such result with the SWNT, which otherwise behave similarly to the MWNT.

Finally, we investigated proliferation. When we knocked out proliferation, the differences in contraction and viability between the various gel types were also removed. While differences in proliferation are responsible for the observed effects on the gels, we believe the underlying mechanism results from crossing a percolation threshold with the dopant nanoparticles.

Literature on network theory has shown the ability of particles to form a network is dependent upon their concentration and aspect ratio. For the nanotubes, the critical threshold for percolation lies between 0.1% and 1% (wt/v) while the spherical nanoparticles would require closer to 20% (wt/v).⁴ It has also been noticed that the formation of such a network increases proliferation. Together, these findings suggest that our effect is actually due to nanotube network formation.

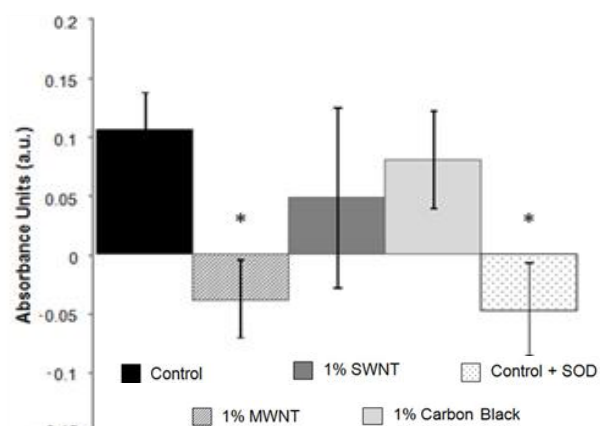


Figure 4: Reactive oxygen species (ROS) present at the end of the antioxidant assay.

CONCLUSIONS

MWNT and SWNT are a promising area of research for treatment of fibrotic scars. Our data shows a clear decrease in contraction with a concomitant increase in viability, which would allow for faster healing time in addition to less fibrotic scarring. The antioxidant ability of the MWNT also contributes to the effect and would serve to further decrease inflammation in *in vivo* applications.

ACKNOWLEDGMENTS

The authors would like to thank the Department of Plastic and Reconstructive Surgery for funding.

REFERENCES

- ¹ "Burn Incidence and Treatment in the United States: 2011 Fact Sheet." American Burn Association. Web. 14 Oct. 2011. <http://www.ameriburn.org/resources_factsheet.php>.
- ² Schneider JC et al J. Burn Care Res 2006 pp 508-514
- ³ Wyndham, Mike. "My Life as a GP Photographer." Pulse, 9 Dec. 2009. <<http://www.pulsetoday.co.uk/story.asp?storycode=4124584>>.
- ⁴ Munson-McGee SH. Estimation of the critical concentration in an anisotropic percolation network. Phys Rev B Condens Matter. 1991, 43, 3331-6.

TISSUE GROWTH AND CELLULAR ORGANIZATION ARE INFLUENCED BY FLOW RATE AND PRESSURE IN DECELLULARIZED LIVER PERFUSION BIOREACTORS

Emma C. Moran^{1,2}, Pedro M. Baptista², Jessica L. Sparks³, and Shay Soker^{1,2}

1. Virginia Tech- Wake Forest School of Biomedical Engineering and Sciences

2. Wake Forest University, Wake Forest Institute for Regenerative Medicine

3. Miami University, Chemical and Paper Engineering

Corresponding Author: Emma C. Moran, Email: emoran@wakehealth.edu

INTRODUCTION

The recent development of organ decellularization techniques to create scaffolds for whole organ engineering enables cell delivery (recellularization) into these scaffolds by using the preserved vasculature of the native tissue. To accomplish this, a perfusion bioreactor has been developed that delivers media and cells into the scaffold via pump-driven flow [1]. The flow rate and pressure of this perfusion bioreactor system can be adjusted to optimize both cell delivery and subsequent maintenance of the forming tissue. The focus of this study was to determine the effects of flow rate on the success of cell seeding and subsequent tissue growth and organization in the perfusion bioreactor system.

METHODOLOGY

Scaffolds were seeded with 30 million liver cells (HepG2) and endothelial cells (MS1) via the portal venous system and then maintained in the bioreactor for up to 7 days.

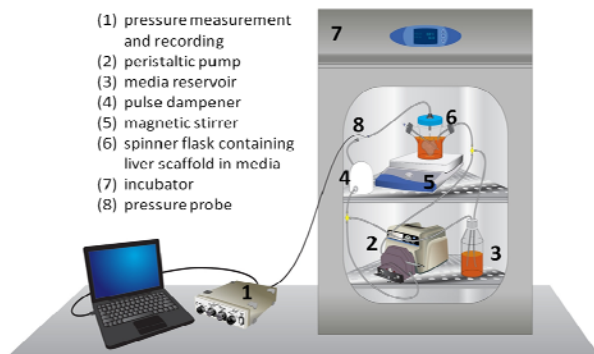


Figure 1: Schematic diagram of perfusion bioreactor for cell seeding and bioscaffold maintenance.

System pressure was measured using a Millar mikro-tip pressure transducer catheter inserted into the bioreactor tubing. Experiments were performed at five different flow rates, ranging from 3-40 ml/min, to determine the effect of flow rate on cell delivery and tissue formation. The seeded bioscaffold was characterized after 1 and 7 days by analyzing cell penetration into the scaffold, percentage of the scaffold seeded with cells, cellular proliferation, cellular stress, re-vascularization, and cellular organization through histochemistry and immunofluorescence, with subsequent image analysis.

Table 1: Cell seeding and bioreactor conditions.

	Flow Rate (ml/min)				
	3	6	9	12	40
Cell delivery rate (10 ⁵ cells/min)	3.6	3.6	3.85	3.6	7.5
Media volume in vessel (ml)	250	250	350	400	400
# cells per injection	30x10 ⁶	15x10 ⁶	15x10 ⁶	12x10 ⁶	7.5x10 ⁶
Total # of injections	2	4	4	5	8
24 hour bioreactors	n = 4	n = 4	n = 4	n = 4	n = 2
7 day bioreactors	n = 2	n = 3	n = 4	n = 2	None

RESULTS

At the 9 and 12 ml/min flow rates, the number of cells within the scaffold as well as the percentage of proliferating cells was maximized, without corresponding increases in cell stress (Figure 2). At lower flow rates, cell seeding was not as effective, as indicated by lower cell penetration and scaffold occupancy. After one week at

flow rates of 9 and 12 ml/min, there was more tissue growth than at 3 and 6 ml/min, indicating the mechanical forces and mass transport at lower flow rates was not optimal for tissue formation. While flow rates above 12 ml/min adequately delivered cells into the scaffold, cell viability at 40 ml/min was compromised, with higher apoptosis detected.

Importantly, a significant change in cellular organization is observed after 7 days in the bioreactor (Figure 3). A mixed population of cells is observed in the parenchyma and vessels at 24 hours. After 7 days, the majority of vascular structures contain only endothelial cells, while the parenchyma of the tissue consists of large liver cell clusters. Quantification of these parameters is shown in Figure 3. The perfusion system provided the proper environment to allow the cells to self-organize, which was observed across all flow rates after 7 days. However, the size of albumin-secreting HepG2 clusters is significantly larger at higher flow rates, suggesting cellular organization and tissue formation are both influenced by flow rate.

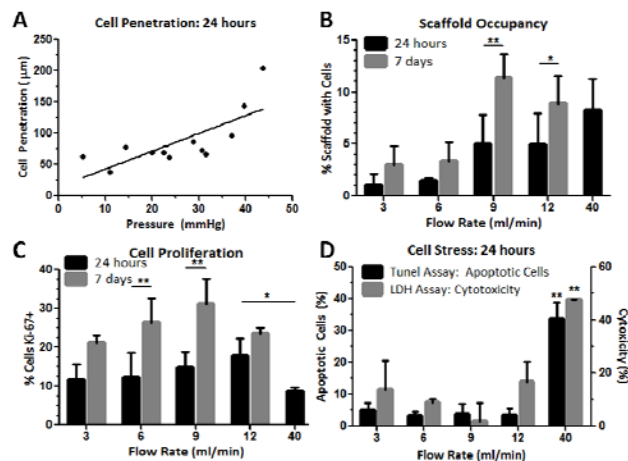


Figure 2: (A) Linear correlation of pressure to cell penetration, using Pearson's correlation coefficient, was statistically significant ($p < 0.01$). (B) Scaffold occupancy significantly increases from 24 hours to 7 days, with the most significant increase occurring at 9 ml/min. Cell occupancy at 9 ml/min is significantly higher than 3 or 6 ml/min for both 24 hour and 7 day bioreactors. (C) Proliferation significantly increases from 24 hours to 7 days as well, indicating that there is tissue formation within the scaffold which seems to be optimized at a flow rate of 9 ml/min. Additionally, there is a significant decrease in cell proliferation between 12 ml/min and 40 ml/min, indicating the mechanical stress is too high. (D) The percentage of apoptotic cells and cytotoxicity significantly increases at 40 ml/min, compared to all other flow rates. * $p < 0.05$, ** $p < 0.01$.

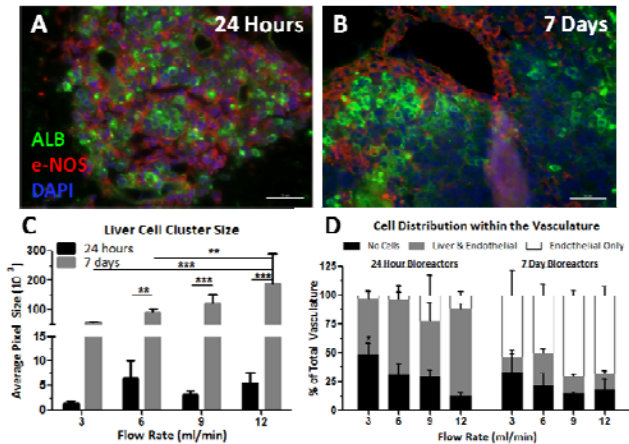


Figure 3: (A,B) Immunohistochemistry of bioreactors at (A) 24 hours and (B) 7 days for a 9 ml/min bioreactor. Liver cells were stained with albumin (ALB, green) and endothelial cells are stained with e-NOS (red). (C) Average size of HepG2 clusters increases significantly from 24 hour bioreactors to 7 day bioreactors, indicating cellular organization as well as proliferation. At 7 days, 12 ml/min clusters are significantly larger than 3 or 6 ml/min clusters. (D) At the 7 day mark, there are significantly more endothelial cells coating the blood vessels, rather than a combination of both cell types, seen at 24 hours. Flow rate also has an effect on blood vessel seeding; 3 ml/min bioreactors have the most vessels without cells in the 24 hour bioreactors. * $p < 0.05$, ** $p < 0.01$.

CONCLUSIONS

Perfusion bioreactor flow rate determines the rate of cell delivery during bioscaffold seeding, the mechanical forces within the acellular matrix and the mass transport of media components to the seeded cells. All of these factors play a role in the success of cell seeding and subsequent tissue growth. While a single flow rate was not found to be optimal across every one of these analyses, we have concluded that 9 ml/min is the optimal flow rate for maximizing tissue growth over one week. Collectively, the results demonstrate that proper perfusion rates within the bioreactor lead to self-organization of the liver cells to their appropriate niche within the acellular liver bioscaffold, an important finding in the liver tissue engineering field.

REFERENCES

[1] Baptista, P. M., Siddiqui, M. M., Lozier, G., Rodriguez, S. R., Atala, A., and Soker, S., 2011, "The use of whole organ decellularization for the generation of a vascularized liver organoid," *Hepatology*, 53(2), pp. 604-617.

FIBER BASED IMAGING ON ELECTROSPUN SCAFFOLD

Etai Sapoznik^{1,2}, Peng Lu³ Guoguang Niu¹, Tracy L. Criswell¹, Yong Xu^{2,3} Shay Soker^{1,2}

1. Wake Forest Institute for Regenerative Medicine
 2. VT-WFU School of Biomedical Engineering and Sciences
 3. Department of Electrical and Computer Engineering, Virginia Tech
- Corresponding Author: Etai Sapoznik, Email: esapozni@wakehealth.edu

INTRODUCTION

A critical issue in tissue engineering is our inability to monitor cellular differentiation and cell-cell interactions in real-time in vivo. Such capability can help understand the cellular level effects of various factors on the development of a functioning tissue in order to optimize the regenerative process. Current methods used to monitor these processes are dependent on histological techniques, which require sacrifice of the animal or tissue. The ultimate goal of this study is to develop multi-modal optical molecular tomography (OMT) techniques for non-invasive real time imaging of engineered blood vessels [1] in vitro and in vivo. The current objective of this research was to examine our ability to image cells labeled with different fluorophores in order to identify the optimal cell labeling scheme, resulting in maximal signal on an electrospun PCL-Collagen scaffold. These fluorophores will be further used for the development and optimization of the fiber optic imaging system.

METHODOLOGY

Smooth muscle cells (10T1/2), endothelial cells (MS-1) and mesenchymal stem cells (MSCs) were infected with lentivirus expressing GFP, mKate or tdTomato, respectively (Fig. 1A, B). The fluorescent labels allowed us to assess our ability to image these cells in culture in real-time. The top 5% expressing cells were sorted by FACS and re-cultured. Cells were further seeded on poly(ϵ -caprolactone) (PCL) collagen electrospun sheet scaffolds with 9:1 PCL-collagen ratio and a bioabsorbable electrospun poly(D,L-lactide) PDLLA scaffold used as an imaging control. The scaffold was embedded with Micro

Imaging Channels (MIC) (Fig. 2B), with $\sim 50\mu\text{m}$ top layer and a bottom layer thickness of $\sim 300\mu\text{m}$, in order to allow for the insertion of a fiber optic mirror for laser delivery (Fig. 2C). The seeded scaffold was placed in an imaging chamber (Fig 2D). By using blue (473 nm) and green (532 nm) lasers GFP and mKate/tdTomato cells were excited respectively. Rotation of the fiber mirror and axial translation gave a scanning region of $300\mu\text{m} \times 1000\mu\text{m}$. A bottom EM-CCD camera was used to map cell excitation. The resulting reconstructed heat map was compared with a direct-line-of-sight using a top camera with a control light similar to a conventional upright fluorescent microscope (Fig. 2A). Image reconstruction was performed in order to examine the ability to separate fluorescent signal from background noise and scaffold autofluorescence.

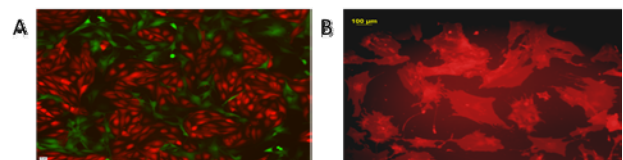


Figure 1: (A) Fluorescently labeled MS-1 (mKate-red) and 10T1/2 (GFP-green) cells on plate (B) MSC (tdTomato-red) cells on plate

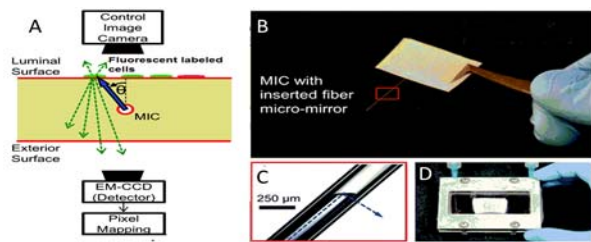


Figure 2: (A) Imaging system diagram (B) scaffold containing MIC (C) Fiber optic mirror used for laser light delivery (D) Imaging chamber [2]

RESULTS

Using the fiber based imaging system, we were able to obtain good cell contrast of GFP-labeled 10T1/2 cells on the PDLLA scaffold (Fig.3-A,F). However, we found poor contrast for the GFP fluorophore on the PCL-Collagen scaffold (Fig. 3-C,H), making it impossible to recognize cell location or morphology. Limited resolution was already apparent by larger beam spot on PCL-Collagen when compared with PDLLA scaffold (not shown).

In contrast, we found good contrast of the mKate-labeled MS1 cells on both the PDLLA scaffold (Fig. 3-B,G) as well as the PCL-Collagen scaffold (Fig, 3-D,I). However, the image resolution was limited, preventing the differentiation of closely adjacent cells in the reconstructed image.

tdTomato-labeled MSC cells on the PCL-Collagen scaffold also gave reasonable image contrast comparable with the mKate cells (Fig, 3-E,J)

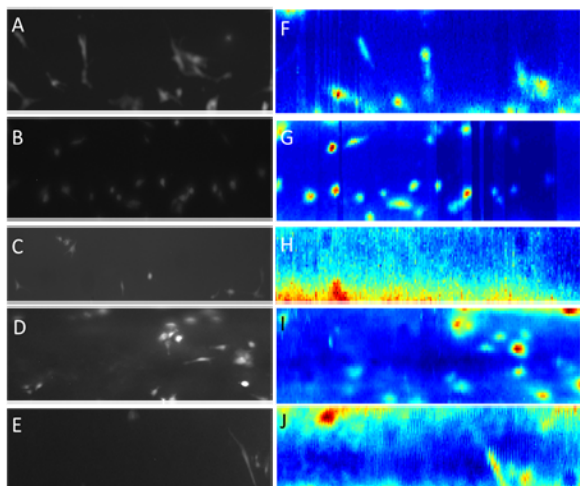
Figure 3: A-E: Control image obtained using conventional fluorescent microscopy; F-J: reconstructed image obtained using fiber based imaging system. Samples: A,F:GFP-PDLLA; B,G:mKate-PDLLA; C,H:GFP-PCL-COL; D,I:mKate-PCL-COL; E,J:tdTomato-PCL-COL

CONCLUSIONS

- 1) Use of the blue laser to excite the GFP-labeled cells on the PCL-Collagen scaffold resulted in high autofluorescence. Therefore, this labeling scheme is sub-optimal for use with this scaffold and the fiber optics imaging system.
- 2) mKate and tdTomato-labeled cells showed high contrast on the PCL-Collagen scaffold, due to low autofluorescence of the scaffold with the green laser. Both of these fluorophores are potential candidates for fiber based imaging reconstruction on PCL-Collagen scaffolds.
- 3) Imaging resolution is limited to 20-30 μm due to the beam spot size which is affected by inherent scaffold properties.

REFERENCES

1. Tillman B.W. et al. Biomaterials 30, 583-588, 2009
2. Hofmann, M.C. et al. Tissue Engineering Part C: p. 677-687. 2012



MIGRATORY BEHAVIOR OF CELLS IN THE PRESENCE OF DUAL AND OPPOSING CUES

Gaurav Jain¹, Padmavathy Rajagopalan^{1,2}

1. School of Biomedical Engineering and Sciences, Virginia Tech

2. Department of Chemical Engineering, Virginia Tech

Corresponding Author: Padmavathy Rajagopalan, Email: padmar@vt.edu

INTRODUCTION

Cell migration is a complex physiological process crucial during morphogenesis, organ development, wound healing, and metastasis of tumors. *In vivo*, cells exhibit directed migration when presented with a wide range of stimuli that are chemical, mechanical, electrical, or optical¹. Directed migration is typically observed when one of these cues is presented to cells as a gradient. Several studies have been conducted into directed migration on gradients that are purely mechanical or chemical. Our goal was to investigate cellular migratory behavior when cells are presented with a choice and have to choose between increasing substrate rigidity or higher protein concentration. We have chosen to focus on this unique environment since it recapitulates several interfacial regions *in vivo*.

METHODOLOGY

Polyacrylamide (PAAM) hydrogels exhibiting a dual chemical and mechanical gradient were designed. A gray scale photo mask was designed to control the differential transmission of UV radiation. By modulating the incident UV intensity, the extent of cross-linking as well the covalent attachment of cell-adhesive ligands was controlled. Irgacure 2959 was used as a photo-initiator which has $\lambda_{\max} = 254\text{nm}$. The Young's modulus of these substrates was measured using Atomic Force Microscopy (AFM).

N-hydroxysuccinimide (NHS) ester chemistry was used to link collagen to the PAAM gels. A heterobifunctional cross-linker, Sulfo Succinimidyl Diazirine (SDA) containing a photo-reactive nitrene group on one end non-specifically conjugated to the PAAM substrate upon

exposure to UV radiation at 365nm while the other moiety bound to collagen through primary amine groups.

PAAM gels were seeded with BALB/c 3T3 fibroblasts and incubated in a humidified 5% CO₂ environment at 37°C for up to 8 hours and visualized under a Nikon TE 2000U fluorescence microscope in a closed cell culture chamber. Phase contrast and fluorescence images were obtained every 30 minutes using time-lapse microscopy. Cell centroids were tracked using Nikon NIS Elements software.

RESULTS

Several parameters like UV exposure time, photo-initiator solubility and the concentrations of the cross-linker were optimized to design dual gradient substrates. Both mechanical and chemical gradients were introduced using grayscale masks that modulated stiffness and the extent of chemical conjugation. First, we characterized these substrates for Young's modulus (YM) using AFM. AFM measurements were obtained at regular intervals. We designed hydrogels that exhibited a mechanical gradient with the modulus ranging from 44-125kPa (Table 1). These data demonstrate that the width of the interfacial region is ~ 200 μm .

Table 1: YM measurement using AFM

Distance from the interface(μm)	YM Stiff side (kPa)	YM soft side (kPa)
0	46.0 \pm 4.5	
100	118.9 \pm 15.4	57.7 \pm 3.6
200	124.5 \pm 5.2	43.6 \pm 1.9

Next, we estimated the surface density of collagen bound to the PAAM gels using an indirect fibronectin binding

assay² (Table 2). We kept the mechanical gradient profile constant (119kPa-57kPa) but varied the concentration of immobilized collagen. We varied the collagen input concentration to achieve ~4 fold (shallow gradient) and ~7 fold (steep gradient) increase in collagen surface concentration on the soft side (57kPa) of the dual gradient substrates.

Table 2: Estimation of surface concentration of collagen

[Collagen] ($\mu\text{g/ml}$)	Stiff Side		Soft Side	
	Binding efficiency (%)	10^{24} molecules/ μm^2	Binding efficiency (%)	10^{24} molecules/ μm^2
15	34.6	1.9	56.9	3.2
30	56.4	6.3	62.1	6.9
50	87.0	16.1	70.2	12.9

Initial studies were conducted to validate durotaxis on two different mechanical gradient profiles (119kPa/47kPa) and (95kPa/50kPa) while keeping the surface concentration of immobilized collagen constant at 15 $\mu\text{g/ml}$. We observed that greater than 60% of the cells on both mechanical gradient profiles exhibited a preference towards the rigid region of the substrate (Table 3). Hence, we concentrated on 119kPa-57kPa gels for future studies as cells exhibited higher displacements on these substrates.

Table 3: Summary of Durotaxis on 119kPa-57kPa gels

Preferred direction of motion	% of cells
Exhibiting preference for 119kPa side	75
Exhibiting preference for 57kPa side	25

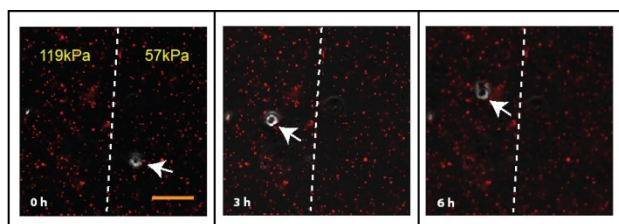


Figure 1: Movement of BALB/c 3T3 fibroblasts on substrates with mechanical gradient. Scale bar= 50 μm

Next, we designed hydrogels with opposing dual chemical and mechanical gradient profiles to investigate which cue would play a dominant role in directing cell locomotion. When the concentration of immobilized collagen was increased ~4 fold on the 57kPa side of the gel, 82% of cells exhibited preference towards the high collagen-soft (57kPa) side of the gel (Table 4). Similarly, when the

immobilized collagen concentration was increased ~7 fold on the 57kPa side, 88% of the cells exhibited preference towards high collagen-57kPa region. We also observed that when the collagen concentration was increased only 4-fold, it elicited higher displacements and speeds in comparison to a chemical gradient that increased 7-fold.

Table 4: Summary of cell motion on dual gradient gels

Preferred direction of motion	Collagen gradient	
	4 fold	7 fold
% of cells exhibiting preference for HIGH Collagen- 57kPa side	82	88
% of cells exhibiting preference for LOW collagen – 119kPa side	18	12

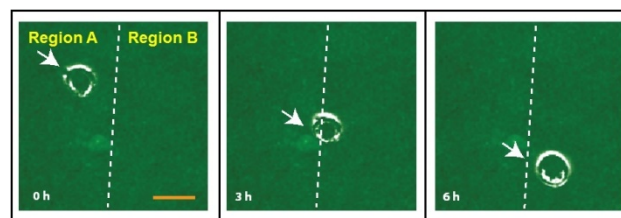


Figure 2: Movement of BALB/c 3T3 fibroblasts on substrates with dual mechanical chemical gradient. **Region A:** 119kPa-1.9*10²⁴ molecules/ μm^2 , **Region B:** 57kPa-1.9*10²⁴ molecules/ μm^2 Scale bar= 50 μm

CONCLUSIONS

We have designed a novel dual gradient hydrogel substrate that can provide new insights into cellular locomotion. In this study, fibroblasts exhibited durotaxis until a suitable chemical gradient reversed this trend. The current study demonstrates that the dual gradient patterns may be useful in enhancing our understanding of cellular motility at tissue interfaces *in vivo*.

ACKNOWLEDGMENTS

We gratefully acknowledge financial support from NSF (CAREER: DMR: 0955873) and the Institute for Critical Technology and Applied Sciences at Virginia Tech.

REFERENCES

- (1) Hale, N. A.; Yang, Y.; Rajagopalan, P. *ACS Applied Materials & Interfaces* **2010**, 2, 2317.
- (2) Gaudet, C.; Marganski, W. A.; Kim, S.; Brown, C. T.; Gunderia, V.; Dembo, M.; Wong, J. Y. *Biophysical journal* **2003**, 85, 3329.

SILK BASED TISSUE ENGINEERED MUSCLE REPAIR (TEMR) CONSTRUCT FOR CONTROLLED RECOVERY IN VOLUMETRIC MUSCLE LOSS (VML) INJURIES

Hannah B. Baker^{1,2}, Catherine Ward³, Benjamin T. Corona³, Masood Machingal², Jelena Rnjak⁴, David L. Kaplan⁴, George J. Christ^{1,2}

1. VT-WFU School of Biomedical Engineering and Sciences, Biomedical Engineering
2. Wake Forest Institute for Regenerative Medicine
3. United States Army Institute for Surgical Research
4. Tufts University, Biomedical Engineering

Corresponding Author: Hannah Baker, Email: hbaker@wakehealth.edu

INTRODUCTION

Traumatic injuries, congenital and acquired diseases and disorders result in volumetric muscle loss (VML) in soldiers and civilians. VML is defined as muscle loss that exceeds the intrinsic regenerative capacity of skeletal muscle resulting in significant and permanent deficits in cosmesis and function. We have developed a Tissue Engineered Muscle Repair (TEMR) construct therapy created from the combination of muscle progenitor cells seeded onto a biologic scaffold and subjected to cyclic stretch preconditioning. This technology significantly improves muscle functional recovery ($\approx 60\text{-}70\%$ restoration of contraction) within 2 months of implantation in a surgically created VML injury (50% resection of mouse latissimus dorsi) approximating the requirements for replacement of the sheet-like muscle following craniofacial injuries to wounded warriors. **Because VML represents a spectrum of injuries, the goal of the current studies was to begin development of next generation technologies that would increase the clinical applications of our technology to a wider range of VML injuries. In this regard we are pursuing silk as tunable biomaterial for optimizing cell and drug delivery while also providing a spectrum of mechanical properties.** Three iterations (IT1-3) of silk constructs have been fabricated with the goal of optimizing resorption, functional recovery, and regeneration. Female Lewis rats underwent surgical resection of $\sim 20\text{-}30\%$ of the TA muscle followed by implantation of acellular silk (IT1 n=2; IT2 n=2; IT3 n=3). The function of the TA was measured *in vivo* (at 4 and 8 weeks post surgery). At either 9 (IT2) or 12 weeks (IT1, 3), the TA was explanted for histology. All iterations of silk without cells enabled a functional recovery of $\sim 40\%$. Histologically, IT1 showed little to no integration and no new muscle formation. IT2 scaffolds

appeared to be resorbed with evidence of new muscle fibers.

METHODOLOGY

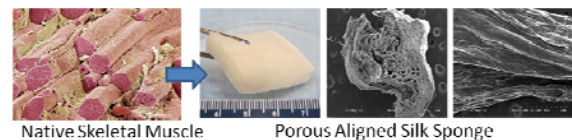


Figure 1. Constructs mimic the architecture of native skeletal muscle. SEM images detail the porosity and fiber alignment.

Silk fibroin from *Bombyx mori* silkworms was degummed, solubilized, and formed into three iterations of porous aligned constructs (Figure 1) as previously described [2, 3]. The freezing rate and annealing process were altered to achieve different porosities and degradation rates. The second generation used a slower freezing rate and water annealing process (as opposed to methanol used in IT-1) to increase pore size and lower the beta sheet content of silk. The third generation included a lower silk content to further increase degradation rate. The VML injury was created by surgically resecting $\sim 20\text{-}30\%$ of the tibialis anterior muscle weight from 3-5 month old female Lewis Rats. Acellular silk scaffolds were then implanted into the wound bed (Figure 2).

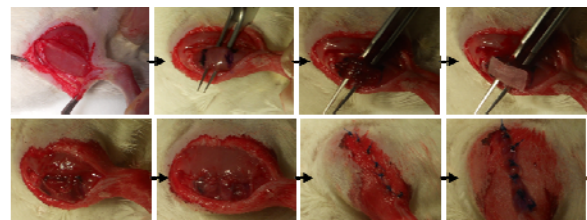


Figure 2. Surgical process: exposure of the muscle, creation of the defect, placement of the scaffold, closure of the wound bed, and closure of the skin.

Muscle function was assessed *in vivo* before surgery and at 4 and 8 weeks post implant by electrically stimulating the peroneal nerve and measuring the force produced by dorsiflexion of the foot via a foot plate force transducer (Figure 3). At 12 weeks (IT1,3) or 9 weeks (IT2) tissues were explanted and either formalin fixed and paraffin embedded or frozen for histological analysis.

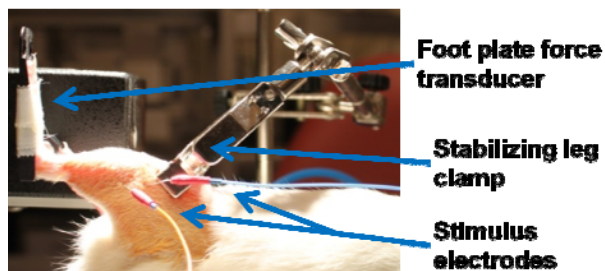


Figure 3. *In vivo* muscle function testing apparatus. The anterior crural compartment muscles are stimulated with electrical output from platinum tip electrodes. The resulting dorsiflexion is measured through a footplate force transducer.

RESULTS

For each iteration of silk, 3-5 month old female Lewis rats underwent a surgical resection of the TA muscle and received an acellular silk construct implant (iteration 1 n=2, iteration 2 n=2, iteration 3 n=3). Muscle functional testing revealed that at 8 weeks post implant functional recovery did not improve for any iteration when compared with animals which underwent surgical resection of the muscle with no treatment (Figure 4).

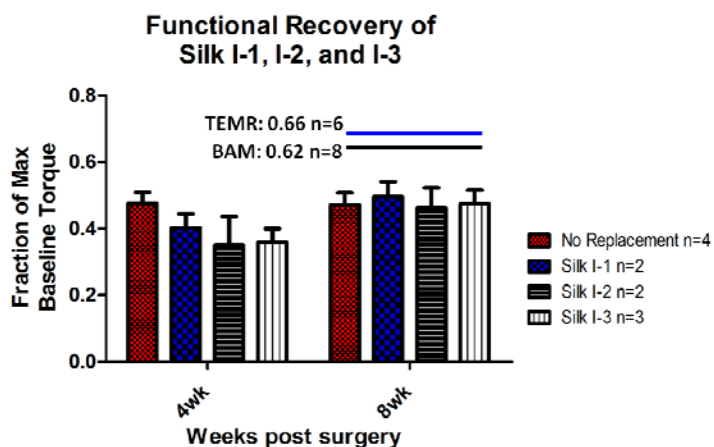


Figure 4. Functional analysis of the tibialis anterior dorsiflexion force normalized to body weight and represented as a fraction of maximal baseline values. Data for the 8 week timepoint for TEMR and BAM treatments are shown for comparison.

At 12 weeks (IT1,3) or 9 weeks (IT2) tibialis anterior explants indicated that iteration 1 silk underwent little to no degradation while iterations 2 and 3 silk appeared to be completely or nearly completely dissolved.

DISCUSSION

When revisiting the original goals for the three iterations of silk scaffold, it is notable that the successive iterations achieved the desired degradation rates and physical structures. In the absence of cells, a biologically inert material such as silk would not be expected to influence muscle functional recovery as well as a biological extracellular matrix scaffold (BAM) or especially a cell seeded extracellular matrix (TEMR). Through the successful addition of a cellular component, we hypothesize that the silk constructs will enhance recovery through delivery of cells at an optimized and controlled degradation. Moving forward, the previous generations of silk will be further evaluated with emphasis on their mechanical properties in order to better tune a subsequent iteration of constructs. Knowing the range of degradation profiles of these first three iterations of silk scaffold will help guide the exploration of the other capabilities of silk as a construct for muscle repair. Specifically, we envision cell-seeded, silk-based implants further optimized to contain appropriate gradations and release profiles for desired drug and growth factors to further enhance muscle regeneration and repair following VML injury.

ACKNOWLEDGMENTS

David Kaplan, Ph.D., Tufts; Jelena Rnjak, Ph.D., Tufts; Tom Walters, Ph.D., USAISR; Armed Forces Institute of Regenerative Medicine, for funding.

REFERENCES

- [1] Machingal MA, et al. *Engineering Part A*. 2011;17:2291-303.
- [2] Murphy AR, et al. *Journal of Materials Chemistry*. 2009;19:6443-50.
- [3] Altman GH, et al. *Biomaterials*. 2003;24:401-16.

PRELIMINARY fMRI STUDY OF VERBAL-ASSOCIATIVE MEMORY

Harshawardhan U. Deshpande^{1,2} and Stephen M. LaConte^{2,1}

1. Virginia Tech – Wake Forest School of Biomedical Engineering & Sciences
2. Virginia Tech Carilion Research Institute

Corresponding Author: Harshawardhan U. Deshpande Email: harsh87@vt.edu

INTRODUCTION

Memory is the ability of the human brain to encode, store and recall information received from a stimulus. Human memory demonstrates a fundamentally associative nature. Thus, a new fragment of information is remembered better if associated with information that has already been acquired. The process of creating a new memory can be separated into encoding (perception and storage) and recall (creative re-imagination of previously encoded information).

The default mode network (DMN), a large and robustly replicable network of brain regions that is associated with task-irrelevant mental processes and mind wandering, shows higher activity and stronger functional connectivity during rest than during externally driven tasks^[1]. An anti-correlated network that includes the dorsolateral prefrontal cortex (DLPFC) and the supplementary motor area (SMA) shows task-positive activation^[2]. The hippocampus, the amygdala and the medial temporal lobe (MTL) have also been proven to be involved in the encoding and recall of memories^[3]. This study is aimed at understanding the activity of brain regions during successful and unsuccessful memory encoding. Knowledge of the memory encoding and recall mechanism will prove to be invaluable to understand and address memory and attention disorders.

METHODS

For the preliminary study, an assumption can be made that can be information successfully recalled has been successfully encoded. On this premise, an fMRI task was designed to image the brain during the processes of encoding and retrieval.

The encoding phase consisted of 4 runs of 30 word pairs each (120 total words), acting as the paired-associate stimulus. One part of the word pair was a common first name (male /female names taken from the Social Security Administration website) while the other was the name of a United States city/town. VisionEgg was used as a stimulus presentation tool while Matlab was used to randomize the word pair and question sequence to avoid bias. For piloting the study design, three subjects (female, mean age = 22) underwent the encoding phase inside a Siemens Trio 3.0 T machine. The subjects were instructed to memorize as many word pairs as possible. The word pairs were presented as verbal visual stimuli for 4 seconds followed by a fixation delay of 8 seconds.

The retrieval phase was administered outside the scanner on a computer. The subjects were presented with one part of the word pairs they tried to memorize earlier and were instructed to choose the correct answer from 4 alternatives.

The prompt with the 4 options were displayed for 4 seconds followed by a fixation cross delay of 2 seconds followed by another prompt. The subjects attempted this task in 4 runs consisting of 30 'questions' each. A keystroke logging mechanism kept track of the correct and wrong responses given by each subject.

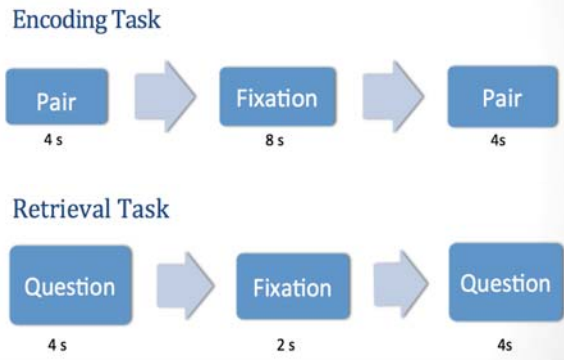


Figure 1: Encoding & retrieval task timing diagrams

RESULTS

The behavioral data obtained from the three subjects was analyzed for memory recall accuracy. The results are summarized in Table 1.

DISCUSSION

We aim to label the brain state data during encoding as “successful” and “unsuccessful” using the behavioral recall task data. If the keystroke logging mechanism has logged the subject’s response as correct, the corresponding encoding phase brain state data collected inside the scanner can be labeled as “successful” memory encoding while the wrong responses will correspond to an “unsuccessful” label in the encoding phase data. Using the labeled data, a Support Vector Machine classifier can then be trained using 3 of the 4 runs. The classification accuracy of the SVM classifier can be tested on the

remaining run using a leave-one-out routine. The data analysis shall be performed in AFNI (Analysis of Functional NeuroImages).

CONCLUSION

This pilot study is also an attempt to get familiar with fMRI task design, data collection and data analysis. The experience gained in this pilot shall be used to address the task design inadequacies. One of the major changes intended is the implementation of the retrieval task inside the MR scanner to enable collection of brain data during this stage. The ability of the trained classifier to distinguish between “successful” and “unsuccessful” memory encoding brain states will enable deeper understanding of the memory encoding and retrieval mechanisms in the brain.

REFERENCES

- [1] Raichle ME, MacLeod AM, Snyder AZ, Powers WJ, Gusnard DA, Shulman GL (2001): A default mode of brain function. *Proc Natl Acad Sci USA* 98: 676–682.
- [2] Fox MD, Snyder AZ, Vincent JL, Corbetta M, Van Essen DC, Raichle ME (2005): The human brain is intrinsically organized into dynamic, anticorrelated functional networks. *Proc Natl Acad Sci USA* 102: 9673–9678.
- [3] Herting et al. (2012): Differences in brain activity during a verbal associative memory encoding task in high-and low-fit adolescents. *Journal of cognitive neuroscience*. (Early Access), 1-18

Table 1: Memory recall accuracy

Subject number	Run number	Correct	Wrong	Unanswered	Accuracy	Mean Accuracy
1	1	16	8	6	53.33	42.4975
	2	9	19	2	30	
	3	14	15	1	46.66	
	4	12	18	0	40	
2	1	24	4	2	80	68.33
	2	21	7	2	70	
	3	20	9	1	66.66	
	4	17	12	1	56.66	
3	1	12	7	11	40	54.1625
	2	17	7	6	56.66	
	3	19	5	6	63	
	4	17	8	5	56.66	

FABRICATION OF ENGINEERED PORCINE KIDNEY SCAFFOLD FOR IN VIVO IMPLANTATION

Jennifer Huling¹, In Kap Ko², Anthony Atala^{2,3} and James Yoo²

1. Wake Forest School of Medicine, Biomedical Engineering
2. Wake Forest School of Medicine, Institute for Regenerative Medicine
3. Wake Forest School of Medicine, Urology

Corresponding Author: Jennifer Huling, Email: jhuling@wakehealth.edu

INTRODUCTION

Chronic Kidney disease is a leading cause of death in the United States. Organ transplant is the only treatment for the end stage of the disease, but the supply of donor organs does not meet the demand. It is the goal of this project to develop an implantable kidney using potentially autologous cells seeded on decellularized porcine kidney scaffolds to restore normal renal function.

Currently, the focus has been to restore the vascular network inside the scaffold. The structure of the vascular tree remains, but needs to be re-endothelialized to prevent blood-ECM contact and clotting. Initial attempts to re-endothelialize the scaffold led to successful cell attachment in vitro, but re-endothelialized scaffolds clotted quickly after in vivo implantation.

In an effort to combat clotting, this project is investigating possible modifications to the vascular surface of the scaffold. First, anti-CD31 antibodies conjugated to the scaffold may form a bond between the scaffold and the CD31 expressed on endothelial cells, leading to fewer cells detaching under the high flow rate after implantation. Second, heparin conjugation to the scaffold may provide a localized anti-clotting effect.

METHODOLOGY

Heparin and CD31 antibody were conjugated to the the vascular structures of whole kidney scaffolds using EDC/NHS crosslinking reaction. MS1 cells were seeding onto kidney scaffolds with previously established static and ramping perfusion methods and re-endothelialization of vascular structures within the kidney scaffolds was determined by H&E staining.

The effect of antibody and heparin conjugation on cell detachment was tested using a silicone flow chamber mounted on a glass slide. The inside of the chamber was coated with collagen to mimic the actual kidney scaffold and antibody or heparin or both could be conjugated to the collagen. After cell attachment, media was run through the chambers at 2, 5, 10, 20 and 50 mL/hr. One region of each chamber was filmed and the number of cells attached was counted and represented as a percent of the original number of attached cells.

Ongoing experiments are being conducted to observe the anticlotting properties of heparinized surfaces.

RESULTS

Cell seeding efficiency did not seem to differ between the heparin, heparin and antibody, and antibody only whole kidney scaffolds tested. Figure 1 displays H&E staining of a cortical section of kidney, showing good cell attachment in all groups. The results were similar in all areas of the kidneys.

Collagen only coated surfaces had a higher, but not significantly different amount of cell detachment at high flow rates. Heparin surfaces with and without CD31 antibody did not affect cell detachment (Figure 2).

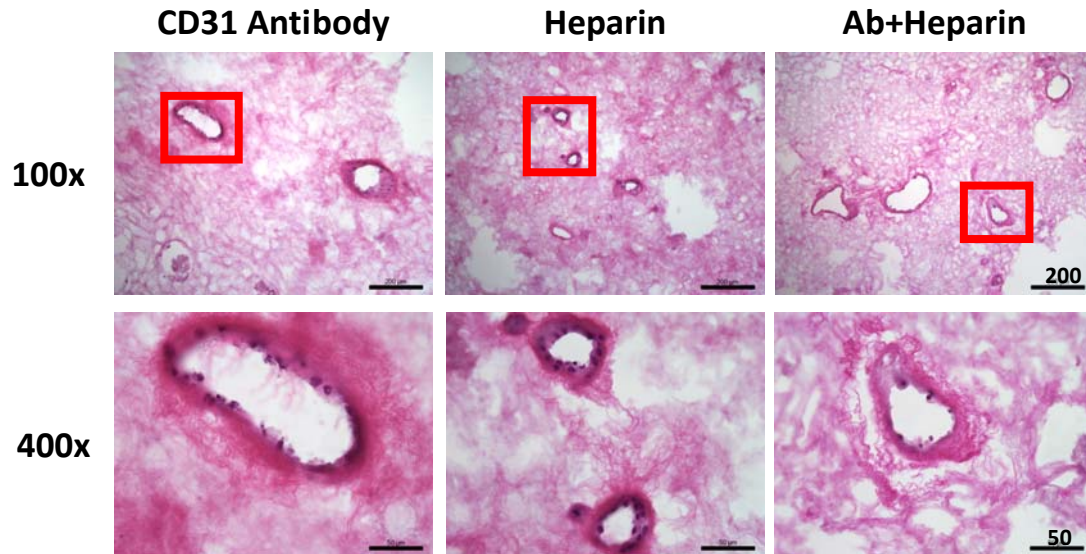


Figure 1: Representative H&E images from the lower pole of the kidneys show good cell attachment to the vascular structures of the scaffold. There appears to be no difference in cell seeding efficiency among the groups.

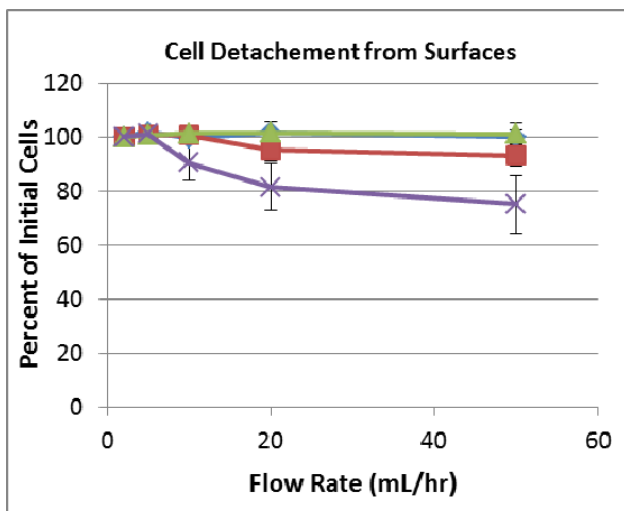


Figure 2: diamond= Hep+AB, square= Heparin, triangle= Antibody, X= collagen. Values are the percent of initial cells still adherent at each flow rate.

DISCUSSION

In an attempt to prevent clotting after implantation of whole decellularized porcine kidney scaffolds, we are investigating the addition of anti-CD31 antibody and heparin to those scaffolds. The conjugation of the CD31 antibody to a collagen surface reduced cell detachment from the surface. In vivo, this may reduce the amount of blood-ECM contact and prevent clotting. The addition of heparin may also reduce clotting.

CONCLUSIONS

This study has so far shown that heparin does not interfere with cell seeding and does not increase cell detachment under flow conditions. Future work will be to investigate the functionality of the heparin in reducing platelet adhesion.

ACKNOWLEDGMENTS

This study was supported, in part, by Telemedicine and Advanced Technology Research Center (TATRC) at the U.S. Army Medical Research and Materiel Command (USAMRMC).

REFERENCES

1. Orlando G, Farney AC, Iskandar SS, Mirmalek-Sani S-H, Sullivan DC, Moran E, et al. Production and implantation of renal extracellular matrix scaffolds from porcine kidneys as a platform for renal bioengineering investigations. *Ann. Surg.* 2012 Aug;256(2):363–70.
2. Sullivan DC, Mirmalek-Sani S-H, Deegan DB, Baptista PM, AbouShwareb T, Atala A, et al. Decellularization methods of porcine kidneys for whole organ engineering using a high-throughput system. *Biomaterials.* 2012 Nov;33(31):7756–64.

CUMULATIVE IMPACT ANALYSIS OF HEAD IMPACT EXPOSURE IN YOUTH FOOTBALL

Jillian E. Urban¹, Elizabeth M. Davenport², Alexander K. Powers^{3,5}, Joseph A. Maldjian^{2,3,4},
Christopher T. Whitlow^{2,3,4,6}, Joel D. Stitzel¹

1. Virginia Tech- Wake Forest University Center for Injury Biomechanics
2. Advanced Neuroscience Imaging Research Laboratory
3. Wake Forest University School of Medicine,
4. Department of Radiology
5. Department of Neurosurgery
6. Translational Science Institute

Corresponding Author: Jillian E. Urban, Email: jurban@wakehealth.edu

INTRODUCTION

Sports-related concussion is the most common athletic head injury. Currently, football is noted as having the highest concussion rate compared to other contact sports such as soccer, basketball, and hockey. It is estimated that nearly 1.3 million students play high school football in the United States, 100,000 players participate in college football, and 2,000 players participate in professional football. With such a large population participating in the sport, it is very important to understand exposure in the context of the total head impact exposure in order to adequately estimate risk.

Traditionally, research on the biomechanics of football-related head impact has been focused at the collegiate level. Much less research has been performed in the high school and youth populations, despite the unknown exposure of the pediatric population with developing brains. Approximately 5.6% (over 67,200) of high school football players sustain concussions in a given year. Approximately 15% of the concussions followed a previous concussion in the same season. However, these values do not reflect the estimated high underreporting rates ranging from 1 in 2 to 1 in 10 concussions.

This study adds to the ongoing investigation of head impact biomechanics in youth and high school football, and introduces a new cumulative exposure metric. This approach should be extended to multiple levels of play, and include younger age group analyses, in order to better understand the longitudinal effects on brain development during youth. These data have implications for assessment of helmet safety and improved helmet design, and ultimately can help make football a safer activity for millions of children and adolescents. The purpose of this study is to gather head impact exposure in youth and high school football athletes and quantify head impact

exposure at these levels. Secondly, a cumulative exposure metric was developed based on previously developed analytical risk curves to elucidate the exposure associated with an entire season of youth and high school football.

METHODOLOGY

Head impact exposure was measured by instrumenting the helmets of 39 high school football players and 36 youth football players (age 9-12) with the Head Impact Telemetry System (HITS) head acceleration measurement device. The HIT system included a sideline base unit with a laptop computer connected to a radio receiver and an encoder unit for each helmet. The data is wirelessly transmitted to the sideline computer where it is processed to compute kinematic data including linear and rotational acceleration, which can be analyzed in terms of the peak g's, direction of impact, or other biomechanical indicators.

The risk associated for each linear and/or rotational acceleration measured for each player was calculated based on linear¹, rotational², and combined probability (CP)³ concussion risk functions (Table 1). These data were summed to define the cumulative exposure risk (CER) for the season for each player given each risk function. CERs for all players for each age group were summed to calculate the estimated number of concussions predicted for each age group. A non-parametric Wilcoxon test was performed to identify differences between groups for each risk function.

Table 1. Logistic regression equations used in the calculation of CER.

Logistic Regression Equation	Risk Function	
$R(a) = \frac{1}{1 + e^{-\alpha + \beta x}}$	Linear	(1)
	Rotational	(2)
$CP = \frac{1}{1 + e^{-(\beta_0 + \beta_1 a + \beta_2 a^2 + \beta_3 a a)}}$	Combined Probability	(3)

RESULTS

A total of 28,559 impacts were collected over the course of the season with 17,171 accounting for high school impacts and 11,388 for youth football impacts. The high school age group observed a median peak linear acceleration of 21.9 g and 973 rad/s² and 95th percentile value of 58.7 g and 2481 rad/s², respectively. The youth age group observed a decreased median peak linear and rotational acceleration of 19.3 g and 947 rad/s² and 95th percentile value of 50.4 g and 2227 rad/s², respectively. The distributions of impacts varied within each age group, as well as between each age group. These data demonstrate that youth players are receiving high magnitude impacts similar to the high school football players.

The calculated CER value for each risk function for each age group was right skewed. A total of 2 high school and 3 youth concussions were reported for the single season. With an under-reporting rate of 1 in 10 concussions³, the CER_{CP} was found to best predict the estimated number of concussions for each age group. The CER_{Linear} was found to be significantly lower for the 9-12 age group compared to the 14-18 age groups (p<0.001). Similar findings were reflected in the analysis of CER_{Rotational} and CER_{CP}. Results demonstrate age-dependent variations in CER.

Table 2. Calculated number of concussions for each player from the CER analysis of each risk function.

IQR = Inter-quartile Range

		Player Median CER [IQR]		
Age Group	# Players	CER Linear	CER Rotational	CER CP
9 to 12	36	0.048 [0.071]	0.028[0.047]	0.214 [0.178]
HS	39	0.132 [0.191]	0.191 [0.405]	0.497 [0.933]

Table 2. Calculated number of concussions for age group from the CER analysis of each risk function.

		Team Predicted Concussions		
Age Group	# Reported Concussions	CER Linear	CER Rotational	CER CP
9 to 12	3	2.59	2.47	8.25
HS	2	7.42	15.25	33.75

DISCUSSION

The method of defining exposure risk in this study is novel as it accounts for cumulative exposure based on the player specific distribution of impacts for a given activity, and the risk of injury associated with each exposure. CER is defined as the summed exposure to the risk of concussion for each impact over the course of the season. In this approach, each linear and/or rotational acceleration experienced by the player is accounted for in the calculation of the CER.

An underreporting rate of 10x was used in the development of the CP risk function predicting 38.8 concussions per 10,000 impacts. When this method is applied to the dataset presented in this study, the predicted values for the data presented in this study reflect the underreporting rate used in the CP risk function. However, an over-estimation of the number of concussions may be observed for this population based on this risk analysis. The predicted value of 7.42 and 2.59 concussions in a single season from the collegiate linear risk function is closer to the actual number of concussions reported, however this method may not adequately represent underreporting. The linear risk function may predict injury as well as the combined probability.

CONCLUSIONS

Results of this study show that although values for the youth population are less severe and less frequent than the older counterparts, youth football players are experiencing high acceleration impacts comparable to the impacts measured in high school and adults. The CER_{CP} was found to be the closest estimate of predicted concussions given the underreporting rates reported in literature. Quantification of a cumulative metric is vital to understand the biomechanical basis of head injury that may occur over the course of the football season, and will have importance in correlating with potential pre- and post-season changes in the brain identified with magnetic resonance imaging, magnetoencephalography, and other neurological tests.

ACKNOWLEDGMENTS

The authors would like to thank the Reagan High School and the South Fork Panther football programs, especially Ashley Lake, ATC (Reagan High School), Corbin Ratcliffe, Lauren Smith and the football program. Thank you to Elizabeth Lillie, Adam Golman, Amanda Dunn, and Matt Bennett. Special thanks to the Childress Institute for Pediatric Trauma at Wake Forest Baptist Medical Center for providing support for this study.

REFERENCES

- [1] Rowson, S. and S. M. Duma, Ann Biomed Eng, vol. 39: pp. 2130-40, 2011. [2] Rowson, S., S. M. Duma, J. G. Beckwith, J. J. Chu, R. M. Greenwald, J. J. Crisco, P. G. Brolinson, A. C. Duhaime, T. W. McAllister, and A. C. Maerlender, Ann Biomed Eng, vol. 40: pp. 1-13, 2012. [3] Rowson, S. and S. M. Duma, Ann Biomed Eng, 2013.

PARTICULATE OXYGEN GENERATING SUBSTANCES (POGS) AS OXYGEN SOURCE FOR ISLET ISOLATION AND PROCESSING

JP McQuilling^{1,2}, Sivanandane Sittadjody¹, Shruti Balaji¹, Benjamin Harrison^{1,2}, Alan C Farney¹, Emmanuel C Opara^{1,2}

1. Wake Forest Institute for Regenerative Medicine, Wake Forest School of Medicine
2. Virginia Tech-Wake Forest University, School for Biomedical Engineering and Sciences

Corresponding Author: Emmanuel C Opara, Email: eopara@wfubmc.edu

INTRODUCTION

Although islets constitute ~1% of the pancreas, they receive about 6 -10% of its blood flow, indicating a disproportionate level of perfusion in which islets receive and consume lots of oxygen (O₂). The O₂ requirement of islets is interrupted during islet isolation and processing prior to transplantation, and studies have shown that hypoxia impairs islet survival and function. There has been an interest in using O₂ carriers such as Perfluorocarbon (PFC) emulsions to decrease hypoxia of islets before transplantation; however, their hydrophobicity limits their use. Particulate Oxygen Generators (POGS) represent viable alternatives to PFC. We hypothesize that continuous O₂ delivery by POGS during isolation and processing would enhance islet cell survival and graft function. The aim of our study was to examine the use of sodium percarbonate (Na₂CO₃ · 1.5H₂O₂)-based POGS, as an oxygen source during isolation and purification of islets.

METHODOLOGY

First, we determined the oxygen release profile of SPO in a saline solution in an open, hypoxic environment with 5% CO₂ at room temperature using a dissolved oxygen probe (Orion 4 Star, Thermo Science). Then, islets were isolated from male Fisher rats by intraductally infusing 1 mg/mL of Collagenase P, digesting for 20 minutes at 37 °C and purifying with an Optiprep density gradient, either with or without 100 μM sodium percarbonate (SPO) and 100 U/mL of catalase in all the isolation/purification reagents. Islet yield was measured after Dithizone staining prior to and after purification. Animal weight and the duration of each step of the isolation procedure were recorded since these two variables can have a direct

impact on islet yield. Islet viability was then assessed immediately after isolation and after 24 hours in culture by MTS assay and live/dead (CFDA/PI) stains with a quantitative procedure using the NIH Image J tool. Additionally islet functionality was assessed by dynamic perfusion with a 3.3 mM and 16.7 mM glucose solution and the insulin secretion was measured using radioimmuno assay.

RESULTS

The oxygen release data shown in Figure 1, indicated that SPO released oxygen continuously for up to 30 hours. Based on the results from the MTS assay, inclusion of SPO and catalase showed a significant increase in cell metabolism (from 0.10 ± 0.02 to 0.30 ± 0.02 absorbance units; p<0.05, n=12) at 24 hours after isolation compared to the control group (figure 2). We also found that the group of islets isolated in the presence of SPO and catalase had a higher level of viability (% mean ± SEM) measured 4 hours (70 ± 3.7 versus 59 ± 3.7; p<0.05, n = 20) and 24 hours (68 ± 2.6 versus 61 ± 1.4, p<0.05, n = 20) after isolation compared to the control group as shown in figure 3. Also, we found that islets isolated with SPO and catalase showed a significant increase in mean ± SEM rate of insulin secretion in response to high glucose immediately following isolation (131.65 ± 32.91pg/islet/min verses 72.02±21.62 pg/islet/min; p<0.05, n=4) (figure 4). Additionally, table 1 indicates there was no significant difference in the isolation times, animals' weights, or islet yield for islets isolated with or without sodium percarbonate.

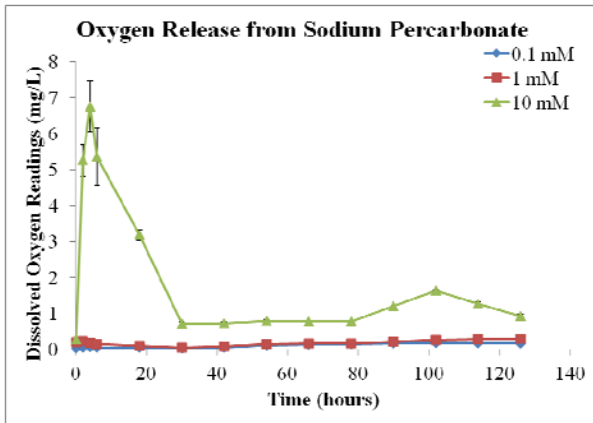


Figure 1: Dissolved oxygen release from unencapsulated SPO (Error bars represent +/- SEM of 3 values).

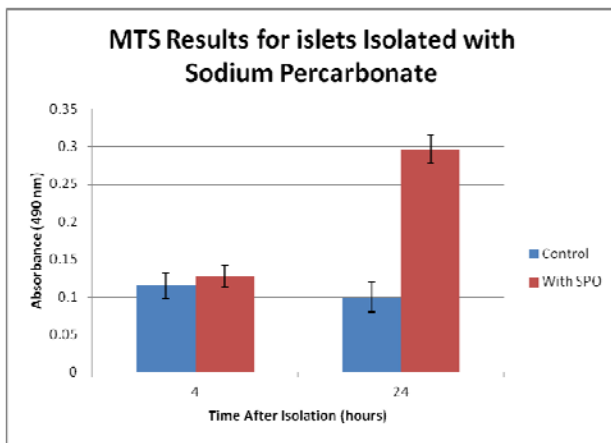


Figure 2: MTS results for islets isolated with and without sodium percarbonate at 4 and 24 hours following the isolation procedure. (n=12, error bars represent SEM)

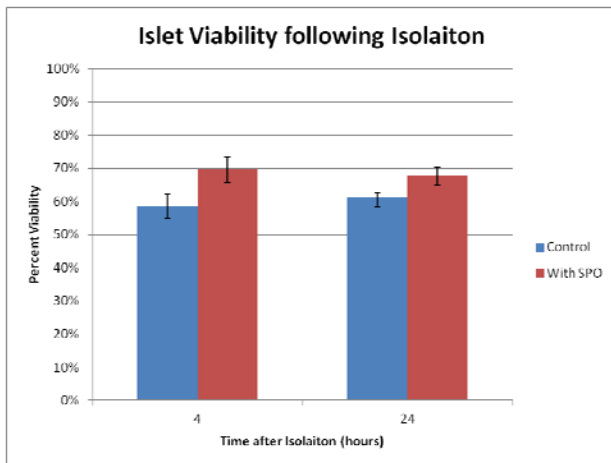


Figure 3: Percent viability immediately following islet isolation procedure and 24 hours after isolation. (n=20, error bars represent SEM)

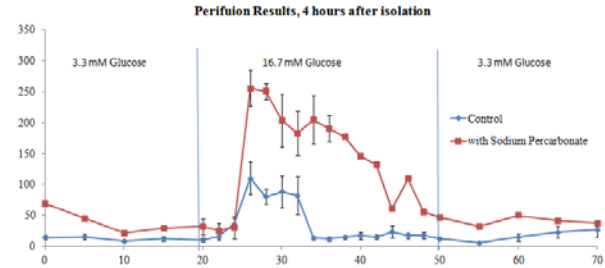


Figure 4: Insulin secretion by isolated islets 4 hours after isolation with SPO and Catalase and without (control). Error bars represent +/- SEM of 4 values.

Table 1: Isolation times, animal weight, and pre- and post-purification yield

	Control (n=4)	With SPO (n=4)
	Average ± SEM	Average ± SEM
Weight (g)	454.5±11.7	456±23.22
Pancreas Extraction Time (min)	28.5±2.92	24.5±2.06
Isolation Time (min)	118.75±2.72	114.5±2.06
Purification Time (min)	51±1.29	83±1.29
Yield (pre-purification)	1150±265.36	1012.5±71.80
Yield (post-purification)	512.5±31.45	487.5±96.55

DISCUSSION

Based on the data presented above, sodium percarbonate could be used as an effective source of supplemental oxygen to enhance islet viability during islet isolation and processing for transplantation without affecting islet yield either prior to or after purification.

CONCLUSIONS

We conclude that continuous supply of oxygen provided by SPO during islet isolation and processing reduces hypoxic injury and significantly improves islet functionality and viability.

ACKNOWLEDGMENTS

The authors would like to acknowledge financial support from the National Institutes of Health (RO1 DK080897) and the Vila Rosenfeld Estate, Greenville NC for the work in Dr. Opara's laboratory at the Wake Forest Institute for Regenerative Medicine.

MOLECULAR AND CELLULAR MECHANISMS OF BLAST-INDUCED NEUROTRAUMA

Hyung Joon Cho¹, Sujith Sajja¹, Pamela J. VandeVord^{1,3}, and Yong Woo Lee^{1,2}

1. Virginia Tech-Wake Forest University, School of Biomedical Engineering and Sciences, Blacksburg, VA 24061

2. Department of Biomedical Sciences and Pathobiology, Virginia Polytechnic Institute and State University, Blacksburg, VA 24061

3. Veterans Affairs Medical Center, Salem, VA 24153

Corresponding Author: Hyung Joon Cho, Email: hjcho79@vt.edu

INTRODUCTION

Majority of the veterans returning from Operation Iraqi Freedom (OIF) and Operation Enduring Freedom (OEF) are suffering from closed head injuries due to blast overpressure (BOP) exposure. However, molecular and cellular mechanisms of brain injury after exposure to BOP have not yet been fully understood. The present study hypothesizes that brain injury mediated by generation of oxidative stress, stimulation of inflammation, and induction of neuronal and endothelial cell deaths may contribute to the pathophysiology of blast-induced neurobehavioral impairments.

METHODOLOGY

Male Sprague Dawley rats were anesthetized and exposed to calibrated BOP of 129.23 ± 3.01 kPa while controls received only anesthesia. Animals underwent novel object recognition (NOR) test 2 weeks following BOP prior to sacrifice. The levels of reactive oxygen species (ROS) were visualized by in situ dihydroethidium (DHE) fluorescence staining. The mRNA expression levels of pro-inflammatory mediators, such as interferon- γ (IFN- γ) and monocyte chemoattractant protein-1 (MCP-1), were determined by quantitative real-time reverse transcriptase-polymerase chain reaction (RT-PCR). The protein expression levels of IFN- γ and MCP-1 were detected by immunofluorescence staining and enzyme-linked immunosorbent assay (ELISA). Additionally, a series of immunofluorescence staining with antibodies against neuronal nuclei (NeuN) and platelet endothelial cell adhesion molecule-1 (PECAM-1 or CD31) was performed to determine neuronal and endothelial cell deaths. One-way ANOVA and two-way ANOVA with replication were employed to compare mean responses with/among the respective comparison groups using Sigmaplot 11. Differences among the means were considered significant at $p < 0.05$.

RESULTS

In situ DHE fluorescence staining revealed that BOP significantly increased production of ROS in brains (Fig. 1), suggesting blast-mediated animals exhibited acutely produces pro-oxidative environment in rat hippocampus.

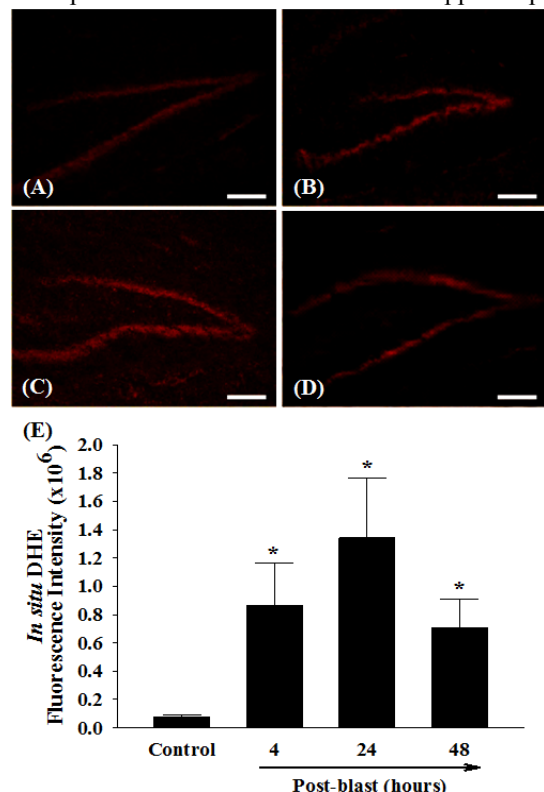


Fig. 1. In situ DHE fluorescence staining following BOP exposure. Data represent means \pm SEM for each group (n=4). * $p < 0.05$ vs. control. Scale bar: 100 μ m.

In addition, real-time RT-PCR, immunofluorescence staining and ELISA demonstrated a significant up-

regulation of mRNA and protein expressions of pro-inflammatory mediators, such as IFN- γ and MCP-1, in brains collected from BOP-exposed animals compared with the controls (Fig. 2). The maximal mRNA expression of both IFN- γ and MCP-1 were observed at 4 hours post-blast (2.38- and 2.34-fold induction, respectively, compared with the controls). Consistent with the gene expression data, blast-mediated increases in mRNA levels of both IFN- γ and MCP-1 translated to elevated protein expressions in rat hippocampus at 24 hours post-blast (4.78- and 1.99-fold induction, respectively, compared with the controls). These results indicate that BOP induces pro-inflammatory environment in rat brain.

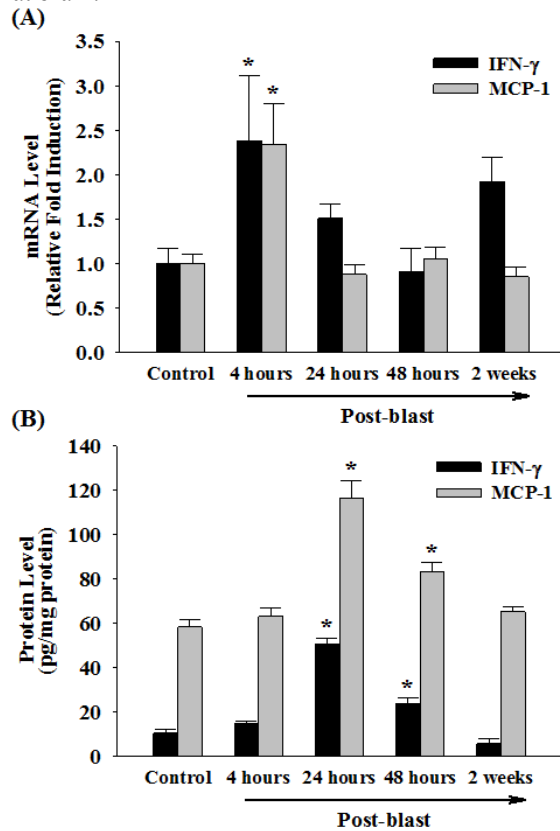


Fig. 2. Expression of pro-inflammatory mediators by real-time RT-PCR and ELISA after blast exposure. (A) mRNA and (B) protein expression levels of IFN- γ and MCP-1. Data represent means \pm SEM for each group (n=5). *p<0.05 vs. control.

Furthermore, immunoreactivity of NeuN in brains indicated that fewer neurons were present following BOP exposure (Fig. 3A). Significantly reduced levels of CD31-immunoreactive endothelial cells were also detected in brains following BOP exposure (Fig. 3B). Moreover, NOR paradigm showed a significant impairment in the working memory following BOP exposure (Fig. 3C). These suggest that BOP may partly contribute to neuronal loss and endothelial cell death with neurobehavioral deficits.

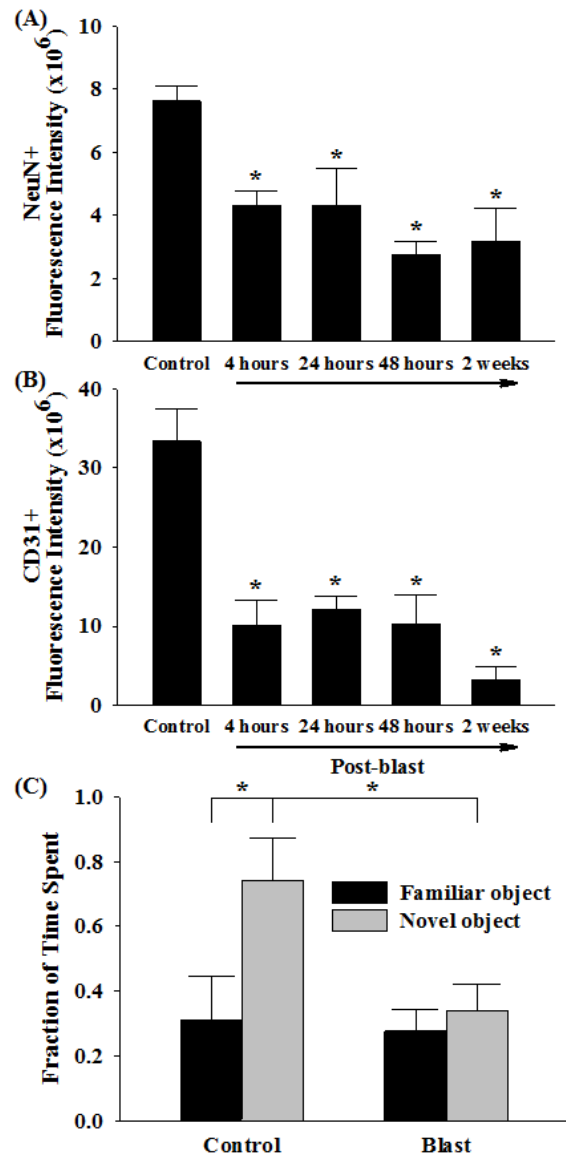


Fig. 3. Neuronal cell loss, endothelial cell death in rat brain and behavioral changes after blast exposure. (A) NeuN and (B) CD31 protein expression by immunofluorescence staining and (C) NOR test. Data represent means \pm SEM for each group (A and B: n=4; C: n=5). *p<0.05 vs. control.

CONCLUSIONS

These results suggest that pro-oxidative and pro-inflammatory environments in brain could play a potential role in BOP-induced neurodegeneration and behavioral deficits. It may provide a foundation for defining a molecular and cellular basis of the pathophysiology of blast-induced neurotrauma. It will also contribute to the development of new therapeutic approaches selectively targeting these pathways, which have great potential in protecting the brain from BOP-mediated damage.

DESIGN OF A FORCE PROBE SYSTEM FOR ACTIVE PULL OF A SINGLE CELL

Kevin T. Sheets¹ and Amrinder S. Nain^{1,2}

1. School of Biomedical Engineering and Sciences, Virginia Tech

2. Mechanical Engineering, Virginia Tech

Corresponding Author: Kevin Sheets: sheetsk@vt.edu

INTRODUCTION

Cells interact with their fibrous surroundings known as extracellular matrix (ECM), which provides structural and chemical cues that dictate several cellular behaviors [1–3]. Cells exert forces against their ECM and knowledge of these forces can be used to develop single cell diagnostic/drug testing platforms. For instance, progressive stages of cancer can be identified by changes in cell elasticity and variations in viscoelastic parameters [4]. Recently, substrates from traction force gels and micropillar arrays to three-dimensional particle tracking have been designed which attempt to capture the evolution of such forces. Force measurement through fibrous scaffolds mimicking the native ECM is still in infancy mainly due to difficulties in fiber spatial deposition and control on dimensions [5–7]. Fiber-based platforms provide curvature and stiffness cues present in ECM which are masked by aforementioned substrates. Additionally, cells may modulate their forces in response to changes in fiber structural stiffness (N/m), a key descriptive which inherently is absent in flat substrate studies.

Our lab has recently demonstrated the ability to produce cellular force measurement scaffolds composed of alternating hierarchical assemblies of aligned nanofibers via the Spinneret-based Tunable Engineered Parameters (STEP) technique (Figure 1) [8–11]. The scaffolds are fused at fiber intersections and thus contain pinned boundary conditions that can be modeled using classical beam theory in the elastic limit, allowing the fibers to deflect appreciably under cell-scale, nano-Newton (nN) loads. With control over structural stiffness parameters such as fiber diameter, length, and modulus (N/m²), tunable structural stiffness (N/m) scaffolds are spun which capture cell migratory forces in real-time.

However, the deflections and corresponding forces observed with these structures may not necessarily depict the true adhesion limit of a given cell. If, as some reports have suggested, cells modulate their force according to their surrounding mechanical environment, an external probe would be needed to demonstrate the extent of the relationship of maximum adhesion strength and fiber structural stiffness. Therefore, this work details the design, fabrication, and use of a cellular micropipette-based single cell adhesion probe puller developed for understanding the changes in cellular viscoelasticity and adhesion dynamics to external mechanical stimuli.

METHODOLOGY

STEP Scaffold Manufacturing

The previously-reported STEP technique was used to manufacture PS-PS scaffolds with fused intersections. To create fibers which show appreciable deflection under cellular loads, thin (~300nm) PS fibers were spun

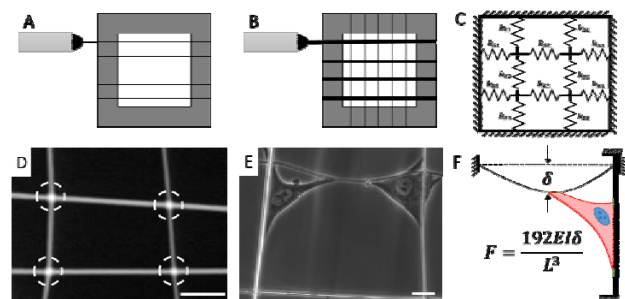


Figure 1: STEP force scaffold design, showing that A) small-diameter fibers are spun first, B) large-diameter fibers are spun on top, C) the fused assembly is modeled as springs in series, D) SEM image showing fiber fusion at intersections, E) optical image of cells migrating along the scaffolds, and F) schematic showing deflection of the small fiber with no appreciable deflection in the large fiber. The equation used to estimate force output is given. Scale bar 20 μm.

orthogonal to thick (~800nm) fibers with at least 200 μm inter-fiber spacing.

Probe Design & Pulling Experiment

Micropipette probes were pulled from 1.0 mm diameter glass rods (Sutter, Novato, CA) using the P-1000 Flaming/Brown micropipette puller (Sutter). A pulling program was developed so that the pulled pipette reduced to a 1 μm tip at a relatively steep gradient. Probes were loaded to an MP-285 motorized manipulator (Sutter) which allowed precise control over probe placement, motion, and strain rate. A typical pull was conducted by pulling apart the first fiber of a parallel fiber system with a cell attached to it using the probe. Using time lapse microscopy, cell adhesion dynamics were recorded, and the resultant adhesion force was determined using the deflection of the second fiber. Strain rate was varied from 0.3 $\mu\text{m/s}$ to 100 $\mu\text{m/s}$, and fiber stiffnesses varied from 0.003 – 0.06 mN/m depending on cell location along the length of the fiber.

RESULTS AND DISCUSSION

By tracking fiber deflection caused by the cells over time, profiles of cell adhesion and eventual failure were calculated (Figure 2). There were typically two modes of failure observed: peeling and breaking. At low strain rates, the cell membrane was visibly able to deform to accommodate the applied load and more commonly failed by peeling off the fiber. At high strain rates ($\geq 10 \mu\text{m/s}$), cells failed before accommodating the directionality of the applied load, exhibiting more abrupt elastic failure.

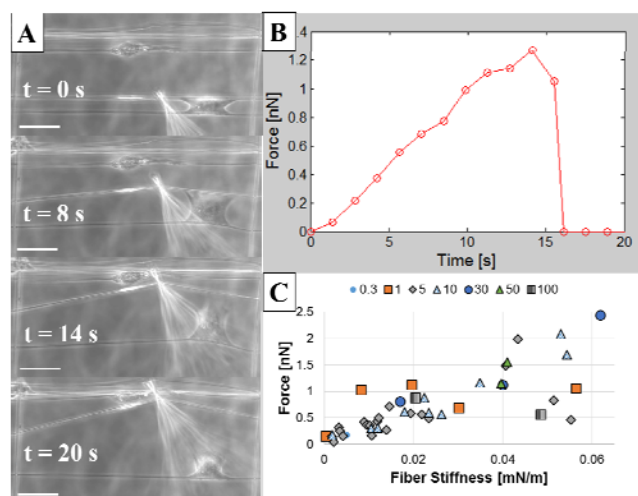


Figure 2: Probe pulling a cell between parallel fibers. Scale bar 50 μm . A) As the probe tip moves, the top fiber moves with it. The adhesion strength of the cell is measured by the deflection of the bottom fiber, B) typical force vs. time plot demonstrating increasing force until breakage, and C) aggregate data of maximum force plotted vs. fiber stiffness, arranged by strain rate ($\mu\text{m/s}$). N = 65.

Interestingly, it was found that there was a statistical correlation between strain rate and adhesion force at failure as well as cell strain at failure. Higher force and lower cell stretch were seen at high strain rates, and lower force and higher cell stretch were seen at low strain rates. The system captures viscoelastic behavior of the cells in response to the externally applied force, stiffening the cells and preventing relaxation at high strain rates. Preliminary relaxation tests performed using this system are also able to capture viscoelastic behaviors, and when incorporated into the standard linear solid (SLS) model, are able to predict cell elasticity. In the future, we hope to use this system to estimate changes in cellular elasticity on suspended fibers in response to cytoskeleton-altering drugs and relate it to dose dependent calcium flux response at single cell resolution.

CONCLUSIONS

STEP force scaffolds were used in conjunction with an in-house micropipette-based probe to externally pull cells off of fibers. We find through tracking fiber deflection that final adhesion force is correlated with fiber stiffness and cell strain, indicating that cells exhibit a stress-stiffening response associated with viscoelasticity.

ACKNOWLEDGMENTS

The authors would like to acknowledge support received from the Institute for Critical Technology and Applied Sciences (ICTAS) at Virginia Tech. This research was funded in part by the Jeffress Memorial Trust Fund and the Bill and Andrea Wade Research Fund.

REFERENCES

- Lo, C.M., H.B. Wang, M. Dembo, and Y.L. Wang. 2000. *Biophys J.* 79: 144–52.
- Engler, A.J., S. Sen, H.L. Sweeney, and D.E. Discher. 2006. *Cell.* 126: 677–89.
- Nakashima, Y., and T. Yasuda. 2007. *Sensors and Actuators A: Physical.* 139: 252–258.
- Ketene, A.N., P.C. Roberts, A.A. Shea, E.M. Schmelz, and M. Agah. 2012. *Integr Bio.* 540–549.
- Han, S.J., K.S. Bielawski, L.H. Ting, M.L. Rodriguez, and N.J. Sniadecki. 2012. *Biophys J.* 103: 640–648.
- Sabass, B., M.L. Gardel, C.M. Waterman, and U.S. Schwarz. 2008. *Biophys J.* 94: 207–20.
- Fu, J., Y.-K. Wang, M.T. Yang, R. a Desai, X. Yu, et al. 2010. *Nat Methods.* 7: 733–736.
- Nain, A.S., M. Sitti, A. Jacobson, T. Kowalewski, and C. Amon. 2009. *Macromol Rapid Comm.* 30: 1406–12.
- Sheets, K., Wunsch, S., Ng, C., Nain, A.S. 2013. *Acta Biomaterialia.* In Press
- Sheets, K., Wang, J., Meehan, S., Sharma, P., Ng, C., Khan, M., and Nain, A.S. 2013. *J. Biomat Tissue Eng.* In Press.
- Nain, A.S., J.A. Phillippi, M. Sitti, J. Mackrell, P.G. Campbell, et al. 2008. *Small.* 4: 1153–9.

SHORT TERM MILD TRAUMATIC BRAIN INJURY MECHANISMS CHARACTERIZED IN AN IN VIVO GÖTTINGEN MINIPIG MODEL

Elizabeth M. Fievisohn¹, Sujith V. Sajja¹, Bethany M. Vaughn¹, Pamela J. VandeVord¹, and Warren N. Hardy¹

1. Center for Injury Biomechanics (Virginia Polytechnic Institute and State University, Virginia Tech-Wake Forest School of Biomedical Engineering and Sciences)

Corresponding Author: Elizabeth Fievisohn, Email: lizf87@vt.edu

INTRODUCTION

Traumatic brain injury (TBI) persists in the United States¹ despite a large research effort over the years. Some of the classic experimental models studying TBI are fluid percussion², inertial rotation³, controlled cortical impact⁴, and weight drop⁵. These models do have limitations with the animal models used, and relevant injury methods.

This study seeks to answer many of the unknowns surrounding mild TBI regarding the mechanisms and pathogenesis involved over 24 hours by using magnetic resonance spectroscopy (MRS) and immunohistochemistry (IHC).

METHODOLOGY

Fifteen Göttingen minipigs were divided into four experimental groups; 1 hour sham control (n=1), 24 hour sham control (n=2), 1 hour rotational injury (n=4), or 24 hour rotational injury (n=8), for which the interval corresponds to the survival time. The animal protocol was approved by Wake Forest University Baptist Medical Center's Animal Care and Use Committee.

Animals undergo baseline 7T MRI scans prior to injury, immediately after injury, and twenty-four hours post injury. MRS is performed on a 216 mm³ voxel placed in the genu of the corpus callosum. Metabolites of interest include glutamate and glutamine (Glu+Gln), N-acetylaspartate (NAA), N-acetylaspartylglutamate (NAAG), choline, and myoInositol.

The rotational injury device (Figure 1) consists of two aluminum plates that are allowed to rotate with respect to each other. The device has the ability to be dropped from different heights onto brass tubing which causes

repeatable rapid deceleration of the whole minipig. Two linear accelerometers, one angular accelerometer, and one angular rate sensor are used to characterize the event. High speed video is taken for overall observation.

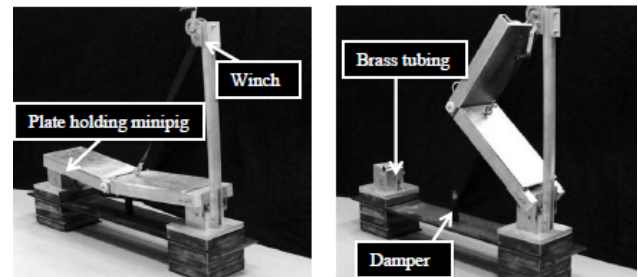


Figure 1: Important components of the rotational injury device⁶.

After post injury scanning, the brains are perfused and harvested for IHC. IHC was performed in the genu of the corpus callosum using six antibodies; light neurofilament, heavy neurofilament, glial fibrillary acid protein (GFAP), caspase-3, β amyloid precursor protein (β APP), and Iba-1. ImageJ was used to calculate integrated density for comparison between groups.

RESULTS

Average peak linear acceleration, average peak rotational acceleration, and average peak rotational speed measured during injury are shown in Table 1.

Table 1: Peak parameters measured from instrumentation including peak linear and rotational acceleration and peak rotational speed.

Severity Level	n	Ave Peak Linear Accel. (G's)	Ave Peak Rotational Speed (rad/s)	Ave Peak Rotational Accel. (rad/s ²)
15°	4	43	8	1800
25°	5	63	10	2000
40°	3	103	11.5	3300

Metabolite trends suggest that as early as 1 hour post injury, Glu+Gln and NAA increases after injury while NAAG decreases. In addition, the ratio of Glu+Gln/NAAG and Glu/Gln increases.

IHC is showing increases in light and heavy neurofilament due to injury (Figure 2). However, caspase-3 and GFAP do not show differences (Figure 3).

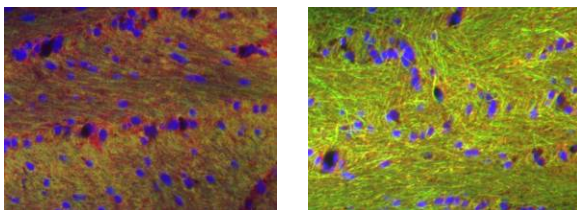


Figure 2: Light (green) and heavy (red) neurofilament stain with a DAPI counterstain. Left: sham; right: 40°.

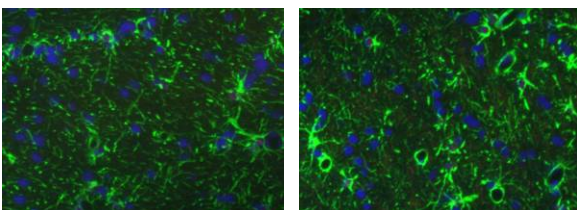


Figure 2: GFAP (green) and caspase-3 (red) neurofilament stain with a DAPI counterstain. Left: sham; right: 40°.

DISCUSSION

The metabolite trends suggest one response due to injury. It is possible that NAAG is being broken down by glutamate carboxypeptidase II into Glu and NAA which explains the increase in Glu and NAA after injury and decrease in NAAG. This is supported by the Glu+Gln/NAAG increase. An increase in glutamate indicates excitotoxicity.

The staining so far has shown trends of mild injury as indicative by the increase in neurofilament buildup after injury, but not in caspase-3 which marks cell apoptosis.

The next step is to study and characterize this type of injury longitudinally over 2 weeks. A behavioral and biomarker component will be added to the study for a more comprehensive understanding of the injury.

High speed biplane x-ray will be used to measure the relative brain/skull kinematics that can be used to develop a finite element model of the minipig that relates brain motion to damage.

Ultimately, a mild TBI threshold will be developed and underlying neuronal damage will be characterized caused by known accelerative inputs to a relevant animal model.

CONCLUSIONS

This study is designed to answer some of the unknowns surrounding TBI. So far, there has been evidence that minipigs have undergone mild TBI as indicated both by MRS and IHC.

In the future, a new head injury criterion can be developed based on neuronal damage caused from an accelerative input. This will be more specific than the current standard (HIC).

ACKNOWLEDGMENTS

This work was funded in part by the National Highway Traffic Safety Administration.

REFERENCES

- 1 Traumatic Brain Injury in the United States. 1-74 (U.S. Department of Health and Human Services Center for Disease Control and Prevention, 2002-2006).
- 2 Lindgren, S. & Rinder, L. Experimental Studies in Head Injury II. Pressure propagation in "percussion concussion". *Biophysik* **3**, 174-180 (1966).
- 3 Unterharnscheidt, F. J. & Higgins, L. S. Traumatic lesions of brain and spinal cord due to nondeforming angular acceleration of the head. *Texas Report on Biology and Medicine* **27**, 127-166 (1969).
- 4 Lighthall, J. W. Controlled Cortical Impact: A New Experimental Brain Injury Model. *Journal of Neurotrauma* **5**, 1-15 (1988).
- 5 Marmarou, A. *et al.* A New Model of Diffuse Brain Injury in Rats, Part I: Pathophysiology and Biomechanics. *Journal of Neurosurgery* **80**, 291-300 (1994).
- 6 Fievisohn, E. M., Vaughn, B. M. & Hardy, W. N. Techniques for the Investigation of Traumatic Brain Injury Mechanisms Characterized by Magnetic Resonance Spectroscopy. *Biomedical Sciences Instrumentation* **48**, 126-133 (2012).

QUANTIFICATION OF THE TRANSPORT OF LIVE AUTONOMOUS DRUG PARTICLES (DRUGBOTS) IN TUMOR SPHEROIDS INTERSTITIUM

Mahama A. Traore¹, Ali Sahari¹, and Bahareh Behkam²

1. Virginia Tech, Mechanical Engineering

2. Virginia Tech, School of Biomedical Engineering and Sciences

Corresponding Author: Mahama A. Traore, Email: mtraore@vt.edu

INTRODUCTION

Limited efficacy of the existing chemotherapeutic treatments of primary cancer tumors is partially attributed to the limited diffusion distance of the drug particles which prevents successful treatment of the quiescent tumor cells.

For an anticancer drug to be effective against a solid primary tumor, it must be able to reach all cancerous cells within the tumor to prevent clonogenic tumor stem cells from regeneration. Current chemotherapeutic drugs have limited penetration within the tumor.

The low selectivity of anti-cancer drugs with respect to cancerous tissue is also problematic due to the exposure of healthy cells to anti-cancer drugs. Thus, chemotherapy can be enhanced through both better anti-cancer drug cargo targeting towards cancerous cells.

Several strains of attenuated bacteria, such as *Escherichia coli*, have been identified to possess the natural ability to target and preferentially colonize tumor tissues. In this work, we demonstrate that the tumor targeting *E. coli* bacteria can be coupled with therapeutic nanoparticles to form intelligent autonomous drug carriers (Hereafter referred to as DrugBots, Fig. 2b).

The use of innate sensing and propulsion capabilities in DrugBots can dramatically improve delivery of chemotherapeutic to solid primary tumors. DrugBots actively sense and target cancer tumors and utilize chemotaxis to carry drug nanoparticles deep into the tumor^{1,2}.

We have demonstrated that DrugBots can penetrate 8.66% deeper within the tumor tissue as opposed to

commonly used passively diffusing chemotherapeutic nanoparticles.

METHODOLOGY

DrugBots consists of an engineered abiotic body (i.e. drug-laden particles) and a living component (i.e. bacteria) for sensing and actuation purposes. Here, the DrugBots consists of *Escherichia coli*, MG1655 bacteria which naturally perform chemotaxis towards chemical compounds produced by quiescent cancer cells and have been shown to penetrate and colonize tumors. They are attached to spherical polystyrene nano-particles.

For the construction of the DrugBots, *E. coli* MG1655 bacteria were grown in L-broth then incubated with goat polyclonal anti-Lipid A LPS antibody labeled with biotin (10 µg/mL) for 1 hour at room temperature³. Streptavidin coated 500 nm diameter nanoparticles were then mixed with the bacteria and incubated at room temperature for 20 minutes.

Tumor spheroids were grown in-vitro using human colon carcinoma cells (HT-29) in low adhesion round bottom 96-well plates⁴. To quantify the extravascular transport of the DrugBots, 0.1% (w/v) of DrugBots suspended in DMEM culture media were incubated with the tumor spheroids for 3 hours and imaged using fluorescence microscopy. As shown in Figure 1, for the distribution and penetration studies, tumor spheroids were divided into two specific regions: proliferative region given by the live cells ring (region 1) and non-proliferative region (necrotic and quiescent cells, region 2). The distribution of passively diffusing nanoparticles and DrugBots within the tumor was quantified.

RESULTS

The distribution of the DrugBots as well as passively diffusing nanoparticles was quantified by measuring the fluorescence intensity in each region of interest (Fig. 1).

Our preliminary results indicate that DrugBots have the capability to transport loads deeper within the tumor tissue. From the penetration analysis (Fig. 3), it can clearly be seen that particles have limited penetration in the tumor spheroid (only 25% of the nanoparticles have reached region 2) as opposed to bacteria carrying nanoparticles that penetrate the tumor farther and have a more uniform distribution in the tumor (34% of DrugBots have penetrated the tumor past region 1).

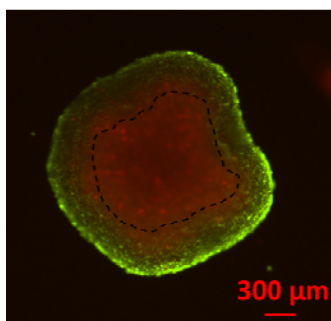


Figure 1. Fluorescent microscopy image illustrating a colon carcinoma HT-29 tumor spheroid. Proliferating ring (region 1) primarily consists of live cells (green) and the necrotic and quiescent cells (region 2) consist of dead and dormant cells (red).

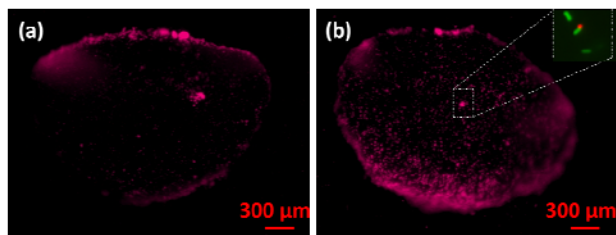


Figure 2. (a) 500 nm diameter particles distribution in tumor. (b) Distribution of DrugBots with 500 nm particles in tumor after 15 hours. (d) Graph illustrating the enhanced penetration of DrugBots vs. passive nanoparticles.

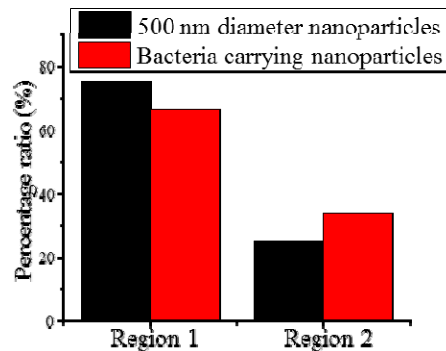


Figure 3. Graph illustrating the enhanced penetration of DrugBots vs. passive nanoparticles.

CONCLUSIONS

This study demonstrates that bio-hybrid tumor targeting systems (drug loaded nanoparticles self-assembled with bacteria via covalent bonding) can be used as live autonomous drug delivery agents with enhanced selectivity and penetration of solid tumors.

As illustrated in this work, bacteria carrying particles can penetrate a solid tumor past the proliferating ring into the quiescent and necrotic core with a fairly homogeneous distribution in the tumor.

ACKNOWLEDGMENTS

The author appreciate the help of Professors Amrinder Nain (ME, VT), Rafael Davalos (BME, VT), and Daniela Cimini (Bio, VT), Shiv Kale (VBI, VT). We would also like to thank Kevin Sheets, Puja Sharma, Sean Meehan, and Meghan Canter for help with the experiment. This work was supported by the National Science Foundation (IIS-117519).

REFERENCES

1. K. Low *et al.* Nature biotech., 17:37-41, 1999
2. R. Kasinskas *et al.* Biotechnol and Bioeng., 94: 710-721, 2006
3. A. Sahari *et al.* Biomed Microdevices., 14: 999-1007, 2012
4. A. Ivascu *et al.* J Biomol Screen., 11: 922-932, 2006

THE DEVELOPMENT OF VOLUMETRIC ORGANS FROM A MULTI-MODALITY IMAGE DATASET FOR USE IN A SMALL FEMALE FULL-BODY FINITE ELEMENT MODEL

Matthew L. Davis^{1,2}, Ashley R. Hayes^{1,2}, F. Scott Gayzik^{1,2}, Daniel P. Moreno^{1,2}, Joel D. Stitzell^{1,2}

1. Wake Forest University School of Medicine

2. Virginia Tech-Wake Forest Center for Injury Biomechanics

Corresponding Author: Matthew Davis, Email: mattdavi@wakehealth.edu

INTRODUCTION

Motor vehicle injuries and fatalities remain a leading public health concern worldwide. In 2009, the World Health Organization reported more than 1.2 million deaths as a result of motor vehicle crashes [1]. With the goal of mitigating the societal impact of this epidemic, researchers are using a variety of tools, including finite element (FE) models, to accurately predict injury. Such models are often developed to represent an average (50th percentile) male occupant. However, in a study conducted in 2010, female drivers were found to represent the majority of drivers 35 year of age and younger [2]. In order to predict the response of a greater portion of the driving public, there is an interest in developing such models for the smallest cohort among the driving public; female drivers in the 5th percentile of height and weight. Traditionally, such 5th percentile female models have been scaled from existing models, since scan data for such a specific target anthropometry is limited. However, as part of the Global Human Body Models Consortium, scan data of the 5th percentile female were acquired. The objective of this study was to develop volumetric representations of organs using this novel multi-modality image set and compare them to organ volumes from population based studies.

METHODOLOGY

Subject recruitment and imaging protocol was approved by the Wake Forest School of Medicine Institutional Review Board (IRB #5705). An individual representing the 5th percentile female (F05) in terms of height (149.9cm), weight (48.0±0.63kg), and body mass index (21.4kg/m²) was selected and imaging data was collected. The selected individual was a close match with a height of 150.9 cm and weight of 49.0 kg. Additionally, 15

external anthropomorphic measurements were taken from the subject to meet criteria published by Gordon et al [3]. In order to be recruited for the study, the average of the screening anthropometry had to be within 5% of the targeted values.

Computed tomography (CT), Magnetic Resonance Imaging (MRI), Upright MRI, and external anthropometry of the individual representing the F05 were obtained in three postures: supine, seated, and standing. A GE Lightspeed (CT), GE Twin Speed (MRI), and Fonar Upright MRI were used to collect image data, with each set of image data deemed anatomically normal after examination by a radiologist. Images were acquired with slice thicknesses from 0.65 mm to 2 mm and field of view (FOV) ranging from 250 mm to 500 mm. The image sets from the various modalities were then merged into a continuous set of images using Amira software (Visage Imaging, San Diego, CA). The merged image sets were then used for segmentation of bones and soft tissue. Image segmentation was completed using Mimics software (v15.0, Materialise, Leuven, Belgium) with manual and semi-automatic techniques. All segmented data were then conditioned using Geomagic Studio software (Studio v.12, Geomagic, Research Triangle Park, NC) [4]. In this study, MRI data were used to segment thoracoabdominal organs that will be represented in subsequent finite element models of the small female. The collected volume data for individual abdominal organs were then compared to 5th percentile female volumes in literature [5]. Volumetric data were also found for three thoracic organs: the heart, left lung, and right lung.

RESULTS

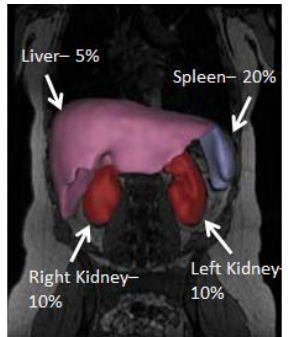
The selected subject was a close representation of the 5th percentile female in terms of height and weight, with deviations less than 2%. The subject had a clean medical record and was in good health. A selection of acquired external anthropometry data is shown in Table 1. For the 5 measurements shown, the recruited subject was within 2.6% of the target measurements and for all 15 measurements the average subject deviation was 4.1%.

Table 1. Anthropometry selection dimensions (cm) [3]

Sitting Height	Hip Breadth	Buttock Knee Length	Knee Height	Chest Circumference
80.0	35.6	52.8	46.0	83.8

The volumes of the segmented abdominal organs were compared to values from the literature describing the F05 abdomen. The liver volume was found to be within the 5th percentile and the right and left kidneys within the 10th percentile. The spleen volume showed the largest deviation falling in the 20th percentile. These results are summarized in Table 2. Three thoracic organs, the heart, right lung, and left lungs, were also segmented. In the case of both the heart and lungs, organ volumes were assumed to be perfused with blood. The volumes for the heart, left lung, and right lung were determined to be 56.8 cm³, 103.9 cm³, and 119.6 cm³ respectively.

Table 2. Subject and F05 Abdominal Organ Volumes

	Subject	F05 [5]	
Liver (mL)	1024.7	974.9	
Right Kidney (mL)	112.1	98.2	
Left Kidney (mL)	122.3	106.7	
Spleen (mL)	131.2	71.1	

DISCUSSION

The data sets were optimized by inclusion of image data from various modalities, each with relative strengths in model development such as CT data for bone segmentation and MRI data for soft tissue segmentation. The segmented abdominal organs showed reasonable agreement with the published data representing the F05 abdomen. However, because the spleen was in the 20th percentile range, scaling methods will be applied to allow for a better representation of the 5th percentile geometry

derived from the literature. Also, the segmented left lung was approximately 15.1% smaller than the right lung, which agrees with the average difference of 15% found in the literature.

CONCLUSIONS

This pilot study presents volumetric organ data from image segmentation of a prospectively recruited small female. The data set is the first of its kind, acquired explicitly for the development of a full-body finite element model of the 5th percentile female. The image set was developed using image data from various modalities used to allow for more accurate segmentation. The set also includes data with the subject seated upright against gravity. The abdominal organs segmented from the image sets showed reasonable agreement with the published volumetric data representative of the F05. Volumetric data was also obtained for three thoracic organs. Future efforts with this set will be to compare the directly segmented abdominal and thoracic organs to previous work in which these parts were scaled to the size of interest from male datasets. This data will be used as part of continued research and development as part of the Global Human Body Models Consortium (GBHMC) project.

ACKNOWLEDGMENTS

This work was funded by the Global Human Body Models Consortium, LLC.

REFERENCES

1. World Health Organization. *Global Status Report on Road Safety*. Geneva, Switzerland 2009.
2. Sivak, M., Schoettle, B. (2012). *A Note: the Changing Gender Demographics of U.S. Drivers*.
3. Gordon, C.C., Churchill, T., Clauser, C.E., Bradtmiller, B., McConville, J.T., "Anthropomorphic Survey of U.S Army Personnel: Methods and Summary Statistics 1988," Prepared for United States Army Natick Research, 1989.
4. Gayzik, F.S., Moreno, D.P., Geer, C.P., Wuertzer, D.S., Martin, R.S., Stitzel, J.D., The development of full body geometrical data for finite element models: A multi-modality approach. 2011. *Annals of Biomedical Eng.*, Oct; 39(10):2568-83. Epub 2011 July 23.
5. Valentin, J., *Basic Anatomical and Physiological Data for Use in Radiological Protection: Reference Values*. 2002. *Annals of the ICRP*.

ELUCIDATING THE TEMPORAL EFFECTS OF TEMPERATURE ON TRANSPORT PROPERTIES AND EFFICACY OF MULTIMODAL PHOTOTHERMAL AND CHEMOTHERAPY TREATMENTS

Matthew R. DeWitt¹, Kristen A. Zimmermann¹, and Marissa N. Rylander¹

1. Virginia Tech-Wake Forest School of Biomedical Engineering and Sciences, Virginia Tech
Corresponding Author: Matthew R. DeWitt, mttdwtt@vt.edu

INTRODUCTION

Photothermal therapy is a cancer treatment that utilizes light energy to deposit specific amounts of heat to effectively kill cells in a specified tumor region. While Hyperthermia has been widely used for centuries as a treatment option for a variety of diseases, Localized Hyperthermia, as seen in photothermal therapies, has seen a rapid increase in use as a cancer treatment due to its non-invasive nature, low cost, simplicity, and reduced complications as compared to other currently available resection options [1]. The inclusion of nanoparticles that are capable of intense absorption in a specific wavelength band allows for higher selectivity of this thermal dose based upon the location of the delivered nanoparticles through both the additional absorption of laser energy, which gets deposited as heat, in the desired location containing the photoabsorbers and by lowering the amount of energy or power of the laser necessary to affect the region of interest, thus lowering the energy applied to the non-desired thermal damage region[2].

Hyperthermia, as seen in photothermal therapies, has been shown to not only act as an effective therapy for many types of tumors including urinary bladder cancers (UCCs) at moderate to severe temperatures(45-60°C), but additionally as an adjuvant to chemotherapy at slightly elevated temperatures(40-45°C), enhancing chemotherapeutics based on different temporally defined hyperthermia. While the synergistic effects of chemotherapeutics(CT) and hyperthermia(HT) has been reported previously, a new avenue of HT treatments, nanoparticle mediated photothermal therapies, has provided a foundation for new treatment regimens. Carbon nanomaterials such as Single Walled Nanohorns(SWNHs) have shown great promise for this multimodal therapy as they have high absorption in the

NIR region, leading to significant heat deposition and, due to their high pore space, can be loaded with a CT[3]. To better understand the complex relationship between HT and CT and between HT and the intercellular transport of the drug carrying, photo-absorptive SWNHs, an in vitro study was realized including fluorescently tagging the inherently non-fluorescent SWNHs for studying uptake kinetics and utilizing a 3D tumor model.

METHODOLOGY

Human breast cancer cells MDA-MB-231(ATCC), human pancreatic cancer cells Panc-1(ATCC), rat bladder transitional cell carcinoma AY-27 and telomerase immortalized human microvascular endothelial cells were all used in this study. All cells were maintained in humidified incubator with 5% CO₂ at 37°C and were passaged at less than 70% confluency.

The collagen for the 3D tumor study was obtained by removing tendons from rat tails and dissolving in 10mM HCl overnight at room temperature. Following centrifugation at 30,000g for 30 min, the collagen containing supernatant was collected, sterilized with chloroform, and evaluated with dry weight analysis to determine collagen concentration.

The 3D culture system, containing the embedded endothelialized microchannel, was prepared by mixing an 8mg/ml collagen solution with 10% by volume 10x DMEM solution with 1 N NaOH to neutralize the HCl. Next, 1x10⁶ tumor cells were resuspended in the mixture and were injected into FEP tubing with PDMS sleeves. A 22G needle was placed directly in the center of the cylinder and the collagen was allowed to crosslink at 37°C for 60 minutes around the needle, inside the tubing. After gelling, the needle was removed, leaving a ~700 μm

diameter central channel in the 3D cylinder tumor model. 2×10^6 TIME cells were then injected into the central cavity, turning the entire setup 90° every 10 minutes to allow for a uniform distribution of endothelial cells in the microchannel.

Flow of media was introduced into the model through a tight fitting 22G needle, partially inserted into the microchannel, connected via PTFE microbore tubing itself connected to a syringe pump containing TIME media in syringes. Media was allowed to flow through the system for 48hrs prior to the introduction of media containing SWNHs. To track the non-fluorescent, carbonaceous SWNHs, we used an acid functionalized ligand exchange approach to attach fluorescent quantum dots to the SWNHs as described in previous work [4]. Media containing SWNHs replaced the media in half of the samples while control samples still maintained the empty media. Uptake kinetics in the endothelial cells was determined using FACS analysis of removed endothelial cells to determine relative fluorescence and mean uptake percentage and confocal microscopy was used to visualize the uptake of SWNHs.

For the HT and CT studies, AY-27s were used for uptake and HT+CT treatment studies. AY-27 cells were seeded 48hr prior to exposure of .025 mg/mL SWNH-QDs for (15-60min) in appropriate temperature controlled incubators. 37°C and 42°C were used for both preconditioning (2hrs) and exposure (15-60min) separated by a 1hr relaxation period. Following exposure, the cells were rinsed in cold PBS and analyzed using FACS to determine uptake kinetics. Cisplatin (10-100 μM) was exposed to AY-27 cells using similar thermal conditions as the uptake studies and was loaded into SWNHs using a method previously described [4]. Cisplatin loading was confirmed by TEM and viability was measured following CT+HT treatments utilizing Alamar Blue.

RESULTS

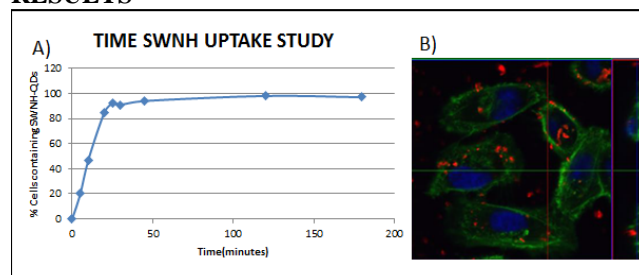


Figure 1: Results. (a) Percentage cellular uptake in endothelium as a function of exposure time (0-180 minutes) (b) confocal image showing SWNH-QD (red) uptake by breast cancer cells.

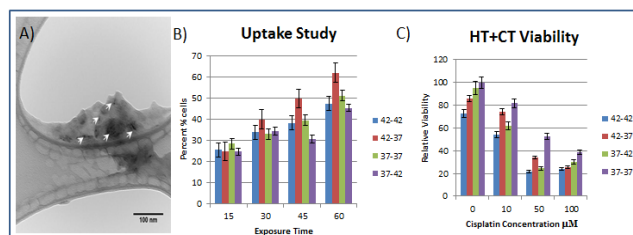


Figure 2: (a) TEM showing Cisplatin loaded into SWNHs (white arrows) (b) AY-27 uptake of SWNHs under different thermal settings (c) AY-27 Viability after HT+CT Data presented as Preconditioning Temp-Exposure Temp for (b)+(c) results.

FACS analysis showed temporal dependence on uptake of SWNHs by the endothelial media in a microchannel and tumor cells in a 3D, physiologically relevant system. Confocal microscopy demonstrates our ability to track these tagged nanoparticle transport intercellularly.

A TEM image shows successful incorporation of Cisplatin (white arrows) into the SWNHs in Figure 2A. FACS analysis of cellular uptake shows that a preheat stress at 42°C for 2 hrs followed by 1hr relaxation and SWNH exposure at 37°C has the greatest nanoparticle uptake into the cell, having an almost 2 fold increase compared to SWNH exposure at 42°C and significant increase in uptake compared to samples with no preconditioning and exposure at 37°C . Additionally, preheating cells for 42°C and exposing cisplatin at 42°C has the highest thermal enhancement ratio (TER).

CONCLUSIONS

While hyperthermia has previously been shown to have synergistic effects when combined with chemotherapeutics, we have shown that the temporal aspect of HT is very important for treatment planning for multimodal photothermal therapies. Although the greatest TER of CT is seen with concurrent heat and chemo treatment, the optimal uptake of nanoparticles is seen at 37°C after a preconditioning of 42°C , a condition that additionally shows thermal enhancement of CT. Our ability to track transport of QD tagged SWNHs and subsequent viability following CT+HT can be combined to determine optimal thermal conditioning for the treatment of UCCs in a 3D tumor microenvironment.

ACKNOWLEDGMENTS

Funding for this work was provided by the NSF Early CAREER award CBET 0955072, Institute for Critical Technology and Applied Sciences at Virginia Tech, and NSF-GRFP.

REFERENCES

- [1] Whitney et al. Lasers Surg Med. 2011
- [2] Iijimam S et al, Chem Phys Let, 1999
- [3] Ajima K, et al. Mol Pharmaceut. 2005
- [4] Dewitt et al, BMES national conference 2012

ARTERIAL TRANSIT TIME MAPPING WITH PSEUDO-CONTINUOUS ARTERIAL SPIN LABELING MRI: MONTE CARLO SIMULATION AND IMPLEMENTATION WITH VARIABLE TR

Megan E. Johnston¹, Joseph A. Maldjian², and Youngkyoo Jung^{1,2}

1. Wake Forest School of Medicine, Biomedical Engineering

2. Wake Forest School of Medicine, Department of Radiology

Corresponding Author: Megan E. Johnston, megjohns@wakehealth.edu

INTRODUCTION

Arterial spin labeling is a non-invasive method of cerebral blood flow (CBF) measurement with MRI. The arterial transit time (ATT) in ASL is defined as the time required for the blood to travel from the labeling location at the neck to its ultimate location of perfusion in the brain. To allow the labeled blood to travel to the exchange location, a post-labeling delay (PLD) is inserted between the application of the label and the acquisition of the image. The selection of a single optimum PLD is difficult because the ATT varies widely across the brain, between patients, and can change with pathology. Simultaneous estimation of ATT and CBF can provide more accurate CBF estimates without sensitivity to ATT. The most basic method of mapping ATT is to collect many ASL images with different PLDs, which is time consuming. Multiple time efficient methods have been proposed for simultaneous ATT and CBF estimation. This work examines the tradeoffs of three major methods: Variable TR method: shortened TR with pre-saturations according to PLD (1), Hadamard encoded ASL: subdivided label into multiple sub-boluses, later decoded into several images with different effective PLDs (2), and Look-Locker acquisition: repeated acquisition of imaging volume with one label application (3). The most promising method will be implemented.

SIMULATION METHODOLOGY

Simulations were performed in order to compare the ATT and CBF estimation efficiencies of each method using continuous or pseudo-continuous labeling. Signal from a single tag/control pair was generated for each method according to the general hemodynamic model (4), see Fig 1. Zero-mean Gaussian noise was added to the simulated signal at all time points independently. Standard deviations of the noise were chosen to set the SNR of a single tag/control difference signal at 1400ms ATT with 1600ms bolus duration to 2 and 4. The signals were

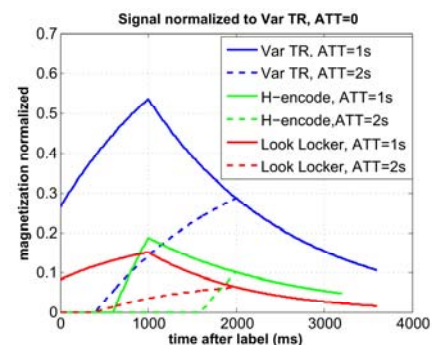


Figure 1. Normalized perfusion signal from a single tag/control pair over time for three methods with ATT=1s (solid line) and 2s (dash line)

averaged according to the number of averages feasible in a given scan time (5 min.). The imaging time was assumed to be 400 ms for all methods. Monte Carlo simulations were performed with 1000 iterations.

SIMULATION RESULTS

Fig 2 shows the percent error in the CBF estimation. The error between ATT estimates and true values is shown in Fig 3. The variable TR method showed lowest errors in the experimental range. The Variable TR method was implemented.

IMAGING METHODOLOGY

All images were collected on a healthy, young female with a 3T Siemens Skyra MRI with a 32-channel head coil. All PCASL data were collected with 1600ms labeling duration. PCASL with a single PLD of 1500ms was collected for reference with 40 tag/control pairs with whole-brain coverage using a 2D EPI acquisition scheme (scan time, 4:35). A series of PCASL scans were collected with 4 tag/control pairs with 8 PLDs ranging from 400ms to 3200ms in increments of 400ms. The TR was minimized for each scan to minimize scan time with

the TR values ranging from 2300ms to 5100ms (total scan time, 4:45). The tag/control pairs were subtracted and averaged to generate a perfusion-weighted image. The perfusion-weighted images were concatenated, smoothed spatially with a 1.5 FWHM Gaussian kernel, and fit voxel-wise to the general hemodynamic model (4) with a non-linear fitting routine which allows for quantification of CBF and ATT. Identical smoothing was applied to the reference scan before quantification to generate a comparison CBF map.

IMAGING RESULTS

The whole brain average CBF was 60.4 ml-blood/100g-tissue/min for the reference PCASL acquisition and 75.9 ml-blood/100g-tissue/min for the variable TR method. The whole-brain average of the ATT was 977ms. The non-linear fitting did not converge for some voxels in the deep white matter due to long ATT and low SNR.

DISCUSSION

For ATT values longer than 2500ms, which is often the case for white matter, none of the methods investigated demonstrated acceptable levels of error (> 100% in CBF estimate with SNR of 2). Even though the variable TR method had the lower error, due principally to the higher signal amplitude (see Fig 1), the Look-Locker method may be more advantageous in that it has low sensitivity to motion due to more signal averaging. A possible reason that the Hadamard encoding method showed lowest errors in CBF for long ATT (>2500ms) may be that the shorter bolus duration allowed for better fitting of the signal. The

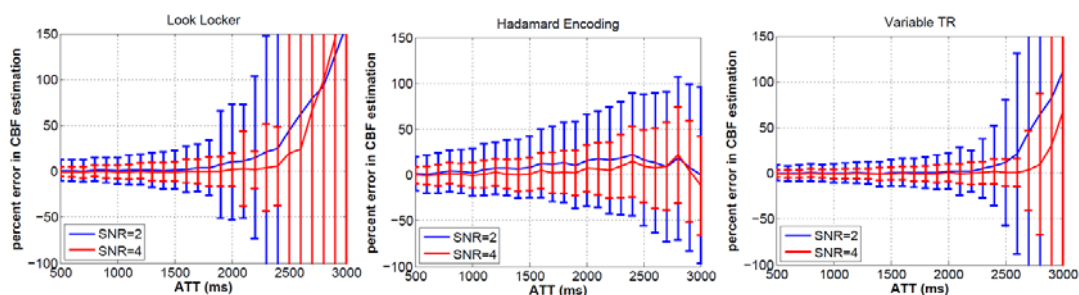


Figure 2. Mean percent error in the CBF estimation for ATT ranging from 500ms to 3000ms. The error bars indicate the standard deviations of the estimations.

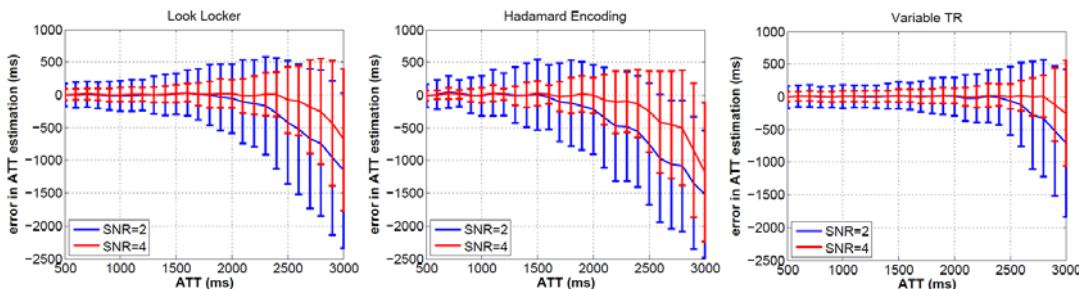


Figure 3. Mean error in the ATT estimation for ATT ranging from 500ms to 3000ms. The error bars indicate the standard deviations of the estimations.

higher average CBF collected by Variable TR method is likely due to the use of peak signal over the variable PLD times; an increase of 20-30% is expected based on simulations (data not shown).

CONCLUSIONS

The variable TR method allows for simultaneous acquisition of ATT maps and whole brain CBF in a clinically feasible scan time. The ATT varies across the brain. Accounting for this variation provides CBF maps insensitive to ATT variation. In addition, ATT can be a valuable clinical tool for the diagnosis of ischemic penumbra and infarction.

ACKNOWLEDGMENTS

Wake Forest Center for Biomolecular Imaging

REFERENCES

- (1) Lu K, Liu TT, Jung Y. ISMRM 2010: 1769.
- (2) Dai W, Shankaranayanan A, Alsop DC. MRM [epub ahead of print].
- (3) Guthrie M, Bock M, Scad LR. MRM 2001; 46(5):975-984.
- (4) Buxton et al. MRM 1998;40(3):383-396

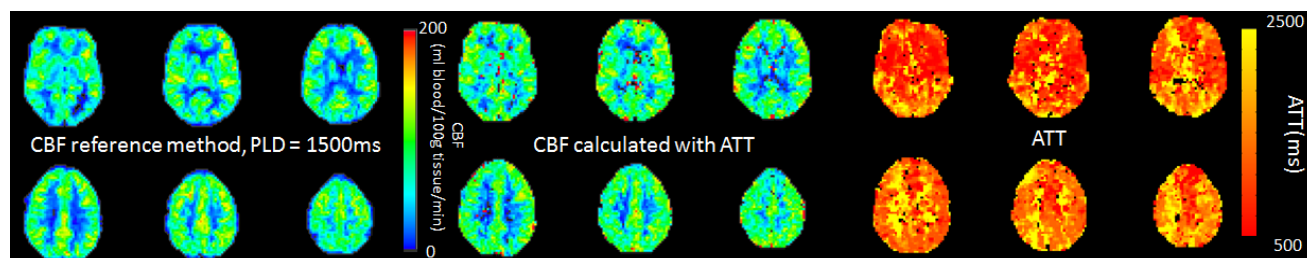


Figure 4. CBF maps of reference method (left) and Variable TR method (middle). ATT map (right)

CORONARY ARTERY CROSS SECTIONAL AREA WITH NON-CONTRAST CARDIAC CT: TECHNIQUE AND FEASIBILITY TESTING

Mingna Zheng¹, John Jeffrey Carr², Yanhua Yang², and Yaorong Ge¹

1. Virginia Tech-Wake Forest University School of Biomedical Engineering and Sciences
2. Wake Forest University School of Medicine

Corresponding Author: Yaorong Ge, Email: yge@wfubmc.edu

INTRODUCTION

A significant cause of coronary artery disease (CAD) is the coronary atherosclerosis which leads to narrowing of coronary arteries. It has been shown in recent studies, using intravascular ultrasound and contrast-enhanced CT, that early atherosclerosis causes coronary artery remodeling, defined as changes in the cross section area. Thus, it is hypothesized that measurement of artery remodeling using non-contrast CT can be a significant factor in sub-clinical assessment of cardiac risk for asymptomatic subjects. However, measuring the cross-sectional area and its changes in coronary arteries in non-contrast CT images is a challenging task because the intensity of coronary arteries is similar to that of surrounding tissues. Automatic segmentation algorithms that are designed to segment coronary arteries in contrast images do not perform well. For the same reason, 3D visualization techniques cannot provide sufficient visualization information for identifying the boundary of coronary arteries in 3D space. To overcome these difficulties, we developed an interactive application to enable efficient and accurate measurement of coronary artery remodeling in non-contrast CT images. In a pilot study, we analyzed 43 CT exams from the Coronary Artery Risk Development in Young Adults (CARDIA) study. These studies are classified into five groups according to lifetime risks of CAD. For each exam, we measured the cross-sectional area in six locations along 3D centerlines of the left main and left anterior descend. Initial analysis demonstrated positive correlation of large coronary artery cross-sectional area with high lifetime risks.

METHODOLOGY

We developed and tested software using the open source 3D Slicer software package for medical image analysis

(www.slicer.org) for measuring coronary arteries. Features added to the tool include: extraction of coronary artery centerlines, precise localization of vessel origin and branch points, user selections of multiple measurement points along the vessel, user defined coronary artery boundaries and calculation of CSA. Comparability testing of the 3D slicer module was performed on 10 contrast enhanced CT angiograms with careful manual segmentation using the commercially available MIMICS software package (www.materialise.com). A second test set of 43 non-contrast cardiac CT images (64 channel CT, 120 KV, voxel sizes of 0.488x0.488x0.625mm, prospective ECG gating and without heart rate control) were used to test the software in a clinical setting.

RESULTS

Comparability testing of the 3D slicer module was performed on 10 contrast enhanced CT angiograms with careful manual segmentation using the commercially available MIMICS software package.

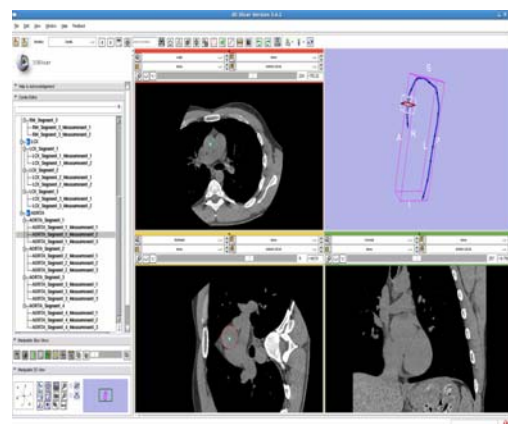


Figure 1: The comparability testing of the 3D Slicer with commercial software MIMICS: 3D Slicer user-interface.

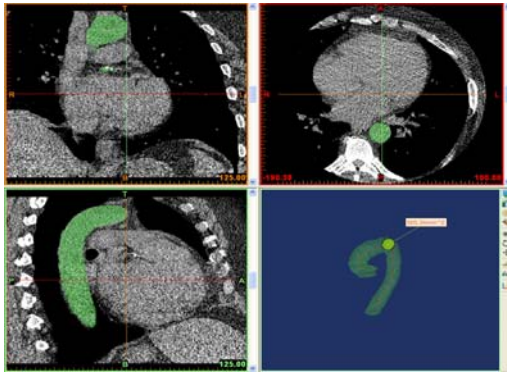


Figure 2: The comparability testing of the 3D Slicer with commercial software MIMICS: the MIMICS user-interface.

The overall mean CSA of the proximal coronary arteries was 10.8 mm² (MIMICS) and 10.6 mm² (3D Slicer) with a difference of 0.26 mm² (3.5%) and a high correlation (R=0.91) between the two methods.

For interobserver reliability, an experienced doctor tested 20 non-contrast cardiac CT exams and a student retested them on the same measurement points and different measurement points respectively; for intraobserver reliability, one observer tested the same 20 exams twice. The results are in table 1.

Table 1: Results of inter- and intraobserver reliability test

Test		Correlation Coefficient
Inter-observer	same measurement points	.96
	Different measurement points	.85
Intra-observer	same measurement points	.98
	Different measurement points	.89

In a clinical setting, results from a set of 43 non-contrast cardiac CT exams found that men compared to women and individuals with a calcium score >0 compared to those with CAC=0 had larger CSA of the LAD.

CONCLUSIONS

This initial study demonstrates that measurement of coronary artery CSA is feasible on cardiac CT images without intravenous contrast and that results are

consistent with the existing literature. Further work is needed to validate the methods in a larger sample size; However, non-contrast high resolution cardiac CT shows promise as a noninvasive measurement of coronary artery remodeling.

ACKNOWLEDGMENTS

This project is supported by a grant from the National Heart, Lung, and Blood Institute of the National Institutes of Health (grant number R01 HL 098445).

REFERENCES

- [1]J. Carr, J. Nelson, N. Wong, et al., “Calcified Coronary Artery Plaque Measurement with Cardiac CT in Population-based Studies: Standardized Protocol of Multi-Ethnic Study of Atherosclerosis (MESA) and Coronary Artery Risk Development in Young Adults (CARDIA) Study”, *Radiology*, 234:35-43 (2005).
- [2]Glagov, S., Weisenberg, E., Zarins, C. K., Stankunavicius, R., Kolettis, G. J., “Compensatory enlargement of human atherosclerotic coronary arteries,” *New England Journal of Medicine* 316 (22), 1371-1375 (1987).
- [3]Groot, P., Veldhuizen, R. W., “Human coronary artery remodeling, beginning and end of the atherosclerotic process,” *PLoS ONE* 1 (1), e91 (2006).
- [4]Pedrazzini, G. B., et al., “Assessment of coronary stenosis, plaque burden and remodeling by multidetector computed tomography in patients referred for suspected coronary artery disease,” *Journal of Cardiovascular Medicine* 12 (2), 122-130 (2011).

BLOOD-BRAIN BARRIER ON CHIP: DRUG DELIVERY ENHANCEMENT BY ELECTROPORATION

Mohammad Bonakdar¹, Rafael V. Davalos²

1. Virginia Tech, Mechanical Engineering

2. Virginia Tech, School of Biomedical Engineering and Sciences

Corresponding Author: Mohammad Bonakdar, Email: mohammad@vt.edu

INTRODUCTION

One significant obstacle to drug development for targeting the central nervous system (CNS) has been the high resistivity of the blood-brain barrier (BBB) in allowing large molecules to penetrate into the CNS. Hence many researches are focused on trying to avoid this obstacle for better drug delivery to the target. Electroporation which is the permeabilization of the cell membrane using pulsed electric fields is a non-viral physical method for drug delivery. Introducing macromolecules into suspended cells by electroporation has been performed using microfluidic devices [1]. Some previous studies have investigated BBB disruptions during reversible and irreversible electroporation [2]. Garcia et al studied the permeabilization of the BBB during irreversible electroporation of the tumor [3].

Organs on a chip which are a class of microdevices that feature a physiologically relevant function, are a method of *in vitro* tissue analysis. The microscale size of the devices and features provide accurate and more physiologically relevant manipulating and analyzing the cells and tissues. The BBB has a significant role in screening certain molecules to the CNS and is a major obstacle to drug development for many CNS diseases. Hence, many researches are focused on studying the physiology of this barrier and how to permeate through it. Booth *et al* [4] developed a microfluidic BBB model incorporating a co-culture of endothelial and astrocytes and monitored the formation of tight junctions using transendothelial electrical resistance. In another study Prabhakarandian *et al* [5] modeled a micro BBB using brain endothelial cells in astrocyte conditioned medium and investigated the effect of astrocytes on the formation of the tight junctions and the transport of certain chemicals across the barrier. Flow induced shear force

and chemical factors are also deployed to modulate the permeability of the BBB [6]. In this study a microengineered BBB model was fabricated and its permeability to different chemicals was investigated. We stimulated the microengineered BBB model by short pulsed electric fields (ECM 830, BTX, Harvard Apparatus) and quantified the amount of transported chemicals with different molecular weights due to the induced cell electroporation. In this work we show how electroporation is able to increase the permeability of the BBB without compromising cell viability.

MATERIALS AND METHOD

Microfluidic devices are fabricated in PDMS using photolithography and replication molding. SU-8 (Microchem) is spun on the 4" silicon wafer and exposed under UV light through a transparency mask and further developed to remove the unexposed regions. PDMS prepolymer (Dow Corning) is mixed with the curing agent and poured on the master. After 1 hour curing at 100 deg C, the PDMS replica is peeled off form the master.

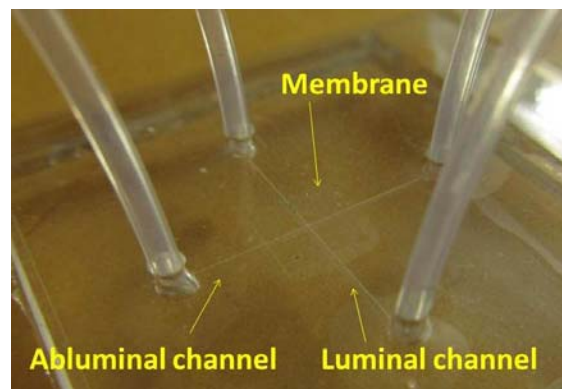


Figure 1: RBE4 cells on chip.

A polycarbonate membrane (Millipore) is sandwiched between two PDMS slabs containing perpendicular channels using the method developed by Takayama group [7]. The whole construct is then bonded to a glass slide using plasma activation for structural integrity. Two electrodes are then inserted into one of the channels for applying the electric field. Figure (1) shows a fabricated microdevice with connection tubes. Rat brain endothelial cells (RBE4) were cultured on the membrane until the formation of a confluent monolayer and the expression of the tight junctions. By applying electric pulses of different amplitudes, the endothelial cells were reversibly electroporated and the permeability of the barrier was changed. We injected Dextran (Sigma) of different molecular weights into one chamber and measured the diffused amount into the other chamber following electroporation treatments. Figure (2) shows a schematic of the experimental setup.

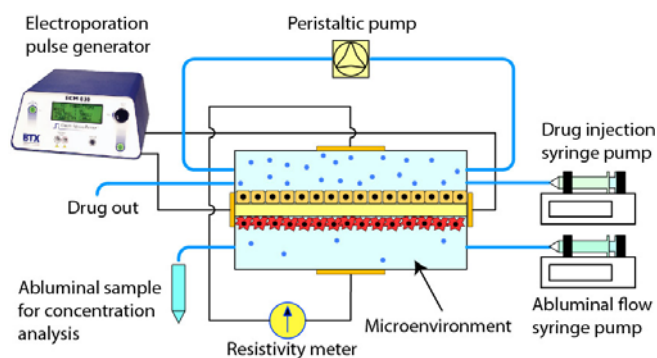


Figure 2: Schematic of the experimental setup including the BBB mimic, electric circuit and flow circuits.

RESULTS AND DISCUSSION

Brain endothelial cells and astrocytes were cultured on opposite sides of the membrane inside the microenvironment until a confluent monolayer of cells was formed. It is shown that astrocytes play a significant role in forming the tight junctions. Figure (3) shows a monolayer of RBE4 cells forming tight junctions in the microenvironment. To have a better representation of the *in vivo* conditions, media was perfused over the endothelial cells in the top chamber. By applying electric pulses to the electrodes, the permeability of the barrier was temporarily increased, allowing certain molecules of high molecular weight to penetrate through the BBB. The permeability analysis after the electroporation and live/dead assay confirms the reversibility of the process without compromising cell viability.

One of the features that distinguish this BBB model from conventional static models is the ability to have a continuous flow of media over the cell layer for a better

simulation of the *in vivo* conditions. We have subjected the BBB cells to different flow rates inside the channel both before and after forming the confluent layer to study the effect of shear force on the morphology and permeability of the BBB.

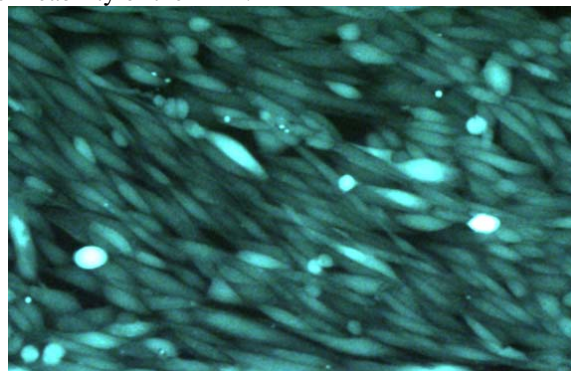


Figure 3: RBE4 cells forming a confluent monolayer on chip.

CONCLUSIONS

We modeled the BBB inside the microfluidic device and stimulated it by electroporation pulses to increase its permeability to certain chemicals without affecting cell viability. Using this method we are able to quantify the required electric field dosage for delivery of certain drugs to the CNS in a dynamic environment. This study paves the way for later *in vivo* experiments.

REFERENCES

- [1] A. Adamo et al, *Analytical Chemistry*, 2013, 85, 1637-1641.
- [1] Mohammad Hjouj *et al*, *PLoS ONE* 2012, 7(8): e42817
- [2] Garcia, P. *et al*, *PLoS ONE*, 2012, 7(11), e50482.
- [3] Booth, R. *et al*, *Lab Chip*, 2012, 12, 1784.
- [4] Prabhak, B. *et al*, *Lab Chip*, 2013, 13, 1093.
- [5] Griep, L. *Biomed. Microdevices*, 2013, 15, 145-150.
- [6] B. Chueh et al, *Anal Chem*, 2007, 79, 3504-3508.

EXPERIMENTAL MEASUREMENT OF THE UTRICLE'S DYNAMIC RESPONSE

Myles Dunlap¹ and Wally Grant^{1,2}

1. School of Biomedical Engineering and Sciences, Virginia Tech
 2. Engineering Science and Mechanics, Virginia Tech
- Corresponding Author: Myles Dunlap, Email: mddunlap@vt.edu

INTRODUCTION

Within the inner ear are linear motion sensors called otolith organs. These organs, the utricle and saccule, measure inertial motion and tilting of the skull with respect to gravity. The otolith organs transduce linear motion into afferent signals. The vestibular nuclei process this information for visual image fixation, motion sensation, and muscle coordination.

The utricle resides in a membranous sac that is firmly attached to the temporal bone. The base layer of the utricle is a neuroepithelium (NE) of sensory cells, termed hair cell receptors that transmit modulated afferent signals to the central nervous system (CNS). Each hair cell receptor has a mechanosensitive hair bundle that protrudes into the layered otoconial membrane (OM). The 3 layers of the OM are the otoconial layer (OL) of densely packed crystals, a thin gel layer (GL), and a column filament layer (CFL) surrounding the hair bundles.

When the skull is exposed to a linear acceleration the denser OL mass lags behind the sensory cells of the NE, causing a shearing in the GL and CFL layers and a neural signal to be reported to the CNS. Similarly, with static tilting of the head the weight of the OL will cause a deformation of the GL and CFL layers.

Both lumped parameter and finite element models [1, 2] have been constructed to determine the mechanical sensing of the utricle, yet the major drawback is the lack of information on material properties.

Within this work, we hypothesize that the relative displacement and phase lag between the NE and OL can be measured using light microscopy, high speed video, and controlled excitations. The data will then be used to characterize the biomechanical properties of this inner ear accelerometer and static tilt sensor via a lumped parameter model. This work is the first to quantify *in*

vitro dynamic responses and shear modulus of the utricle's OM.

METHODOLOGY

The utricle, from turtle, was removed from the skull and the dorsal surface of the membranous sac encapsulating the utricle was trimmed away to expose an unobstructed view of the OL and membranous shelf (MS) (Fig. 1). The MS serves as an excellent reference point for the NE.

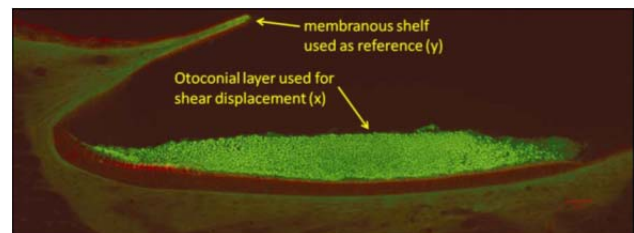


Figure 1: A cross-sectional view of the medial-lateral direction of the turtle utricle. The bright green dots indicate the dense OL layer of aragonite crystals.

A fundamental step in performing this experiment was to ensure the utricle was securely held and anatomically level while connected to an oscillating stage that generated natural inertial stimulations. The ventral surface of the ampullae and vestibular nerve were attached by dental floss to a glass slide. Glass chips were placed under the ventrolateral surface of the utricle to make the OL approximately perpendicular to the gravity vector.

The OL and MS displacements were measured using a transmitted light microscope (Zeiss Akioskop) mounted on a vibration isolation table. The stage of the microscope was outfitted with a precisely controlled piezoelectric actuator. The piezoelectric stage was oscillated using a linear sinusoidal-sweep from 0-500 Hz in the medial-lateral (ML) and anterior-posterior (AP) directions (Fig.1) of the utricle while either viewing the OL or MS. Magnification ranged from 100X-250X and oscillations were filmed using a Photron APX-RS high

speed camera at 2000 fps and an exposure time of 0.1 msec.

Image registration was used to determine frame-by-frame displacements of the MS (u) and OL (y). These displacements were used to develop an OM frequency response function shown by Eq. 1

$$FRF = \frac{S_{yy}(m\omega)}{S_{yu}(m\omega)} \quad (1)$$

where, S_{yy} is OL displacement auto-spectral density and S_{yu} is the OL and MS displacement cross-spectral density.

A single degree-of-freedom linear lumped parameter model was used to calculate a 2nd order dynamic equation that models the utricle's dynamics during an oscillation as

$$H(s) = \frac{Y(s)}{U(s)} = \frac{\left(\frac{\rho e}{\rho_0}\right)s^2 + \left(\frac{2\zeta\omega_n}{1+D_r}\right)s + (\omega_n^2)}{s^2 + (2\zeta\omega_n)s + (\omega_n^2)}. \quad (2)$$

The unknown parameters of interest are the natural frequency (ω_n) and damping (ζ). A frequency domain system identification technique was used to curve fit the model of Eq. 2 to the experimental data of Eq. 1 in order to determine the utricle's ω_n and ζ (see Fig. 2).

With ω_n measured the shear modulus (G) can be calculated using Eq. 3, where h is gelatinous layer thickness, m_{ol} is otoconial mass, and A is otoconial layer area.

$$G = \frac{hm_{ol}}{A} \omega_n^2 \quad (3)$$

RESULTS

A total of 20 utricles were oscillated with a variety of linear sinusoidal-sweeps at different acceleration magnitudes and frequency directions (0-500 Hz and 500-0 Hz) to observe if nonlinearities existed. No nonlinearities were found from a statistical comparison of the experimental data.

The mean and 95% confidence intervals for the measured ML and AP-axes parameters are listed below:

Parameter	Medial-Lateral	Anterior-Posterior
ω_n	373 (350, 396) Hz	405 (382, 428) Hz
ζ	0.50 (0.47, 0.53)	0.51 (0.45, 0.57)
G	9.52 (8.32, 10.71) Pa	11.1 (9.89, 12.32) Pa

Anisotropic material properties were checked for ML and AP-axes, with no significant difference concluded from our experimental results.

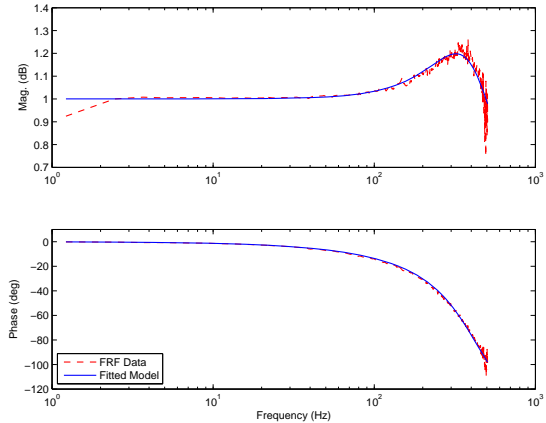


Figure 2: FRF data (red line) from Eq. 1 and curve fit of Eq. 2 (blue line) for a linear sinusoidal-sweep oscillation of the utricle's OM.

CONCLUSIONS

A significant finding from our data is that the utricle behaves as an underdamped system ($\zeta < 1$). This allows the utricle to achieve maximum deflection per unit acceleration without having substantial overshoot.

The corner frequency of the utricle occurs at the upper limits of natural head frequencies for the turtle, indicating optimal usage of the utricles dynamic bandwidth.

The measured shear modulus is approximately 10 Pa which provides excellent sensitivity for motion detection and head tilt. A shear modulus of this magnitude has been predicted for cupular membranes, which are the gelatinous structure overlying hair bundles in the semi-circular canals [3].

ACKNOWLEDGMENTS

Supported by NIH NIDCD R01 DC 005063.

REFERENCES

- Grant JW, Best WA. Mechanics of the otolith organ-dynamic response. *Ann Biomed Eng* 1986;14:241–256.
- Kondrachuk AV. Computer simulation of the mechanical stimulation of the saccular membrane of bullfrog. *Hear Res* 2000;143:130–138.
- Selva P, Oman CM, Stone HA. Mechanical properties and motion of the cupula of the human semicircular canal. *J Vestib Res* 2009; 19: 95-110.

THE DEVELOPMENT OF A SIMPLIFIED THORAX MODEL FOR PARAMETRIC STUDIES OF A FULL BODY FINITE ELEMENT MODEL

Nicholas A. Vavalle^{1,2}, Daniel P. Moreno^{1,2}, Joel D. Stitzel^{1,2}, F. Scott Gayzik^{1,2}

1. Wake Forest School of Medicine

2. Virginia Tech – Wake Forest University Center for Injury Biomechanics

Corresponding Author: Nicholas A. Vavalle, Email: nvavalle@wakehealth.edu

INTRODUCTION

Complex computational human body models are becoming commonplace in the study of injury biomechanics. However, such models can be taxing on computational resources. For instance, the Global Human Body Models Consortium (GHBMC) 50th percentile male model (M50) requires 10 – 24 hours to run in a typical impact simulation, using 48 cores on a computational cluster. While there are numerical techniques that can be used to decrease run time, there is a need for simplified models that capture the essential biomechanics of the system in question but that can be run quickly. Simplified models with decreased run time can be used for parametric studies to determine if potential changes to the model will be beneficial. The objective of this study is to implement a simplified thorax model to facilitate parametric studies applied to a complex model of the average male. The simplified model is based on the geometry of the Global Human Body Models Consortium (GHBMC) mid-sized male model (M50).

METHODOLOGY

The simplified thorax model dimensions were created using the dimensions of the GHBMC M50 Thorax. The distance from the top of the shoulders to the diaphragm was used as the height of the simplified model. The chest breadth and depth at the level of the axilla were used for the width and depth of the simplified model, respectively. All dimensions were rounded to the nearest 5 mm for mesh simplicity.

The basic geometry was used to allow for a mesh made entirely of hexahedral and quadrilateral elements. Element edge lengths were all 5mm, representative of the typical element size of the full-complexity thorax model. The simplified model consists of 10 parts – outer flesh, inner flesh, a muscle layer, nine ribs with associated intercostal muscles, heart, lungs, an upper rib 2D layer, and a diaphragm 2D layer. The upper rib and diaphragm

layers contain the heart and lungs above and below, similar to the full thoracic model. Additionally, point masses were added above and below to bring the total mass of the simplified model to 75.8 kg, the same as the full body model. The material properties from the GHBMC M50 were used as the initial input for the simplified model. To further reduce simulation time, symmetry was introduced at the mid-sagittal plane so that the number of nodes could be reduced by half. **Figure 1** shows the simplified model.

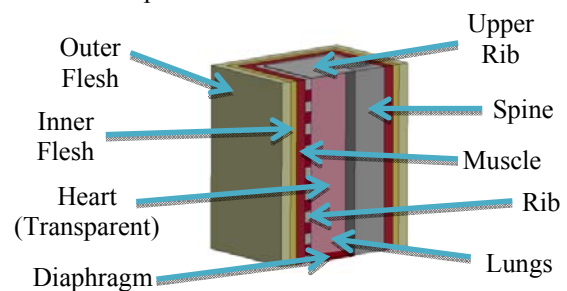


Figure 1. The simplified thorax model with the model reflected about the symmetry plane.

To test the simplified model a validation case for the GHBMC M50 model was chosen. This case was based on the experiments by Kroell. In this experiment, a cylindrical impactor was driven into the chest of post-mortem human surrogates (PMHS) at a velocity of 6.7 m/s. The force vs. deflection curve was used for comparison since it is an indicator of general model stiffness.

For the parameter study, eight material model changes and one numerical control change were implemented in addition to running the simplified model with the GHBMC parameters as a baseline. This gave a total of 10 simulations, seen in **Table 1**. The models ranged in complexity from a simple elastic model to more detailed hyperelastic models designed to model specific organs.

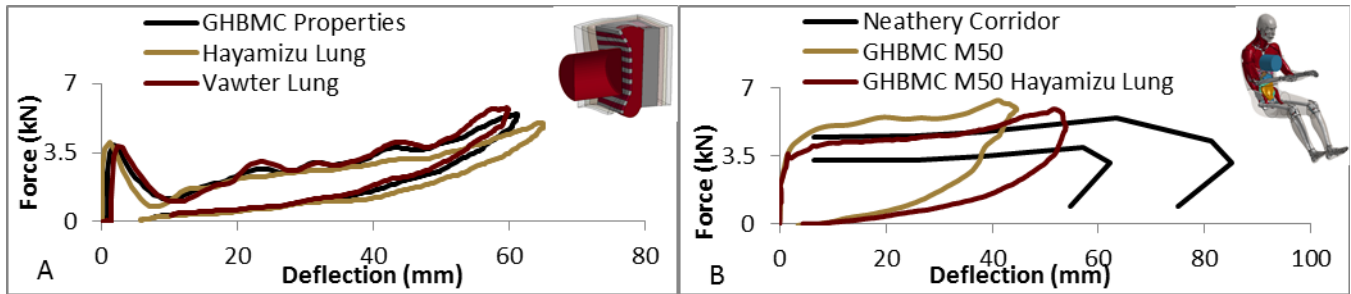


Figure 2. A) Force vs. deflection of three models simulated with the simplified thorax. B) Hayamizu lung implemented in the full complexity model showing improved response.

RESULTS

The average length of the simulation to run on a single CPU was 41.6 minutes. For the full body model to run the same simulation it takes on average 10.7 hours using 48 CPUs. This equates to the simple model reducing run time by 93.5% compared to the full model.

Table 1. Simulations that were completed in this study.

#	Description	Pk. F % Δ	Pk. D % Δ
1	Baseline	-	-
2	Baseline + Hayamizu lung	-8.2	6.3
3	Baseline + Vawter lung	5.2	-2.2
4	Baseline + Gayzik lung*§	N/A	N/A
5	Baseline + Yamada heart	8.1	-1.4
6	Baseline + Duck muscle*	13.0	-6.6
7	Baseline + Lee and Yang muscle	-16.9	23.0
8	Baseline + Lee and Yang flesh	5.0	-5.2
9	Baseline + Lee and Yang muscle and flesh	-14.0	16.6

*Modified from animal study to human parameters
§Did not run to completion, numerical instabilities

Of the 10 parameter variations that were run, three involved the lung since it is the largest organ in the thorax and is often injured in vehicle crash loading. Two of the trial material changes ran to completion, the Hayamizu lung and the Vawter lung. Figure 2A shows the results of runs 1, 2 and 3 from Table 1.

DISCUSSION

It is clear that the simplified thorax model saves a great deal of computational expense. This allows for a greater number of simulations testing the various parameters to be used in the model. Importantly, numerical studies using the simplified model can be run on local workstation enabling the engineer to conserve computational cluster usage for the parameter changes that were found to improve the response in the simplified case. The effect of these changes would not be immediately apparent without the simulation.

This process is demonstrated in Figure 2B, **Error! Reference source not found.** where the Hayamizu lung was implemented in the full complexity model. The changes in the full complexity model response are of roughly equal magnitude in terms of the increase in deflection and decrease in force as seen in the simplified model.

There are some apparent limitations to this work, including the clearly oversimplified geometry of the thorax. However, this geometry was used intentionally to simplify the mesh of the model and thus, reduce the computation time. Even with this simplification, the model was within the corridor at peak deflection and force.

CONCLUSIONS

A simplified thorax model was developed to conduct parametric studies on various aspects of a human body finite element model. Material model changes of the lungs, flesh, and muscle of the thorax model were investigated to determine if outcomes in the full body model would be favorable. Changes studied in the simplified model have been implemented successfully in the full complexity GHBMC M50 model and indicate that this simplified model approach may be a valuable tool in further M50 model development.

ACKNOWLEDGMENTS

The authors would like to acknowledge the GHBMC for funding and support as well as all modeling partners for their work on regional models.

REFERENCES

- GHBMC (2011). Ghbmc M50 Users Manual
- Hayamizu, N., I. Watanabe, T. Ishihara and K. Miki (2003). Measurement of Impact Response of Pig Lung. *JSME Tokia Branch Conference*: 94-95.
- Kroell, C., D. Schneider and A. Nahum. Impact Tolerance and Response of the Human Thorax. *Stapp Car Crash J* Vol. 15, 1971.
- Vawter, D. L. A Finite Element Model for Macroscopic Deformation of the Lung. *J Biomech Eng* Vol. 102, No. 1, pp. 1-7, Feb 1980.

A COMPOSITE MESH FOR LIGAMENT TISSUE ENGINEERING

Patrick S. Thayer¹, Anna F. Dimling², Daniel S. Plessl³, Mariah R. Hahn⁴, Scott A. Guelcher⁵, Aaron S. Goldstein^{1,2}

¹School of Biomedical Engineering and Sciences, Virginia Tech

²Department of Chemical Engineering, Virginia Tech

³Virginia Tech Carilion School of Medicine

⁴Department of Biomedical Engineering, Rensselaer Polytechnic Institute

⁵Department of Chemical and Biomolecular Engineering, Vanderbilt University

Corresponding Author: Dr. Aaron Goldstein, Email: goldst@vt.edu

INTRODUCTION

Electrospinning is extensively used for tissue engineering applications due to its ability to create fibrous meshes with microarchitectures that permit cellular adhesion, alignment, and proliferation. This technique, however, suffers from limitations including the shallow infiltration of cells due to small pore size, and overall thickness restrictions of less than one millimeter, hampering applications beyond thin tissues such as skin. Electrospaying cells concurrently with electrospun fiber deposition can eliminate the need to introduce porogens – which compromise mesh integrity and microstructure – to induce cellularized infiltration. The goal of this project was to fabricate a robust, cellularized composite mesh using a dual electrospinning/electrospaying technique and increase its overall thickness through the subsequent addition of a cross-linked PEG network. Specifically the PEG network integrated the adjacent cellularized layers together, creating composite meshes thicker than traditional electrospun meshes. In this study, composite meshes were developed for ligament regeneration, but this technique can be applied broadly to tissue engineering applications (e.g., peripheral nerve, blood vessel or muscle).

METHODOLOGY

A conventional electrospinning process was modified by the inclusion of an additional syringe for cell electrospaying in conjugation with the deposition of PEUR fibers (**Figure 1**). The addition of a PEG hydrogel network to a rolled, cellularized mesh post-fabrication integrated the successive electrospun layers together (**Figure 2**). The composite meshes were imaged by SEM, and the meshes were mechanically tested to determine if the hydrogel cross-linking changed the

mechanical properties under tension and cyclic loads. DNA content was measured and cross-sections of composite meshes were imaged to quantify and visualize cell viability.

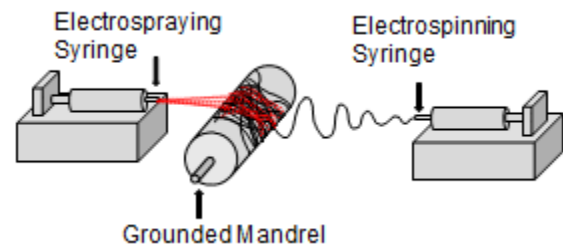


Figure 1: Dual-electrospinning/electrospaying set up. A polymer solution is electrospun from a throw distance of 23 cm, rate of 3 mL/hr and 15 kV potential. The cell solution is electrospayed concurrently from a throw distance of 4 cm, 6 mL/hr rate and 9 kV potential.

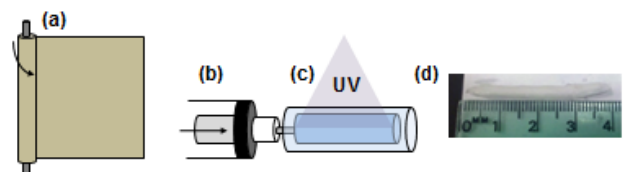


Figure 2: Composite mesh assembly: (a) wet mesh is rolled up, (b) a syringe containing the PEGDA solution is inserted into the rolled mesh and placed in a glass tube, (c) the 20% PEGDA solution is injected into the rolled up mesh and cross-linked, (d) resulting composite mesh

RESULTS

SEM of rolled and composite meshes revealed that the PEG hydrogel network penetrated and integrated the adjacent electrospun layers. The elastic modulus of the linear region (1-2% strain) of the composite PLGA/PEGDA meshes (41.7 ± 5.8 MPa) was

significantly higher ($p = 0.0132$) than the rolled PLGA/PEGDA meshes (29.2 ± 4.3 MPa). In contrast, the PEUUR-based materials showed no significant ($p = 0.080795$) difference in elastic modulus of the linear region (4-7% strain) with PEG cross-linking (1.62 ± 0.28 MPa for rolled PEUUR/PEGDA mesh versus 2.19 ± 0.46 MPa for composite PEUUR/PEGDA mesh).

MTT assays performed on the unrolled meshes revealed the survival of electrosprayed cells up to 5 days post-electrospraying. A distinct band of formazan salt (purple) (Figure 3a) was present at the electrospraying target; in contrast, the non-stained region was where the cells were not deposited. The DAPI stained cross-sections indicated cell presence post-fabrication and at day 1 and 5 (Figure 3bcd). DNA quantification of composite PEUUR and PEUUR/PEGDA meshes revealed an increase in DNA content from post-fabrication to day 1 followed by a return to post-fabrication quantities at day 5 (Figure 4).

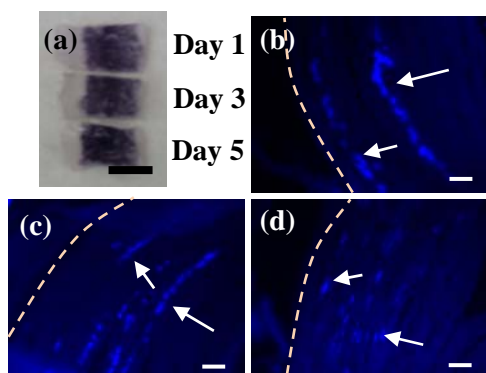


Figure 3: Formazan salt distribution on PLGA meshes containing electrosprayed cells. Scale bar: 0.5 cm. Representative DAPI stained cross-sections of PEUUR/PEGDA composite meshes at (b) Day 0, (c) Day 1, and (d) Day 5 post-fabrication. Cell nuclei stained blue. Composite mesh exterior marked by dashed line. Scale bar: 100 μ m

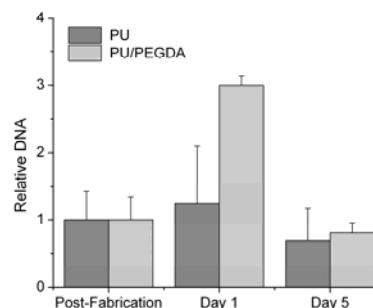


Figure 4: DNA content after 1 and 5 days of incubation relative to DNA content composite PEUUR or PEUUR/PEGDA meshes immediately post-fabrication

DISCUSSION

The goal of this study was to create a thick, cellularized, fibrous mesh for tendon/ligament applications using a two-step approach. Successful integration of adjacent layers was confirmed using SEM imaging. These composite meshes were mechanically tested under monotonic and cyclic regimens. The PEUUR composite meshes possessed mechanical properties such as elasticity and minimal creep that are relevant for application in cyclic mechano-stimulation studies. Cells remained distributed in the cellularized composite meshes after culture as shown through DNA assays and histology. A circulation loop has been developed to perfuse medium through the cellularized composite meshes for long-term culture.

CONCLUSIONS

Electrosprayed cells were distributed through a robust, three-dimensional composite mesh, and maintained in culture. Current work includes incorporating biological cues into the hydrogel network and exposing the cellularized composite meshes to external stimulation such as cyclic strain or perfusion. This two-step process shows promise for the rapid creation of cellularized, composite meshes for engineered tissue applications and could be extended for other tissue applications such as vascular, nerve and muscle tissue.

ACKNOWLEDGMENTS

The authors would like to thank the National Science Foundation (0854149) and the IGERT Regenerative Medicine program for funding, the NCFL at Virginia Tech, and Mike Vaught for the bioreactor fabrication.

NATURAL AGING EFFECTS ON TENDON-TO-BONE HEALING IN A RAT MODEL OF ROTATOR CUFF REPAIR

Plate, Johannes¹, Brown, Philip², Walters, Jordan¹, Clark, John²,

Smith, Thomas¹, Tuohy, Christopher¹, Stitzel, Joel², Mannava, Sandeep¹

1. Department of Orthopedic Surgery, Wake Forest School of Medicine, Winston-Salem, NC
 2. School of Biomedical Engineering and Sciences, Virginia Tech - Wake Forest University, Winston-Salem, NC
- Corresponding Author: Philip J. Brown, Email: phibrown@wakehealth.edu

INTRODUCTION

The incidence of rotator cuff tears is approximately 50% in adults over age 70 and is predicted to rise with increased life expectancy and higher activity level of the older population [1,2]. Despite surgical advances, rotator cuff repair surgery still has a high rate of recurrent tearing (20-70%) [1-3]. Advanced patient age was found to be associated with a higher risk of recurrent tearing following repair surgery [1,3], possibly due to the impaired biological “healing environment” in older patients.

The purpose of this study was to examine the effect of normal aging on tendon-to-bone healing in an established rat animal model of rotator cuff repair [4,5] using aged animals from a well-characterized colony from the Institute on Aging (NIA) of the National Institute of Health (NIH). We hypothesized that normal aging leads to decreased biomechanical strength at the tendon-to-bone insertion of the supraspinatus tendon on the humeral heads following acute repair.

METHODOLOGY

Twenty-four old (24 months) and 24 young (8 months) F344xBN hybrid rats were received from the NIA Aged Rodent Colonies validated for studying aging similar to humans [6]. All rats underwent supraspinatus tendon transection and acute repair of the tendon back to its insertion on the humeral head with a modified Mason-Allen stitch using 4-0 Ethibond suture through a bone tunnel. The humerus including the tendon-to-bone insertion of the supraspinatus tendon, and muscle were harvested 2 weeks or 8 weeks from repair and frozen at -20°F for biomechanical testing.

Specimens were thawed and the humerus embedded in cuvettes using epoxy (Loctite). Specimens were mounted in a MTS servohydraulic load frame (MTS) using pneumatic grips in a posture representing 90° of shoulder abduction. Specimens were preloaded to 1N followed by a 10 cycle preconditioning after which a quasi-static load to failure test at a rate of 0.1mm/s was performed. Load and displacement were recorded at 100Hz and tendon thickness was collected using an IG-028 digital laser caliper system (Keyence) and optical camera system.

All measurements were reported as ratios \pm standard error of the mean between the repaired side and the healthy contralateral side of each animal. Statistical differences between groups were assessed using ANOVA with Bonferroni post-hoc analysis with alpha at 0.05.

RESULTS

The results of biomechanical testing for each group are presented in Table 1. Young animals showed significantly higher maximum load-to-failure strength at 8 weeks (86% of normal) after repair compared to old animals (65% of normal, $p < 0.05$), while maximum load-to-failure was similar 2 weeks after repair ($p > 0.05$). Maximum load-to-failure increased significantly from 2 to 8 weeks after repair in young and old animals ($p < 0.05$). At 8 weeks, the load at initial failure was significantly lower in old (49% of normal) compared to young animals (75% of normal, $p < 0.05$). However, initial failure strength was similar at 2 weeks.

The energy absorption up to ultimate load was significantly higher in young and old animals 8 weeks after surgery compared to the contralateral side ($p < 0.05$). Repaired specimen failed at the tendon-to-bone repair

site. Healthy specimen either failed in the tendon midsubstance or by greater tuberosity avulsion.

Mean linear stiffness ratios between the groups were significantly different; the average ratio for all groups ranged from 0.33 to 0.71. However, between the repaired sample and control sample within each group there was a trend in increased stiffness of the repaired tendon ($0.068 < p < 0.127$).

DISCUSSION

This study assessed the influence of normal aging on tendon-to-bone healing in an animal model of rotator cuff repair. The findings of this study revealed decreased maximum load-to-failure strength in old animals compared to young animals with less energy required to reach ultimate failure compared to the contralateral side. Eight weeks following repair the maximum strength was similar to the healthy control side in young animals, while in old animals maximum strength was only 63% of the healthy side. These findings suggest that in a validated rat model of aging, tendon-to-bone healing was significantly reduced following an established method of supraspinatus tendon repair [4]. It may also be noted that there was a trend in increased stiffness in the repaired tendon samples from each group.

Previous clinical studies have shown higher re-tear rates in older patients following rotator cuff repair compared to relatively younger patients [1]. Various age-related changes of the muscle-tendon unit may contribute to decreased healing potential after injury [7,8]; however most previous studies focused on increasing repair strength only for improved healing. The findings of our study suggests that tendon-to-bone repair in older individuals may lead to decreased load-to-failure strength during the later healing phases prompting caution during rehabilitation.

More recent basic science studies assessed the inclusion of growth factors, stem cells, or enzyme inhibitors to the tendon-to-bone repair [9]. While some improvements were in tendon-to-bone healing were observed, further analysis is needed to determine their use specifically in the older patient population. The findings from this study suggest that the aging rat model reveals decreased tendon-to-bone healing and strength similar to clinical findings, and therefore may be used for future studies of biologic materials for improvements in rotator cuff repair for elderly patients.

CONCLUSIONS

The influence of age on tendon-to-bone healing following rotator cuff repair remains poorly understood, as re-tear rates in older individuals have remained elevated despite improvements in repair techniques. This study assessed how normal aging decreases tendon-to-bone healing in a rat model to understand the underlying pathophysiology of rotator cuff repair in the older population to improve treatment strategies in the future.

REFERENCES

1. Oh JH. *Arthroscopy*, 25(1): 30-9, 2009
2. Yamaguchi K. *JBJS Am*, 88(8): 1699-704, 2006.
3. Galatz LM. *JBJS Am*, 86-A(2): 219-24, 2004.
4. Soslowky LJ. *JSES*, 9(2): 79-84, 2000.
5. Bedi A. *JSES*, 19(7): 978-88, 2010.
6. Betik AC. *Exp. Physiol*, 93(7): 863-71, 2008.
7. Delbono O. *Biogerontology*, 3(5): 265-70, 2002.
8. Delbono O. *Aging Cell*, 2(1): 21-9, 2003.
9. Bedi A. *Am J Sports Med*, 38(2): 308-17, 2010.

Table 1. Comparison of load-to-failure parameters between young and old animals 2 or 8 weeks after repair. Data presented as mean ratio to contralateral healthy side (standard deviation).

Parameter	Young animals (8 months)		Old animals (24 months)	
	2 weeks	8 weeks	2 weeks	8 weeks
Number of animals per group	n=10	n=12	n=10	n=10
Maximum load [N]	0.31 (0.09)*	0.86 (0.22)*§	0.26 (0.06)¥	0.65 (0.15)¥§
Initial failure load [N]	0.31 (0.12)*	0.75 (0.27)*§	0.22 (0.06)¥	0.49 (0.17)¥§
Energy to initial failure [J]	0.27 (0.12)*	1.72 (0.87)*	0.44 (0.21)¥	1.30 (0.48)¥
Energy to maximum load [J]	0.28 (0.20)*	1.06 (0.91)*	0.20 (0.12)	0.63 (0.58)
Ramp to failure stiffness [N/mm]	0.36 (0.15)	0.71 (0.40)	0.33 (0.24)	0.53 (0.44)
Average cross-sectional area [mm ²]	1.19 (0.56)	1.11 (0.40)	0.98 (0.43)	1.18 (0.41)

A p-value less than 0.05 was considered statistically significant; statistically significant difference between *Young 2weeks vs. 8 weeks; ¥Old 2 weeks vs. 8 weeks; ¶Young 2 weeks vs. old 2 weeks; §Young 8 weeks vs. old 8 weeks.

CANCER CELL MIGRATION DYNAMICS IN MECHANISTICALLY TUNABLE FIBROUS SCAFFOLDS

Puja Sharma¹, Shikha Bhatia², Carolyn Hughes³, Colin Ng⁴ and Amrinder S. Nain^{1,4}

1. Virginia Tech-Wake Forest University, School of Biomedical Engineering and Sciences
2. Virginia Tech, Biological Sciences
3. Virginia Tech, Biochemistry
4. Virginia Tech, Mechanical Engineering

Corresponding Author: Puja Sharma, pujas@vt.edu

INTRODUCTION

It is well established that the spreading of tumors is a complex phenomenon that includes a myriad of genetic, biochemical and biophysical changes in tumor cells and their microenvironment¹. For instance, mutations of tumor suppressor genes like p53, BRCA1 and APC², and genetic instability like aneuploidy have been associated with chromosomal abnormalities, proliferation, and invasion in cancer³. Similarly, higher expression of fibroblast growth factor (FGF) and vascular endothelial growth factor (VEGF) have been known to promote angiogenesis and metastasis⁴. Furthermore, changes in the mechanical properties like stiffness of cells⁵, and tumor microenvironment⁶ have been shown to increase the metastatic potential of cancer cells. While cancer studies in the past decade have developed sophisticated cancer models and probed several fundamental mechanisms, the fact that cancer metastasis still remains to be the leading cause of death in cancer patients⁷ suggests that we still do not understand the mechanisms underlying cancer metastasis well. It is also becoming increasingly pronounced that the influence of biophysical cues on cancer metastasis is much less understood than genetic or biochemical cues.

Cancer cells are constantly interacting with their surrounding extracellular matrix (ECM). In general, the

ECM is composed of nano-micron size diameter fibrous proteins, non-fibrous proteins, growth factors, glycoproteins and proteoglycans⁸. Most research platforms today, utilize 2D flat glass or 3D hydrogels to investigate the influence of mechanical properties like material stiffness on cancer cells^{8b, 9}. However, it has been observed that cells respond differently when presented with 2D flat surfaces and 3D substrates. Furthermore, studies have also suggested that local changes in mechanical properties of substrates may strongly influence cancer cell behaviors¹⁰. Therefore, in order to closely represent the native tumor microenvironment *in vitro*, a mechanistically tunable fibrous scaffold with fiber diameter and spacing in the nano-micro range is advantageous.

In this study, we utilize a previously explained Spinneret based Tunable Engineered Platform (STEP)¹¹ that is able to deposit highly aligned fibers in nano-micron diameter range whose mechanical properties like structural stiffness (N/m) can be changed by user defined choice of fiber diameter or length. Furthermore, using in house fusing techniques, these fibers have been fused to create nanonets that enable the calculation of migratory forces. The nanonet consists of higher and lower diameter fibers fused in a cross-hatch pattern (Fig. 1 (i)). As single cancer cells migrate along the fibers, they deflect the lower stiffness fibers allowing the calculation of migration forces using simple Euler beam equations¹² (Fig. 1 (iii) and (iv)). Investigating migratory forces is important as cancer cells constantly remodel their microenvironment to facilitate migration. The forces exerted by these cells would represent the extent of their remodeling abilities. Also, we show that the structural stiffness (N/m) influences migration speed of these cells. Effect of structural stiffness on cell migration is a new finding and we hope that this will encourage the community to investigate this in detail.

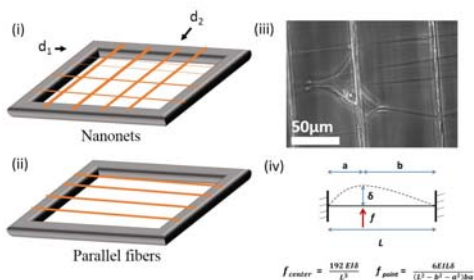


Figure 1. STEP (i) nanonets, (ii) parallel fibers, (iii) glioma cell deflecting smaller diameter fibers, and (iv) migration force calculation using Euler beam mechanics.

METHODOLOGY

Polymer solutions of polystyrene dissolved in xylene were used to manufacture highly aligned nanonets with two distinct fiber sizes using previously described STEP technique (Fig. 1). Fiber junctions were fused to form nanonets, and coated with fibronectin to facilitate cell adhesion. A glioma cell line, Denver Based Tumor Research Group (DBTRG-05MG), breast cancer cell line (MDA-MB-231), and a prostate cancer cell line (PC-3) were purchased from ATCC® and seeded on to the scaffolds. Time lapse video images of the cells were taken as the cells interacted and migrated along the nanonets. Deflections (δ) of the lower stiffness fibers, fiber length (L), and cell migration were measured using AxioVision® software. Single cell force measurements were performed using Euler beam mechanics theory¹². In order to assess the influence of structural stiffness on cancer cell migration, cells were seeded on highly aligned, suspended (Fig. 1 (ii)), 500nm diameter and 4mm long polystyrene fibers. Migration of the cells as a function of suspended fiber distance from the fixed edge was recorded.

RESULTS

Single cell force measurement: DBTRG05-MG cells migrated along the fibers and deflected the thin fibers (400nm diameter). Using Euler beam mechanics (Fig. 1), the force exerted by these cells were calculated to be 0.58 ± 0.06 nN. The diameters of the fibers were verified using scanning electron micrographs.

Cell migration and structural stiffness (N/m): Cell migration was calculated on highly aligned parallel fibers with 500nm diameter and 4mm length (Fig. 1 (ii)). On average, PC-3 (N=212), MDA-MB-231 (N=151), and DBTRG-05MG (N=67) cells were found to migrate at speeds 53, 63, and $85 \mu\text{m/hr}$ respectively. Furthermore, we observed that cells migrated slightly faster near the middle span lengths of the individual fibers (Figure. 2; Pearson correlation, $p=0.0021$ for DBTRG-05MG, $p=0.0212$ for PC-3 and $p=0.1823$ for MDA-MB-231).

DISCUSSION

We have observed that glioma cells exert migratory forces in the nanoNewton range as they migrate along the nanofibers. In future, we aim to calculate migratory forces exerted by normal astrocytes and compare the difference in forces exerted by normal and cancerous cells. Also, the efficiency of anti-migratory drugs can be evaluated by assessing the differences in migratory forces exerted by cells while being subjected to drug treatments. The

glioma cells prefer migrating along white matter tracts *in vivo* which range from less than 500nm to $3 \mu\text{m}$ in diameter. Since the nanonet diameters also occupies this range, we can assume that the STEP platform very closely represents the native glioma migration microenvironment.

Furthermore, we observed that glioma cells migrated the fastest in lower stiffness fibers. As the structural stiffness decreases towards the center of the fiber, glioma cells migrated faster while at the center of the fiber. While this influence was also considered statistically significant for prostate cancer cells, the breast cancer cells did not show such prominent influence of structural stiffness on cell migration speed. This suggests that the influence of structural stiffness as exhibited by one cell type may not always apply to the other. However, structural stiffness is a mechanical property that can influence cell behavior, and needs to be studied further.

CONCLUSIONS

The study shows that cancer cells exert very low forces on their microenvironment as they migrate. But, using the STEP nanonets, these forces can be measured. Also, we show that structural stiffness (N/m), negatively influences cell migration speed. However, this influence is dependent on the cell type and requires more investigation. These fundamental studies will allow us to capture the migration index of cancerous cells in different stages of disease and thus add to current understanding of the metastatic potential of single cancerous cells.

ACKNOWLEDGMENTS

The authors would like to acknowledge ICTAS, VT, Jeffress Memorial Trust, Andrea and Bill Wade Research funds, and the member of the STEP lab, VT.

REFERENCES

1. D. Hanahan, R. A. Weinberg, *Cell* 2011, 144, 646-74, DOI: 10.1016/j.cell.2011.02.013.
2. A. C. Society, 2011, vol. 2013.
3. D. J. Gordon, B. Resio, D. Pellman, *Nature reviews. Genetics* 2012, 13, 189-203, DOI: 10.1038/nrg3123.
4. R. Cao, H. Ji, N. Feng, Y. Zhang, X. Yang, P. Andersson, Y. Sun, K. Tritsaris, A. J. Hansen, S. Dissing, Y. Cao, *Proceedings of the National Academy of Sciences of the United States of America* 2012, 109, 15894-9, DOI: 10.1073/pnas.1208324109.
5. W. Xu, R. Mezenzev, B. Kim, L. Wang, J. McDonald, T. Sulchek, *PLoS one* 2012, 7, e46609, DOI: 10.1371/journal.pone.0046609.
6. P. Lu, V. M. Weaver, Z. Werb, *The Journal of cell biology* 2012, 196, 395-406, DOI: 10.1083/jcb.201102147.
7. P. Mehlen, A. Puisieux, *Nature reviews. Cancer* 2006, 6, 449-58, DOI: 10.1038/nrc1886.
8. (a) S. Suresh, *Acta biomaterialia* 2007, 3, 413-38, DOI: 10.1016/j.actbio.2007.04.002; (b) R. G. Wells, *Hepatology (Baltimore, Md.)* 2008, 47, 1394-400, DOI: 10.1002/hep.22193.
9. (a) M. H. Zaman, L. M. Trapani, A. L. Sieminski, D. Mackellar, H. Gong, R. D. Kamm, A. Wells, D. A. Lauffenburger, P. Matsudaira, *Proceedings of the National Academy of Sciences of the United States of America* 2006, 103, 10889-94, DOI: 10.1073/pnas.0604460103; (b) G. Schlunck, H. Han, T. Wecker, D. Kampik, T. Meyer-ter-Vehn, F. Grehn, *Investigative ophthalmology & visual science* 2008, 49, 262-9, DOI: 10.1167/iovs.07-0956.
10. S. P. Carey, C. M. Kraning-Rush, R. M. Williams, C. A. Reinhart-King, *Biomaterials* 2012, 33, 4157-65, DOI: 10.1016/j.biomaterials.2012.02.029.
11. (a) J. W. Kevin Sheets, Colin Ng, Puja Sharma, Sean Meehan, Mohammad Khan, and Amrinder S. Nain, *Journal of Biomaterials and Tissue Engineering In press*, 2013; (b) A. S. Nain, J. A. Phillippi, M. Sitti, J. Mackrell, P. G. Campbell, C. Amon, *Small (Weinheim an der Bergstrasse, Germany)* 2008, 4, 1153-9, DOI: 10.1002/smll.200800101; (c) S. Bakhru, A. S. Nain, C. Highley, J. Wang, P. Campbell, C. Amon, S. Zappe, *Integrative biology : quantitative biosciences from nano to macro* 2011, 3, 1207-14, DOI: 10.1039/c1ib00098e; (d) J. W. Amrinder S Nain, *Nature Polymer Journal* 2013, DOI: 10.1038/pj.2013.1; (e) S. W. Kevin Sheets, Colin Ng, Amrinder S Nain, *Acta Biomaterialia, In press* 2013.
12. R. C. Hibbeler, Pearson Prentice Hall: United States of America, 2011.

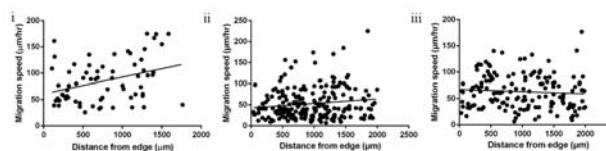


Figure 2. Migration speeds of (i) DBTRG-05MG, (ii) PC-3 and (iii) MDA-MB-231 cells on 4mm polystyrene fibers.

SMARTPHONE BASED CLINICAL ASSESSMENTS IN FRAIL PATIENTS

Rahul Soangra¹, and Thurmon E. Lockhart^{1&2}

1. School of Biomedical Engineering and Sciences, Virginia Tech

2. Industrial and Systems Engineering, Virginia Tech

Corresponding Author: Rahul Soangra, Email: srahul@vt.edu

INTRODUCTION

Falls are the most frequent cause of unintentional injuries in elderly people and occur in thirty percent of elderly above 65 years of age and in around fifty percent in elderly above 85 years of age. There is serious need for strategies to prevent falls in elderly but an important challenge in its prevention is paucity of objective evidence of the mechanisms that lead to falls. There is still no consensus in approach to predict and manage elderly falls, which has multifactorial risk factors associated with its occurrence in elderly. As U.S. population is aging, both the number of falls as well as the cost of treatment of fall injuries is continuing to grow. But since the past decades of research in fall prevention could not decrease the fall incidence, new strategies need to be introduced to understand falls over existing ones. Frailty is highly prevalent biological syndrome in elderly population, but all elderly are not frail. Aging along with disease, reduce the capacity of the frail people to adapt to various forms of stressors that can potentially be hazardous in maintaining stability and balance and may therefore result in fall.

Variability is an inherent, unavoidable as well as an important feature of all kinds of movements performed by humans. Human movement variability relates with already acquired motor skills and state of health. Understanding variability in activities of daily living may characterize mechanistic behaviors associated with movement stability or with less adaptability to perturbations. With aging there are several changes in muscle properties, which may influence movement execution. Some of these changes include reduced muscle cross section area[1] with reduction in strength and fiber type distribution [2] which reduces the movement speed. There is also decrease in motor units [3] and all these changes have implications for execution of movement in

old age[4]. Variability allows different choices among available options, selection of appropriate strategies, and flexibility to adapt to variations in the environment[5]. Variability may be viewed as increased flexibility of skill to allow adaptation to external perturbations.

Frailty has been investigated as a predictor of disability and adverse outcomes in older adults, and it has recently been investigated as a risk factor for patients undergoing cardiac surgery [18]. Cardiac surgeries are performed in half of elderly patients in North America and 78% of these surgeries result in major complications and deaths[19, 20]. Afilalo reported about 62% of cardiovascular disease (CVD) patients as frail in a population of 54,250 patients[21] and emphasized on relationship between frailty and CVD; frailty may lead to CVD, just as CVD may lead to frailty as they share common biologic pathways. CVD is also associated with threefold increase in frailty. The 6-month mortality is around 14.1%, which is around fourfold greater than in non-frail subjects. Elderly patients admitted to emergency departments with unexplained or recurrent falls including falls associated with unexplained loss of consciousness constitute 77% of cardiovascular disease disorders[22]. Also these fallers with intrinsic cardiovascular cause have higher mortality[23].

METHODOLOGY

The data acquisition device used in this study is an iPhone 5, which contains an ultra-compact low-power high performance 3-axis “nano” MEMS accelerometer, LIS331DLH. The LIS331DLH has dynamically user selectable full scales of $\pm 2g/\pm 4g/\pm 8g$ and it is capable of measuring accelerations with output data rates 0.5Hz to 1kHz. It is capable of measuring acceleration data with data sampling rate of 1000Hz. It also contains low-power 3-axis angular rate sensor, L3G4200D. The

L3G4200D has a full scale of $\pm 250/\pm 500/\pm 2000$ degrees per second and is capable of measuring angular rates at user-selectable bandwidth. An iOS 6 based App, named as "Lockhart Monitor" was designed to collect data. The App is written in objective C language using Xcode 4 IDE (Integrated Development Environment). The data is collected from inbuilt sensors, accelerometers and gyroscopes.

Five participants (three males and two females, age= 76.8 ± 6 years, height= 175.2 ± 12.3 cm, weight= 179.2 ± 25 lbs) participated in the study at Carilion Roanoke Memorial Hospital, Roanoke. An iPhone was mounted on ASIS and postural stability, and walking velocity data was collected using the app.

RESULTS

An algorithm was developed to evaluate walking speed using time taken after initiation of gait to its termination. Postural stability was assessed using .

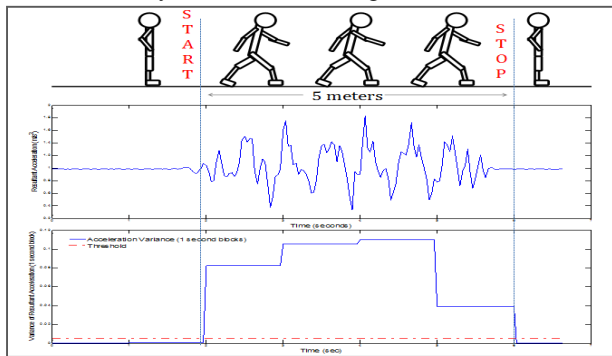


Figure 1: Schematic diagram showing computation of start and stop times from the app using threshold based real time algorithm

Table1: Walking speed of frail patients in clinical environment compared with stopwatch, light sensor and iPhone

Participant	StopWatch		Light Sensor		Iphone	
	Mean	STD	Mean	STD	Mean	STD
ID01	1.154	0.086	1.245	0.049	0.765	0.098
ID02	1.165	0.121	1.125	0.035	0.746	0.072
ID03	0.771	0.062	0.829	0.040	0.607	0.026
ID04	1.312	0.163	1.270	0.226	1.005	0.082
ID05	1.379	0.010	1.210	0.000	1.055	0.064

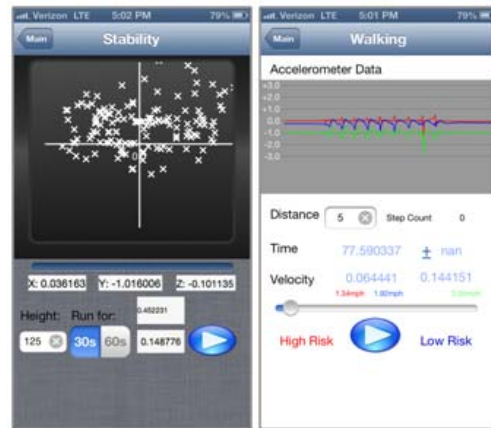


Figure 2: Screenshot of Lockhart Monitor Research App for postural stability (left) and walking speed (right).

It was seen that there was an error of $\pm 10\%$ in gait speed using stopwatch when compared with light sensors as gold standard. Where as iPhone always reported about 20% lower speed than that computed using light sensors.

DISCUSSION

A simple pilot study was conducted to screen frail patients using a smartphone application, with these results used to assist in steering the future study participant size requirement. Although this proof of concept has been developed, there are several smartphone related implementation issues that must be addressed before transitioning this technology to the clinical environment. To facilitate the acceptance of smartphone based systems, their mounting methods to the subject's body must be easy and comfortable while still providing accurate data. The longterm vision of the proposed quantitative fall risk assessment system is to change the existing paradigm for the at-risk elderly population by providing affordable, accurate and widely available fall assessments in the clinical setting.

REFERENCES

- [1] J. A. Kent-Braun and A. V. Ng, "Specific strength and voluntary muscle activation in young and elderly women and men," *J Appl Physiol*, vol. 87, pp. 22-9, Jul 1999.
- [2] J. Lexell, "Human aging, muscle mass, and fiber type composition," *J Gerontol A Biol Sci Med Sci*, vol. 50 Spec No, pp. 11-6, Nov 1995.
- [3] V. Galea, "Changes in motor unit estimates with aging," *J Clin Neurophysiol*, vol. 13, pp. 253-60, May 1996.
- [4] M. J. Kurz and N. Stergiou, "The aging human neuromuscular system expresses less certainty for selecting joint kinematics during gait," *Neurosci Lett*, vol. 348, pp. 155-8, Sep 18 2003.
- [5] R. T. Harbourne and N. Stergiou, "Movement variability and the use of nonlinear tools: principles to guide physical therapist practice," *Phys Ther*, vol. 89, pp. 267-82, Mar 2009.

HEAD IMPACT EXPOSURE IN MIDDLE SCHOOL FOOTBALL

Ray W. Daniel¹, Steven Rowson¹, and Stefan M. Duma¹

1. Virginia Tech – Wake Forest University, School of Biomedical Engineering and Sciences
Corresponding Author: Ray Daniel, Email: rwdaniel@vt.edu

INTRODUCTION

It is estimated that between 1.6 and 3.8 million sports concussions occur each year in the United States.¹ Emerging research suggests that repetitive sports-related concussions may result in neurodegenerative processes, including chronic traumatic encephalopathy.² Football is a leading activity that individuals under the age of 19 will experience a concussion during participation. Understanding the head impact exposure that players experience during participation in football will allow informed changes to league rules and equipment design to be made in efforts to reduce the incidence of concussion. Head impact exposure is defined as the characterization of the cumulative frequency, location, and head acceleration magnitude of impacts experienced by players.

Overall, there are approximately 5 million athletes participating in football, of which 3.5 million are youth players.³ To date, concussion research has primarily focused on the high school, college, and professional levels of play. These data have been used by researchers to quantify human tolerance to head impact and characterize the head impact exposure that players experience during play. Although 70% of football athletes are competing at the youth level, this is the area with the least amount of published research. Compared with adults, it has been suggested that younger persons are at an increased risk for concussions with increased severity and prolonged recovery.⁴ The objective of this study was to quantify the head impact exposure of a middle school football team, consisting of players between 12 and 14 years old. This was accomplished by instrumenting the helmets of players with accelerometer arrays. These data have applications towards improved helmet design and modifications to youth football in efforts to reduce the incidence of concussion.

METHODOLOGY

A middle school football team consisting of children ranging in age from 12 to 14 years participated in this study approved by the Virginia Tech Institutional Review Board. This study investigated head impact exposure in middle school football by instrumenting the helmets of ten players with an accelerometer array (Head Impact Telemetry (HIT) System, Simbex, Lebanon, NH). The instrumented players were chosen due to anticipation of high participation in practices and games. The instrumented players had an average body mass of $55 \text{ kg} \pm 10 \text{ kg}$ and had an average age of 13 ± 0.8 years. Players were equipped with accelerometer arrays for every game and practice, and linear and rotational head accelerations were measured for each head impact. Every time a player experienced an impact exceeding 14.4 g, data collection was triggered. Data collection lasts for 40 ms, with 8 ms of pre-trigger data. Data were then wirelessly sent to the sideline computer following an impact.

The accelerometer arrays consist of 6 single-axis high-g iMEMS accelerometers and are designed to integrate into Riddell Speed football helmets. Video analysis was used to verify impacts occurring in games and practices.



Figure 1: Instrumented helmet and sideline computer.

RESULTS

A total of 3414 impacts were recorded during practices and games for the 10 instrumented players during the middle school football season. The distributions for linear and rotational acceleration were right-skewed, being heavily weighted toward low magnitude impacts (Figure 2). The impact distribution for the average instrumented player had average accelerations of 27 ± 3 g and 1085 ± 157 rad/s², median accelerations of 21 ± 2 g and 890 ± 112 rad/s², and 95th percentile accelerations of 59 ± 10 g and 2641 ± 433 rad/s². Head impact exposure varied on an individual player basis, with certain players being more prone to high severity impacts. A total of 1317 impacts (39%) occurred during games and 2097 impacts (61%) occurred during practices. The average instrumented player experienced 341 ± 254 head impacts, which included 131 ± 112 impacts during games and 210 ± 147 impacts during practices. Furthermore, the average instrumented player experienced 17 ± 13 impacts per game and 7 ± 3 impacts per practice. Two instrumented players sustained concussions diagnosed by physicians. Player 1 sustained an impact of 87 g and 582 rad/s² to the top of the helmet, while player 2 had an impact of 67 g and 5207 rad/s² to the front of the helmet, both resulting in a concussion. The two impacts associated with diagnosed concussions resulted in acceleration magnitudes that were among the top 5% of all impacts for the respective player.

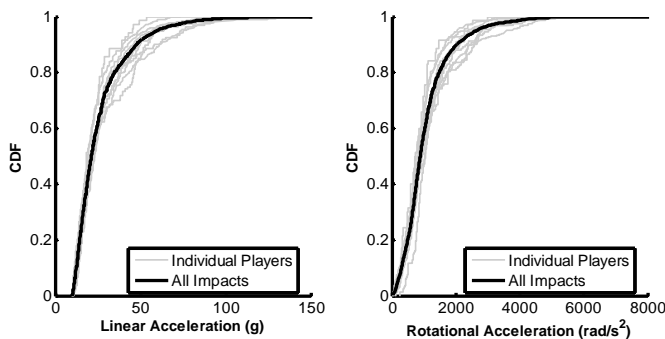


Figure 2: CDF plots for linear and rotational acceleration.

DISCUSSION

Head impact exposure in 12 to 14 year old football players was quantified. This age group is unique due to the greatest potential of variability between player size and ability relative to other age groups. Although impact distributions were weighted towards lower magnitude impacts, instrumented players still experienced high magnitude impacts (> 80 g). This level of severity is similar to some of the more severe impacts that college players experience, even though these players have less body mass and play at relatively slower speeds. When

comparing the frequency of impacts across level of play, the number of head impacts a player sustains each season rises with increasing level of play. As level of play increases, the number of games and practices also increase, which likely attributes to this trend. Acceleration magnitudes experienced at the middle school level were very similar to those experienced at the high school level, and notably higher than those at the 7 to 8 year old level of play. This may partially be attributed to middle school football players being more similar to high school players in musculoskeletal development, as well as the game structure being similar.

The instrumented middle school players impacted the front of their helmets most frequently, closely followed by the number of impacts to the rear of the helmet. This is similar to the trends exhibited by high school and collegiate players, and contrasts that of 7 to 8 year old players. The more developed musculature of the neck for the middle school players may lead to a substantially lower number of impacts to the sides of the helmet. Furthermore, players at the middle school level tend to be more experienced and have a better tackling technique than 7 to 8 year old football players.

CONCLUSIONS

In conclusion, valuable data describing the head impact exposure in middle school football has been presented for the first time. With an increased understanding of the head impact exposure in pediatric football, better equipment can be designed to prevent head injuries at the youth level. Methods to limit head impact exposure can also be implemented in order to create a safer environment for players.

REFERENCES

1. Langlois, J. A., et al. The epidemiology and impact of traumatic brain injury: A brief overview. *J Head Trauma Rehabil.* 21(5):375-8, 2006.
2. De Beaumont, L., et al. Long-term and cumulative effects of sports concussion on motor cortex inhibition. *Neurosurgery.* 61(2):329-37, 2007.
3. Guskiewicz, K. M., et al. Epidemiology of concussion in collegiate and high school football players. *Am J Sports Med.* 28(5):643-50, 2000.
4. McCrory, P., et al. Consensus statement on concussion in sport 3rd international conference on concussion in sport held in zurich, november 2008. *Clin J Sport Med.* 19(3):185-200, 2009.

INJECTABLE AND SELF-ASSEMBLING SPONGE AS A PROTECTIVE LAYER AT DEVICE-TISSUE INTERFACES IN WOUND REPAIR

Rui Wang^{1,2}, Louis C. Argenta², Michael J. Morykwas^{1,2}, and William D. Wagner^{1,2}

1. Virginia Tech – Wake Forest University School of Biomedical Engineering and Sciences
2. Wake Forest University School of Medicine, Plastic and Reconstructive Surgery

Corresponding Author: Name, Email: rwang@wakehealth.edu

INTRODUCTION

Injectable biomaterials with wound healing properties are of interest in surgical applications, especially at sites of device-wound interfaces. A self-assembling foam (sponge) was fabricated by cryogelation using silk fibroin protein (SF) and hyaluronic acid (HA). The cryogel can be injected locally to form a porous bioresorbable layer that prevents tissue injury at the wound bed, and allow easy removal of surgical devices and associated nondegradable foams. In this study, the mechanical property, morphology, and functionality of SF-HA cryogel were analyzed. An ex-vivo liver model was used to compare the outcome of using black nonabsorbable polyurethane (PU) foam with and without a cryogel layer under negative pressure wound therapy (NPWT). This system mimics the clinical setting. It is hypothesized the blend of silk fibroin (strength) and HA (wound repair promoting activity) will optimize the wound bed repair following NPWT. Residual cryogel containing HA left on the wound bed following removal of PU foam should favor wound repair.

METHODOLOGY

Silk fibroin protein was extracted from raw silk using an aqueous solvent processing method and identified based on amino acid analysis, molecular weight and functional groups prior to use [1]. Composites of silk fibroin, and hyaluronic acid were fabricated using cryogelation by first sonicating to form the gel, followed by lyophilization. Atomic force microscopy was used to measure gel elastic modulus, and scanning electron microscopy was used to observe the gel morphology. An in vitro free flow system was designed to measure the volume of fluid removed under NPWT. An ex-vivo liver test under clinically relevant settings (at -125 mmHg for

72 hours) was performed to compare the outcome of NPWT using PU foam with and without SF-HA, and with commercially available tissue protective silicon film (Mölnlycke Health Care, Sweden) [2]. The contacting device-tissue interface was examined.

RESULTS

Silk fibroin was successfully extracted and fabricated with hyaluronic acid using cryogelation. A highly porous and homogenous structure was observed in SF-HA cryogel compared to SF gel. The SF-HA cryogel had water binding ability with absorption of $234 \pm 35\%$. The elastic modulus was 4.79 kPa. Functional tests demonstrated comparable fluid removal with SF-HA coating. The black nonabsorbable PU foam was easily removed with SF-HA protective layer with minimal tissue damage comparing to the control PU foam alone.

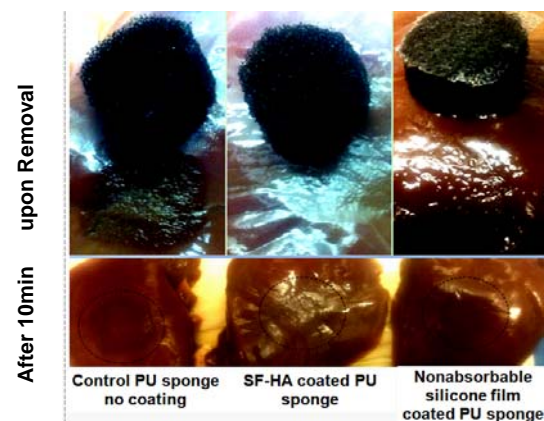


Figure 1: Photo showing wound-material interface after 72 hours of negative pressure wound therapy at -125 mmHg.

CONCLUSIONS

The cryogel made from silk fibroin and hyaluronic acid can be used as a potent tissue protective layer in negative pressure wound therapy to reduce dressing change associated pain and to prevent secondary injury to the wound bed. More widely applied, the SF-HA could significantly improve trauma patient care in clinics.

ACKNOWLEDGMENTS

Department of Plastic and Reconstructive Surgery, Center for Nanotechnology and Molecular Materials, and Department of Physics at Wake Forest University.

REFERENCES

[1] Hu, X., et al. *Biomacromolecules* 2010, 11 (11), 3178-3188. [2] DeFranzo, A. J. et al. *Plastic and Reconstructive Surgery* 2001, 108 (5), 1184-1191.

ELECTROPORATION ENHANCES ANTISENSE EFFECT OF PEPTIDE NUCLEIC ACIDS AGAINST INTRACELLULAR BACTERIA

Sai Ma¹, and Nammalwar Sriranganathan², Chang Lu^{1,3}

1. School of Biomedical Engineering and Science, Virginia Tech
2. Department of Biomedical Sciences & Pathobiology
3. Chemical Engineering, Virginia Tech

Corresponding Author: Chang Lu, Email: Changlu@vt.edu

INTRODUCTION

Salmonella enterica is an intracellular facultative Gram-negative anaerobe that infects a variety of hosts, including human beings. *S. enterica* causes over 33 million cases of disease in human beings around the world annually, which may even result in severe life-threatening systemic disease.

Antisense oligonucleotides (ODN) represent an innovative gene-silencing technology which has been successfully employed in regulating specific target genes. Peptide nucleic acid (PNA) is an ODN analog. It compliments to DNA and inhibit bacterial growth by blocking the function of essential genes.

One the critical factor that limits the antisense activity is the bioavailability of PNA inside of bacteria. The ability of the PNAs to cross the cytoplasmic membrane was facilitated by the cell penetrating peptide (CPP) via linker. The antibacterial activity decreased in cell culture compared in vitro since the PNA-peptide conjugates need to go through two additional phospholipid membrane to reach the target gene.

The other problem that hinders the widely use of PNA is the high expense of PNA. 25nmol PNA which takes more than \$500 is only enough for one batch of experiments in macro scale. Thus there is a strong incentive to improve the delivery efficiency of PNA in order to decrease the needed PNA amount.

In order to enhance the antisense activity of PNA in cell culture and cut down the expense for experiments, we employ electroporation to improve the therapeutic effects of PNA. Electroporation happens when an externally applied electrical field is applied. During the electroporation the electrical field opens nanoscale pores

which allow outside molecules to get into the cells. The main operational parameters of electroporation include field intensity and duration. They can be precisely and reproducibly controlled.

In our experiment, we treat a murine adherent macrophage cell line (J774A.1) infected by *Salmonella enterica* serovar Typhimurium LT2 (ATCC 700720) with PNA designed for RNA polymerase sigma 70 (sigma D) factor (rpoD). The rpoD PNA shows significant antibacterial activity in vitro but much weaker activity in infected cells. The infected macrophages are cultured in a microfluidic channel and are applied electric pulses of defined intensity and duration to improve the uptake of PNA. Our results show that the application of electroporation leads to the killing of *Salmonella* by a factor of 3 at least.

METHODOLOGY

The microfluidic chip for electroporation fabricated in polydimethylsiloxane (PDMS) using standard soft lithography. Briefly, a silicon wafer was pattern by SU-8 2025 to form a master. PDMS slab was produced by pouring and curing a PDMS prepolymer mixture (10:1 ratio) on the master. A glass slide pretreated with RCA cleaning and PDMS slab were oxidized with a plasma cleaner and sealed. The channel was filled with PBS buffer containing 0.1mg/μl fibronectin immediately after fabrication.

J774A.1 was infected with *S. enterica* serovar Typhimurium for 20min at a 1:1 multiplicity of infection. The infected J774A.1 with density of 10^7 cells/ml was incubated 1h in the microfluidic channel. Gentamicin which kills bacteria outside the macrophages was contained in the medium during incubation. The adherent macrophages after incubation was flushed by

electroporation buffer containing PNA. External electrical field with different intensity and duration time was applied to macrophages. The experimental setup is showed in **Figure 1**. The PNA treated macrophages were incubated for 4h before counting macrophages cell numbers, lysis macrophages and plate counting of survived *Salmonella*.

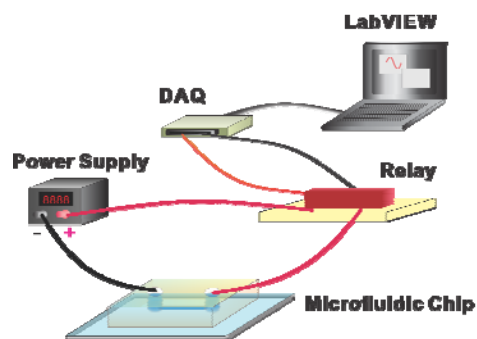


Figure 1: Experimental setup. LabVIEW controls pulse duration of the external electric field via Data Acquisition (DAQ) board. A relay is an electrically operated switch which connects power supply and microfluidic chip.

RESULTS

The macrophages are applied with different electroporation conditions to test the tolerability. The macrophages can stand electric pulse with duration time up to 7ms and field intensity up to 1400V/cm. (data not shown)

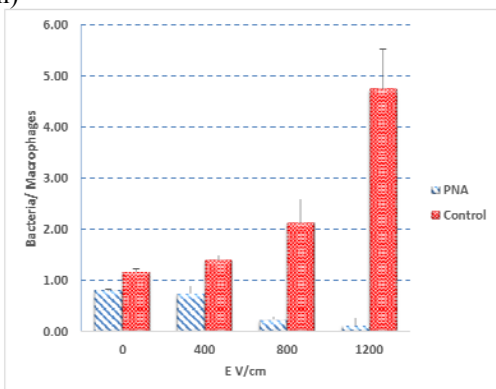


Figure 2: The ratio of bacteria to macrophages under different electroporation conditions.

Figure 2 indicates that PNA slightly reduces the bacteria in macrophages by 30% when there is no pulse applied (0 V/cm). When high field intensity was applied, more than 90% of bacteria was killed compare to control group. CPP-based delivery is not efficient and has a lot of space for improvement.

Figure 3 shows the PNA starts to inhibit bacteria growth when the concentration is larger than 30 μ M if there is no electroporation. When electroporation is applied, the PNA starts to inhibit *Salmonella* at concentration lower than 10 μ M. This suggests the electroporation significantly improves the PNA uptake.

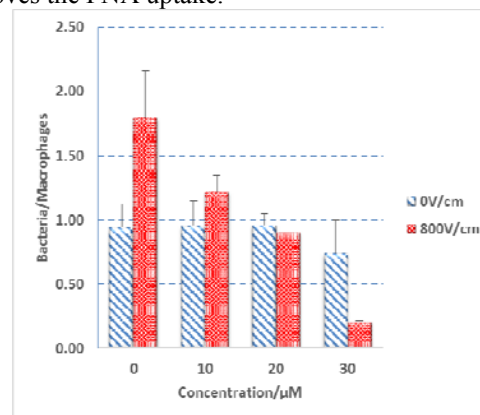


Figure 3: The ratio of bacteria to macrophages with different PNA (rpoD) concentrations.

CONCLUSIONS

Our results suggest that electroporation enhances the uptake of PNA which inhibit the growth of *Salmonella* in the macrophages. Electroporation with duration of 5ms and electric field of 800V/cm is the optimized condition that balances macrophages viability and bacteria inhibition.

ACKNOWLEDGMENTS

We thank NSF CBET 1016547 and 0967069 for the financial support of this research.

REFERENCES

- Soofi, M.A. and M.N. Seleem, Targeting *Salmonella* essential genes with antisense peptide nucleic acid. *Antimicrobial Agents and Chemotherapy*, 2012.
- Bai, H., et al., Antisense inhibition of gene expression and growth in gram-negative bacteria by cell-penetrating peptide conjugates of peptide nucleic acids targeted to rpoD gene. *Biomaterials*, 2012. 33(2): p. 659-667.

DEVELOPMENT OF AN OCCULT METRIC FOR COMMON MOTOR VEHICLE CRASH INJURIES

Samantha L. Schoell^{1,2}, Ashley A. Weaver^{1,2}, and Joel D. Stitzel^{1,2}

1. Virginia Tech-Wake Forest University Center for Injury Biomechanics
2. Wake Forest University School of Medicine

Corresponding Author: Samantha L. Schoell, Email: sschoell@wakehealth.edu

INTRODUCTION

Detection of occult injuries, which are not easily recognized and are life-threatening, in motor vehicle crashes (MVCs) is crucial in order to reduce fatalities [1]. Fatalities due to occult injuries arise due to injury severity, time sensitivity, and treatment criticality [2]. Detection of occult injuries in MVCs can be difficult because patients often sustain multiple injuries and these can mask the symptoms of other serious injuries. In addition, the injury may not be apparent initially at the scene. If the injury is left untreated, the victim can deteriorate fairly rapidly, suffering serious complications and even mortality.

Previously, the Center for Transportation Injury Research (CenTIR) developed an Occult Injury Database (OID) based on the NASS-CDS for the years 1997 to 2001 to analyze crash-related occult injuries [1,3]. The database contains the estimated frequency of occurrence of injuries sustained as well as the estimated frequency of occurrence of injuries that were cited as a cause of death. In addition, the OID study identified occult and non-occult head, thoracic, and abdominal injuries based on subjective expert opinion. For MVCs from 1997-2001, it was determined that nearly 65 percent of all injuries cited as a cause of death were due to occult injuries. The objective of this study was to develop an occult injury model based on underlying injury characteristics to derive an Occult Score for common MVC-induced injuries.

METHODOLOGY

Data used in this analysis was obtained from the National Automotive Sampling System-Crashworthiness Data System (NASS-CDS) for the years 2000 to 2011 [3]. For NASS-CDS 2009-2011 data, cases which involved motor

vehicles with a model year older than ten years were excluded from the analysis due to missing occupant and injury information. A list of the top 95 percent AIS 2+ weighted injuries (termed “Top 95% list”) was generated from NASS-CDS 2000-2011 for the analysis which included 240 injuries.

Statistical analysis was performed using JMP 9 software (SAS Institute, Inc., Cary, NC). A multiple logistic regression model was developed to generate a quantitative Occult Score on a scale from zero to one, where zero is a less occult injury and one is a more occult injury. The model was developed using the 120 head, thorax, and abdomen injuries with known occult or non-occult designations from the previous OID study and was applied to the Top 95% List [1].

The dependent variable in the analysis was the designation of an occult or non-occult injury which was coded as a binary variable. Many different combinations of independent or ‘predictor’ variables were tested to develop the best model for occult injury. Statistical analysis determined that one continuous variable and five categorical variables listed in Table 1 were the best predictors of an occult injury. Cause MRR/year was created from an updated OID analysis performed for NASS-CDS 2000-2011. Cause MRR/year is the annual proportion of occupants sustaining a given injury whose cause of death was attributed to that injury. Abbreviated Injury Scale (AIS) severity was defined as a dichotomous variable grouping AIS 2 and AIS 3 injuries versus AIS 4, AIS 5, and AIS 6 injuries. The variables Internal/External, Fracture, Laceration, Contusion, Hemorrhage/Hematoma, and Intracranial were all manually coded based on the AIS injury description. To distinguish between internal and external injuries, external injuries were defined as injuries which were visible or open including fractures,

lacerations, and bleeding which could be detected by visual examination. All other injuries which were not external were coded as internal.

RESULTS

The results of the multiple logistic regression model are shown in Table 1. Of the six variables entered into the model, five were significant ($p < 0.05$) as designated by (*). The whole model test ($p < 0.001$) and the lack of fit test ($p = 0.2350$) verified the fit of the model. Overall, the model predicted 84.17% of the 120 injuries correctly in comparison to the previous OID study. The model had an area under the receiver operating characteristic curve (AUROC) value of 0.876 which is excellent.

Table 1: Multiple logistic regression analysis results.

Variables	Parameter Coefficient	p-value
Intercept	-1.864	0.0010*
Cause MRR/year	0.526	0.6535
AIS 2-3 [1] vs. AIS 4-6 [0]	0.723	0.0396*
Laceration [1]	-1.721	<0.0001*
Hemorrhage/Hematoma [1]	-1.167	<0.0001*
Contusion [1]	-0.792	0.0216*
Intracranial [1]	-1.641	<0.0001*

From the model, a probability formula was generated to determine the probability (P) that a given injury is an occult injury as follows:

$$P = \frac{1}{1 + \exp(a + BX)} \quad (\text{eq.1})$$

where a is the intercept, B and x are vectors of the parameter coefficients and predictor variables, respectively. The a+BX term in Equation 1 which describes the contributions of each independent variable for the model is as follows:

$$-1.864 + 0.526 * [\text{Cause MRR/year}] + 0.723 * [\text{AIS}] - 1.721 * [\text{Laceration}] - 1.167 * [\text{Hemorrhage}] - 0.792 * [\text{Contusion}] - 1.641 * [\text{Intracranial}] \quad (\text{eq.2})$$

An Occult Score which ranged from zero to one was assigned to each injury based on the calculated probability with zero representing a non-occult (highly predictable) injury and one representing an occult (highly unpredictable) injury. The probability of an injury to be classified as occult is increased with more negative parameter coefficients and is decreased with more positive parameter coefficients. The distribution of the Occult Score is shown in Figure 1. A threshold value of 0.5 was set to distinguish between occult and non-occult

injuries. Of the 240 injuries on the Top 95% list, it was determined that 54% of head, 26% of thorax, and 23% of abdominal injuries were occult injuries. No occult injuries were identified in the face, spine, upper extremity, or lower extremity regions.

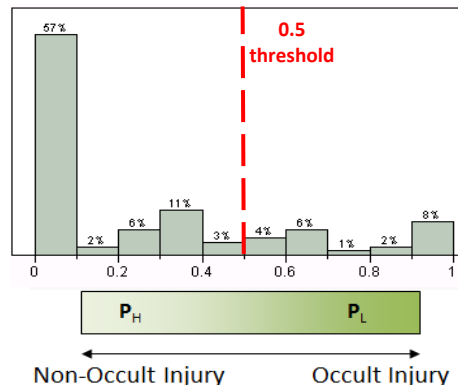


Figure 1: Histogram for Occult Score of the 240 injuries on the Top 95% list.

CONCLUSIONS

An Occult Score was developed to quantify the likelihood of an injury being occult for common MVCs. A multiple logistic regression model determined that Cause MRR/year, AIS 2-3 vs. 4-6, Laceration, Hemorrhage/Hematoma, Contusion, and Intracranial Injury were the best predictors of an occult injury. It was determined that 21% of the 240 Top 95% injuries in the head, thorax, and abdomen were occult injuries. The Occult Score developed can be useful in advanced automatic crash notification research and for the detection of serious occult injuries in MVCs requiring prompt treatment at a trauma center.

ACKNOWLEDGMENTS

We acknowledge Katrina Swett for her guidance in the development of the statistical model. Funding has been provided by Toyota Motor Corporation and its affiliates. Views expressed are those of the authors and do not represent the views of any of the sponsors.

REFERENCES

- Blatt, A.J., Bellis, E., *Occult Injury Database*, [Online]. <http://www.cubrc.org/centir/occult.html>.
- Champion, H.R., et al., *New tools to reduce deaths and disabilities by improving emergency care: URGENCY software, occult injury warnings, and air medical services database*. ESV Conference, Washington, DC, 2005.
- National Highway Traffic Safety Administration. *National Automotive Sampling System*, Department of Transportation, 2011.

KNOWLEDGE INTENSIVE LEARNING IN DISEASE RISK PREDICTION

Shuo Yang¹, Sriraam Natarajan¹

¹Wake Forest School of Medicine, Translational Science Institute

Corresponding Author: Sriraam Natarajan, Email: snataraj@wakehealth.edu

INTRODUCTION

Biasing learning algorithms that build predictive models with knowledge about the domain have been extensively explored in the field of Artificial Intelligence. In the case of probabilistic modeling such as Bayesian network classifiers, they have been employed to identify the relevant features and to specify the structure of the probabilistic distributions, prior distributions etc. A more recent method of providing guidance to probabilistic models is based on qualitative influences^{1,2,3,4,5}.

Medical literature provides a plethora of such knowledge due to decades of published research. In this work, we propose to use such knowledge in the context of building predictive models for informatics problems. More precisely, we extend the research in two directions -- First, current methods for qualitative influences can handle monotonicity statements while we extend these directions by allowing for synergistic interactions between random variables. Second, we treat each "set" of monotonicity and synergistic interaction as independent of each other and combine them with a combining rule. We employ Noisy-Or⁶ for combining the independent influences.

Qualitative influence statements essentially outline how the change of one variable affects the change of another variable. A classic example of such qualitative influence statements is monotonicity^{1,2,7} where an increase in value of one random variable (say cholesterol) increases the value of another variable (say risk of heart attack). From a probabilistic perspective, it simply says that the probability of heart attack is higher when the cholesterol level is high than when it is low.

While monotonicities model the qualitative dependency between two random variables, synergistic interactions allow for richer influence relationships. Assume that two variables X_1 and X_2 have monotonic influences on a third variable Y and they have a synergistic relationship. This means that increasing X_1 has a greater (lesser for anti-synergy) effect on Y for high values of X_2 than low values of X_2 (and likewise for increasing X_2 with fixed X_1). For instance, with synergies, it is possible to specify statements such as "increase in blood sugar level leads to a higher risk of heart attack when the cholesterol level is high than when cholesterol level is low". This statement explains how sugar level and cholesterol level interact when influencing the risk of heart attack.

A different method of encoding prior knowledge in probabilistic classifiers is to provide a set of conditional independencies that exist in the domain⁸. Also called as Independence of Causal Influences (ICI)^{6,9,10,11}, this form of knowledge identifies sets of features (attributes) that are independent of each other when affecting the target. The effects of these sets of risk factors can typically be combined using a (possibly stochastic) function such as Noisy-Or.

We evaluate the usefulness of such knowledge in the medically relevant task of predicting deaths from cardiovascular disease based on the patient's physiological indexes. Our extensive experiments show that the use of such knowledge leads to better predictive models in the presence of sparse data. In all the domains that we evaluate, the use of qualitative statements improves the performance over the model that assumes no prior knowledge. Also, such statements can be naturally provided by the expert who does not have to understand the use of the learning algorithm.

METHODOLOGY

In order to learn this distribution, we consider the final model to be a Bayesian network¹¹. In this work we are learning a function $f = P(y|x)$ which essentially gives the probability of the target attribute y – in our case, CV death – given other attributes x – in our case, the risk factors from using training examples. We are able to group these risk factors into several sets: blood pressure set, diabetes set and cholesterol level set which compose the medical test relevant set and the others (sex, age and smoke) into medical test irrelevant set, which then lead to the final output in a Noisy-Or structure. In addition to the setting described above, we propose to use knowledge from a domain expert or relevant medical literature in accelerating learning the probability distribution.

RESULTS

We considered a study on individuals with diabetes mellitus. The study has 14 years worth of data that includes various physiological indexes of 1102 diabetic patients among which there were 89 patients who died from cardiovascular disease. The goal of our experiment is to predict CVD caused death based on the 12 risk factors picked out from their records.

Both the parameters in conditional probability tables and the inhibitor parameters are learned by implementing six different types of learning algorithms: (1) learning only from data (denoted as None) (2) monotonic constraints only (denoted as Mono) (3) synergy constraints only (denoted as Syn) (4) learning assuming independence of all risk factors (denoted as N-Or) (5) monotonic constraints with Noisy-Or (Mono+N-Or) and (6) synergy constraints plus Noisy-Or (Syn+N-Or).

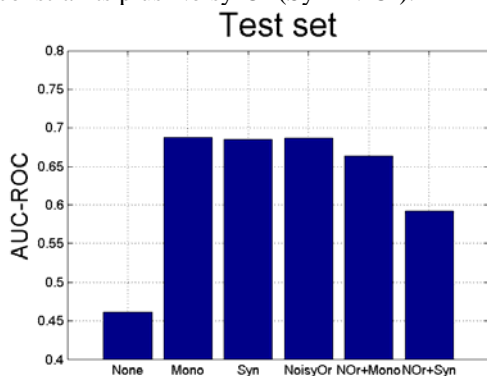


Figure 1. Results of clinical CVD data

As Figure 1 shows, the use of the qualitative constraints always improves the performance when compared to the use of no knowledge.

CONCLUSIONS

In this work, we have considered the problem of learning in the presence of knowledge-rich problems such as clinical prediction problems. In particular, we considered two forms of advice – qualitative constraints that specify the effect of the risk factors on the target of interest and a declaration of independence between the risk factors when influencing the target variable. We showed that this knowledge can be turned as constraints when learning conditional distributions and showed how to learn the parameters in presence of these models. We then evaluated the algorithms on a real study and established that the qualitative knowledge was very useful in prediction.

ACKNOWLEDGMENTS

Shuo Yang and Sriraam Natarajan gratefully acknowledge the support of Joseph Yeboah MD, MS, Donald W. Bowden, PhD and John Jeffrey Carr, MD at Wake Forest School of Medicine.

REFERENCES

1. M. Wellman. Fundamental concepts of qualitative probabilistic networks. *Artificial Intelligence*, 44:257303, 1990.
2. E. Altendorf, A. Resticar, and T. Dietterich. Learning from sparse data by exploiting monotonicity constraints. In *UAI*, pages 18-26, 2005.
3. A. Feelders and L. van der Gaag. Learning bayesian network parameters with prior knowledge about context-specific qualitative influences. In *UAI*, pages 193-200, 2005.
4. C. Campos, Y. Tong, and Q. Ji. Constrained maximum likelihood learning of bayesian networks for facial action recognition. In *ECCV*, pages 168-181, 2008.
5. Y. Tong and Q. Ji. Learning bayesian networks with qualitative constraints. In *CVPR*, 2008.
6. J. Pearl. *Probabilistic reasoning in intelligent systems: Networks of plausible inference*. Morgan Kaufmann Publishers Inc., 1988.
7. H. Brunk. Maximum likelihood estimates of monotone parameters. *The Annals of Mathematical Statistics*, 26(4): 607-616, Dec 1955.
8. J. Vomlel. Noisy-or classifier. *International Journal of Intelligent Systems*, 21(3): 381398, March 2006.
9. D. Heckerman and J. Breese. A new look at causal independence. In *UAI*, 1994.
10. S. Srinivas. A generalization of the noisy-or model. In *UAI*, pages 208-215, San Francisco, CA, 1993. Morgan Kaufmann.
11. J. Vomlel. Exploiting functional dependence in bayesian network inference. In *UAI*, pages 528-535, Edmonton, Canada, 2002.

KINETICS OF RELAXED VOLUNTEERS, BRACED VOLUNTEERS, AND HYBRID III ATD IN LOW-SPEED FRONTAL SLED TESTS

Stephanie M. Beeman¹, Andrew R. Kemper¹, Michael L. Madigan², and Stefan M. Duma¹

1. Virginia Tech – Wake Forest, Center for Injury Biomechanics

2. Virginia Tech, Kevin P. Granata Biomechanics Lab

Corresponding Author: Stephanie M. Beeman, Email: smbeeman@vt.edu

INTRODUCTION

Human occupant responses in motor vehicle collisions are commonly predicted and evaluated using computational models and anthropomorphic test devices (ATDs). However, these are validated using post mortem human surrogate studies, which do not include the effects of muscle activation [1, 2]. Continued development and validation of the aforementioned research tools necessitates further analysis of the effects of dynamic muscle activation on an occupant's biomechanical response in automotive collisions. Therefore, the purpose of this study was to investigate the effects of muscle activation on occupant kinetics in low-speed frontal sled tests and compare human volunteer responses to that of an ATD in matched test configurations.

METHODOLOGY

In this study, a total of 14 dynamic sled tests (5.0g, $\Delta v=9.7\text{kph}$) were performed with 5 male human volunteers and a Hybrid III 50th percentile male ATD using a custom mini-sled and rigid test buck accelerated by a pneumatic piston. Selected volunteers were approximately 50th percentile male height and weight (175 cm; 76.7 kg) [3]. Each volunteer was exposed to 2 impulses, one relaxed and the other braced prior to the impulse. The ATD was exposed to 4 impulses.

Relaxed and braced volunteer test conditions have been previously described [1]. The ATD was positioned in the center of the test seat, pelvis pushed backwards. Feet were centered on foot plates and the hands were held in place on a simulated steering wheel with masking tape. Prior to testing, all supportive masking tape was cut slightly to ensure that it would tear free during the test. All joints of the ATD were set to 1g, barely restraining the weight of

the limb when it was extended horizontally prior to each trial. For all tests, a load limiting driver side seatbelt was placed around the test subject and the slack was removed.

Reaction forces were measured at each subject-buck interface, including each foot plate, steering column, seat pan, seat back, lap belt, and shoulder belt. Load cell data channels were compensated for crosstalk and inertia. All load data was filtered using SAE Channel Frequency Class (CFC) 60 except for the lap and shoulder belt (CFC 180). Peak resultant force for each interface was compared between the two test conditions. Significance was determined using Student's t-tests ($p \leq 0.05$). Approval to conduct this human subject testing was granted by the Virginia Tech IRB.

RESULTS

Comparing the volunteer results, the average peak resultant force for the left foot, right foot, and steering column were larger during the braced trials, while the average peak force for the seat pan, seat back, lap belt, and shoulder belt were larger during the relaxed trials (Figure 1).

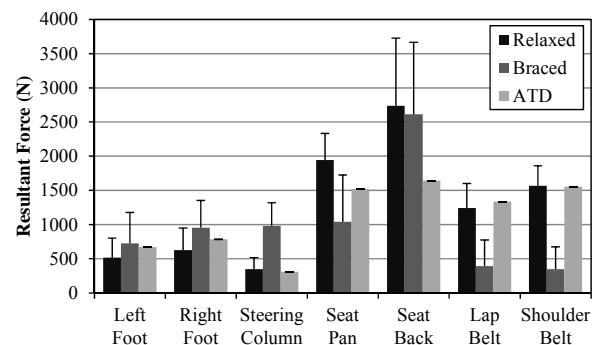


Figure 1: Average peak resultant forces.

The ATD response was different from both the relaxed and braced volunteer responses (Figure 1), but was less dissimilar from the relaxed volunteer responses (Table 1). The steering column force for the braced volunteers was significantly greater than that of the ATD, while the lap and shoulder belt forces for the ATD were significantly greater than those of the braced volunteers.

Table 1: Summary of Abrasion Test Results

Force Measurement	Relaxed vs Braced	Relaxed vs ATD	Braced vs ATD
Left Foot	0.15	0.02	0.66
Right Foot	0.02	0.07	0.27
Steering Column	0.00	0.54	0.00
Seat Pan	0.01	0.07	0.21
Seat Back	0.72	0.00	0.02
Lap Belt	0.00	0.58	0.00
Shoulder Belt	0.00	0.91	0.00

DISCUSSION

During the acceleration of the sled, the body of the subjects translated forward, loading the steering column, seat pan, foot plates, and belt. The seat back was loaded after the subject rebounded off of these interfaces.

When a subject was actively bracing, their arms and legs were extended, exerting a substantial initial force on the foot plates, steering column, and seatback. As a result of the sled acceleration, the body translated forward and the load was transmitted directly through the extended limbs of the braced subjects to the foot plates and steering column. Conversely, the initial joint flexion and passive resistance in the relaxed subjects and the ATD resulted in reduced loading at these interfaces and increased loading of the lap belt and shoulder belt.

CONCLUSIONS

This study illustrates that muscle activation has a significant impact on the biomechanical response of human occupants in low-speed frontal impacts. The kinetic analysis revealed that muscle bracing resulted in different reaction forces at the subject-buck interfaces and that the ATD response was dissimilar from both relaxed and braced volunteers at the low severity accelerations in this test series. Logically, differences in interactions with a vehicle's interior components can potentially result in different injury patterns. Overall, this study provides novel biomechanical data that can be used to refine and validate computational models and ATDs used to assess injury risk in automotive collisions.

ACKNOWLEDGMENTS

The authors would like to thank Toyota Motor Engineering & Manufacturing (TEMA) and Toyota Central Research and Development Laboratories (TCRDL) for sponsoring this research.

REFERENCES

- [1] Beeman, S.M. et al., 2011. "Effects of bracing on human kinematics in low-speed frontal sled tests." *Ann Biomed Eng* 39 (12), 2998-3010.
- [2] Beeman, S. M., et al., 2012. "Occupant kinematics in low-speed frontal sled tests: Human volunteers, Hybrid III ATD, and PMHS." *Accid Anal Prev*; 47, 128-39.
- [3] Schneider, L.W. et al., 1983, "Development of anthropometrically based design specifications for an advanced adult anthropomorphic dummy family", volume 1. NHTSA Contract No. DTNH22-80-C-07502.

JUMPING ON WATER: LOCOMOTION DYNAMICS OF *ACRIS SPP.* AND *E. CYANOPHLYCTIS*

Talia M Weiss¹

¹Virginia Tech, School of Biomedical Engineering and Sciences

Corresponding Author: Talia Weiss: talcat@vt.edu

INTRODUCTION

The exit and entry of bodies across a liquid interface is important for many engineering and biological problems. Such dynamics are important not only in designing submarines that surface efficiently and quietly or hydroplanes that land consistently and smoothly, but also in understanding how basilisk lizards can run on water or how dogs and cats drink by lapping. Despite the significance of these phenomena across various disciplines, the underlying physics are not well understood. Furthermore, most current engineering applications that function on the air-water interface occur at extreme values of a variety of non-dimensional comparative constants. For example, seaplanes and torpedoes occur at a Strouhal number (unsteady flow/stead flow: a measure of periodic motion involved in propelling a body) of zero and a Reynolds number (inertial/viscous forces) of 10^6 .

In contrast, many animal behaviors that occur on the water surface are performed at *intermediate* non-dimensional numbers. Thus, studying the physics and mechanisms behind animal locomotion on the water surface can not only yield new insight into the underlying biomechanics that produces the behavior, but also inform engineering decisions for devices operating at the air-water interface.

There are very few large animals that locomote on the surface of the water. A majority of the smaller insects that live on the water surface are light enough and have large enough surface areas due to hairy appendages to rely primarily on surface tension to offset their weight [3]. However, while there are several larger vertebrates which can also ‘run’ on the water surface, few have been studied in depth. The best studied is the basilisk lizard (*Basiliscus spp.*), which is hypothesized to support their weight while running by slapping the water

with their webbed feet and creating a deep air cavity, against the back of which they push. However, these animals almost always have one leg in contact with the water at a time [6], and the vertical position of their center of mass barely moves.

In contrast, there are several species of frogs reported to be able to *jump* on the surface of the water. While cricket frogs (genus *Acris*) native to the Eastern United States, especially *Acris crepitans*, the Northern Cricket Frog, have had several published reports of ‘skipping’ on the water in the 1950s [4], there has been no real study, or even videos taken, of this skipping motion. The frog best known for this skipping behavior, however, is *Euphlyctis cyanophlyctis*, the Indian Skipper Frog (depicted in Figure 1). This frog’s default escape mechanism from a disturbance is to jump on the water several times before diving under the water. *E. cyanophlyctis* can also jump up to three body lengths high from floating motionlessly in water [1]. The kinetics, kinematics, and fluid dynamics involved with this behavior have yet to be studied at all.

In order to start studying these frogs’ unique jumping behavior, high speed video of *E. cyanophlyctis* was analyzed using a combination of auto and manual tracking.



Figure 1: *E. cyanophlyctis* jumping on water. Each superimposed frame is 50 ms apart. Video taken from [2]

METHODOLOGY

High speed, 1080p video of *E. cyanophlyctis* jumping on water was taken from an episode of the BBC documentary *Natural World* [2]. It consists of 4 shots totaling around 30 seconds of footage at 25 fps. Only two

of the shots actually show several subsequent jumps. Frames were extracted from the video using FFMPEG in PNG format.

Both auto-tracking and manual tracking software were written in Python 2.7.3. To use either software, the user first draws a rectangle of the region of interest (ROI) in which the tracking should be done. In the auto-tracking algorithm, features are then calculated in the same ROI in pairs of frames using either SIFT, SURF, or ORB feature detectors and descriptors from OpenCV. Features from pairs of frames are then matched, and the average movement of the features is used to move the ROI to the next frame. The same features from previous steps are used until the total number of features matched is less than three, in which case features for a pair of frames are recalculated.

In the manual software, the user selects a point in the region of interest in each frame. The ROI is moved for each frame based on the movement of the manually selected point. If the ROI does not move enough due to errors in manual selection, the ROI can also be moved in each frame by the user by moving the arrow keys.

Estimates of *E. cyanophlyctis* body length and weight were taken from a variety of sources [1, 6, 7, 8]

RESULTS & DISCUSSION

The main challenges with trying to get any useful information out of the frog video was (1) a lack of markers and (2) the lack of resolution of the actual frog.

Auto tracking with either SIFT, SURF, or ORB features does not work well. Often, the automatic feature detector latches onto sprayed water droplets and thus the ROI moves off the frog's body. In addition, sometimes features match incorrectly, vastly changing the estimated displacement of the frog between frames.

To try and counteract the auto-tracking problems, a manual tracker was developed such that a user could pick a point on the frog and try to visibly track it. Due to the lack of resolution of the images, tracking the most likely center of mass position (on the main body of the frog) was extremely difficult, due to the uniformity of the frog in that area. Thus, tracking was attempted on the head right behind the eye. The resulting traces were not smooth, but at least showed the jumping motion of the frog.

CONCLUSIONS & FURTHER WORK

Unfortunately, due to the framing of the BBC video, the resolution of the actual frog is so low as to make any tracking information extracted from it minimally informative. In addition, the weight and length information collected on the frog species varied greatly in both terminology (is body length equivalent to snout-vent

length?) and values (5g – 15 g reported for ~5 cm frog). Due to these factors, almost no useful quantitative information can be recovered from these videos.

However, as summer approaches, it is possible to get specimens of *Acris spp.* Permits for collection of *Acris crepitans* in the wild have already been granted. In the near future I plan to thus run experiments with *A. crepitans* and *A. gryllus*. Frogs will be marked with non-toxic paint and filmed with multiple cameras skittering on the surface at >500 fps. By tracking the marks in the videos and calibrating the cameras, 3D kinematic information about the angles and velocities of joints can be calculated. By seeding the water with particles and illuminating the water with a laser sheet, digital particle image velocimetry (DPIV) can also be performed under the frog's feet. This can yield the forces that the frog is exerting on the water.

Large efforts have also gone into acquiring specimens of *E. cyanophlyctis*, which is native to South East Asia. The hope is that these frogs can also be acquired and run through similar experiments.

ACKNOWLEDGMENTS

I would like to thank NSF IGERT MultiSTEPS for providing funding for this project, and my advisors Dr. Jake Socha and Dr. Pavlos Vlachos for their continued advice and support.

REFERENCES

- [1] Nauwelaerts, Sandra, Jan Scholliers, and Peter Aerts. "A functional analysis of how frogs jump out of water." *Biological Journal of the Linnean Society* 83.3 (2004): 413-420.
- [2] "The Real Jungle Book Bear." BBC Natural World. BBC Two. April 5, 2012. Television (Documentary).
- [3] Bush, John WM, and David L. Hu. "Walking on water: biolocomotion at the interface." *Annu. Rev. Fluid Mech.* 38 (2006): 339-369.
- [4] Gans, C. "The process of skittering in frogs." *Annals of Zoology* 12 (1976).
- [5] Hsieh, S. Tonia. "Three-dimensional hindlimb kinematics of water running in the plumed basilisk lizard (*Basiliscus plumifrons*)." *The Journal of experimental biology* 206.23 (2003): 4363-4377.
- [6] Altevogt, R., H. Holtmann, and N. Kaschek. "High frequency cinematography studies on locomotion and preying in Indian skitter frogs *Rana cyanophlyctis*." *Journal of Bombay Natural History Society* 83 (1986): 102-111.
- [7] Shaikh, Kalsoom, et al. "A Study of Morphological Variations in Populations of *Euphlyctis cyanophlyctis* (Schneider, 1799)(Anura: Ranidae) From District Jamshoro, Sindh." *Pakistan J. Zool* 44.5 (2012): 1450-1452.
- [8] Singh, Ravi Kumar, et al. "Status and morphometric data of some anurans with reference to Agra district, Uttar Pradesh." *frog leg*: 7.

DEVELOPMENT OF HYALURONAN BASED NANOPARTICLES FOR INTRAOPERATIVE BREAST CANCER IMAGING

Tanner Hill^{1,2}, Aaron Mohs^{1,2,3,4}

1. Virginia Tech/Wake Forest School of Biomedical Engineering and Sciences
 2. Wake Forest Institute for Regenerative Medicine
 3. Dept. of Cancer Biology, Wake Forest University
 4. Comprehensive Cancer Center, Wake Forest University
- Corresponding Author: Tanner Hill, tahill@wakehealth.edu

INTRODUCTION

Breast cancer is the second most commonly occurring cancer in women next to skin cancer and is one of the leading causes of cancer deaths in women¹. Approximately 93% of all stage I/II breast cancers and 75% of stage III/IV breast cancers are treated surgically with either breast conserving surgery or full mastectomy. Unfortunately, approximately 30% of patients with stage I/II/III cancers treated surgically will experience recurrence of the disease^{2,3}.

In order to prevent this unnecessary recurrence of disease in patients with breast cancer, and potentially patients with other surgically treated cancers, we are investigating the potential for intraoperative near-infrared imaging to assist in full removal of tumors. Specifically, we are investigating the use of hyaluronan (HLA) based nanoparticles for targeted delivery of indocyanine green (ICG) to solid breast cancer tumors.

Hyaluronan is a naturally occurring polysaccharide that constitutes part of the extracellular matrix. HLA normally functions as lubrication for joints and connective tissues but it has also been found to be overproduced in many tumor types and may have a strong role in tumor progression⁴. Additionally, many tumor types over-express hyaluronidases, which are enzymes that break down HLA, and CD44, a cell surface receptor for HLA. These properties provide the potential for tumor specific targeting of HLA based nanoparticle delivery to tumors.

ICG is an amphiphilic near-infrared fluorescing molecule currently approved for retinal angiography. ICG has absorption and emission maxima ca. 790 nm and 820 nm, respectively. In circulation ICG will bind to the serum proteins and collect in tumors due to the EPR effect. However, this does not allow for active targeting that

association with an HLA-based nanoparticle may provide. In order to entrap ICG within the nanoparticle conjugation of HLA with a hydrophobic chemical moiety is required. In this work we present the examination of the effect of altering the structure and quantity of the hydrophobic ligand on the HLA backbone on nanoparticle size, ICG entrapment, and fluorescence quenching.

METHODOLOGY

5- β cholanic acid or pyrene butyric acid (Sigma Aldrich) were first refluxed in methanol and HCl at 60-65 °C for 6 hours to form 5- β cholanic methyl ester. The product was then precipitated and washed in cold methanol and dried under vacuum. This product was then dissolved into 1,3 diaminopropane and refluxed for 6 hours at 130-140 °C. This solution was then cooled to 0°C and the product was precipitated by addition of pure water to provide either 5- β -cholanamide (white solid) or pyrenebutanamide (brown waxy solid). These products were washed with cold water to remove remaining 1,3 diaminopropane. The presence of these products was confirmed using mass spectrometry and/or NMR.

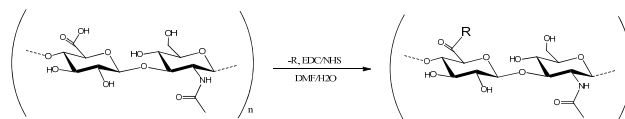


Figure 1. Conjugation of hydrophobic ligand to HLA.

Conjugation of hydrophobic ligands to HLA (Lifecore Biomedical, Chaska, MN) was obtained using the following method. HLA with molecular weight of 10-20 kDa. HLA was dissolved in pure water. Either 5- β cholananamide or pyrenebutanamide were dissolved in 24 ml *N,N*-dimethylformamide (DMF) at either 5, 10, or 20 wt%. 1-ethyl-3-(3-dimethylaminopropyl)carbodiimide and *N*-hydroxysuccinimide were dissolved in

water at 10X molar amounts of 5- β cholanamide or pyrenebutanamide and added to the HLA solution. The hydrophobic ligand containing DMF solution was then added dropwise to the HLA-water solution under constant stirring and reacted for 24 hours. The product was then dialyzed against 1:1 MeOH:H₂O for 1 day and pure water for 2 days. This solution was then lyophilized to obtain the nanoparticle material. ICG was loaded into nanoparticles by dissolving the hydrophobically-modified HLA and ICG into a 1:1 solution of dimethyl sulfoxide (DMSO): H₂O solution and dialyzing against pure water for 36 hours. Products were then filtered through PD-10 columns (GE Lifesciences) to remove free ICG and lyophilized again to obtain ICG-loaded nanoparticle material. The resulting nanoparticle was then tested for size distribution, absorbance and fluorescence.

RESULTS

Mass spectrometry confirmed the successful synthesis of both 5- β cholanamide and pyrenebutanamide. Conjugation to HLA was confirmed by formation of nanoparticles in pure water by DLS.

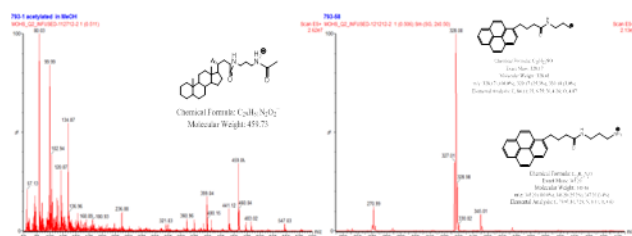


Figure 2. Mass spectrometry of hydrophobic ligands.

Both 5- β cholanamide and pyrenebutanamide HLA conjugates formed nanoparticles in water. These particles had a range from 10 nm to 5 μ m in diameter depending on weight percent and type of hydrophobic ligand. All materials that formed nanoparticles were capable of entrapping ICG.

Absorbance spectroscopy of ICG loaded nanoparticles showed a broadened ICG peak surrounding 800 nm, indicative of the presence of ICG concurrent with scattering expected of aggregated ICG. Fluorescence analysis showed successful fluorescence quenching of ICG-loaded nanoparticles.

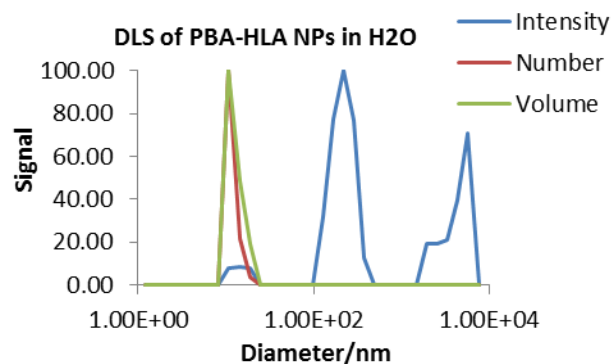


Figure 3. Dynamic light scattering of 10wt% PBA nanoparticles in water.

Both empty and ICG-loaded nanoparticles were examined for cytotoxic behavior. Cellular toxicity was found to exist at concentrations of .05 mg/ml and higher but physiologically relevant concentrations did not display toxicity.

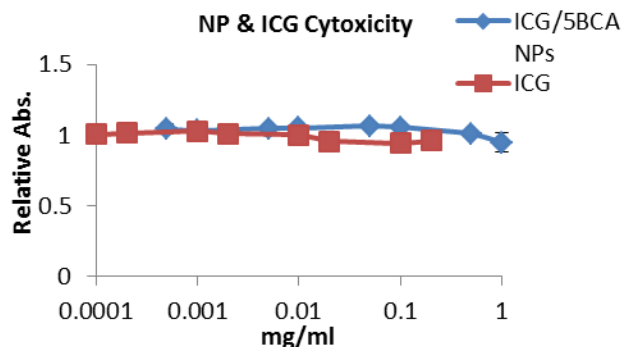


Figure 4. Cytotoxicity analysis of NPs.

CONCLUSIONS

Readily available hydrophobic amine ligands were successfully synthesized and conjugated to HLA. These conjugates formed nanoparticles in pure water and salt solutions and were capable of entrapping ICG and quenching fluorescence. While the size distribution of the nanoparticles varies, there are enough of appropriate sized for use *in vivo* after further physical separation techniques. These results provide a solid foundation for an *in vivo* analysis of nanoparticle mediated ICG delivery to tumors.

ACKNOWLEDGMENTS

R00 CA153916 (Mohs)
WFU-VT SBES

REFERENCES

1. <http://www.cdc.gov/cancer/breast/statistics/>
2. Siegel R. et al. 2012. *CA*. 2012.
3. Meric F et al. *Cancer*. 2003.
4. O'Toole, B. *Nature Reviews: Cancer*. 2004.

HEAD IMPACT EXPOSURE IN YOUTH FOOTBALL: ELEMENTARY SCHOOL AGES 7 TO 8 YEARS AND THE EFFECT OF RETURNING PLAYERS

Tyler J. Young¹, Ray W. Daniel¹, Steven Rowson¹, Stefan M. Duma¹

¹Virginia Tech – Wake Forest University, School of Biomedical Engineering and Sciences

Corresponding Author: Tyler Young, Email: tjy@vt.edu

INTRODUCTION

In the United States, 500,000 children between the ages of 8 and 19 years old visited emergency departments seeking treatment for concussions between the years of 2001 and 2005.¹ Of these injuries, approximately 50 to 60% occurred during organized sporting events. Due to its popularity and physical nature, football accounts for 50% of all sports related concussions in organized team sports.¹ To date, the primary focus of biomechanics research on concussions in football has been on professional, collegiate, and high school level players.³ However, of the 5 million athletes participating in organized football in the United States each year, 3.5 million are between the ages of 6 and 13 years old.² Athletes in this age group may be more susceptible to damage from head trauma due to a lack of full development in neural tissue and neck musculature. Thus, it is important to understand the exposure and tolerance to head impact at this level of play.

In order to make educated decisions toward reducing the incidence of concussion in football, head impact exposure must be quantified in terms of impact frequency, acceleration magnitude, and location. However, very limited data quantifying the head impact exposure in youth populations currently exists.

The objective of this study was to provide further data describing head impact exposure at the youth level and compare the differences in impact exposure between returning and first time players. These data are a further step toward developing effective strategies to reduce the incidence of concussion in youth football and have applications toward youth-specific football helmet designs.

METHODOLOGY

A youth football team consisting of children ranging in age from 6 to 8 years participated in this study. Head impact exposure was measured using accelerometer arrays installed into the helmets of 19 players. Instrumented players had an average age of 7.8 ± 0.4 years and an average body mass of 32.5 ± 8.1 kg. Each player was provided with a Riddell Revolution or Riddell Speed helmet that was fit to manufacturer specification. Helmets were instrumented with one of two accelerometer arrays that were used in parallel: the commercially available Head Impact Telemetry (HIT) System (Simbex, Lebanon, NH) or a custom 6 degree of freedom (6DOF) head acceleration measurement device.⁴ Head impact exposure was quantified in terms of impact frequency, acceleration magnitude, and location for games, practices, and the season as a whole. To compare differences in the impact exposure between returning and first time players and between games and practices, Kruskal-Wallis one-way analysis of variance tests were used. Statistical significance was determined using a threshold of $p < 0.05$.

RESULTS

A total of 3061 impacts were collected from the 19 instrumented players throughout the 2011 and 2012 seasons. The average instrumented player sustained 9 ± 6 impacts per practice, 11 ± 11 impacts per game, and 161 ± 111 impacts per season. Practices accounted for 60% of the recorded impacts and games accounted for the remaining 40% of impacts. The average instrumented player had a median impact of 16 ± 2 g and 686 ± 169 rad/s² and a 95th percentile impact of 38 ± 13 g and 2052 ± 664 rad/s² throughout a season. For both seasons of data collection, a total of 11 impacts collected were associated

with peak linear accelerations of 80 g or greater. These data demonstrate that players as young as 7 and 8 years old are experiencing head impacts that are similar in magnitude to severe impacts seen at the high school and collegiate level.^{2,3} Interestingly, the high severity impacts measured in this study tended to occur more frequently during practices ($p = 0.031$) (Figure 1), while high severity impacts tend to occur more frequently in games at high levels of play.^{2,3}

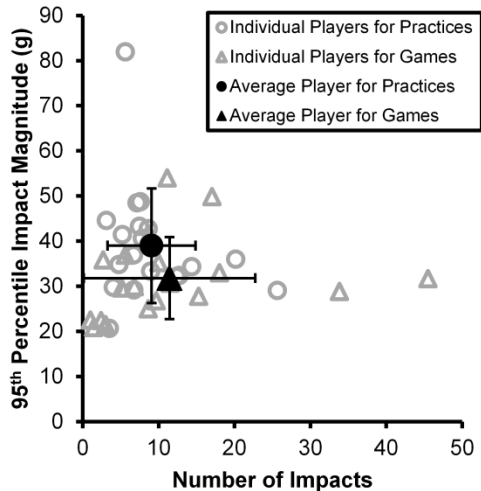


Figure 1: High severity impacts occur more frequently in practices.

Returning players had a significantly higher impact frequency than first time players ($p = 0.007$) (Figure 2). The average instrumented returning player experienced 15 ± 13 impacts per game, 11 ± 6 impacts per practice, and 211 ± 104 impacts per season; while the average instrumented first time player experienced 6 ± 3 impacts per game, 5 ± 2 impacts per practice, and 75 ± 59 impacts per season.

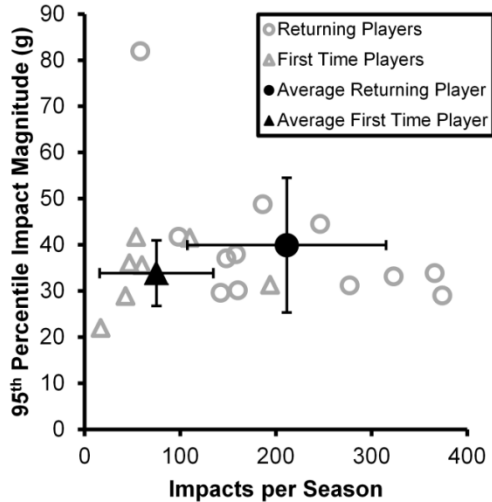


Figure 2: Returning players sustained more impacts than first time players.

DISCUSSION

Practices accounted for a larger proportion of high severity impacts and total impacts over the course of a season. Practice modifications that limit the amount of hitting and the use of high severity impact drills would reduce the overall impact exposure and the severity of impacts sustained by each player in a season. Because it is the earliest level at which players are allowed full contact, players who have been tackling for one year or longer may be less hesitant to engage with other players on the field resulting in the observed variation in player impact exposure. While the results of this study provide insight into the impact exposure of 7 to 8 year old football players, it was subject to limitations: a small sample size, a specific age group, and head acceleration measurement errors on the order of 1 to 6%.⁴

CONCLUSIONS

In conclusion, this study provides data further describing the impact exposure in youth football and provides insight to the differences in head impact exposure between games and practices, and between returning and first time players. This study demonstrated that some head impacts at this level are similar in magnitude to high severity impacts at the high school and collegiate level. High magnitude impacts were more frequently associated with participation in practices. Returning players experienced significantly more impacts than first time players. The data presented in this study will serve as a foundation for making scientifically based recommendations on practice modifications and youth-specific helmet design and standards.

ACKNOWLEDGMENTS

The authors gratefully acknowledge the National Highway Traffic Safety Administration for supporting this work.

REFERENCES

1. Bakhos LL, Lockhart GR, Myers R, et al. Emergency Department Visits for Concussion in Young Child Athletes. *Pediatrics*. 2011.
2. Daniel RW, Rowson S, Duma SM. Head Impact Exposure in Youth Football. *Ann Biomed Eng*. Apr 2012;40(4):976-981.
3. Duma SM, Manoogian SJ, Bussone WR, et al. Analysis of real-time head accelerations in collegiate football players. *Clin J Sport Med*. Jan 2005;15(1):3-8.
4. Rowson S, Beckwith JG, Chu JJ, et al. A six degree of freedom head acceleration measurement device for use in football. *J Appl Biomech*. Feb 2011;27(1):8-14.

PORCINE EYE RESPONSE TO BLAST OVERPRESSURE

Vanessa D. Alphonse¹, Andrew R. Kemper¹, Craig McNally¹, Ian P. Herring²,
Philip J. Brown¹, Joel D. Stitzel¹, and Stefan M. Duma¹

1. Virginia Tech – Wake Forest University Center for Injury Biomechanics
 2. Virginia– Maryland Regional College of Veterinary medicine
- Corresponding Author: Vanessa D. Alphonse, Email: vda@vt.edu

INTRODUCTION

Combat-related blast injuries are occurring more frequently with the increased use of explosives and improvised explosive devices (IEDs) in current military conflicts. Although it is suggested blast overpressure can cause severe eye injuries, there is no empirical evidence to support this. Additionally, there is a paucity of experimental data available in the literature to validate computational and physical models of the eye during blast overpressure loading. Therefore, the purpose of this research is to quantify the response of porcine eyes potted in synthetic orbits to blast overpressures of 10 psi and 20 psi and generate data for model validation.

METHODOLOGY

A 12 inch square helium gas-driven shock tube was used to simulate open-field blast overpressures. Six porcine eyes were exposed to a single face-on blast overpressure; three eyes were tested at 10 psi and three eyes were tested at 20 psi. The 10 psi and 20 psi levels refer to the static (“side-on”) pressure at the test location. Eyes were potted in a synthetic orbit with a 10% Knox gelatin solution to simulate the bony structures of the face and the fat/musculature around the eye (**Figure 1**). The synthetic orbit had a simplified orbital geometry with flat surfaces to serve as a precursory step to studying complex orbital geometry. A miniature pressure sensor was inserted into the eye to quantify intraocular pressure (IOP). Reflected (“face-on”) pressure measured at the forehead of the orbit and static (“side-on”) pressure measured both at the wall of the tube and in the flow field were recorded to quantify blast wave characteristics. All pressure data were collected at 300 kHz. Additionally, high-speed video of the eye was recorded at 10k fps. Injury risk for hyphema, lens damage, retinal damage, and globe rupture were calculated for each test based on intraocular pressure using published injury risk curves [1,2].

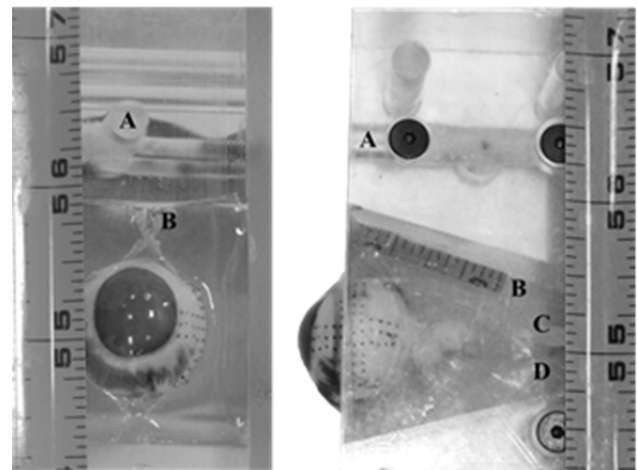


Figure 1: Front (left) and side view (right) of porcine eye potted in a synthetic orbit. (A) Reflected pressure sensor. (B) Ruler embedded in gelatin. (C) Pressurization tube. (D) Intraocular pressure sensor.

The reflected pressure (p_r) on a rigid surface normal to blast wave propagation was theoretically approximated using the Rankine-Hugoniot relationship (**Equation 1**). The equation was simplified by assuming the blast event occurred in air ($\gamma = 1.4$) [3]. Atmospheric pressure (p_a) was calculated to be 13.63 psi due to the 2132 ft elevation at the test location. Static pressure (p_s) at the wall of the tube was used for consistency between tests.

$$p_r = 2p_s \frac{7p_a + 4p_s}{7p_a + p_s} \quad (1)$$

Theoretical reflected pressure was compared to measured reflected pressure to verify instrumentation functioned properly in the face-on configuration at the 10 psi and 20 psi overpressure levels.

RESULTS

Minimal deflection of the cornea and sclera was observed and no serious eye injuries such as globe rupture occurred for any test. Pressure data and wave characteristics are reported in **Table 1** and **Table 2**, respectively.

Table 1. Peak measured pressures.

	Static Flow (psi)	Reflected (psi)	IOP (psi)
10 psi	11.26 ± 0.37	24.70 ± 0.87	20.36 ± 3.72
20 psi	22.55 ± 2.23	55.91 ± 5.58	34.33 ± 3.62*

*One test excluded due to outlying peak IOP (78.53 psi).

Table 2. Pressure wave characteristics.

	Static Wall (psi)	Duration (ms)	Impulse (psi*ms)
10 psi	10.27 ± 0.51	1.81 ± 0.02	8.30 ± 0.16
20 psi	17.68 ± 1.70	2.16 ± 0.33	15.57 ± 1.77

Predicted injury risk was $\leq 1.26\%$ for hyphema and $\leq 0.01\%$ for lens damage, retinal damage, and globe rupture. Measured reflected pressure was an average of 7.18% different from theoretical reflected pressure. Peak IOP was an average of 2.4 times greater than peak static pressure. Peak reflected pressure was an average of 1.2 times greater than peak IOP. Representative pressure traces are shown in **Figure 2**.

DISCUSSION

The finding that the IOP response was more similar to reflected pressure than static pressure is logical, as the eye and reflected pressure sensor experience both the static and dynamic components of the pressure wave in the current face-on configuration. The measured and theoretical reflected pressures differ by less than 10%,

indicating that the instrumentation worked properly in the current configuration. The data presented herein provides the first step toward a better understanding of how orbital geometry affects eye response to blast overpressure. Future work should include studying the effects of the complex orbital geometry.

CONCLUSIONS

This is the first study to quantify the response of porcine eyes to blast overpressures of 10 psi and 20 psi. The low predicted risk of serious eye injuries is consistent with the lack of observed injuries. The synthetic orbit and gelatin in which eyes were potted provided a more realistic set of boundary conditions around the eye than previously modeled [1]. Lastly, the blast overpressure measurements recorded in the current study provide valuable data for the validation of computational and physical models of the eye used to assess injury risk from exposure to blast overpressure.

ACKNOWLEDGMENTS

The authors would like to acknowledge the United States Army Medical Research and Materiel Command for their support of this research and development program.

REFERENCES

- [1] Alphonse VD, Kemper AR, Strom BT, Beeman SM, Duma SM. Mechanisms of eye injuries from fireworks. *JAMA*. 2012;308(1):33-4.
- [2] Kennedy EA, Duma SM. Eye injury risk functions for human and FOCUS eyes: hyphema, lens dislocation, and retinal damage. Prepared for: US Army Medical Research and Materiel Command, Fort Detrick, MD.
- [3] Iremonger MJ. Physics of detonations and blast waves. *Scientific Foundations of Trauma*. 1997;189-99.

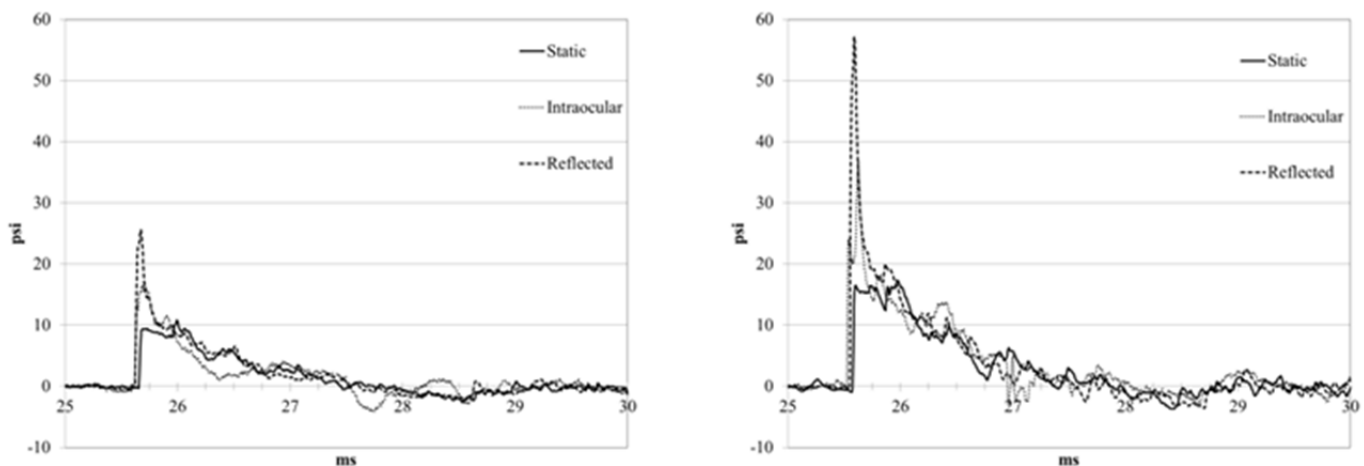


Figure 2: Representative pressure traces for a 10 psi test (Left) and a 20 psi test (Right).

CREATION OF NOVEL FLOW SYSTEMS INSPIRED BY INSECTS UTILIZING MICROFABRICATION TECHNIQUES

Yahya Hosseini¹ and Masoud Agah¹

¹Virginia Tech, The Bradley Department of Electrical and Computer Engineering
Corresponding Author: Masoud Agah, Email: agah@vt.edu

INTRODUCTION

Integrated pumping devices are essential components of microfluidic systems. They can be utilized for the transportation of biological samples, chemical reagent mixing, cooling of microdevice's units, micropropulsion and other applications, in precise, inexpensive and energy efficient manner. Over the last decade, numerous microfluidic devices have been developed for such purposes utilizing a peristaltic pumping mechanism first employed in the micro-scale by Unger et al [1].

In this study, utilizing the same microfluidic platform, we take a bio-inspired approach to experimentally demonstrate a novel pumping mechanism to generate continuous flow with the vision to harnessing the agility, low power requirements and efficiency of flow delivery.

The results from studying insect respiratory system have the potential to dramatically transform current microfluidic paradigms and tackle the emerging challenges of flow delivery at the micro-scale. It is hypothesized that flow is generated in the tracheal tubes of insects when the wall of these tubes undergoes localized collapse [2] (figure 1).

In this regard, we have fabricated a multi-layer PDMS device and demonstrated its application with the help of the studies and observations performed on the insect physiology [2] and computational modeling [3].

METHODOLOGY

The multi-layer PDMS device comprises of a simple fluidic channel, a thin membrane, and two actuation channels, plasma-bonded perpendicular to the fluidic channel, as shown in Figure 2. The fluidic channel is

250 μ m-wide and 50 μ m-deep, and the membrane is 50 μ m-thick. The membrane is actuated over the fluidic channel utilizing two syringe pumps (Harvard Apparatus Elite 11, MA, USA). The flow generation hypothesis in insects is modeled with the computational modeling, and is shown that if the walls of the tubes start to collapse at the same time with a phase delay at their maximum collapse point, flow can be generated. In order to generate optimum amount of flow employing this mechanism, the PDMS membrane is actuated as depicted in Figure 3. In order to measure the induced flow rate, fluorescent polystyrene beads with 1 μ m-diameter were introduced to the fluidic channel as shown in Figure 4. The experiments were performed 3-4 hours after injecting micro-beads in order to ensure they are in rest position inside the microfluidic channel. In order to measure the movements, the time-lapse images of micro-beads were captured every T (sec) for different actuation rate.

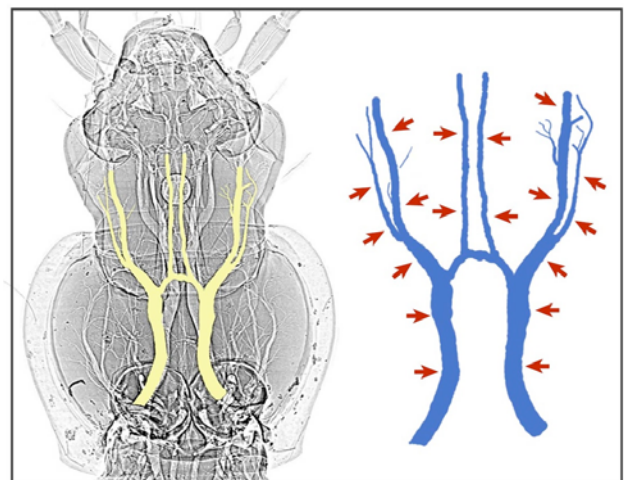


Figure 1: Tracheal compression in carabid beetles.
(Image is taken from Dr. Socha's lab website)

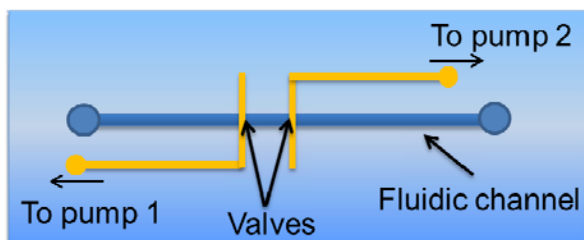


Figure 2: Top view of multi-layer PDMS device.

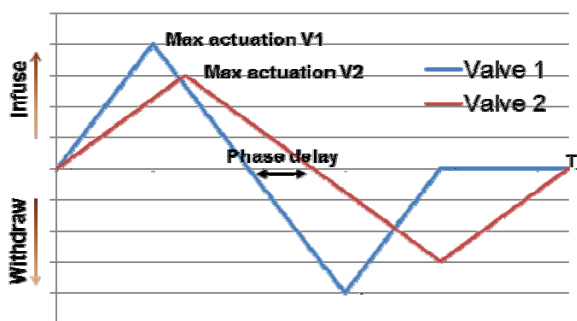


Figure 3: Actuation diagram of valves

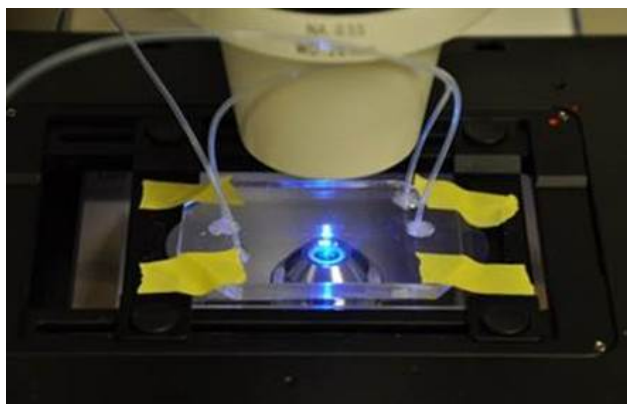


Figure 4: Multi-layer PDMS device on microscope stage.

RESULTS

Table 1 shows the induced flow rate inside the fluidic channel while the membrane is actuated at two different locations with different actuation rate. Subsequently, the phase delay was calculated and the result is shown in Figure 5. The optimum flow rate is currently under calculation based on the modeling and curve fitting methods.

Table 1: Induced flow rate at different flow rates

Actuation rate ($\mu\text{m}/\text{sec}$)	Actuation time T (sec)	Flow rate ($\mu\text{m}/\text{sec}$)	SD (n=11)
400 and 400	2.131	0.406	0.114
400 and 300	2.795	1.057	0.16
400 and 200	4.131	1.24	0.192
400 and 100	8.131	0.733	0.075

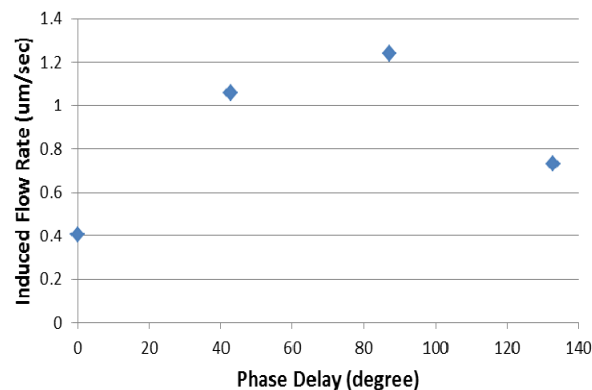


Figure 5: Induced flow rate at different phase delays.

CONCLUSIONS

We have successfully developed a multi-layer device in PDMS and implemented a naturally evolved paradigm to induce flow inside a microfluidic chamber. We are currently investigating the efficiency of such system compared to similar systems that are currently being used.

ACKNOWLEDGMENTS

This work has been primarily supported by the National Science Foundation under awards EFRI-0938047, ECCS-0747600 (CAREER Award), and Institute for Critical Technology and Applied Science (ICTAS).

The authors also would like to thank Dr. Alireza Salmanzadeh, Dr. Rafael Davalos, Dr. Yasser Aboelkassem, Dr. Anne Staples, and Dr. Jake Socha for providing helpful feedback and discussions.

REFERENCES

- [1] M.A. Unger *et al*, "Monolithic Microfabricated Valves and Pumps by Multilayer Soft Lithography," *Science*, 2000, vol. 288, pp. 113–116.
- [2] J.J. Socha *et al*, "Correlated patterns of tracheal compression and convective gas exchange in a carabid beetle," *J. Experimental Biology*, 2008, vol 211, pp. 3409–3420.
- [3] Y. Aboelkassem *et al*, "Flow transport in a microchannel induced by moving wall contractions: a novel micropumping mechanism," *Acta Mech*, 2012, vol. 223, pp. 463–480.

ULTRASENSITIVE MICROFLUIDIC DEVICE FOR THE STUDYING OF DNA-PROTEIN INTERACTIONS FROM SMALL NUMBER OF CELLS

Zhenning Cao¹, Changya Chen², Kai Tan², and Chang Lu^{1,3}

1. School of Biomedical Engineering and Sciences, Virginia Tech-Wake Forest, USA
2. Department of Internal Medicine and Biomedical Engineering, University of Iowa, USA.
3. Department of Chemical Engineering, Virginia Tech, USA

Corresponding Author: Zhenning Cao, Email: caozn@vt.edu

INTRODUCTION

Molecular biology tools for analyzing protein-DNA interactions are highly desired for the epigenetic study. Historically, *in vitro* methods such as electrophoresis mobility shift assays (EMSA) and DNase 1 protection assay were developed to evaluate protein-DNA interactions[1]. However, these methods cannot properly validate *in vivo* relevance. Chromatin immunoprecipitation (ChIP) assay has become the technique of choice for examining endogenous DNA-protein interactions over the years [2-5]. In a ChIP assay, chromatin fragments (200-600 bp) are mixed with IP beads functionalized by the antibody that specifically targets a protein. During the IP, both protein and DNA associated with the protein will be precipitated. After digestion of the protein, the identification of the associated DNA sequences can then be done by qPCR (i.e. ChIP-qPCR) if there are candidate genes. Alternatively, unbiased and genome-wide mapping of protein binding is possible by combining ChIP with high through-put sequencing (ChIP-seq) [4]. However, conventional ChIP requires a large number of cells ($\sim 10^6 \sim 10^7$ cells) and long processing time (~ 3 days). This sensitivity issue largely hinders its application to scarce primary samples from animals and patients. In this project, we developed an ultrasensitive microfluidic ChIP technology. Our microfluidic technology leads to dramatic improvement over the current state-of-the-art and enable studies of scarce primary cells from mice. In addition, the automated microfluidic based platform can dramatically reduce the total time (from ~ 3 days to several hours) and the hands-on time required for this assay and has the potential for future scale-up.

METHODOLOGY

Our lab demonstrated a microfluidic platform for native ChIP-qPCR based on as few as 50 cells without DNA pre-amplification (representing the highest sensitivity in the literature)[6]. As a significant extension to this work, I have generated solid preliminary data on high-efficiency extraction of ChIP DNA for ChIP-seq analysis. The prototypical microfluidic chip, which was fabricated by multilayer soft lithography[7, 8], is able to manipulate magnetic IP beads in various ways, including formation of compact packed bed (for surface adsorption of target molecules), oscillatory movement (for removal of nonspecific adsorption), and retention of beads by a magnetic field. Thus, all steps involved in immunoprecipitation can be handled by our microfluidic chip without manual operation. On the chip, the fluid and particles (chromatin fragments or beads) were directed to specific locations of the chip by micromechanical valves on the chip. The valves can be partially open to stop particle flow while permitting liquid passage, or be fully open/closed to allow/stop both liquid and particles. The inset images show the actual process operated in the microfluidic device. First, the antibody-coated magnetic beads were loaded into the microfluidic chamber and packed against a partially closed valve to form a packed bed (Fig. 1A). Second, we flowed solution containing chromatin fragments through the packed bed of IP beads where the target chromatin fragments were captured (Fig. 1B). Third, we have created a novel bead-washing method by applying alternative pressure pulse at the two ends of a microfluidic chamber (automatically performed by a LabVIEW program). The oscillatory movement of the magnetic IP beads removed non-specific binding from the bead surface (Fig.1C). Fourth, after the oscillatory movement, the beads were retained by a magnet while neat buffer was flowed to rinse the beads and chamber

(Fig. 1D). Finally, the IP beads were collected into a vial and ready for DNA analysis (either by qPCR or sequencing) (Fig. 1E).

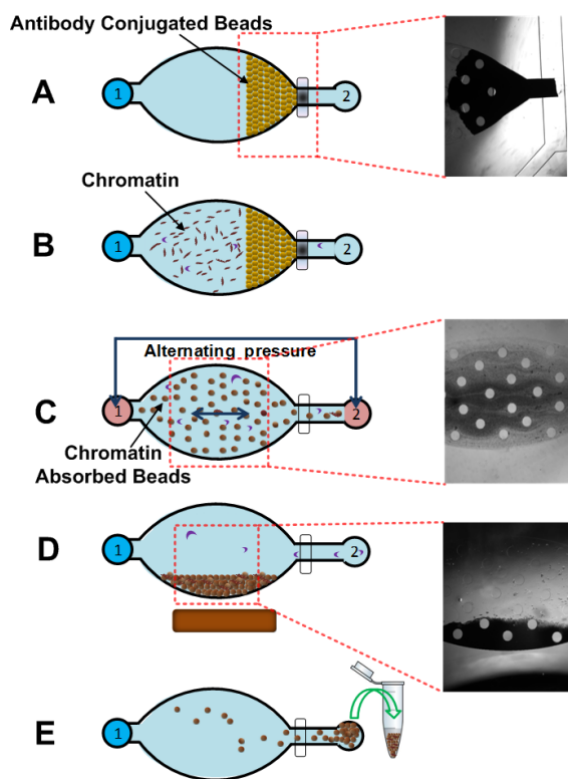


Fig. 1 The device design and the protocol for a microfluidic ChIP assay. Reservoirs 1 and 2 are the inlet and outlet. The inset optical images show the steps in a actual device (with supporting pillars in the chamber). (A) Magnetic IP beads loading. (B) Chromatin solution loading and IP. (C) Oscillatory movement of magnetic beads for removing nonspecific adsorption. Alternating pressure pulses will be applied at the ends of the chamber to create “washing”. (D) Rinse while beads retained by a magnet. (E) Beads collection.

RESULTS & DISCUSSION

We were able to produce high-quality ChIP DNA of 1~2 ng from 10,000 cells (concentration measured by Qubit 2.0 Fluorometer, quality confirmed by qPCR). Such ChIP efficiency was roughly over 100 higher than that of current state-of-the-art (~10 pg from 10,000 cells). With further optimization, we are confident that microfluidic ChIP-seq (requiring over 1 ng DNA) can be conducted based on 10,000 cells directly without pre-amplification.

CONCLUSIONS

In this project, we developed ultrasensitive and integrated microfluidic ChIP assays to study DNA-protein interactions. These microfluidic assays can be easily extended to benefit the study of many important biological problems (e.g. cancer development and stem cell differentiation) that require understanding of transcriptional regulation or epigenetic modification with experiments based on primary samples or rare cell types.

REFERENCES

1. Alberts, B., A. Johnson, J. Lewis, M. Raff, K. Roberts, and P. Walter, *Molecular biology of the cell*. 4th ed 2002, New York: Garland Science.
2. Massie, C.E. and I.G. Mills, *ChIPping away at gene regulation*. *Embo Reports*, 2008. **9**(4): p. 337-43.
3. Park, P.J., *ChIP-seq: advantages and challenges of a maturing technology*. *Nat Rev Genet*, 2009. **10**(10): p. 669-80.
4. Farnham, P.J., *Insights from genomic profiling of transcription factors*. *Nat Rev Genet*, 2009. **10**(9): p. 605-16.
5. Collas, P., *The current state of chromatin immunoprecipitation*. *Mol Biotechnol*, 2010. **45**(1): p. 87-100.
6. Geng, T., N. Bao, M.D. Litt, T.G. Glaros, L. Li, and C. Lu, *Histone modification analysis by chromatin immunoprecipitation from a low number of cells on a microfluidic platform*. *Lab Chip*, 2011. **11**(17): p. 2842-8.
7. Thorsen, T., S.J. Maerkl, and S.R. Quake, *Microfluidic large-scale integration*. *SCIENCE*, 2002. **298**(5593): p. 580-4.
8. Unger, M.A., H.P. Chou, T. Thorsen, A. Scherer, and S.R. Quake, *Monolithic microfabricated valves and pumps by multilayer soft lithography*. *SCIENCE*, 2000. **288**(5463): p. 113-6.